The University of Canterbury

Christchurch,

New Zealand

Application of the 3ω method to micro- and nano-scale thermal systems

A thesis submitted in partial fulfilment of the requirements for the degree of Doctor of Philosophy

By

Claude Meffan

Supervised By

Dr-Ing Volker Nock

Dr. Emilio Calius

September 26, 2019

Abstract

This thesis explores the application of the 3ω method of thermal conductivity measurement to new nanoparticle based thermal meta-materials, and novel microfluidic systems. Thermal meta-materials are systems in which the thermal energy is controlled and directed through meta-structure. These are one potential avenue through which high performance thermal insulation may be achieved. The 3ω method is well suited to thermal meta-materials as a characterisation tool, as it is one of only a few methods capable of thermally measuring micro- and and nano- sized features. In addition to this, this thesis also adapts the general concept of the 3ω method into a novel, spatially resolved, flow sensing device.

First, the classical and differential 3ω methods were implemented and calibrated. The classical 3ω method was calibrated on soda-lime glass and borosilicate glass. The values found were $1.15 \pm 0.01\ W/m-K$ and $0.99 \pm 0.01\ \ W/m-K$ respectively which were within experimental error of literature values. The differential 3ω method was also calibrated using spin-coated polymethylmethacrylate thin films. Measured values were $0.24\ W/m-K$ which was also within uncertainty of the literature value.

Following the calibration of the measurement technique, the thermal conductivities of two types of acoustically dissimilar nanoparticle meta-materials were measured. The first material consisted of blends of acoustically dissimilar nanoparticles, which had been formed into a close packed/packed bed structure. Blends of SiO_2, Al_2O_3, and Carbon nanoparticles were homogenised and formed into large circular pucks. These pucks were measured using both the classical 3ω method, and the guarded hot plate method. The lowest thermal conductivity in the packed nanoparticle bed materials was found to be $0.039\ W/m-K$. This value is substantially higher than previously reported values for these types of materials. The second thermal meta-material explored was a thin film nanoparticle-polymer superlattice. A $1\ \mu m$ thick Hybrid Bragg stack, composed of alternating layers of $22\ nm$ diameter SiO_2 nanoparticles and PMMA was fabricated using conventional semi-conductor spin-coating. This thin film was then measured using the previously established differential 3ω method. The thermal conductivity of this structure varied between 0.023 and $0.055\,W/m-K$, which

was attributed to the variability in the fabrication procedure. The average value was $0.043 \pm 0.014\, W/m - K$.

In the microfluidic flow sensing aspect of this work, the 3ω method was adapted into a novel tool for the measurement of fluid flow. A modified, serpentine design, 3ω resistance thermometer was integrated into the base of a multi-layered polydimethylsiloxane (PDMS) microfluidic device. The microfluidic device consisted of two vertically-stacked channels, isolated from each other by a thin PDMS membrane. Fluid flow could be actuated in each of the channels individually or collectively. The flow sensing resistance thermometer was capable of sensing fluid velocities as low as 1.6 mm/s in either channel. In addition to this, it was able to measure fluid flow with spacial resolution, and sense fluid flow through the PDMS membrane and through layers of static fluid. This system has a wide range of applicability from pure flow sensing, to the assay of micro-organisms. One particular area of interest is the assay of filamentous microorganisms. As an example of the utility of this sensor, the growth and thermal properties of the oomycete *Achlya bisexualis* was measured in a modified microfluidic/3ω system. The thermal conductivity of a bundle *Achlya bisexualis* hyphae was measured, and produced an $\sim 10\%$ shift in thermal conductivity compared to the static fluid control. This example application shows that, while more work is required, this technique can be utilised as a tool for the assay of biological organisms.

Acknowledgements

I would firstly like to thank Callaghan Innovation, the Ministry of Business, Innovation and Employment, and the Electrical and Computer Engineering Department, University of Canterbury for funding. Without your support this work would not have been possible. I would like to express my gratitude to my supervisors, Dr. Volker Nock, and Dr. Emilio Calius for their encouragement, advice and support throughout this research.

Thank you Alana, Azadeh, Louise, Rebecca, Nicola, Christine, Caixia, Jonty, Peter, Julian, Linda, Sevgi, Yiling, Maan, Helen, Gary and all the members of the NEST group for their help, mentorship, and encouragement in the lab.

Thank you to my parents, Patrick and Wendy Meffan, and my brothers Peter, Allister, and Ricky for their belief in me.

Finally, thank you Caitlin, for your patience.

Contents

Chapter 1

Introduction

Heat energy of uniform temperature [is] the ultimate fate of all energy. The power of sunlight and coal, electric power, water power, winds and tides do the work of the world, and in the end all unite to hasten the merry molecular dance.

-Frederick Soddy

1.1 Project Motivation

The initial motivation for this thesis was as a part of a Ministry of Business Innovation and Employment (MBIE)-led research project on architectured materials. One of the goals of this group was to study thermal meta-materials, and how they could be applied for the purposes of thermal insulation. In the beginning of this research, the 3ω method was established as a way of measuring the performance of these materials in this context. This lead to discovering the currently under-explored potential of this technique in the field of microfluidics. As such, this thesis is divided into two discrete fields, linked by the generalised 3ω method. The first three chapters of this thesis explore nanoparticle composite materials. Both the classical and differential 3ω methods are used to study their thermal performance in a variety of conditions and morphologies. The second section of this thesis explores the application of the 3ω method to microfluidics. It discusses the challenges of integrating a 3ω Resistance Thermometer (RT) into a microfluidic system, and shows how, as one example, the technique can be used to assess the growth of pathogenic micro-organisms.

The first three chapters of this thesis explore thermal meta-materials. The thermal meta-material field has grown with the advancement of microelectronics, and nanotechnology fabrication techniques. In modern devices, critical dimensions are becoming directly comparable to the wavelength and mean free path of thermal energy carriers. This in turn can create exotic heat flow phenomena which have only been observed recently. Some interesting examples of these phenomena include coherent phonon conduction [1], phonon confinement [2], solid materials which conduct heat like liquids [3], and the observation of chiral phonons [4]. The implications of these phenomena, as both challenges and opportunities, are wide ranging. As an example of a challenge, when the size of transistors in a computer chip are comparable to or less than the mean free path of thermal energy carriers, the rate of heat transfer out of the chip can become restricted due to the increased scattering rate. This reduces the power able to be dissipated, and decreases the chip performance. In contrast, a new area of research which has emerged is phase change materials. For example, vanadium oxide has been shown to facilitate the control and amplification of heat flux through thermal transistors [5]. This

allows heat flow to be controlled and amplified in much the same way electrical signals are in traditional transistors. In this research, the focus is how these new ideas and materials could be used as a tool to create high performance thermal insulation for buildings.

In order to study these new materials, a thermal measurement technique capable of measuring micro- and nano-structures is required. For this thesis, the 3ω method was chosen. This method is an electrothermal technique which uses the third harmonic voltage of a conductor to measure its temperature. Its most common use in literature is as a method of thermal conductivity measurement for sub-millimetre thin films [6]. Since its initial discovery, it has continued to be adapted by researchers and now is one of several advanced techniques for investigating micro- and nano-thermal systems [7]. This thesis extends the application of the 3ω method to new materials, and adapts it to new areas. Specifically it establishes and calibrates the 3ω method based on existing literature, uses the technique to measure several advanced thermal meta-materials, and advances its application by applying it to a novel microfluidic device. This research was carried out under supervision by Dr Volker Nock from the Electrical and Computer Engineering department, University of Canterbury, and Dr Emilio Calius from Callaghan Innovation, Auckland.

1.2 Thesis Structure

This thesis is structured into five main chapters, as well as the introduction, literature review, and conclusions. As previously mentioned, this thesis is divided into two distinct fields, and is linked by the 3ω method. To clarify, a pictorial representation of the thesis structure is shown in Figure 1.1. The first chapter discusses the 3ω method and the steps that were taken to establish the technique at the University of Canterbury, New Zealand. The second chapter applies the "classical" 3ω method to a composite pressed nanoparticle material. Three different blends of nanoparticle materials were measured and compared to literature values for similar systems. The third chapter discusses a highly structured nanoparticle-polymer superlattice. The thermal conductivity of this thin film is investigated using the differential 3ω method, and compared to the raw constituent materials. The fourth chapter

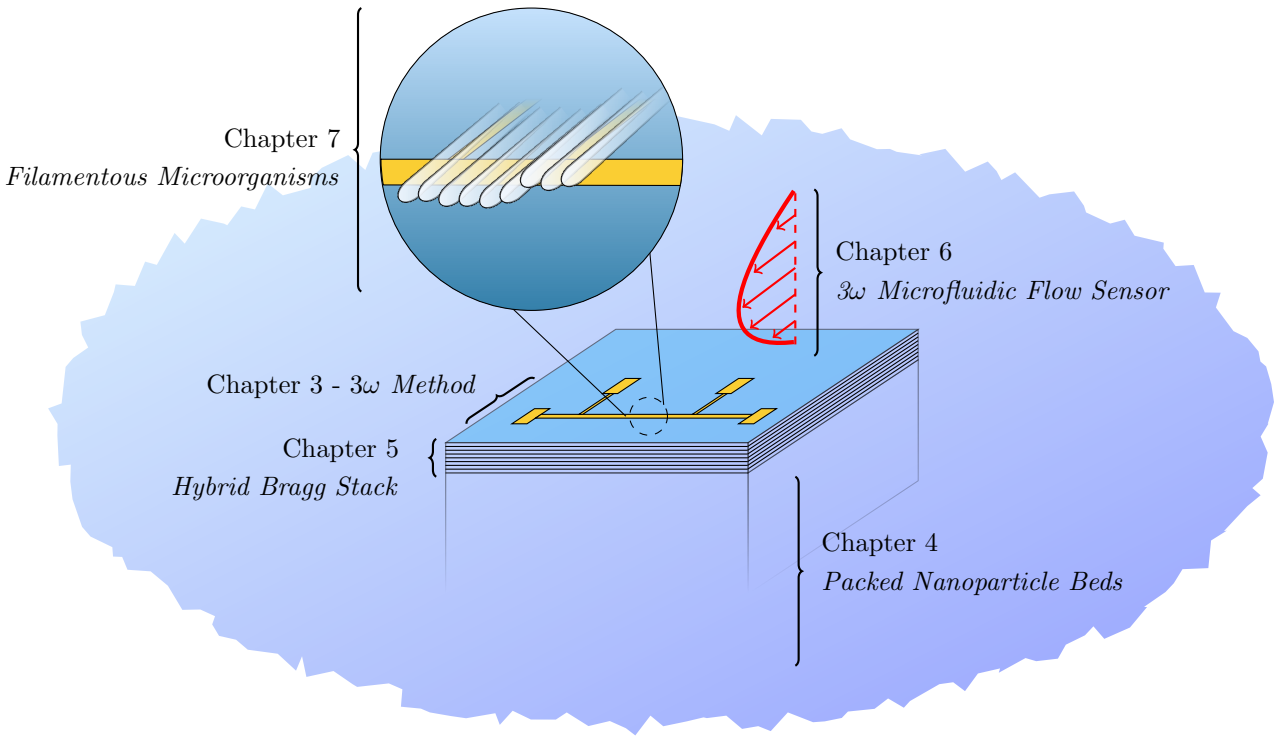

Figure 1.1: *A pictorial representation of the thesis structure. Chapter 3 covers the steps that were taken to physically establish the* 3ω *method at the University of Canterbury, New Zealand. Chapter 4 uses the classical* 3ω *method to measure bulk nano-particle thermal meta-materials. Chapter 5 uses the differential* 3ω *method to measure the thermal conductivity of a thin film nanoparticle meta-material. Chapter 6 adapts the* 3ω *RT to sense fluid flow with spatial resolution. Finally, Chapter 7 discusses how this modified system can be used as a technique for investigating filamentous micro-organisms.*

adapts the 3ω method for use in a microfluidic channel and uses it to measure fluid velocity with spatial resolution. The fifth chapter uses the microfluidic device to assess the growth of a species of oomycete, a type of water moulds related to species currently causing widespread damage to New Zealand's ecosystem.

1.3 Thesis Contributions

In Chapter 3 *"The 3ω method"*, the classical and differential 3ω method are established and calibrated based on existing literature.

In Chapter 4 *"Packed nanoparticle beds"*, packed nanoparticle materials were investigated using the classical 3ω method. Some of the highest performing packed nanoparticle materials in literature consist of blends of mechanically dissimilar nanoparticles. These materials have been shown to have thermal conductivities as low as $0.007\ W/m-K$ [8]. However, there is significant variation between the reported thermal conductivities depending on the measurement technique used. This work adds to the pool of knowledge on this topic by measuring the top performing nanoparticle materials from literature with two additional measurement techniques. The degradation mechanisms of these materials are also studied and compared to recent molecular dynamic simulations from literature [9]. Of the varying materials studied, the highest performing thermal insulator consisted of a blend of silica, alumina, and carbon nanoparticles, blended in a weight ratio 1/2/3 (SiO_2 / Al_2O_3 / Carbon Black). This resulted in a thermal conductivity of $0.039\ W/m-K$. It was also found that the materials degraded significantly over the course of one month in the presence of humidity.

Chapter 5 *"Hybrid Bragg stacks"* studies a Hybrid Bragg stack, a thin film nanoparticle material. This is composed of interleaved layers of polymethylmethacrylate (PMMA) and SiO_2 nanoparticles. These structures have been studied in the past for their ability to create phononic bandgaps in the direction perpendicular to the layer structure [10,11]. The thermal conductivity of this material had not been studied before however. In this work the thermal conductivities of the Hybrid Bragg stack is studied with the differential 3ω method for the first time, and compared to thin-film forms of the constituent materials. It was found that

the multilayered structure reduced the thermal conductivity by 3 to 10 times, when compared to the constituent materials. The average thermal conductivity of the Hybrid Bragg stack was found to be $0.043 \pm 0.014\, W/m - K$.

Chapter 6 *"3ω microfluidic flow sensor"* begins the microfluidics section of this work. A 3ω RT is integrated into a unique three layer microfluidic system, and used as a fluid velocity sensor. This is used to test the idea of using the finite thermal penetration depth of AC thermal waves to measure spatially resolved fluid flow parameters. It is shown in this work that a 3ω resistance thermometer, when configured in this way, is able to measure fluid flow in direct contact with the RT, and also from behind solid barriers such as membranes.

In Chapter 7, *"Filamentous micro-organism"*, it is proposed, based on the previous chapters work, that the modified 3ω RT could be used as a method of assessing the growth of the oomycete *Achlya bisexualis*. The oomycete was cultured in the microfluidic channel, and allowed to grow across the 3ω RT. It was found that there was a measurable thermal conductivity change when a group or bundle of *Achlya bisexualis* hyphae overlaid the top of the RT. However single hypha were not detectable compared to the empty channel control. Furthermore, fluid flow parameters inside the hyphae could not be identified from either of these responses.

This research has been prepared and presented in a range of formats. These are chronologically enumerated in the following sections.

1.3.1 Journal Publications

- "Beyond membrane flow sensing with AC resistance thermometry", Claude Meffan, Emilio Calius, Mathieu Sellier, and Volker Nock (*In preparation*)

- "Thermal Conductivity of packed nanoparticle meta-materials", Claude Meffan, Emilio Calius, and Volker Nock. (*In preparation*)

1.3.2 Conference proceedings

- *"Spatially resolved* 3ω *method for microfluidics and biology"*, Claude Meffan, Nicolas Cheradame, Mathieu Sellier, Emilio Calius, and Volker Nock. Proceedings of the 20^{th} International Conference on Solid-State Sensors, Actuators and Microsystems (Transducer/Eurosensors) (pp 1-4), 2019.
- *"Thermal conductivity of PMMA-*SiO_2 *phononic crystals measured by AC resistance thermometry"*, Claude Meffan, Emilio Calius, and Volker Nock. In Proceedings of 2017 IEEE SENSORS (pp. 1-3). IEEE, Xplore, 2017

1.3.3 Presentations

- *"Application of the* 3ω *method to microfluidics"*, poster presentation, 9th international conference on Advanced Materials and Nanotechnology, Wellington, New Zealand, 2019.

- *"Spatially resolved* 3ω *method for microfluidics and biology"*, Poster presentation, 20^{th} International Conference on Solid-State Sensors, Actuators and Microsystems (Transducer/Eurosensors), Berlin Germany, 2019

- *"Thermal flow sensor for micro-velocimetry and sub surface flow measurements"*, oral conference presentation, The annual Australia and New Zealand Nano and Microfluidics (ANZNMF) meeting, Auckland, New Zealand, 2018.

- *"Thermal conductivity of packed nanoparticle beds, measured by the* 3ω *method"*, oral conference presentation, 16th International Conference on Phonon Scattering in Condensed Matter (Phonons 2018) and the 4th International Conference on Phononics and Thermal Energy Science (PTES 2018), Nanjing, China, 2018.

- *"The 3ω method"*, Departmental seminar, Electrical and Computer Engineering department, University of Canterbury, Christchurch, New Zealand, 2018.

- *"AC resistance thermometry for thermal characterisation sensing inside a microfluidic channel"*, Claude Meffan, and Volker Nock. Poster presentation, International Conference on Nanoscience and Nanotechnology, Wollongong, Australia, 2018.

- *"AC resistance thermometry for thermal characterisation sensing inside a microfluidic channel"*, oral conference presentation, International Conference on Nanoscience and Nanotechnology (ICONN), Wollongong, Australia, 2018.

- *"Using Python as a tool for microelectronic, and nanotechnology research"*, University of Canterbury Microelectronic and Nanotechnology Laboratory users meeting, Christchurch, New Zealand, 2018

- *"Thermal conductivity of PMMA-SiO_2 phononic crystals measured by AC resistance thermometry"*, oral conference presentation, IEEE Sensors, Glasgow, Scotland, 2017.

- *"Fabrication of phononic meta-materials*, Thesis in three competition,University of Canterbury, Christchurch, New Zealand, College of Engineering Finalist, 2017

- *"Nanothermal insulation materials"*, Departmental seminar, Electrical and Computer Engineering department, University of Canterbury, Christchurch, New Zealand, 2016.

- *"Thermal conductivity of Hybrid Bragg stacks"*, oral conference presentation, 8th international conference on Advanced Materials and Nanotechnology, Queenstown, New Zealand, 2016

- *"Fabrication of phononic meta-materials*, Thesis in three competition, University of Canterbury, Christchurch, New Zealand, University Finalist, 2016

- *"Fabrication of thermal meta-materials"*, Claude Meffan, Emilio Calius, and Volker Nock. The MacDiarmid Institute Annual Symposium, Wellington, New Zealand. Poster presentation, 2015.

- *"Thermal Meta-materials"*, University of Canterbury Microelectronic and Nanotechnology Laboratory users meeting, Christchurch, New Zealand, 2015

Chapter 2

Literature review

The work in this thesis is divided into two distinct areas of inquiry; thermal meta-materials and microfluidics. As such, this literature review is structured into three sections. The first section is a brief discussion of the general "textbook" material and functional principles of thermal meta-materials. For an in-depth discussion of these principles, the reader is referred to literature [12]. Following this, the literature on thermal insulation and meta-materials is reviewed. Finally, a review of the 3ω methods use in microfluidics, flow sensing and microbiology is presented.

2.1 Thermal transport

Thermal transport in bulk materials can be described using Fourier's law [13]. This is a first order differential equation, which describes the rate of thermal energy transport due to a temperature gradient. It is formally described as,

$$q = -k \bigtriangledown T \tag{2.1}$$

where q is the heat flux density ($\frac{W}{m^2}$), k the material's thermal conductivity (W/mK), and $\bigtriangledown T$ the temperature gradient (K/m). Fourier's equation is the basis of many, if not all, thermal conductivity measurement techniques, i.e. a temperature gradient is placed across the material of interest and the heat flux through it is measured in some way. Fourier's law is mechanism independent, it does not describe the specific thermal transport mechanisms, just the rate of energy transfer. It can be compared to Ohms law in the sense that it relates energy, and rate of energy transport through a mechanism independent bulk material property [14]. In Ohms law this bulk property is resistance (Ω), and in Fourier's law this is the thermal conductivity (k). In order to engineer thermal meta-materials however, a more in-depth description of thermal energy carriers is necessary.

There are three broad thermal transport mechanisms: conduction, convection, and radiation [13]. Conduction is the transfer of thermal energy through the collision of particles, convection is the transfer of thermal energy by bulk particle movement, and radiation is

thermal energy transferred by electromagnetic waves. Conduction can be further subdivided into electrical and phonon conduction. In electrical conductors, electronic conduction dominates the total thermal transport for the material. As such, there is a well established linear relationship in electrical conductors between electrical and thermal conductivity. This is known as the Wiedemann-Franz Law [15]. By contrast, phonon conduction is dominant in electrical insulators. A phonon is a quasi-particle which represents a quantum of vibrational energy. These can be treated as particles or waves, depending on the material they exist in [12, 16].

Recently, there has been increasing research interest in phonon science and engineering. This is partly due to nano-fabrication capabilities passing a length scale which is comparable to thermal phonon wavelengths, meaning phonons are directly effected by the structure of modern devices rather than the material alone [12]. This has enabled the creation of phononic crystals (PnC), which create bandgaps for vibrational energies that propagate through them [10]. This is analogous to photonic crystals [17]. A phononic bandgap often has the effect of reducing the materials thermal conductivity, however this is not always the specific goal when engineering phononic crystals [10, 11, 18].

The name phonon comes from the greek root $\varphi\omega\upsilon\eta$ (*foné*), meaning voice, and in fact low frequency phonons are the carriers of sound in solids. In contrast, higher frequency phonons are thermal energy carriers. The highest frequency phonon possible is that with a wavelength twice the inter-atomic spacing of the material it exists in [12]. Phonons are classified as bosons, and as such follow Bose-Einstein (**BE**) statistics [12]. One important feature of **BE** statistics is that bosons are not limited by the Pauli exclusion principle. In brief, this means that many bosons can occupy a single quantum state. While phonons are inherently a quantum mechanical entity, many key principles can be described using classical mechanics, as long as the occupation is limited to a single mode [12]. For simplicity and brevity in this thesis, the key principles following are described through classical mechanics only.

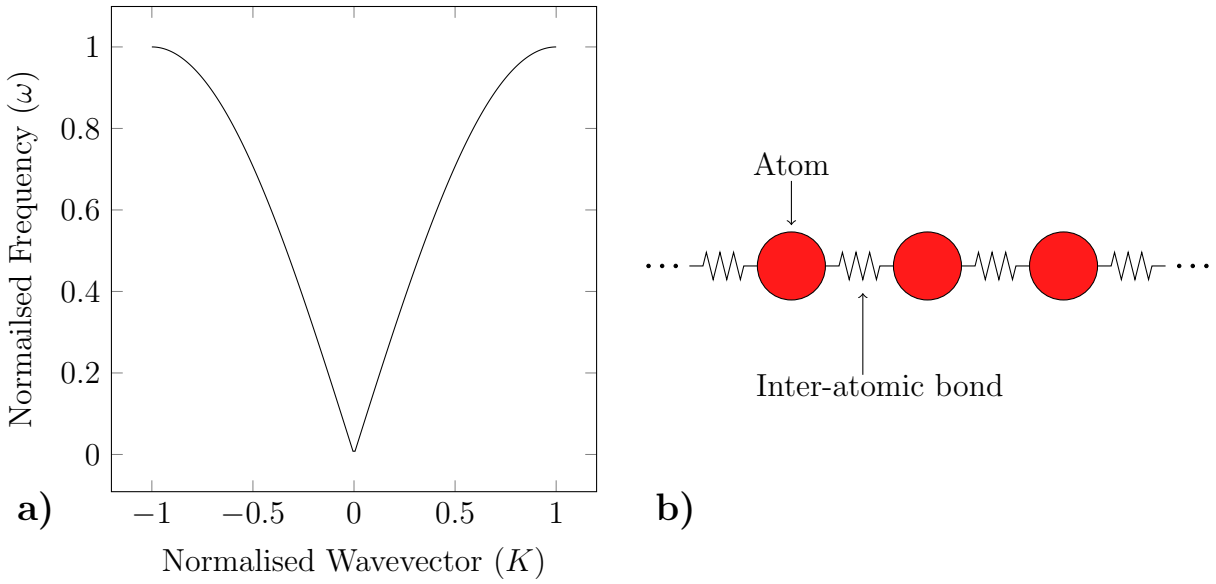

Figure 2.1: *The dispersion relation of a one dimensional chain of atoms, calculated using classical mechanics.* **a)** *The dispersion relation of the lower acoustic phonon branch.* **b)** *A pictorial representation of the mass-spring system used to calculate the lower acoustic phonon mode. The mass (red) represent atoms, while the springs between them represent the inter-atomic bonds.*

2.1.1 Dispersion relation

A dispersion relation is very similar to an electronic band diagram. It relates the allowable phonon frequencies (energy, equivalently) to wave vectors in a material. An example of a simple phonon dispersion relation is shown in Figure 2.1. There is only a single phonon mode shown in this dispersion relation, the longitudinal acoustic mode. This mode contributes strongly to thermal energy transport in solid materials. However, there can be multiple polarizations and additional phonon modes coexisting in the same material, which will all contribute in some way to thermal conduction. When real three-dimensional materials, and molecules with their own vibrational modes are considered, calculating this relation can become very complex.

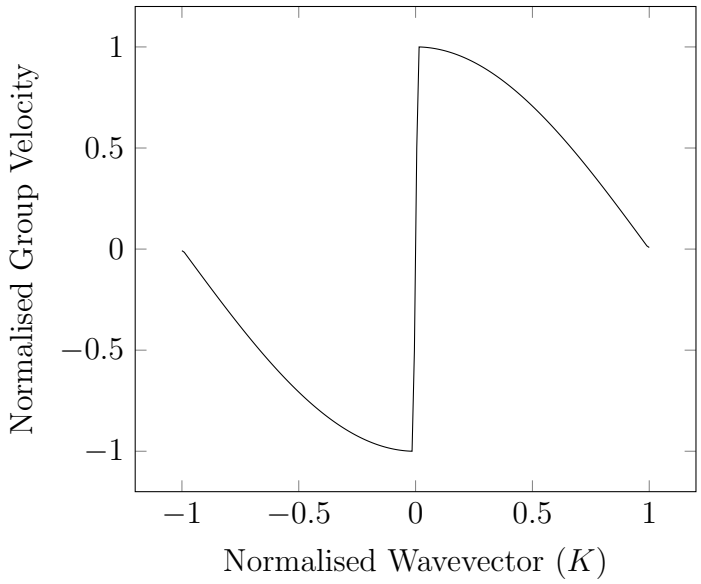

Figure 2.2: *The group velocity for wave-vectors along a 1 dimensional chain of atoms. In the long-wave ($K \to 0$), the group velocity approaches its highest magnitude. This corresponds with the speed of sound in the material.*

2.1.2 Group and phase velocity

The group and phase velocity are a derivative property of the dispersion relation. These velocities describe the rate that vibrational energy is transmitted through a material. The group velocity is the rate at which the envelope of an elastic wave propagates through space. From the dispersion relation the group velocity is defined as,

$$v_g = \frac{\delta\omega}{\delta K} \tag{2.2}$$

Where $\omega(K)$ is the dispersion relation, K is the wave-vector, and v_g is the group velocity. An important feature of the group velocity is the long-wave limit, $\lim_{K\to 0}\omega(K) = c$ in which the group velocity approaches the speed of sound in the solid (c). The group velocity of the example dispersion relation is shown in Figure 2.2. From this it can be seen that the group velocity approaches its largest value in the long-wave, ($K \to 0$) limit. The group velocity is an essential property of solid state thermal conduction, and literature on PnCs will often discuss the group velocity as the mechanism of thermal conductivity reduction.

The phase velocity meanwhile, is the rate the phase of a wave propagates through space. This is defined as,

$$c = \frac{\omega}{K} \tag{2.3}$$

2.1.3 Thermal conductivity from kinetic theory

The thermal conductivity of a material is defined by the relative contribution and density of thermal energy carriers. Continuing the analogy with electrical systems, the flow of thermal energy in a material can be analysed with kinetic theory, similar to the Drude model of electrical conduction [15]. Based on this idea, the thermal conductivity of a material can be expressed as,

$$k = \frac{1}{3} v_g \Lambda c_v \tag{2.4}$$

where v_g is the group velocity, Λ is the mean free path of available thermal energy carriers, and c_v is the specific heat capacity of the material. By inspecting Equation 2.4, ways to limit heat conduction in a fully dense material can be deduced. If any of the three terms which make up Equation 2.4 are decreased, the thermal conductivity will also. Phononic bangap materials often achieve this by reducing the group velocity. When a bandgap is placed such that it flattens the acoustic phonon modes, it has the effect of reducing the overall group velocity [19]. Alternatively, some materials seek to reduce the mean free path of phonons by placing scattering points within the material [20].

2.1.4 Transmission function

In PnCs, a bandgap is often achieved via engineering the transmission of phonons over the interface between two distinct materials [21–23]. When a phonon is incident upon an interface, it can either be transmitted or reflected. The likelihood of which is based on the acoustic properties of the materials surrounding the interface. There are two common and accepted models which describe this behaviour. The Diffuse Mismatch Model (DMM), and the Acoustic Mismatch Model (AMM) [12]. These models describe if a phonon is transmitted

or reflected through what is called the transmission function. The basic idea of interface transmission is shown in Figure 2.3. A phonon incident on an interface between two materials can either be transmitted or reflected, the likelihood of this is defined through a combination of the interface roughness, and the acoustic properties of the two materials. The DMM and AMM can both describe this transmission, however the applicability depends on the form of interface and the phonon being scattered. In particular, the roughness of the interface when compared to the phonon wavelength. A transmission function less than unity, in turn can be expressed as an interfacial thermal resistance, also known as Kapitza resistance [12]. For phonons the Kaptiza resistance is,

$$R = \frac{T_2 - T_1}{Q_p h} \tag{2.5}$$

where T_2 is the temperature on one side of the interface, T_1 is the temperature on the other side of the interface, and $Q_p h$ is the phonon flux across the interface. This expression provides further insight into how thermal conductivity might be controlled. When derived from kinetic theory, k was a function of group velocity, specific heat capacity and mean free path (Equation 2.4). However, when thermal energy carriers are completely scattered, such as in amorphous materials, a minimum known as the "amorphous limit" is reached [24]. In contrast, from Equation 2.5 it can be observed that material interfaces can create temperature jumps or discontinuities. The addition of many kapitza resistances and discontinuities in a material can allow for the amorphous thermal conductivity limit to be surpassed by composite and multilayered materials. A thermal conductivity beneath that of the amorphous limit is often termed "ultra-low" [21].

In the next sections, the specific criteria of the acoustic and diffuse mismatch models are discussed.

2.1.5 Acoustic mismatch model

The acoustic mismatch model is applicable for the transmission of phonons across "smooth" interfaces, where the roughness of the interface is much less than the phonon wavelength being transmitted [12]. A basic representation of this is shown in Figure 2.3. In this model,

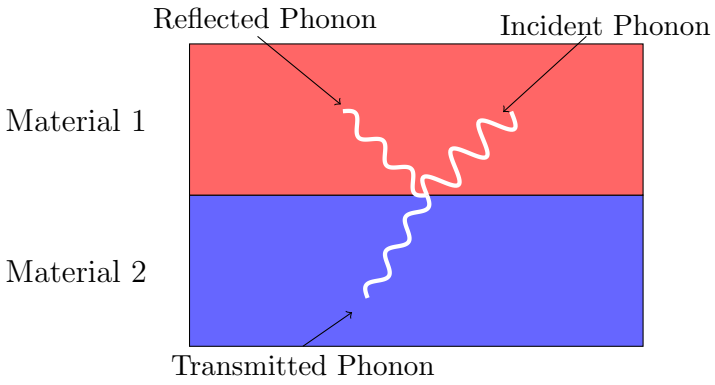

Figure 2.3: *The acoustic mismatch model is applicable for interfaces which are smooth. The wavelength of phonons must be much larger than the roughness of the interface. Note the interface is drawn with zero roughness.*

phonons are refracted or reflected in a similar manner to Snell's law. The multi-dimensional form of the acoustic mismatch model [12] is,

$$t_{1,2}(\theta_1,\omega) = t_{2,1}(\theta_1,\omega) = \frac{\frac{4Z_2}{Z_1}\cdot\frac{cos(\theta_2)}{cos(\theta_1)}}{\left(\frac{Z_2}{Z_1}+\frac{cos(\theta_2)}{cos(\theta_1)}\right)^2} \tag{2.6}$$

where $t_{1,2}$ and $t_{2,1}$ are the directional energy transmittance functions from one side of the interface to the other, Z_1 and Z_2 are the acoustic impedance of side 1 and 2, respectively, and θ_1 and θ_2 are the incident and refracted phonon angles. The acoustic impedance of a solid (Z) is defined as,

$$Z = \rho c \tag{2.7}$$

where ρ is the density of the material in kg/m^3, and c is speed of sound in the material in ms^{-1} [12]. Computing the phonon heat flux from the basis of Equation 2.6 is complex. It is a function of the phonon wave-vector, energy, as well as the interface it is incident upon. For a more in depth discussion of this topic, the reader is directed to literature [12]. For the purposes of this work, a simplified and directionally averaged form of the acoustic mismatch model has been used. This was calculated and tabulated for a range of group velocities and density ratios in literature [12, 25].

The acoustic mismatch model is the functional principle used in engineering many ultra-

low thermal conductivity materials [8, 10, 21, 23]. Component materials are chosen such that their acoustic properties are significantly contrasted, which reduces the overall thermal conductivity through additional Kapitza resistance.

2.1.6 Diffuse mismatch model

In contrast to the AMM, the Diffuse Mismatch Model (DMM) is applicable for interfaces where the roughness is significant when compared to the phonon wavelength. In this model, phonons are fully scattered and do not preserve their mode or polarity. When a phonon is scattered at an interface, it is simply transmitted into any phonon branch which is active at its energy level, on either side of the interface. As such, phonons are simply transmitted based on their energy and the available energy states on the opposite side of the interface. As such, the energy transmittance function is simply a ratio of the available phonon modes in the two materials. Formally,

$$t_{1,2}(\omega) = \frac{\sum\limits_{p} M_2(\omega)}{\sum\limits_{p} M_1(\omega) + \sum\limits_{p} M_2(\omega)} \tag{2.8}$$

where $t_{1,2}(\omega)$ is the transmittance from one side of the interface to the other, and $\sum\limits_{p} M_2(\omega)$ and $\sum\limits_{p} M_1(\omega)$ are the summation of all phonon modes and polarisations in the each side of the interface.

This concludes the main theoretical framework used in this thesis. In the next section, some common, and advanced thermal insulation materials are described.

2.2 Thermal insulation materials

Thermal insulation materials have been, and are still, a substantial and multi-faceted design challenge for the architecture and building industries. As well as the thermal conductivity, a range of other factors such as flammability, moisture sensitivity, cost effectiveness, ease

of installation/application, toxicity to humans, and environmental impact must also be considered when selecting an insulation material for a new building [26]. In the following, a review of the traditional and current technology is presented as a point of comparison for the emerging materials studied in this thesis.

The building industry typically classifies thermal insulation in terms of "R-value", which is measured in m^2K/W [27]. The R-value of a material is the thickness of the insulation (m), normalised to the thermal conductivity ($W/m-K$). As such, a higher R-value signifies better thermal insulation. While R-Value is widely used in building industry, in material science and engineering the thermal conductivity is far more common. In this thesis, the thermal conductivity will be reported to align with research convention. Generally, the thermal conductivity of an insulation material is dependent on a number of environmental parameters. It can vary depending on the temperature [13], humidity [28], and the physical condition of the material itself (moisture absorption and physical damage [27]). Unless otherwise stated, the values reported in this thesis are for pristine/new condition materials, and the measurement temperature will be recorded.

Many traditional insulation materials are inspired by nature, and function by trapping air or restricting its flow to minimise convection. Some examples of common "traditional" insulation materials are wool, cellulose, expanded polystyrene, and fibre-glass bats [26, 27]. Similar functional principles are also used in modern double-glazing for windows. These have a double-layered structure, where the volume in between the outer and inner windows is filled with dry air or a speciality gas, creating a closed convection system [29]. Alternatively, the cavity in some advanced products has a partial vacuum, which largely eliminates convection [30]. Leading on from this, the following sections discuss a range of common and high performance thermal insulation materials, and briefly introduces the principles on which they are known to function.

2.2.1 Mineral wool

Mineral wools are a class of materials defined by their fibrous structure, similar to that of natural wool [26]. This class includes fibre-glass insulation, one of the most common choices for residential applications. The material is manufactured in a matting form factor referred to as bats [31]. As a material, it is widely popular because it is cost-effective, and it can be cut to fit at a building site without major impact to the thermal properties. The thermal conductivity of mineral wool-type materials typically ranges from 0.03 to 0.04 $W/m - K$ when new [26].

2.2.2 Expanded and extruded foam

Another popular choice for residential applications, expanded and extruded foam materials are based on (typically) dense polystyrene beads, which are expanded to form a porous board structure [26]. In expanded polystyrene insulation, dense polystyrene beads are expanded into the porous board structure using a chemical expansion agent. As a material it will be familiar to many people via its use as a packaging product. Extruded Polystyrene on the other hand, is manufactured by extruding the dense polystyrene through a gas pressurized nozzle. Insulation based on extruded polystyrene is distributed as a panel form factor. It is installed between the framing studs of a building, and while it can be cut-to-fit at a building site it is less convenient to do so than with mineral wool type materials. Both expanded and extruded polystyrene have typical thermal conductivities of 0.030 to 0.040 $W/m - K$ [26].

2.2.3 Asbestos

Asbestos is an infamous material in modern society, mainly because of its unfortunate adverse side effects to humans. It was widely used in the past as a fire-resistant and thermally-insulating material [32]. Unfortunately, it was discovered to be a major cause of lung cancer when the material was inhaled as dust. Its widespread use in building and vehicle brake systems, has been conclusively linked to lung cancer [33]. Asbestos insulation is still present

in many New Zealand buildings and requires careful removal when construction is carried out. This material is included in this review as an example because of its widespread use, but also to demonstrate the importance of toxicity in selection and study of building materials. There are six naturally occurring types of asbestos each of which can be processed into many different forms depending on the intended application [34]. Asbestos Insulation Board (AIB) was the most common form used for residential applications [32].

2.2.4 Vacuum insulation panels

Vacuum insulation panels represent the best-performing thermal insulator widely available on the market today [26]. These panels consist of a porous silica core, which is vacuum-sealed in a multi-layered metal-polymer bag. The vacuum inside the micro-porous silica structure means that the heat transport is limited to lattice vibrations in the pressed silica core, which in itself has a low thermal conductivity. In new condition, these panels have an extremely low thermal conductivity of 0.003 to 0.004 W/mK [26]. The disadvantages of this material is that it is expensive and that it cannot be punctured or cut to fit on a building site without damaging or negating its high thermal insulation performance. As such, this has limited its adoption to high performance sectors like refrigerated shipping.

2.2.5 Gas-filled panels

Gas-filled panels are similar in structure to vacuum insulated panels in that they have a sealed, baffled internal structure. However, their volume is filled with a heavy gas such as Argon, Krypton or Xenon, as opposed to a vacuum [26, 31]. This is advantageous as it is easier to maintain a positive pressure inside the panel, than a negative pressure. While their performance is not as impressive as vacuum insulation panels (k=0.040 $W/m-K$ [26, 31]), they do represent an interesting class of materials.

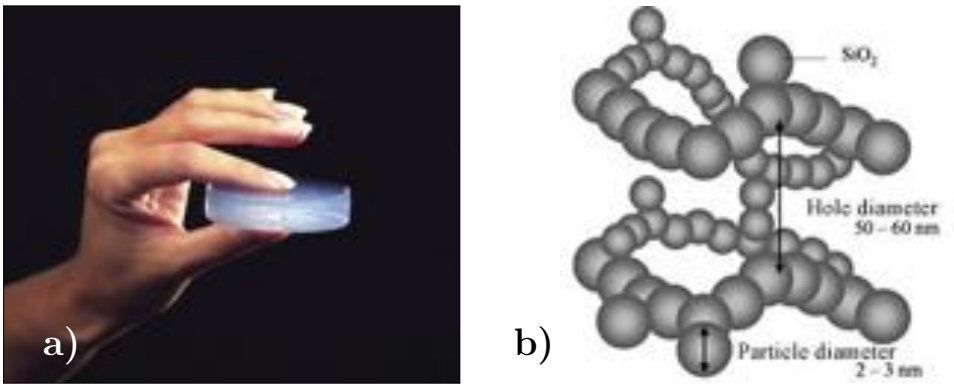

Figure 2.4: *Images showing the macro, and nanoscale structure of silica aerogel. Images reprinted with permission of NASA [35].* **a)** *An example of silica aerogel material.* **b)** *A schematic diagram of the microscopic structure of aerogel materials.*

2.2.6 Aerogels

Aerogels are an expanded nanoparticle material, which is well known for its high thermal insulation performance and low density [36]. An example of an aerogel, and a rendering of its microscopic structure is shown in Figure 2.4. In research, aerogels have been found to have a thermal conductivity as low as 0.004 $W/m-K$, while commercially available aerogels are closer to 0.013 to 0.014 $W/m-K$ [26]. The most common, or well-known, procedure to fabricate aerogels is called the sol-gel process [37]. In this procedure, a colloidal dispersion of nanoparticles (sol) is turned into a gel by addition of a solvent. In the gel, the nanoparticles are linked together in a large three-dimensional network of polymer–like chains. It is this that forms the characteristic aerogel nanoparticle network, shown in Figure 2.4 b). The liquid solvent is then removed from the network of nanoparticles via a super-critical drying process, turning the gel into an aerogel [36]. The super-critical drying step is crucial to the formation of aerogels. If the liquid is removed using atmospheric pressure drying, the surface tension of the liquid evaporating out of the structure will crush the gel. This material has been intensively researched for many years, however its adoption has been limited to only the most expensive applications (e.g. Martian rovers) due to the high expense and low production volumes [38].

2.2.7 Packed nanoparticle beds

An emerging thermal insulation material is packed nanoparticle beds [8,39–46]. This material has similarities to the aerogels in that it is primarily composed of nanoparticles. However, unlike aerogels, packed nanoparticle beds are a close-packing of nanoparticles (face centred cubic or hexagonal close packed nanoparticles), as opposed to an expanded network [36, 39]. This material creates low thermal conductivities via its' high interface density and extremely high thermal resistance between adjacent nanoparticles [39, 42]. One of the most popular models which describes the thermal behaviour of this material was reported by R. Prasher [39]. This model is based around phonons as the majority thermal energy carrier, traversing a nano-constriction formed between two spherical nanoparticles in contact. In this model, phonons are "funnelled" into the interface, and are filtered proportional to the area of the nano-constriction, relative to the nanoparticle radius. As such, the phonon transmission is proportional to,

$$\tau(\omega) \propto \frac{a^2}{R} \tag{2.9}$$

where $\tau(\omega)$ is the frequency dependent transmission function, a the radius of the inter-nanoparticle contact patch, and R the nanoparticle radius [39]. This effect alone has been shown to produced extremely low thermal conductivities, far beneath the amorphous limit of the constituent materials [8, 39–46].

The highest performing example of these pressed nanoparticle materials from literature is the work of Voges et al. [8]. This work aimed to increase the inter-nanoparticle thermal resistance by introducing an acoustic mismatch between the nanoparticles, in addition to the phonon filtering effects produced by the nano-constriction geometry. This was achieved by blending multiple different types of nanoparticles with varied acoustic properties into the packed bed. The thermal conductivity reported by the researchers was as low as $0.007\ W/m-K$, depending on the specific blend of nanoparticles used. However, it was also reported that there was significant variation between measurement techniques, especially for samples with larger dimensions. When the size of the sample was increased to $100 \times 100\ mm$, the measured thermal conductivity was approximately ten times larger than the minimum value

measured previously ($0.07\ W/m-K$) [8]. It was speculated that the material had degraded substantially in the time delay between fabrication and measurement. This class of material is particularly interesting for the purposes of this research, as the mechanism of thermal conductivity reduction is largely solid state.

2.3 Thermal meta-materials and phononic crystals

In this section, some interesting thermal meta-materials, and phononic crystals are discussed. For the purposes of this review, thermal meta-materials are distinct from general thermal insulation materials in that they do not necessarily have extremely low thermal conductivities. Rather, they produce large *reductions* in thermal conductivity compared to bulk, or they use solid state mechanisms to produce the reduction.

A crystalline material is often defined as a material in which there is a long-range microscopic order [47]. The microscopic order is usually thought to be an ordering of atoms or molecules. However, crystal structures can also be composed of more macroscopic elements, such as nanoparticles, thin films or even voids [48]. These kinds of meta-material crystals can produce a range of interesting effects not seen in the raw materials alone. A phononic crystal in this context is an ordered structure of alternating materials, such that the phononic dispersion relation is altered [10, 11, 18, 49]. Two common ways of achieving this effect is through shortening the phonon mean-free path [50], or by reducing the group velocity of phonons in the material [51]. Several classes of phononic crystals are discussed in the following, all of which modify phononic properties of the material. There is a focus on the reduction of group velocity in multilayer superlattices for the purposes of this work.

2.3.1 Superlattices

A superlattice is a periodic layering of thin films, composed of two or more materials. Superlattices have been used in the semiconductor industry for many years, notably to create laser diodes and quantum wells [2,52]. However, the effects of superlattices in general are not

limited to electrical properties alone, and phononic bandgaps have been observed in superlattices also [10, 18]. These thin film superlattices are considered a pseudo one-dimensional phononic crystal, as the phononic bandgap is created in only the dimension perpendicular to the layering [11]. The wide range of applications for superlattice structures, and the wealth of existing technology on the topic, means that there has been considerable research focus on the evaluation of superlattice material combinations [10, 11, 16, 18, 21, 23, 49, 53–56]. Their relative simplicity as a pseudo one dimensional phononic crystal also makes them an ideal platform for simulation and examination of the general physics [10, 11].

A non-exhaustive list of reported thermal meta-material superlattices includes oxide-oxide [16], metal-semiconductor [21,56], semiconductor-semiconductor [57], insulator-insulator [10], inorganic-organic [58], and crystalline-amorphous [53] material combinations. These all seek to reduce the thermal conductivity through phonon interface engineering, discussed previously. Further to this, one of the most common design approaches in these studies is to mismatch the acoustic impedance of the constituent materials, analogous to photonic crystals mismatching refractive indices. When there is an interface between two materials with substantially different acoustic impedances, phonons are reflected off the boundary through the acoustic mismatch model. However for the acoustic mismatch model to be applicable, the interface must have a roughness much smaller than the wavelength of the phonon being transmitted [12]. For many thermal phonons this is not the case, and their transmission is more accurately described by the Diffusive Mismatch Model (DMM) [12]. In the DMM, phonons incident on the interface lose coherence, and phonon transmission is proportional to the ratio of phonon modes on each side of the interface [12].

Superlattice structures utilising diffuse transport still create interesting thermal phenomenon however. Dechaumphai et al. [21] have demonstrated that mismatching the Debye temperatures of the constituent superlattice materials can create ultra-low thermal conductivities. In this case, approaching superlattice design from the point of view of Debye temperatures is equivalent to mismatching the acoustic properties of the materials. Dechaumphai et al. use a summation of bulk and interface resistances (using the DMM for interface transmission) to explain their experimental results. The superlattice investigated was a 10 period

semiconductor-metal superlattice made of silicon and gold. The layer thicknesses of the silicon and gold were 3 nm and 5.7 nm, respectively. The superlattice was grown onto a silicon substrate using high-vacuum DC sputtering. The resulting multi-layer had a thermal conductivity of 0.33 ± 0.004 $W/m-K$, much lower than the amorphous limit of either gold or silicon. The bulk thermal conductivities of gold and silicon are 318 $W/m-K$ and 148 $W/m-K$ respectively. Meanwhile, the amorphous limits for these materials are 0.49 $W/m-K$ for gold, and between 1.05 and 1.6 $W/m-K$ for silicon [21]. Many similar studies have investigated the how interface density, size effects, and other such factors effect the thermal properties of multilayer structures [1, 19, 21, 23, 51, 53, 55–64].

Engineering phononic bandgaps in materials has a wider set of applications than reducing thermal transport however. One such application is a cross-over between photonic and phononic crystals. Such structures have been coined Phoxonic crystals [10, 11, 18, 49]. A phoxonic crystal has a phononic and photonic bandgap, which overlap in energy levels. This allows the wavelength of light in the crystal to be modulated by acoustic waves. While phoxonic crystals are not specifically applicable to the goals of this thesis, the techniques used to fabricate the crystals have been shown to produce phononic bandgaps with relatively simple fabrication protocols [10, 11, 18, 49]. This is in contrast to many other superlattice studies, which used advance fabrication techniques like molecular beam epitaxy [16], atomic layer deposition [23], and pulsed laser deposition [62]. In the Phoxonic crystal research examined, the materials predominantly used were PMMA and SiO_2 nanoparticles. These materials were deposited onto substrates through a standard spin-coating protocol. The bandgaps were produced through mismatching the acoustic and optical properties, similar to previous superlattices.

2.3.2 Van der Waals solids

Van der Waals materials such as graphite have some morphological similarities to multilayered superlattice, in that they have a distinct layered structure. Indeed, at the time of writing the lowest thermal conductivity reported for a "fully dense" material was for tungsten diselenide (WSe_2) [59, 65]. This material had a measured thermal conductivity of 0.05 $W/m-K$

at room temperature. The layer structure of this Van der Waals material can create interesting anisotropic phonon conduction across layers. WSe_2 is synthesized via the modulated elemental reactants method [66]. In this technique layers of tungsten and selenium are sequentially deposited onto a substrate in high vacuum. Then, once all the desired layers have been deposited, the material is annealed at a high temperature such that the deposited layers react and transform into the desired Van der Waals molecular structure.

It was suggested by Chiritescu et al. [59, 65] that the misalignment in the basal planes, also called turbostratic disorder, of the WSe_2 material localises phonons to the basal plane. This effect, coupled with the weak Van der Waal's forces between the layers, mean very few phonon modes are available for transmission between neighbouring basal planes. This theory has been studied with molecular dynamics simulations by Erhart et al. [67]. It was found that turbostratic disorder reduced the thermal conductivity by 30% to 50% compared to perfectly crystalline WSe_2, while basal plane separation further reduced the thermal conductivity by a factor of ten. It was hypothesized that any discrepancy between simulations and experiment was due to the limitation of the phonon mean-free path by the layered structure of the material.

2.3.3 Holey materials, nano-meshes, and surface engineering

Two and three dimensional phononic crystals are another class of thermal band-gap material which are a popular method of investigating phonon transport. Some examples of these structures include:

- Nano-meshes and "holey" materials. [68–72]
- Surface patterned silicon thin films. [73, 74]
- Three-dimensional holey nano-structures. [75]
- Intercalated layered solids. [3]

These structured are noted here mostly for interest, and are not specifically applicable to thermal insulation materials. However these studies do provide fascinating insight into un-

derlying phonon heat conduction mechanisms and in the future these could be used to further improve high performance thermal insulation systems. For example, coherent phonon conduction and reflection has been a topic of interest for some time [1, 16]. However, preserving coherence in high frequency thermal phonons has required advanced fabrication technologies which approach atomic or molecular levels of control [1, 16]. One method to circumvent this bottleneck is to simply lower the measurement temperature, thereby reducing the phonon–phonon scattering rate, and increasing the mean free path of the thermal phonons so they can be treated as coherent [20, 76]. However this is not a strategy which can be applied to residential buildings. Another approach which can achieve this same effect, which could be applied to room temperature phononic crystals, is the integration of nanoscale scattering barriers inside of a much coarser phononic crystal [76, 77]. It is thought that this type of material will scatter high frequency thermal phonons off of alloying points in the base material, causing a shift in the dominant thermal phonon wavelength upwards to a length scale which may be manipulated by the "coarse" phononic crystal.

In another separate example, there have recently been reports of liquid-like phonon conduction in intercalated $AgCrSe_2$ solids [3]. Intercalated in this context refers to a small crystalline protrusion which sits interstitially between the basal sheets of Van der Waals-like material. Liquid-like in this context refers to the polarisation of phonon modes which can be sustained in the material. In solid materials, there are typically three phonon polarisations. There is one longitudinal polarisation, and two transverse polarisations. Liquids, meanwhile, cannot sustain transverse phonon modes, which naturally gives them lower thermal conductivities than solid materials [3]. It was found that the intercalated solid $AgCrSe_2$ was able to strongly suppress the transverse phonon transport across its layer structure, and therefore produce "liquid-like" thermal conduction.

Following on from liquid-like solids, the general thermal conduction properties of liquids is an interesting topic. Indeed, one original use of the 3ω method by Birge et al. was as a liquid specific-heat spectrometer [78]. In recent years, the 3ω method has continued to be adapted for a wide variety of use cases along these lines [79, 80]. The final section of this literature review now switches contexts from solid materials, and discusses the specific application of

the 3ω method as a flow sensor, and its use inside of microfluidics and microbiology.

2.4 3ω method for microfluidics

Conventional thermal fluid flow sensors are based around a three element system, with two thermometers and a separate discrete heating element [81]. However, one of the primary advantages of the 3ω thermal measurement technique, which this thesis is based upon, is that the resistance thermometer acts as both heater and thermometer simultaneously [6, 78]. This naturally lends this type of system to flow sensing applications. Similar ideas have been explored in the past by Kwon et al. who related the phase and magnitude of the oscillating temperature of a platinum wire to fluid velocity when integrated into a microfluidic channel [79].

More recently, Clausen et al. investigated how a millimetre scale 3ω RT could be used for a range of applications, such as fluid-velocity, bio-film thickness and surface contact [80]. In the flow measurement aspect, the researchers showed that the sensor rate of response could identify the transition between the laminar and turbulent regimes. As the fluid flow-rate increased and eventually became turbulent, the sensors rate of response to volumetric flow increased. In the bio-film thickness and surface contact measurements, the 3ω RT was used to measure a change in thermal conduction properties surrounding it. Using this, the deposited biofilm thickness could be determined, as well as its contact with water [80]. It was proposed that this sensor could be used as a fouling sensor for pipes and waterways.

The concept of measuring fluid composition changes around the RT has also been extended to droplet detection in a microfluidic systems [82]. Droplet generation is well established building block of digital microfluidic total analysis systems. Yi et al. have used a 3ω RT to sense the timing, rate and composition of droplets generated by a microfluidic droplet generator. This operates on the same principle as the surface contact and bio-film thickness measurement method previously discussed, i.e. the RT detects changes in thermal properties above it. In this case, the measurement was taken with a set driving frequency and the time domain 3ω signal was measured. A similar approach has also been used to track liquid gas

interfaces in a microfluidic channel [83].

As a pure flow rate measurement system, the 3ω method has been studied using arrays of thermistors and heaters in order to add vector measurement of gas or fluid flow [84]. Similar systems have also measured the thermal conductivity of nano-litre liquid samples in both static and flowing conditions [85, 86], the thermal conductivity of nano-dispersions [87], and to probe nano-scale thermal transport mechanisms in surfactant solutions with varying concentration [88].

In recent years, microfluidics and biology have become increasingly inseparable fields. Microfluidics allows for improved automation, repeatability, compartmentalization, and reagent reduction in biological processes. Therefore, exploring the opportunities that a microfluidics configured 3ω RT affords to biology is a natural progression from the previous body of work on the subject. For example, Park et al. have explored how a 3ω RT could be used for quantifying the viability, concentration and disease state of cells [89–91]. In one of these examples, a 3ω RT was micro-fabricated onto a borrofloat glass carrier and immersed into a cell suspension [89]. The cell suspensions were composed of HeLa hepatocyte and NIH-3T3 J2 fibroblasts. It was found that there was a strong correlation between the thermal conductivity of a cell suspension, and its concentration and overall cell viability [89]. In another example, the thermal conductivity of single biological cells was measured and correlated with cancerous disease state [90, 91]. This measurement required a nanoscale 3ω resistance thermometer, orientated at the base of a cell-confining well. The resistance thermometer was fabricated with electron beam lithography and was $400\,nm$ wide in order to fit in the micro-well. In order to test the hypothesis that disease state and thermal conductivity were linked, Hs 578Bst/Hs 578 T (human breast cells) and TE 353.Sk/TE 354.T (human skin cells) were measured using the micro-well/3ω system [91]. It was found that there was a statistically significant ($p < 0.01$) difference between healthy and cancerous cells. Primary and metastatic cancerous cells were also tested to determine if the thermal conductivity would continue to change with disease progression. There was a difference in thermal conductivity between the cell lines, however the change was not statistically significant.

An area in which the 3ω method has not yet been applied to is filamentous microorgan-

isms. Microorganisms such as these have a filament-like structure, which includes an outer membrane with internal fluid transport [92–94]. Some of these micro-organisms are plant pathogens with which there is a desire to understand and counteract their pathogenicity [92]. The literature on the 3ω method, in conjunction with biological cells, microfluidics, and flow-sensing suggests that there could be novel insight available when applied to these organisms.

This concludes the literature review for this thesis. The next chapter, *"The* 3ω *method"* discusses the background of the 3ω technique, and describes how it was established at the University of Canterbury, New Zealand.

Chapter 3

The 3ω method

3.1 Introduction

In this chapter the process of establishing and calibrating the classical and differential 3ω method at the University of Canterbury is described. The techniques are calibrated on a range of standard materials, and their future application to less known samples is discussed.

The 3ω method generally refers to a set of electro-thermal characterisation techniques which all use a common sensor design [6, 78]. It has become a standard technique for measuring the thermal conductivity and thermal diffusivity of micro- and nano- size samples, or samples with unusual geometry [21, 95–98]. The most common use in literature is for measuring the thermal conductivity of thin films between 50 nm and 30 μm thick. The 3ω methods' relative simplicity and versatility, compared to other micro-thermal techniques, has led to its wide adoption in a range of fields, as well as for a range of different purposes. Most recently, the generalised technique has been applied to physical properties other than thermal conductivity, with a coupling to the thermal domain.

In physics, the 3ω method is being applied to study phonon mechanics in new materials [99–101]. There is work towards reading the magnetic state of Hall crosses using the 3ω voltage [99]. Another application is measuring the mean free path of thermal energy carriers in suspended thin films. In this experiment, the thickness of a suspended film was varied, and the thermal conductivity measured. When the film thickness was less than the mean free path of a thermal phonon, the thermal conductivity reduced in accordance. Through measurement of a range of thin films, the thermal phonon spectrum was able to be experimentally deduced.

Recently, there has been an increase in use of the 3ω method for biological applications. For example, Park et al. have used the technique to assess cell viability in suspension, and in single cells [89, 90]. Other researchers investigated the thermal conductivity of diseased cells, and found that there was a statistically significant correlation between disease state and thermal conductivity [91]. This lead to the hypothesis that there is a cytoplasm phase change in the disease progression.

The versatility of the 3ω method stems from the fact that it is an AC technique. The use of AC temperature waves allows a single resistive device to provide stimulus to a system, and simultaneously measure the resulting temperature response. This enables much smaller structures to be measured with much greater accuracy compared to conventional thermal techniques [6, 78, 102]. Another advantage is that AC thermal oscillations have a finite penetration depth [102, 103]. The thermal penetration depth, also called the thermal wavelength, is defined as,

$$\lambda = \sqrt{\frac{D}{2\pi f_{thermal}}} \tag{3.1}$$

where D is the thermal diffusivity, and f is the thermal frequency. This means that the AC thermal oscillations can be limited to a region of interest, thus removing or minimising the effect of the device-environment boundary conditions, which constitutes a substantial source of error for other measurement techniques [102, 104]. There are extensive resources on the background of the 3ω method elsewhere [6, 78, 102]. However a brief discussion on the origin of the 3ω voltage follows to assist in future discussion.

3.1.1 Background - 3rd Harmonic Voltage

A top down schematic of a typical 3ω resistance thermometer (RT) is shown in Figure 3.1 a). The RT is a thin metal film which has been deposited directly onto the surface of a sample, and patterned to match the schematic representation shown in Figure 3.1 a). The resistance thermometer functions as a "four-point" resistance device. In this configuration a large current is passed from $I+$ to $I-$, while the voltage across V_+ to V_- arising due to this current is measured. From the known current (I), and the measured voltage ($V_+ - V_-$) the resistance of only the central portion of the RT can be calculated. This effectively eliminates the contribution of interconnects from the resistance measurement because the current drawn by the voltmeter input impedance is comparatively small compared to the probing current, I. A typical probing current is on the order of mA, while the the input current drawn by a high quality source-meter is on the order of fA.

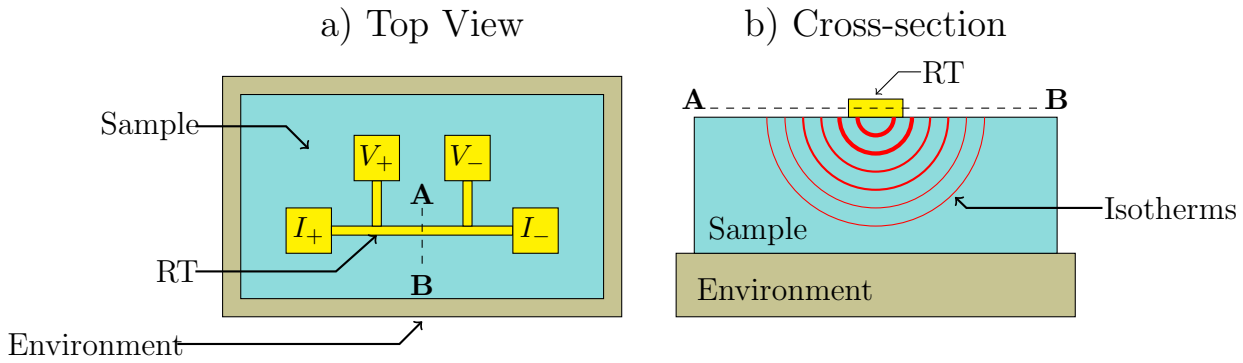

Figure 3.1: *A schematic of the RT on top of a sample. The line* **A** - - - **B** *indicates the plane of the cross-section line.* **a)** *A birds-eye view of the resistance thermometer design. The device is micro-fabricated on the surface of a sample. The device is configured to be a four point resistance measurement set-up. A heating current is passed through the body of the thermometer while the voltage is measured across the central width.* **b)** *A cross-section of the resistance thermometer, and material of interest. The heating frequency allows the thermal penetration depth to be limited to the sample only. This means the thermal resistance from Sample to the environment can be eliminated. This is one of the major advantages of AC techniques as opposed to DC or transient techniques.*

When such a RT is used in the 3ω method, a constant AC current, I_ω, is passed through the resistance thermometer (from $I+$ to $I-$). A harmonic voltage at 3 times the primary driving frequency is measured across $V_+ \rightarrow V_-$. It can be shown that the third harmonic voltage is linearly related to the magnitude of the temperature oscillation over the central portion of the line [6, 78, 102]. This is what the technique is named for; the third harmonic of the fundamental frequency is related to the temperature of the RT, and by extension of the sample with which it is in intimate thermal contact.

The origin of the third harmonic is through the expression for electrical power. The heating current I_ω supplied to the RT is,

$$I_\omega(t) = I_0 cos(\omega t) \tag{3.2}$$

where I_0 is the peak current, t is time, and ω is the angular frequency of the signal. The power dissipated in the RT, due to the heating current I_ω is then,

$$P_{RT} = I_\omega^2 R_{e,0} \tag{3.3}$$

where $R_{e,0}$ is the zero-current resistance of the RT. When Equation 3.2 is substituted into Equation 3.3 it is shown that the power in the RT occurs at twice the angular frequency of the input current, (2ω)

$$P_h(t) = \frac{1}{2} I_0^2 R_{e,0} \left(1 + cos(2\omega t)\right) \tag{3.4}$$

The 2ω heating is known as joule (also called resistive or ohmic) heating. The heat flux from the joule heated RT is transferred into the sample and causes the temperature waves in the material. The RT is in intimate thermal contact with the material, so its' temperature is considered to be the same as the surface of the material. The resistance of metal then changes linearly with temperature [105] as,

$$R(T) = R_{e,0} \left(1 + \alpha \Delta T\right) \tag{3.5}$$

where $R(T)$ is the resistance as a function of temperature, $R_{e,0}$ is the nominal heater resistance, α is the temperature coefficient of resistivity, and ΔT is the change in temperature from the nominal temperature. When separated into DC and AC components, T_{DC} and T_{AC}, the resistance of the RT can be fully described as,

$$R_h(t) = R_{h0} \left(1 + \beta \Delta T_{DC} + \beta |\Delta T_{AC}| cos(2\omega t + \phi)\right) \tag{3.6}$$

where ΔT_{DC} is the temperature rise due to the DC component of power, and $|\Delta T_{AC}|$ is the RMS temperature rise produced by the AC component of power. The AC component has a frequency of 2ω, with a phase delay of ϕ. In order to measure the change in resistance as a voltage, Equation 3.6 is multiplied by the heating current I_ω again. This results in,

$$\begin{aligned} V_h(t) = I_0 R_h((1 + \beta T_{DC}) cos(\omega t) + \frac{1}{2}\beta |\Delta T_{AC}| cos(\omega t + \phi) \\ + \frac{1}{2}\beta |\Delta T_{AC}| cos(3\omega t + \phi)) \end{aligned} \tag{3.7}$$

Equation 3.7 shows the 3rd harmonic frequency and how it is related to the AC temperature

oscillations of the RT. The final result of Equation 3.7 is that by measuring the 3rd Harmonic voltage of a RT on a sample, the AC thermal oscillation induced in the material can be inferred. Further to this, as the input power to the system is also known, the thermal transfer function, $Z_{thermal}(\omega) = T_{AC}(\omega)/P_h(\omega)$ for the sample can be constructed. Depending on the geometry of the system, this transfer function can be used for the extraction of the property of interest; commonly the thermal conductivity, thermal diffusivity, or specific heat capacity.

As alluded to earlier, there are many different forms of the 3ω method. The geometry of the sample and the placement of the RT will change the thermal model which is required to extract the parameter of interest. There are two specific measurement techniques which are most commonly used. The "classical" 3ω method is used for bulk samples and thin films greater than 30 μm thick. The second common technique is referred to as the differential 3ω method. This is used for thin films down to 50 nm. The classical 3ω method relies on the frequency response of a single RT element. The differential method meanwhile, utilises a control sample with a separate RT to isolate the effect of a thin film from that of the substrate, capping, and supporting structures. Both of these common techniques are used in this thesis.

3.2 Methods

A block diagram of the 3ω instrumentation can be seen in Figure 3.2. There are three main instrumentation components required for the 3ω method. These are the RT , the buffering electronics, and a lock-in amplifier. The specific implementation of these components are discussed in the following sections.

3.2.1 Resistance thermometer

The RT sensing element is arguably the most important component of the 3ω system. The device must be fabricated and calibrated such that it precisely applies heat, and measures

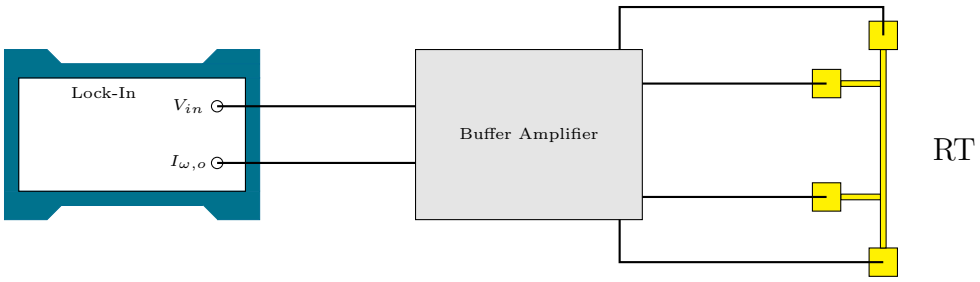

Figure 3.2: *A block diagram of the 3ω method. The RT is interfaced with buffering electronics using a microelectronic probe station. The buffer electronics use the on-board signal generator of the lock-in amplifier to supply the constant AC current to the RT. The resulting differential voltage across the resistance thermometer is buffered by differential amplifiers and connected to the lock-in amplifiers signal input.*

temperature. As such, the RT must have consistent dimensions, and be fabricated in intimate thermal contact with the sample surface. Therefore, the most common fabrication approach for the RT is via the conventional photo-lithographic lift-off process [106]. Unfortunately this process is incompatible with many interesting samples which are either delicate or organic in nature. This incompatibility stems predominantly from the solvent used for lift-off processing which, along with ultra-sonication, would destroy these types of sample.

Two of the advanced thermal system investigated in this work are polymer composite materials. Due to this, an alternative fabrication methodology for the RT had to be found. Two possible options were shadow-mask patterning [107, 108], and etching [106]. The following sections discuss the specific approach taken for these alternative patterning options.

3.2.1.1 Electron beam metallisation

The physical vapour deposition system used to micro-fabricate the RT devices was an Edwards, Auto 500 physical vapour deposition system. This system contains multiple deposition sources, including electron-beam evaporation, Direct Current (DC) sputtering, and Radio Frequency (RF) sputtering. For deposition of gold, electron beam evaporation is the preferred option. Gold films grow well from evaporation, and a small crucible can be employed to make efficient use of all of the material to be deposited. This is particular advantageous for precious materials such as gold, and platinum.

Figure 3.3: *A Photograph of the Edwards Auto 500 Multi-source PVD system available in the UC Nano-fabrication Laboratory. The systems integrated electron-beam evaporator was used to fabricate the RT devices for the 3ω method.*

Samples to be coated are mounted on a carrying plate, which can be positioned directly above the material source. The chamber is then pumped down to a vacuum pressure less than 0.9×10^{-5} Torr. When the electron beam source heats the gold material above the melting temperature, the reduced vacuum pressure increases the mean free path of now gaseous gold atoms so that they can travel to and coat the sample mounted above it. During deposition, the growth of the film is monitored by a crystal growth monitor mounted near the sample. The crystal growth monitor is a micro-mechanical oscillator which can measure a change in material deposited onto it via its' resonant frequency. E-beam metallisation is used in all of the patterning methods discussed below.

3.2.1.2 Shadow-mask patterning procedure

A shadow mask is a physical mask which blocks material from making contact with the surface of a sample [107–109], very similar in morphology to a common stencil. A schematic depicting the shadow mask fabrication process can be seen in Figure 3.4. A negative image of the desired pattern is cut completely through a masking material, which is then then mounted to the surface of a sample. Finally the stack of the sample and mask are placed in the physical

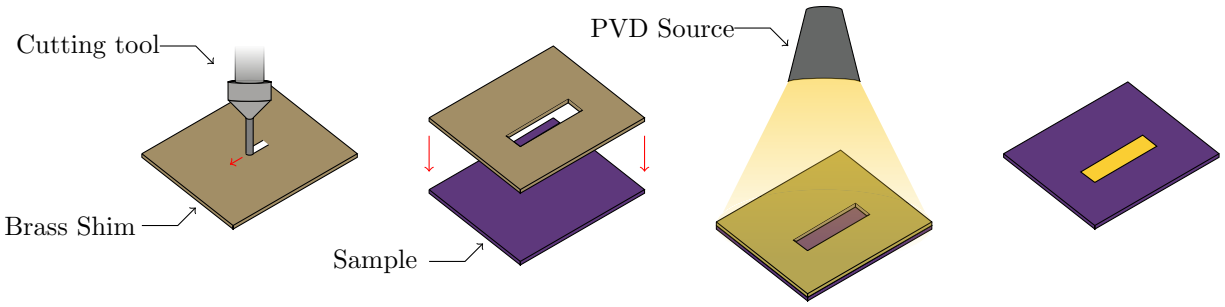

a) Pattern Cutting b) Mask mounting c) Depostion d) Patterned Sample

Figure 3.4: *A schematic of the shadow-mask patterning procedure.* **a)** *A milling machine is used to cut the desired pattern through a brass shadow mask blank. Some post-processing is often necessary to remove imperfections from the milling procedure.* **b)** *The completed shadow mask is mounted on to the surface of the sample.* **c)** *A physical vapour deposition source deposits material through the shadow mask and onto the sample.* **d)** *The mask is removed. Only material inside the pattern area remains on the surface of the sample.*

vapour deposition system. After deposition, the shadow-mask is simply removed from the sample to leave only the desired pattern on the surface. The simplicity and lack of solvent processing steps in the shadow masking procedure makes it suitable for use with chemically or mechanically delicate samples [109]. The main limitation of the shadow masking procedure is the size and accuracy of features that can be fabricated. Imperfect contact between the mask and a sample can lead to the pattern "spreading"; this issue can lead to rough pattern edges, and a generally low yield rate from metallisation processes. The smallest feasible size which can be fabricated with the shadow masking procedure used in this work was $20-40\,\mu m$.

The basic design of a 3ω RT can be seen in Figure 3.5. The classical 3ω method requires the thermometer be thin compared to the film thickness [6], while the differential method requires that the RT width is large compared to the thin film thickness [102]. A versatile choice of RT geometry has a width of $50\ \mu m$. A $50\ \mu m$ RT will be wide enough for thin film samples from $50\ nm$ to $4.5\ \mu m$ to be measured to 5% error using the differential 3ω method [102]. In addition, the design will allow thicker films, from $30\ \mu m$ upwards, to be measured using the classical 3ω method. Furthermore, $50\,\mu m$ is compatible with established shadow masking manufacturing techniques.

There are many fabrication methodologies which can be used to fabricate shadow masks.

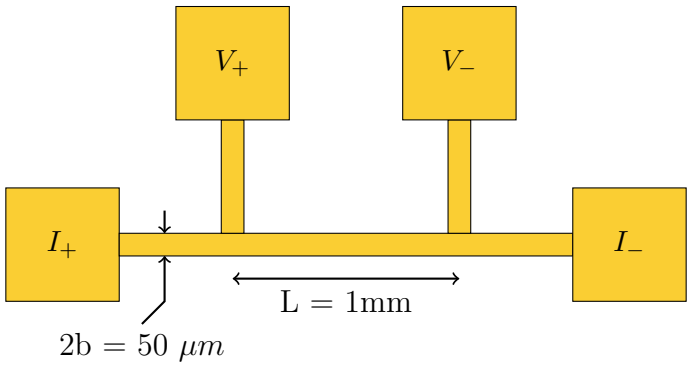

Figure 3.5: *A schematic diagram of the basic resistance thermometer pattern (not to scale) to be transferred on to the surface of the material to be measured. Dimensions which are used in the calculation of thermal properties are annotated on the diagram. The RT width defines how the heat flux is applied to the system, a wide RT is a kind of plane source, while a thin RT is a line source. The length needs to be precisely defined so the RT area is known. The annotations V_+, and V_- indicate the pads where the 3ω voltage is measured across. Similarly, I_+, and I_- represent the contacts through which the heating current I_ω is applied.*

These include CNC milling [110], laser cutting [95], and wet/dry etching [111]. The technique chosen to fabricate the shadow masks in this work was CNC micro-milling, as this was available in the UC Nanofabrication Laboratory and offered the necessary flexibility for prototyping.

The Minitech milling machine used for this process can be seen in Figure 3.6. The RT pattern was milled into a 25×25 mm square of 55 μm thick brass shim (Industrial Tooling). Brass was chosen due to its ease of machining, and good mechanical strength. A sacrificial wooden substrate was mounted in the CNC milling vice, and the surface of the wood was cut flat and parallel with the axis of the mill using a fly-cutter (1/4" Shank, Arc Euro Trade). The shadow mask blank was attached to the sacrificial wooden substrate with an adhesive (Crystalbond 504, SPI Supplies). Crystalbond is a thermoplastic adhesive commonly used for mounting SEM cross-sections [112]. For bonding, the shadow mask blank was heated to 100 $°C$ on a hot-plate, and powdered adhesive applied to the top of the material. When hot, the Crystalbond adhesive is liquid and spreads over the surface of the blank. The blank could then be removed from the hot-plate and pressed onto the wood. A brass weight was placed on top of the mask blank to ensure good contact with the surface of the wood substrate. Once cooled, the adhesive sets, and the weight could be removed.

Figure 3.6: *A photograph of the Minitech micro-milling machine used for shadow mask fabrication in this work. The addressable step size is* $1\,\mu m$*. Tooling for this machine ranges has sizes ranging from 3 mm down to 10* μm*.*

The pattern features were then formed using a $50\,\mu m$ two-flute end-mill (50M2X150S, Performance Micro-Tool). As these micro-sized end-mills are fragile, the manufacturer recommendation is a maximum chip-load of 2% of the cutter diameter. For example, a spindle speed of 25,000 rpm, and a $50\,\mu m$ two-flute end-mill, leads to a calculated feed-rate of $50\,mm/min$. Immersion cooling in water was used for coolant and lubricant for all operations. For micro-milling, cooling and irrigating the cutter increases the tool life and also reduces undesirable side effects such as edge burring. For additional information about milling parameters, feed rates and cutting speeds, refer to Appendix A.

To ensure that the pattern is cut entirely through the mask blank, the cutter must be accurately zeroed on the material surface. The most reliable way to achieve this is using a microscope to directly observed the end-mill approaching the surface. In the process, the cutter is incrementally moved closer to the material surface, while the spindle is running. When the surface of the material is reached, a small amount of dust can be observed as the first cut is made. Figure 3.7 shows an example of a $50\,\mu m$ end-mill being zero-ed on the surface of a mask blank. Once the machine coordinates of the material surface have been recorded, the Minitech mill contact probe can be used for any subsequent tool changes.

Once the milling program has been run, and the pattern has successfully been machined

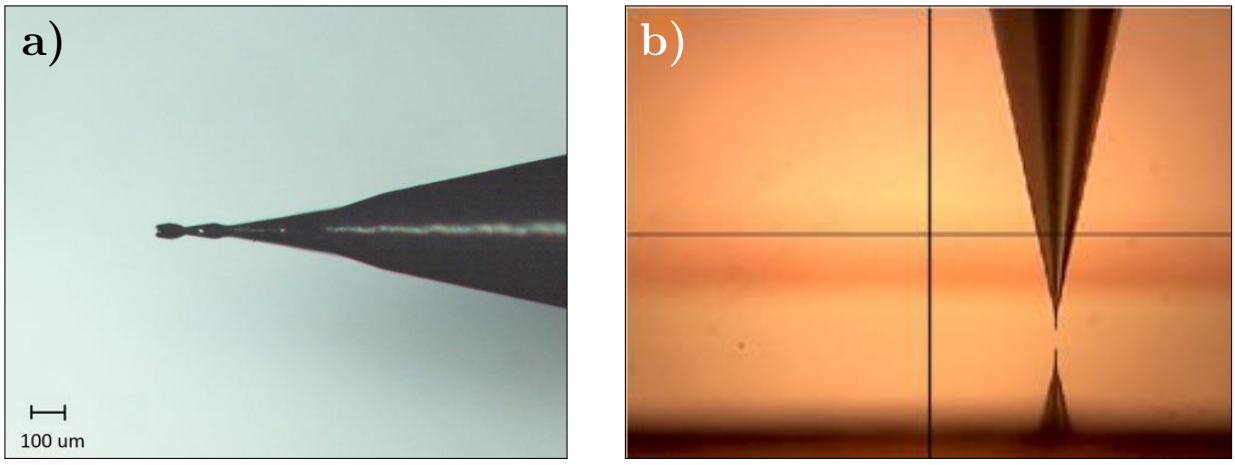

Figure 3.7: *Images depicting the micro-cutter used to fabricate the 3ω shadow mask.* **a)** *An optical micrographs of a 50 μm, two cutter, fish-tail end-mill.* **b)** *The end-mill on the CNC mini-mill, approaching the surface of the brass shim. The reflection of the end-mill in the shim assists with the approach.*

through the blank, additional post-processing was required to remove artefacts of the milling process. To remove the mask from wooden machining substrate without damaging the pattern, the wood was immersed into acetone (Analytical Grade, Thermo Fisher). Since the Crystalbond is soluble in acetone, the mask could be gently removed from the substrate with tweezers after a short time for the adhesive to dissolve. Once the mask had been removed from the machining substrate, there was often waste material blocking the machined pattern. In addition, undesirable milling artefacts were present the edge of the machined features. To remove the waste material, the mask was briefly cleaned in acetone in an ultra-sonic bath.

In addition, to remove any edge burr on machined features, a nitric acid etching procedure was developed. It was found that a 20% nitric acid etch for 30 s to 1 min would remove edge burrs, with minimal impact to the intended feature size. It is theorised that the high surface area of edge burrs allows this procedure to effectively removed the burrs without significantly distorting the pattern. Given that an underlying assumptions in the 3ω method is that the RT has a constant width, it is important to remove edge burring and rough edges from the pattern edge. If rough edges remain on the shadow mask, the resulting RT will be of poor quality. Furthermore, edge burring defects create imperfect contact between the shadow

mask and sample; further distorting the pattern. The effect of the de-burring procedure can be seen in Figure 3.8.

3.2.1.3 Lift-off Patterning Procedure

Photolithography is the most common patterning method used in micro-electronics and nano-technology [106]. In this method, a light-sensitive polymer called a photo-resist is applied to a sample and UV light is shone through a photomask on to the surface to define a desired pattern. However, photoresist requires chemical processing after exposure. This in turn requires that the sample be mechanically stable and non-soluble in the processing chemicals.

There are two common procedures used to transfer the pattern from a photoresist to a metal layer, lift-off and etching. An overview of the lift-off patterning procedure is shown in Figure 3.9. In this work, a positive tone photoresist (AZ1518, Microchemicals GmbH) was spin-coated at 3000 rpm for 60 s onto a cleaned substrate. The film was baked at $100\,^{\circ}C$ for 1 min and 30s to remove solvents. Following this, the sample was briefly immersed in developer (AZ 326 MIF, Microchemicals GmbH) for 10s, rinsed with DI water, and dried with N_2. This pre-exposure development step was performed to assist with the formation of an undercut. The formation of an undercut at the edge of the pattern allows the photoresist to dissolve easier in final lift-off step. This greatly improves the reliability of the patterning process. The sample and photomask are loaded into the Suss MA6 mask aligner. The mask aligner can precisely place the pattern on the surface of the substrate. The sample was then exposed to UV light through the photo-mask. An exposure energy of $45\,mJ/cm^2$ was used for this resist type and thickness [113]. While, this constitutes a slight over-exposure compared to the data sheet value, it assisted further in the formation of an under-cut.

Following exposure, the sample was developed (AZ 326 MIF) for 1-2 minutes with agitation, rinsed with DI water, and blow-dried with N_2. Full development was then confirmed by inspection under an optical microscope (Olympus BX30).

After development, a residual amount of photo-resist can remain in the patterned area. This residue can negatively impact the adhesion of the deposited metal film to the substrate. An

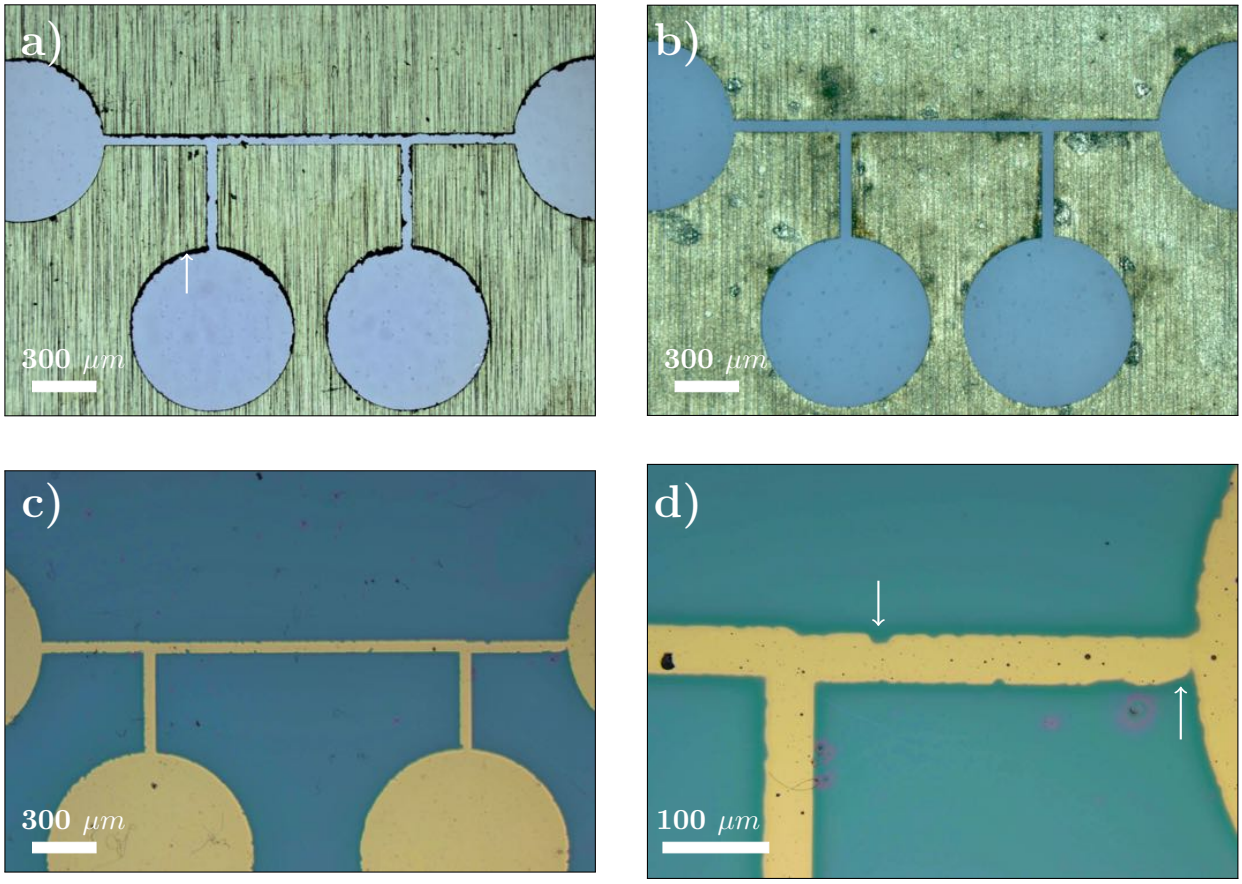

Figure 3.8: *Micrographs of the RT shadow masking results.* **a)** *A shadow mask immediately after being removed from the milling machine. Arrows indicate the edge-burring and waste material which is left from the mask cutting procedure.* **b)** *A weak nitric acid etch removed edge burring, as indicated in* a). **c)** *A RT fabricate using the indicated shadow mask. Mask post-processing greatly improves the clarity of the edge, however mask cleanliness and imperfect mask contact can create pattern defects.* **d)** *Pattern defects created by mask imperfections. Arrows indicate areas where the mask imperfections are transferred to the RT device.*

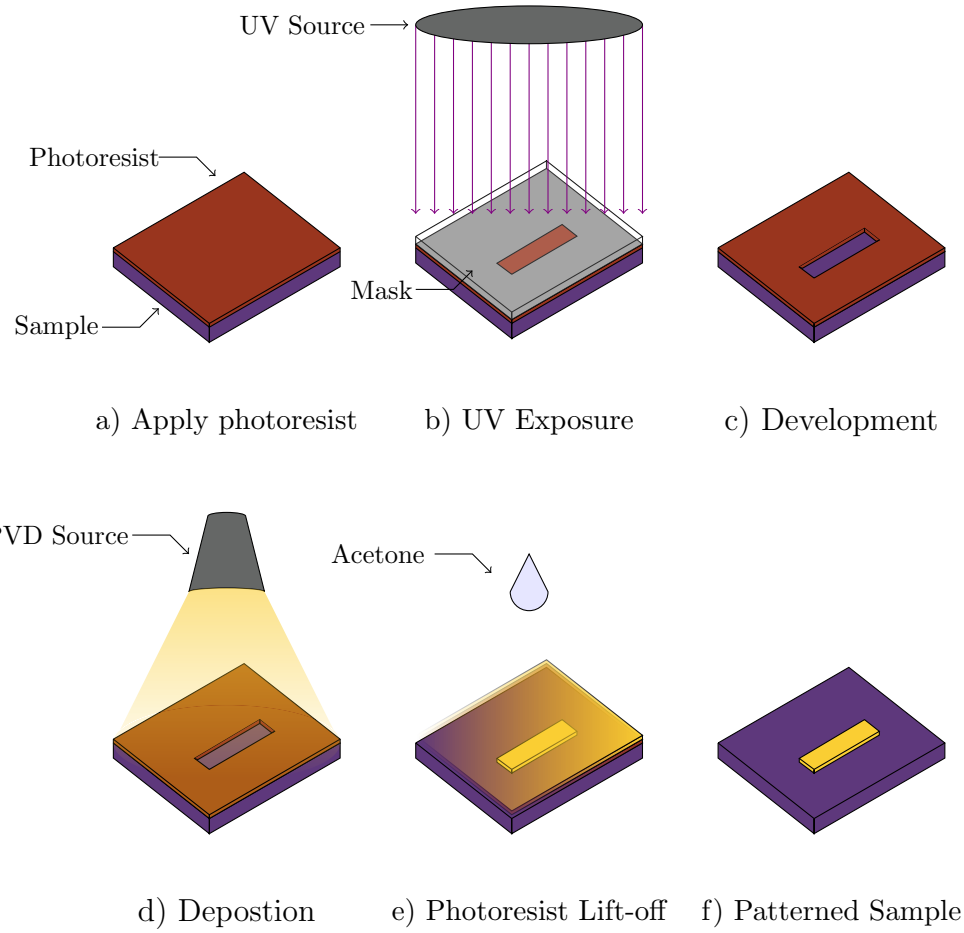

Figure 3.9: *Schematic depicting the process of lift-off micro-fabrication.* **a)** *Photo resist is applied to the surface of the sample, and baked to remove solvents from the film.* **b)** *The film is exposed to UV light through a photomask.* **c)** *In the development step, the resist is removed where it was exposed to UV light. (This is the case for positive photo-resist. In negative resist, the exposed resist is cross-linked and remains after development).* **d)** *The metal film is physically deposited on to the developed sample.* **e)** *The sample is immersed in acetone, dissolving the photoresist and thus removing the material deposited it.* **f)** *The acetone has removed all deposited material except for the patterned areas where the metal was in direct contact with the substrate.*

oxygen plasma (15 Watts, O_2, Tergeo, Pie scientific) was used to remove the residual layer photoresist layer. The metal layer was then deposited onto the sample following the physical vapour deposition procedure described in Section 3.2.1.1.

Once the metal layer had been deposited, the sample was placed into acetone and left to soak for 1 to 24 hours. This dissolved the photoresist and suspended the metal outside the pattern area away from the substrate. The sample was then placed in the ultra-sonic cleaner for 1 to 5 min. Ultra-sonication disintegrates the suspended metal film and only the patterned metal attached to the surface remains. The pre-ultrasonication soak helps to ensure the quality of the lift-off pattern. If the film is not fully suspended away from the substrate prior to ultra-sonication there is a tendency for the metal particles to redeposit onto the surface, sometimes rendering the device unusable.

After the ultrasonication, the sample was rinsed with acetone, methanol, and IsoPropyl Alcohol (IPA), and blow-dried with N_2. Finally, the patterned substrate was cleaned in the plasma asher (100 W, O_2, 10 min) to remove any residual photo-resist, or contaminants introduced by processing.

3.2.1.4 Etch-based Patterning Procedure

An alternative photo-lithography procedure to pattern metal films is wet-etching. This method is useful for polymer or organic materials which are soluble in acetone, or other solvents used in the lift-off procedure. In place of the solvents, an etchant with which the material has good chemical resistance can be chosen [114]. An overview of the etch-based procedure is shown in Figure 3.10.

Following the procedure outlined in Section 3.2.1.1, a metal film was deposited on to the surface of a cleaned substrate. A negative photoresist (AZ15NXT, Microchemicals GmbH) was spin-coated on the sample at 4000 rpm for 30s. This creates an approximately 3 μm thick resist film [115]. The film was baked on a hotplate at 110 $^{\circ}C$ for 2 min to evaporate the solvents. Following this, the sample was aligned with a photomask and exposed to UV light using a mask aligner (Suss MA-6). The exposure energy used was 200 mJ/cm^2. After

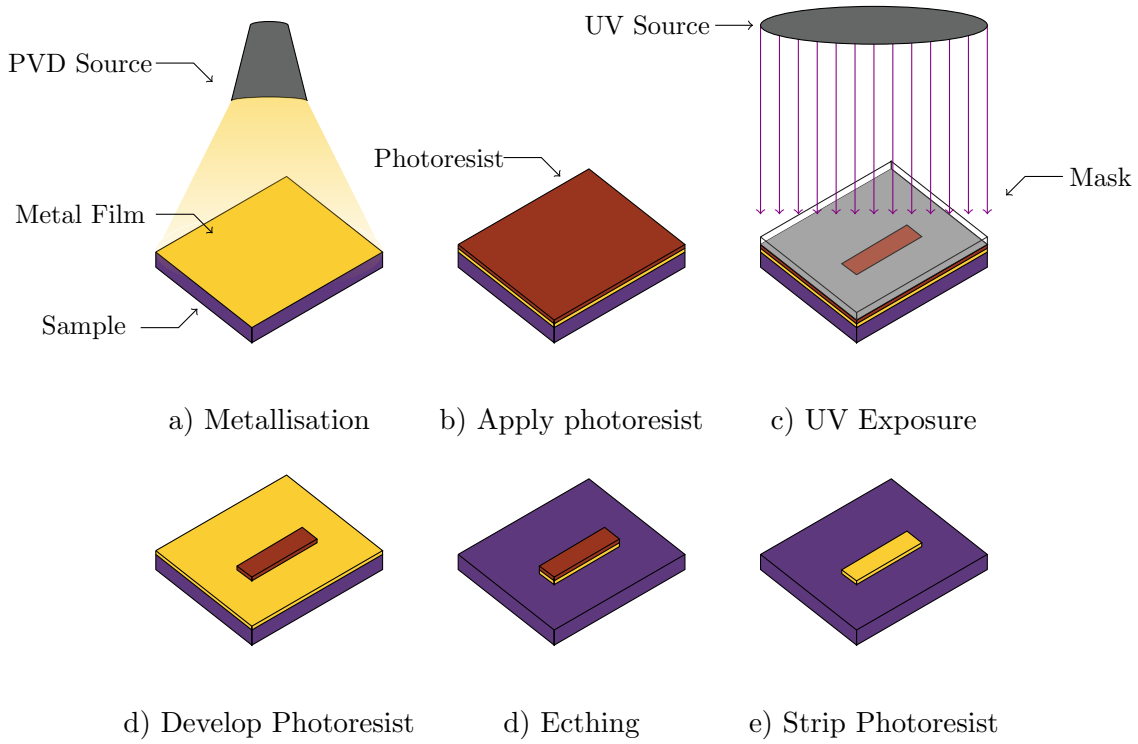

Figure 3.10: *A schematic the process used for etching metal films. a) A metal film is deposited on the surface of the sample using a physical deposition system. b) Photo-resist film is applied to the surface using a spin-coater. c) The photoresist film is exposed to UV light through a mask. The exposed areas define the photoresist pattern. d) The development chemical removes the photo-resist where it was not exposed to UV light. d) Exposed metal is etched away. The patterned photo-resist shields the metal underneath it from the etching chemical. e) The photoresist is stripped away. This can be chemical stripping, or plasma treatment.*

exposing the sample, the resist was developed for 1 to 2 minutes with agitation in AZ326 MIF developer. The full development of the pattern was confirmed by inspection under an optical microscope (Olympus BX30). The fully developed sample was then hard baked on a hotplate at $120°C$ for 2 min to improve adhesion between the photo-resist and metal layer.

In this work, gold is used as the RT material. Gold has a known linear temperature coefficient of resistivity, and is friendly with micro-fabrication methodologies. The gold layer was etched in stock potassium iodide solution (34.0 g potassium iodide, 200ml DI, 7 g Iodine) at $60\,°C$ for 2 to 3 min. It is important that the gold layer is etched completely, otherwise the chrome etchant may undercut the gold layer, and the entire pattern will lift-off. A room-temperature chrome etch for 10 s typically removed the $5\,nm$ nickel chromium adhesion layer. Depending on the sample, the photoresist can either be removed with a solvent wash, or when solvents cannot be used, an O_2 plasma ash will strip the resist.

3.2.2 Buffering Electronics

Common lengths for 3ω RTs are 1 to $2\,mm$. This generally creates a 3rd harmonic voltage between $1\ mV$ and $10\ \mu V$. This small signal requires a buffering amplifier before being passed to the lock-in amplifier for measurement. For this, unity gain differential amplifiers were used. The differential amplifiers used in this work were constructed using the LM342N operational amplifiers (Texas Instruments), and 0.01% precision resistors. The resistor tolerance was important to ensure symmetrical gain of the amplifiers.[1] In the following, the voltage output by the sample amplifier is referred to as V_A, while the voltage output by the control amplifier is referred to as V_B. A schematic of the differential amplifier buffering electronics can be seen in Figure 3.11.

There are two amplifiers used in these buffering electronics. One amplifier buffers the RT signal, while another buffers the ballast resistance. A trimmer resistor (Vishay Components), $R_{ballast}$ was used for the ballast resistance in this system. The importance of the ballast is

[1] In retrospect, it is recommended to use a established differential SOC such as the Analog Devices LTC-6363, or an sysyem-on-a-chip (SOC) instrumentation amplifier. This would greatly simplify the design and initial trouble-shooting process.

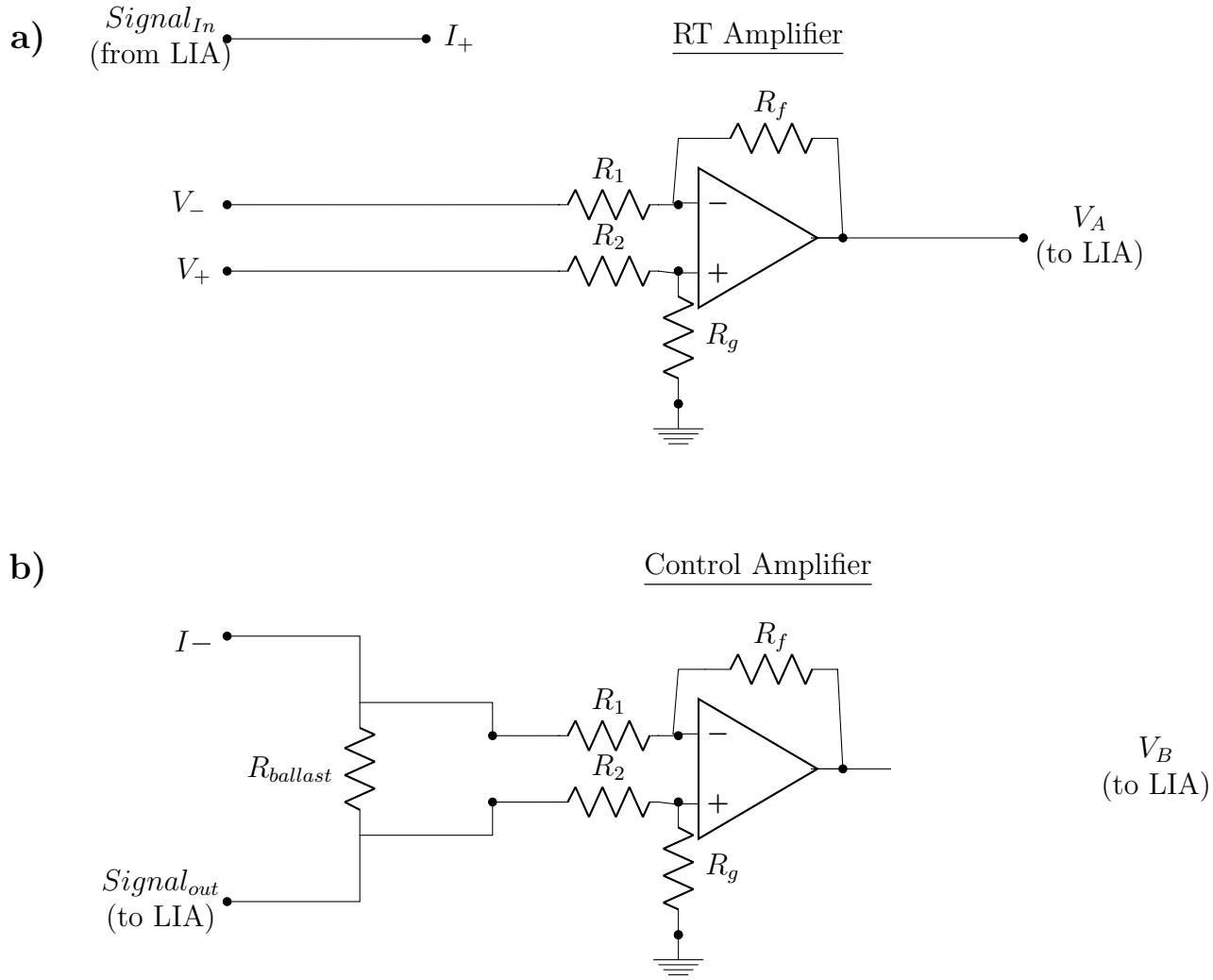

Figure 3.11: *A schematic of the buffering electronics. Two differential amplifiers measure the voltage across the resistance thermometer, and a control resistance. A Digital to Analog Converter, configured as a variable gain element, allows for the common mode background voltage to be subtracted from the RT voltage.*

to act as a third harmonic "control" resistance. As such, the ballast resistance should have a temperature coefficient of resistivity 1/100th that of the RT, and be well heat-sunk to the environment [102]. This minimises any spurious 3rd Harmonic signal in the ballast. When the heating current $I_\omega(t)$ is a true constant AC current source, $R_{ballast}$ is set to have the same resistance as the RT (R_{e0}). The comparatively small temperature coefficient of resistivity of the control sample means that sample experiences the same heating as the sample, but creates a 3rd harmonic less than 1% magnitude of the sample. Due to this, the differential V_A - V_B will remove the background fundamental voltage, and leave only the 3rd harmonic voltage from the sample amplifier. In reality it is very difficult to perfectly match the resistance of the control and sample. For this reason, a digital-to-analog converter is used as a variable gain element to match the fundamental voltage of the ballast to the fundamental voltage of the RT [95].

If a true AC constant current source is not available, there are several alternative approaches which provide the required constant current. The first approach is to set the ballast trimmer potentiometer to a value 100 times greater than the sample resistance. This will mean that a voltage source is an acceptable approximation of a current source [103], as the 2ω resistance fluctuations of the sample will cause less than 1% variation in $I_\omega(t)$. In addition to this, there is a correction available which eliminates residual error. For the voltage correction to be applied, background substitution cannot be used [103].

An alternative to using a ballast resistance, is a voltage-to-current converter. There are many voltage-to-current source operational amplifier circuits available in literature. In this work, an "improved Howland current pump" was implemented [116].

3.2.3 Lock-In Amplifier

A Lock-In Amplifier (LIA) is a phase-detection based measurement device, which can measure small signals in relatively large amounts of noise. In a 3ω system, the LIA is used to measure the magnitude and phase of the 3ω voltage, and provides the sinusoidal heating current to the device. The 3rd harmonic voltage of a joule-heated RT is typically 100-1000 times

Figure 3.12: *Photograph of the Zurich Instruments MFLI Lock in amplifier used in this work. The instrument has a built-in frequency sweeping utility, which makes it ideal for* 3ω *measurements.*

smaller than the fundamental voltage [102]. This requires that the measurement system be precise and able to take measurements with frequency selectivity. The most common and accurate method to achieve this in 3ω systems is a LIA, however a Fourier Transform of a time domain signal has also been used in the past [80]. LIAs operate in a very similar method to an AM radio. An incoming signal is multiplied by a sine wave at angular frequency ω, which is phase-locked to a reference signal. This has the effect of shifting the desired signal in frequency space by $\pm\omega$. This shifts the signal of interest down to DC, a low pass filter is then applied which filters out high frequency results of the demodulation, leaving only a DC voltage which is proportional to the magnitude of the signal of interest. The phase of the signal can also be accurately measured by applying the same technique, with a phase shifted demodulator reference signal.

The LIA used in this work was Zurich Instruments MFLI, a FPGA based digital lock-in amplifier. It has many features which are advantageous for the 3ω method, including built-in sweeping utilities, the ability to monitor harmonics of the reference signal, high power signal generator, and a web-based digital interface.

3.2.3.1 Voltage-to-Current converter

The background of the 3ω method assumes a pure sine constant current source is used for heating [6]. As discussed earlier, two alternatives exist which can be used where this is not available. The first option is to use a voltage-to-current converting circuit [6]. Alternatively,

a voltage source can be used to approximate a current source using a ballast resistance [102]. The main limitation with the voltage source approximation is the power requirements for long, or high resistance RTs. For example, the signal generator of the Zurich Instruments MFLI Lock in Amplifier can generate 14 V_{rms} when configured in differential driving mode. When considering the requirement that the ballast resistance is $100 \times R_{e0}$, this can provides sufficient power for RT elements up to approximately 20 Ω in resistance. This is equivalent to 10 mA heating current.

For RTs which do not fit the above requirement, a voltage-to-current converter was built. The design chosen for this work is an improved Howland current pump design [116]. This current pump design is based on an operational amplifier circuit, which uses both positive and negative feedback to drive a constant current through a load [117].

The bandwidth, and load characteristics of the implemented circuit were tested, and can be seen in Figure 3.13. The bandwidth of the current pump was tested with 19 and 542 Ω loads. As expected for an op-amp, the increased loading reduced the available bandwidth. At approximately 19 Ω, the bandwidth was 10 kHz, while a 542 Ω load the bandwidth was approximately 2 kHz.

3.2.4 Interfacing, and measurement control

3.2.4.1 Cascade microtech probe station

In order to interface the thin-film 3ω RT with external instrumentation, the Cascade microtech electronic probe station was used. The probe station features four gold coaxial probe arms (DCP-100 series, Cascade Microtech), which are mounted onto individual stages with micrometer screws. This allows very fine $x-y-z$ positioning of each of the individual probes. The probes are interfaces with external instrumentation via tri-axial cabling. However for the purposes of 3ω measurements, the triaxial guard ring was grounded via a triaxial to coaxial cable converter.

The sample chamber is a weakly sealed chamber designed to limit exposure to light, and

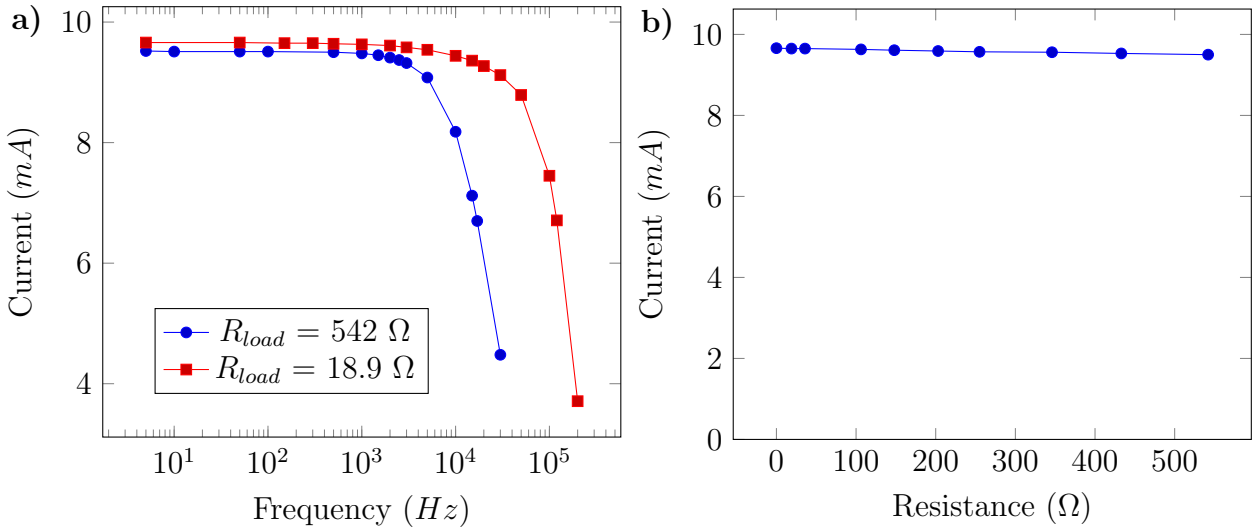

Figure 3.13: *The electrical characteristics of the current pump used in this work* **a)** *The frequency response of the current pump used in this work. Both an 18 Ω, and 542 Ω load connected were tested. An increase in load on the current pump reduced the available bandwidth as expected.* **b)** *The load response of the current pump used in this work. The circuit keeps the current stable to within 150 μA for load resistances ranging from 0 Ω to 542 Ω.*

also to facilitate measurement in the presence of shielding gases. As such, there is a gas inlet in the back plate of the testing chamber. An optical microscope, with integrated top illumination, assists with fine positioning of the probes. The sample chuck is a gold surfaced, temperature controlled chuck. Using the external refrigeration unit (Temptronic), the chuck can be controlled between -60°C and 180°C. In order for measurement beneath room temperature, the measurement chamber must be flushed with dry air, or dry laboratory nitrogen. A photograph of the cascade microtech probe station can be seen in Figure 3.14.

3.2.4.2 R_{e0} measurement

R_{e0} is defined as the resistance of the RT at zero current. Alternatively, this can also be thought of as the intrinsic resistance of the thermometer, in the absence of any joule heating. To measure the intrinsic resistance of the RT, multiple resistance measurements were taken at increasing probe currents. A linear regression was then fitted to the data and extrapolated to the resistance at zero current [95].

A Keithley Sourcemeter 2400 was set up to take four-point resistance measurements. The

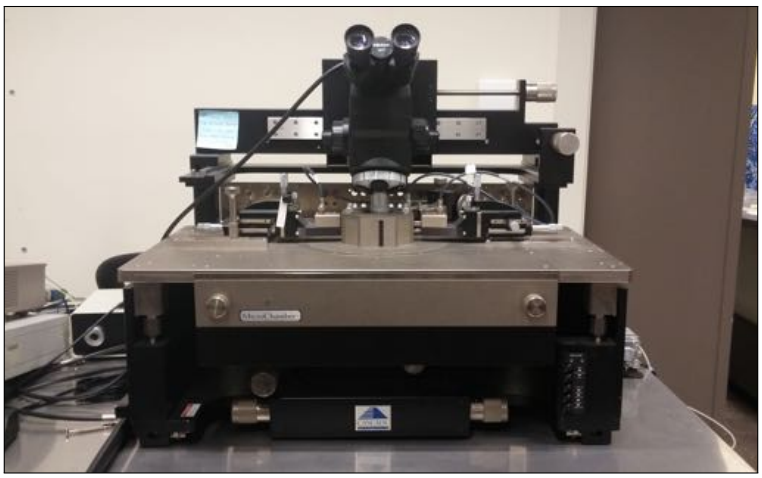

Figure 3.14: *A photograph of the Cascade Microtech microelectronic probe station. This was used in this work to make electrical contact with the 3ω RT and interface it with instrumentation.*

sourcemeter was interfaced with the cascade using RG58U coaxial cabling. The Sourcemeter was programmed through RS-232 to take a series of four-point resistance measurements with driving currents between 1 mA and 20 mA. A linear regression is then fitted to resistance-current data to find the intrinsic resistance of the RT. It was found for some devices, that large measurement currents would cause the RT to self-anneal [118]. In this case, the annealing current was continually applied until the device stabilized. Following this, the measurement procedure was repeated.

3.2.4.3 Thermal coefficient of resistance measurement

One of the largest sources of error in the 3ω method is the Temperature Coefficient of Resistance (TCR) of the RT element [95]. It is well known that the resistivity of thin films depends strongly its thickness, as well as the microscopic crystal structure of the material [119]. The same is true for the TCR [120, 121]. When materials experience an increase in resistivity, they experience a corresponding decrease in their TCR. To calibrate a RT device, the sample was mounted on the temperature controlled chuck of the Cascade Microtech probe station. A k-type thermocouple (80PK-1, Fluke) was attached to the surface of the sample using adhesive tape. The chuck of the probe station was heated from 25°C to 100 °C in steps of 25°C. At each temperature step, 2 to 5 minutes was waited for the sample to reach thermal

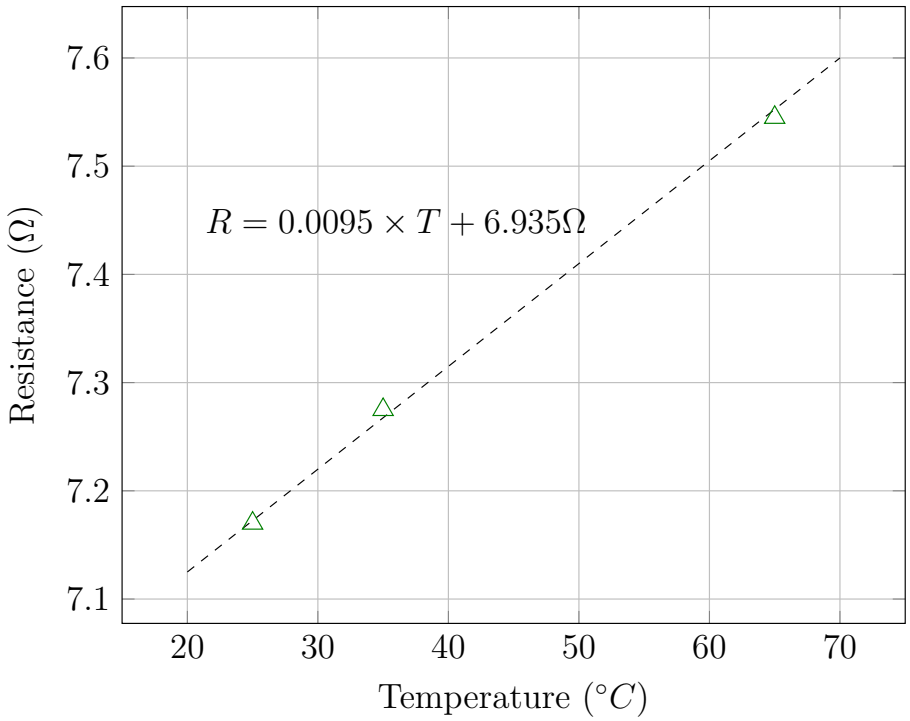

Figure 3.15: *Graph of the TCR for a 50 µmx 1 mm RT. The linear regression yields* $R = 0.0095 \times T + 6.935\Omega$. *This is equivalent to a temperature coefficient of resistance of,* $\alpha_{25°C} = 13.3^{-4}/°C$.

equilibrium. The zero-current resistance of the sample was then measured.

An example TCR calibration of an RT being used in this work is shown in Figure 3.15. A linear regression was fitted to the resistance-temperature measurements. The linear regression was $R = 0.0095 \times T + 6.935\Omega$. The RT responded to temperature at a rate of $\frac{dR}{dT} = 0.0095$ $\Omega/°C$. The temperature coefficient of resistance is the rate of resistance change expressed as a percentage of the total resistance at a reference temperature. The recorded thin film value was $\alpha_{25°C} = 13.3 \times 10^{-4}/°C$, while the TCR of bulk gold is $\alpha_{25°C,bulk} = 37 \times 10^{-4}/°C$, almost three times the thin film value [121].

3.2.5 Data Processing Methods

3.2.5.1 Frequency Domain Measurement

The frequency domain measurement, also referred to as the classical 3ω method, is a very well established method of thermal conductivity measurement for thin-films [6, 21, 95, 102]. The thermal model, and further background material for the classical method can be found discussed extensively in literature [6, 102].

In the classical 3ω method, a frequency sweep is recorded, and the 3rd harmonic is measured. Following the discussion in Section 3.1.1, the 3rd harmonic voltage can be transformed into the thermal resistance via,

$$V_{3\omega,in-phase,rms} = -\frac{1}{2}\alpha R_{e,0}^2 I_{1\omega,rms}^3 Re[Z(2\omega)] \tag{3.8}$$

where α is the thermal coefficient of resistance, $R_{e,0}$ the zero current resistance of the RT at the measurement temperature, $I_{1\omega,rms}$ the RMS heating current, and $Z(2\omega)$ the thermal transfer function at twice the electrical driving frequency (i.e. the thermal frequency). Over a range of thermal frequencies, there is a linear relationship between $Re[Z(2\omega)]$ and $ln(2\omega)$; this is called the linear regime in literature [6, 102]. The slope, $\frac{\delta Re[Z(2\omega)]}{\delta ln(2\omega)}$, can be used to calculate the thermal conductivity via Equation 3.9,

$$\frac{\delta Re[Z(2\omega)]}{\delta ln(2\omega)} = -\frac{1}{2\pi k_s L} \tag{3.9}$$

where L is the length of the RT element, and k_s the thermal conductivity of the material surrounding the RT element. All the properties used in Equation 3.8 and Equation 3.9 can be measured or calculated using procedures previously described. One of the major limitations of the frequency domain 3ω method for thin films, is the requirement that the thermometer half width is 1/5th of the thin film thickness [6, 102]. This can become limiting, as films less than $30\,\mu m$ will need to have a near mirror finish to support a continuous RT. This limitation is one reason for the development of the differential 3ω method.

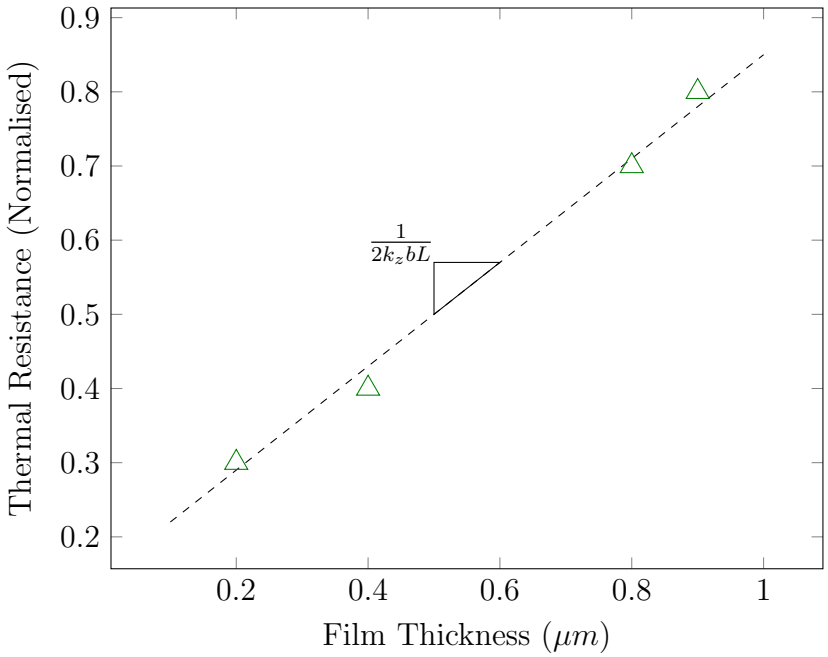

Figure 3.16: *A graph showing the concept behind the differential* 3ω *method. Multiple* 3ω *samples are measured, each with an varied thickness. The slope of the linear regression fitted to the thermal resistance and film thickness will contain the thermal conductivity of the film. This is indicated by the annotation.*

3.2.5.2 Differential 3ω Method

The differential 3ω method is a variation of the technique which extends the capabilities of the classical method to much thinner films. The method involves using two samples; one sample with, and a control without, the structure of interest [102]. In contrast to the classical 3ω method, a wide RT is fabricated on the surface of both samples. The wide RT design, relative to the thin film thickness, creates one-dimensional heat conduction through the film [102]. This one-dimensional heat conduction allows the control to be simply subtracted from the thin-film result, in order to isolate the conduction due to the thin film. This strategy enables the measurement of thin films down to 50 nm [102].

The thermal transfer function for both the sample, and control can be calculated following Equation 3.6 (the same method as the classical 3ω method). The average thermal resistance in the linear regime is then taken, and can be plotted against film thickness. An example of this can be seen in Figure 3.16.

As long as the heat-flow is quasi-static and one-dimensional [102], then the thermal resistance will vary linearly with thin film thickness. The relation between thermal resistance and thermal conductivity is given by,

$$R_{th} = \frac{d}{2k_z bL} \tag{3.10}$$

where d is the film thickness, k_z the thermal conductivity in the z direction, b the heater half-width, and L the heater length. A linear regression fitted to thermal resistance and film thickness will thus have a slope proportional to the inverse of thermal conductivity, as defined by Equation 3.10.

The differential 3ω method is a powerful extension of the classical technique. The differential method is able to eliminate sources of error from insulating and adhesion layers by including those layers in the control measurement. As already mentioned, this allows much smaller structures to be measured. This is very relevant as many emerging applications, such as phononic materials, involve measurement of structures less than 1 μm thick. A possible limitation of this technique is the assumption that thermal conductivity varies linearly with film thickness. It has been established already that many thin films behave in anomalous ways. Phononic structures which are similar dimensions to phonon mean free paths are another example of this [101, 122].

3.3 Results and Discussion

To first calibrate and troubleshoot the newly established measurement system, some well understood materials were measured for this work. The classical 3ω method was initially calibrated using two materials; Soda-lime glass, and borosilicate glass. Soda-lime microscope slides are recommended in literature as an initial measurement material [6]. The mid-range thermal conductivity, and millimetre thickness of soda-lime glass slides creates a 3rd Harmonic voltage with a high SNR, and large slope [6]. This can be used to carry out a useful series of data validity checks. In this work, an array of RT's were fabricated on top of a

a)

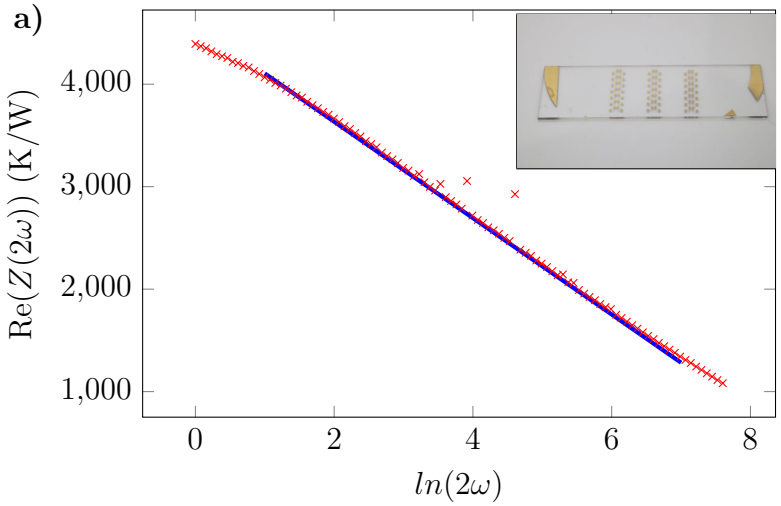

b)

R_{e0}	6.555 Ω
α	$29 \times 10^{-4}\ °C^{-1}$
$I_{1\omega,rms}$	13.13 mA
L	0.3 mm
$\frac{\delta Re[Z(2\omega)]}{\delta ln(2\omega)}$	-459.33
$k_{sodalime}$	1.154 $W/m-K$

Figure 3.17: *A graph and table showing the results from the soda-lime classical 3ω measurement. a) An initial calibration 3ω measurement on soda-lime glass. The final thermal conductivity measured was 1.154 $W/m-K$, which is within experimental uncertainty of the range of literature values of 0.7 to 1.7 $W/m-K$. (Inset) Photograph of the fabricated RT's on the surface of a soda-lime microscope slide. b) Tabulated results from the initial 3ω measurement.*

standard soda-lime glass microscope slide (Thermo Fisher) using the photo-lithographic lift-off process described in Section 3.2.1.3. The 3ω process introduced in Section 3.2.5.1 was then applied. The 3ω in-phase frequency response, and a macro-image of the RT array on the soda-lime glass is shown in Figure 3.17 a). A linear regression fitted against the natural logarithm of thermal frequency is also displayed. The slope of this linear regression can be transformed into the thermal conductivity of the substrate. The results of this measurement is displayed in Figure 3.17 b). The measured result for this slide was $1.15 \pm 0.01\ W/m-K$. This was well inside the literature range for soda-lime glass.

While soda-lime is an ideal test platform for initial 3ω experiments, and can provide many insights into sources of error in the technique, it does not have a well-defined elemental composition, or microscopic structure [123]. In literature soda-lime is listed as having a thermal conductivity from 0.7-1.7 $W/m-K$ [124, 125]. With this in mind, soda-lime is not an ideal choice for a precise calibration material, as the true thermal conductivity of any single sample could vary by over 100% on even a single slide.

Borosilicate glass meanwhile, often referred to by the brand name Pyrex, has a well defined

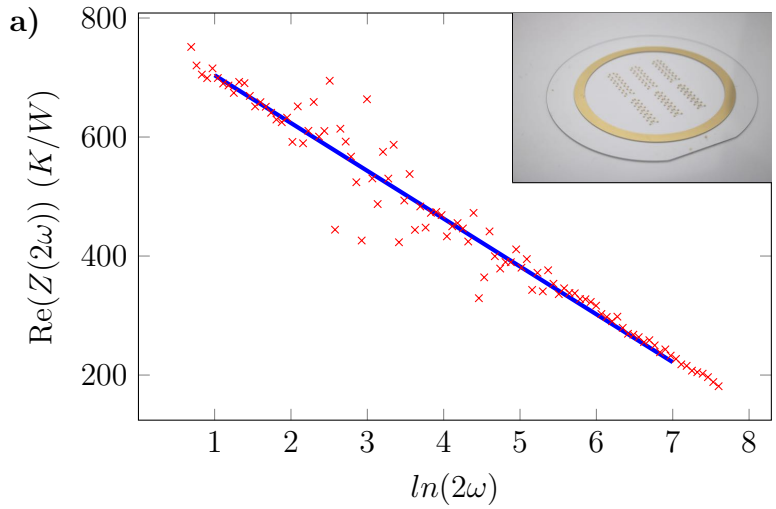

b)

R_{e0}	20.38 Ω
α	$34 \times 10^{-4}\ °C^{-1}$
$I_{1\omega,rms}$	12.4 mA
L	2 mm
$\frac{\delta Re[Z(2\omega)]}{\delta ln(2\omega)}$	-80.36
$k_{borosillicate}$	$0.99\ W/m-K$

Figure 3.18: *The results of the precision 3ω calibration test. a) The in-phase thermal resistance from the 3ω measurement on borosilicate glass. The final thermal conductivity measured was 0.99 $W/m-K$, which is within experimental uncertainty of the nominal literature value 1.005 $W/m-K$. (Inset) A photograph of an array of 3ω thermometers on a borosilicate glass wafer. b) Tabulated results from the full 3ω measurement.*

composition and crystal structure. As a result, is often used as a reference material for thermal measurements [95]. Borosilicate glass also has many of the same advantages as soda-lime glass, such as large thickness and low to mid-range thermal conductivity. This makes borosilicate glass a good choice to assess the precision of the 3ω method. The same 3ω fabrication and measurement procedures used for the soda-lime glass were applied to a borosilicate glass wafer (University Wafer). The fabricated test wafer can be seen in Figure 3.18 as an inset. Figure 3.18 shows a summary of the 3ω measurement. A linear regression is fitted to the in-phase temperature response against the logarithm of thermal frequency, as before.

The resulting thermal conductivity measured is 0.99 ± 0.01 W/m-K. The literature value is 1.005 W/m-K[125]. This is within tolerance of the literature thermal conductivity for borosilicate glass.

3.3.1 Differential 3ω method

To calibrate the differential 3ω method, spin-coated Poly(Methyl Methacrylate) (PMMA) thin films were chosen. PMMA is an accessible, easy to fabricate thin-film, which also has a low thermal conductivity. A low thermal conductivity creates larger temperature oscillations which are easier to measure. The standard RT design described in Section 3.2.1.2 can measure thin films between 50 nm to 4.5 μm. As such, PMMA thin films were prepared by spin-coating dissolved PMMA onto soda-lime cover slip substrates (Thermo Fisher). The prepared spinning solutions were 2.2% (w/v) PMMA (35 kDa, Sigma Aldrich) dissolved in toluene (Analytical grade, Thermo Fisher). The PMMA solution was spin-coated at 5000 rpm for 30s to form approximately 50 nm layers. This was repeated multiple times until the total layer thickness was >200 nm i.e. 4 layers. Following the procedure outlined in Section 3.2.1.2, two RTs were fabricated. The first on the surface of the PMMA thin film, and a second on a control cover-slip without a thin film. Both RTs were fabricated using shadow mask patterning due to the solvent sensitive nature of PMMA.

The thickness of the PMMA layer was measured by scratching the PMMA with tweezers, and measuring a step using a profilometer (Dektak 150, Bruker). Three line sections were scanned using the surface profilometer. From this the average RT width, and the RT thickness can be extracted. The average Δ of thermal resistance was then plotted against thickness, the result of which can be seen in Figure 3.19.

The measured thickness of the PMMA layer was $433\,nm$ thick. The difference in thermal resistance created by this film was approximately 35 K/W. Using Equation 3.10, the calculated thermal conductivity was $k_{PMMA} = 0.24W/m-K$. This value is well within the known range for PMMA materials (0.1-0.26 $W/m-K$) [126]. While there is a large amount of variance in the literature value, the result fell within the expected range for spin-cast PMMA. Only two thickness values were used in this measurement, which is common in literature [102], however a larger range of thickness's would improved measurement confidence.

a)

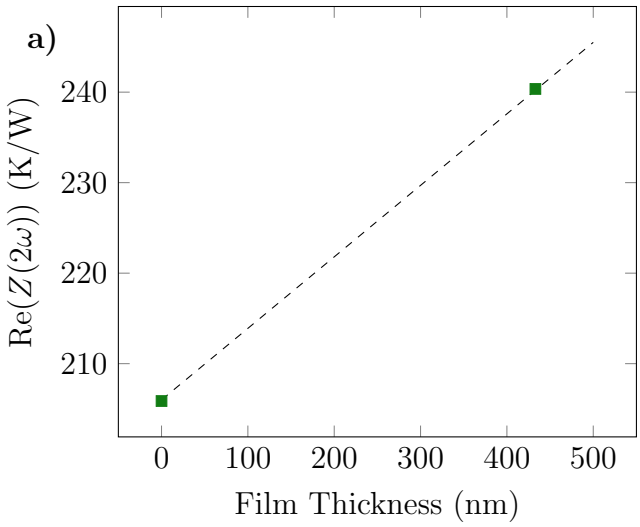

b)

$R_{e0,sample}$	2.548 Ω
$R_{e0,control}$	2.855 Ω
b	28.4 μm
α	34×10^{-4} $°C^{-1}$
$I_{1\omega,rms}$	35.0 mA
L	1 mm
$\frac{\delta Re[Z(2\omega)]}{\delta d}$	7.263×10^7
k_{PMMA}	0.242 $W/m-K$

Figure 3.19: *A complete differential* 3ω *method measured on spin-cast PMMA thin films. The measured thermal conductivity for the thin film was 0.24* $W/m-K$*.* **a)** *A graph showing the thermal resistance measured by the RT changing with film thickness.* **b)** *A summary of the RT properties from this calibration measurement.*

3.3.2 Resistance and TCR

3ω RTs are typically metal thin films micro-fabricated on the surface of a sample. However the resistivity, and temperature coefficient of resistivity, of thin films can vary dramatically from that of bulk materials [102, 119–121]. Large changes in these properties occur when the mean free path of electrical charge carriers is comparable to the film thickness [120]. In thin films, the mean free path is reduced, and the resistivity of the material will experience a corresponding increase via the Drude model [127].

In addition, the increase in resistivity due to thin film geometry creates a corresponding *reduction* in the temperature coefficient of resistivity. This is because the increase in resistivity due to temperature is caused by a reduction in mean free path of electrical charge carriers which is the same underlying mechanism behind temperature related changes in resistance. i.e. charge carriers which would have been scattered by thermal phonons are now scattered by the geometry of the thin film [119–121].

This large variance in TCR and resistivity means that the TCR and $R_{e,0}$ are the largest source of error in the 3ω method [95]. To explore and understand this concept further, a

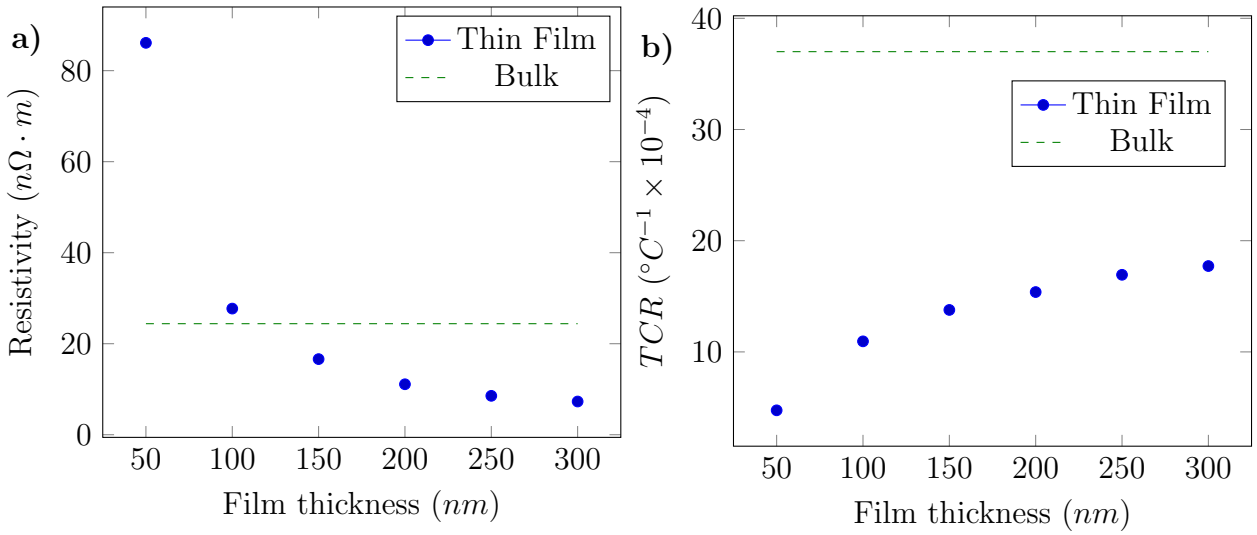

Figure 3.20: *Graphs showing the co-dependency of a resistivity, and TCR on thin film thickness.* **a)** *The resistivity of gold versus film thickness. Resistivity of thin films less than* 200 *nm thick are dramatically larger than the bulk literature values.* **b)** *Plot of the TCR of gold thin films changing with thin film thickness. The TCR of the gold thin films was less then half of the literature value, and had a strong dependence of film thickness.*

brief study on the TCR and $R_{e,0}$ thickness curves has been carried out for the purposes of this thesis.

To calibrate the TCR and resistivity curve of the electron-beam deposited gold used for this work, a thickness series was prepared. Six titanium-gold RTs arrays with varying thin film thicknesses were prepared using the standard e-beam metallisation technique discussed above. The zero-current resistance and TCR of three thermometers per substrate was then measured. The results of the thin film measurements compared to bulk values, taken from literature, can be seen in Figure 3.20.

As Figure 3.20 demonstrates, the resistivity and TCR is offset substantially compared to the bulk literature values. This is most likely due to the crystal structure of the deposited gold film . However another possibility is that the 5 to 10 *nm* titanium adhesion layer alloyed with the gold; titanium's resistivity is 18 times higher than gold, so alloying may shift the bulk resistivity substantially . As previously discussed, the resistivity and TCR are both linked to the mean free path of the electrical charge carriers. Figure 3.20 demonstrates the strong thickness dependence of the resistivity and TCR. When these properties are normalised and

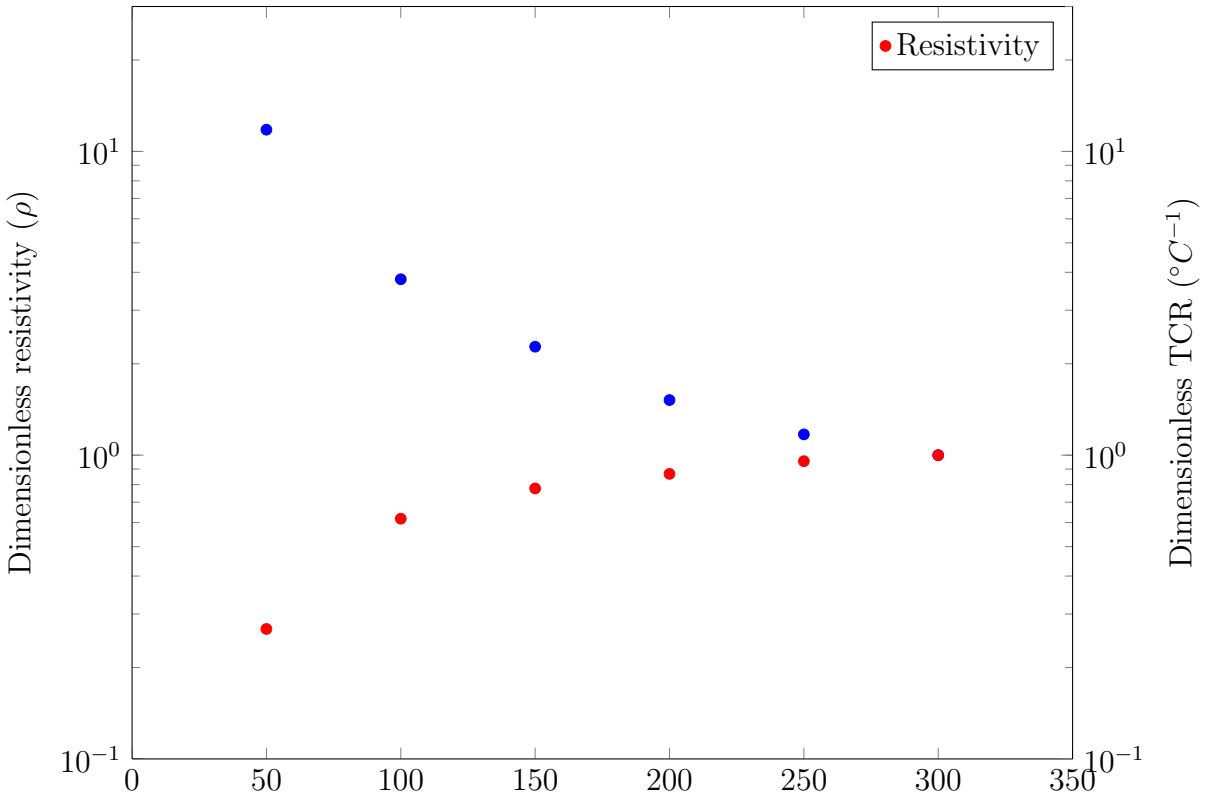

Figure 3.21: *A graph showing the normalised resistivity and TCR of gold thin films against the film thickness. The graph shows how the two properties are interconnected. An increase in resistivity creates proportional reduction in the temperature coefficient of resistivity. This is due to both properties being linked to the mean free path of electrical charge carriers. The Note the log axis.*

plotted on the same axis, the codependency of the properties on the scattering rate can be clearly seen. This is shown in Figure 3.21.

To function as an effective resistance thermometer, the TCR of the material should be maximised. For the 3ω method, the thermometer should also be as thin as possible so the heat capacity of the thermometer itself does not interfere with the measurement. From the results shown in Figure 3.21 it was concluded that a thickness of 200 nm would satisfy this condition. Figure 3.20 also demonstrates that e-beam gold thin films are substantially offset from the literature bulk values for gold.

3.4 Conclusion

This chapter described the establishment and verification of the 3ω method for a variety of different material structures and use cases. The classical 3ω method was verified using both soda-lime, and borosilicate glass. Both of these measurements fell within the measurement uncertainty of the accepted value. In addition, the differential 3ω method was verified using spin-cast PMMA films. This gave a result of $0.24\ W/m-K$, well within the accepted range for PMMA and aligning with the expected value for spin-cast PMMA films. A brief study on the thickness relation between resistivity and TCR for titanium-gold thin films revealed a codependent relationship to the film thickness. The thin film values were also substantially different from bulk literature values for gold. This is demonstrates the importance of TCR and resistance calibration for these measurements.

In the future a commercial AC constant current supply would substantially increase the capabilities of the established system. While the ballast resistance is an adequate current source approximation for many materials and RT geometries, the requirement that $R_{ballast} = 100 * R_{e0}$ can limit the power able to be supplied by common voltage sources. A commercial supply would allow for samples with very small thermal resistances, or equivalently very high thermal conductivities to be measured by removing the ballast resistance requirement. A commercial AC supply would also expand the bandwidth of the measurement into the range were the specific heat capacity of biological organisms could be investigated [78].

In the next chapter, the classical 3ω method is applied to a composite pressed nanoparticle material. The thermal conductivity of three different blends of nanoparticle blends are fabricated and tested, and the thermal transport mechanisms are discussed in the context of the literature.

Chapter 4

Thermal characterisation of packed nanoparticle beds

4.1 Introduction

Nanoparticle based materials create some of the highest performing thermal insulation in the world. In particular aerogels are known for their excellent mechanical, and thermal insulation properties [36, 128, 129]. As such, Aerogels in general have become the high performance comparison value for any new material being studied for thermal insulation purposes. One of the largest limitations of aerogels however, is that they require expensive and complicated processing. While there have been recent advances in this area, its application can still be somewhat limited due to these factors [38].

An attractive alternative to aerogels, with comparable thermal insulation performance and interesting mechanical properties, are packed nanoparticle beds [8, 39, 40, 43, 104]. In this work, and in literature, a packed nanoparticle bed refers to a close-packing of spherical nanoparticles. Through a combination of high interface density, high interface resistance, and small pore sizes, these materials can create thermal insulation performance that is extremely competitive to aerogel materials [8, 43].

To help explain the origin of this high thermal insulation performance, a two-dimensional schematic of a packed nanoparticles bed is displayed in Figure 4.1. The diameter of the nanoparticle is annotated as $2R$, and the inter-nanoparticle contact patch diameter is annotated as $2a$. The geometry made from the interface between two nanoparticles, shown in detail as an inset, is referred to as a "nano-constriction". In electrically insulating nanoparticles, phonons are the majority thermal energy carrier. The phonon transmission through the nanoconstriction has been shown to scale with the ratio of inter-nanoparticle contact area, and nanoparticle radius ($\frac{a^2}{R}$). This is analogous to phonon filtering through the nanoconstriction [39]. This is the origin of the high interface resistance between nanoparticles, and is of particular interest to this work, as the mechanism is predominately solid-state [39].

This phonon filtering effect can be further improved via *composite* packed nanoparticle beds. Such composites use mechanically mismatched nanoparticles in a single packed bed structure. This adds additional inter-nanoparticle thermal resistance to the nanoconstriction, as the phonon transmission function will be further restricted by the abrupt change in acoustic

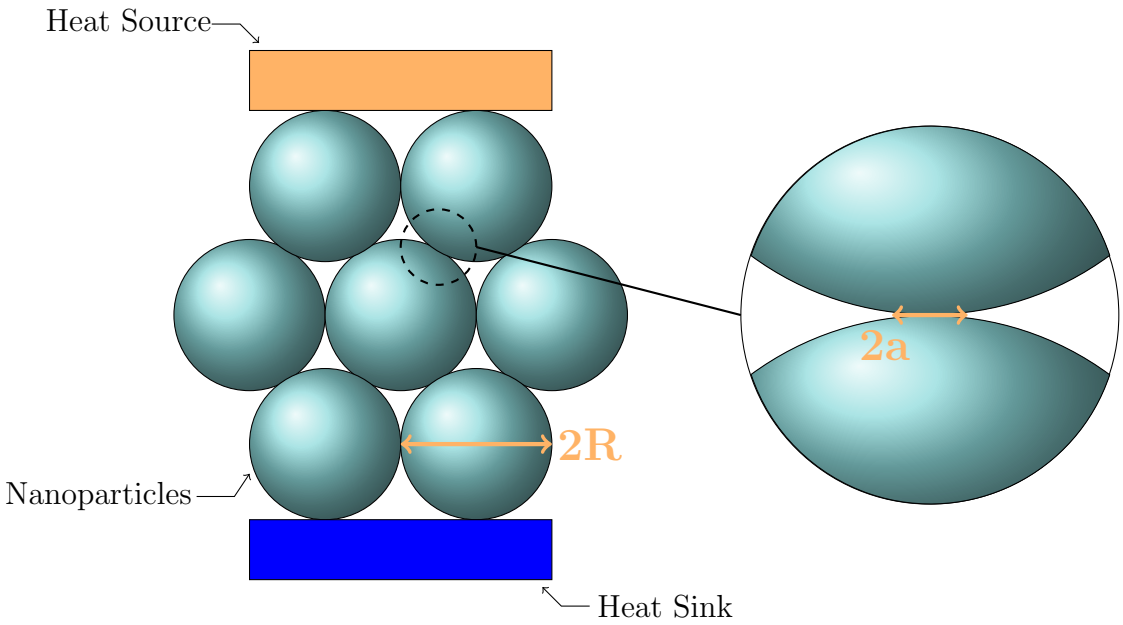

Figure 4.1: *An illustration demonstrating a cross-section of the close packed nanoparticle bed. The nanoparticle diameter is annotated as 2R, and the diameter of the inter-nanoparticle contact patch is annotated as 2a. The phonon conduction between nanoparticles scales with the ratio of contact patch area to nanoparticle radius.*

Material	v_l (km/s)	v_t (km/s)	ρ (g/cm^3)
SiO_2	5.953	3.743	2.2
Al_2O_3	10.844	6.421	3.97
C	10.7	-	2.25

Table 4.1: *A summary of the relative mechanical and acoustic properties of silica, alumina and carbon materials. When phonons traverse the interface of two acoustically-dissimilar materials, they are reflected or transmitted proportional to the difference in acoustic impedance.*

properties, via the acoustic mismatch model [12]. The addition of an acoustic properties mismatch has already been shown to improve the thermal insulation performance of packed nanoparticle beds in literature [8]. In literature, the highest performing packed nanoparticle beds were formed by blends of silica, alumina and carbon black nanoparticles [8]. A summary of the acoustic and mechanical properties of silica [130, 131], alumina [131–133], and carbon [131, 134, 135] is shown in Table 4.1.

Computing the exact three-dimensional acoustic mismatch transmission function which results from these values is difficult however. It is a function of the phonon angle of incidence through Snells' law, the frequency-dependent group velocity, and the density of states. How-

	SiO_2	Al_2O_3	C
SiO_2	100%	50%	70%
Al_2O_3	20%	100%	93%
C	25%	90%	100%

Table 4.2: *The acoustic mismatch transmission function for phonons. The averaged transmission function was found using the tabulated results calculated by Cheeke et al. [12, 25].*

ever, Cheeke et al. have calculated and tabulated a direction and frequency averaged approximation of the acoustic mismatch function for a range of density and velocity ratios [25]. This can be used to estimate the efficacy of the blended nanoparticle materials. The tabulated average transmission functions for the identified materials is shown in Table 4.2. From this, it can be seen that there is low (0.25%) transmission from the alumina and carbon into the silica nanoparticles.

One outstanding issue with these high performance packed nanoparticle beds, is moisture infiltration and performance degradation over time. The probable causes of this degradation can be examined using Prashers packed nanoparticle bed model [39]. As previously stated, the phonon transmission is proportional to a^2/R. The contact patch radius, a between two spheres is a function of the sphere radius, Young's modulus, surface energy, and the force exerted on the two spheres [39, 136]. At the macro scale, the contact area of two spheres is dominated by the sphere diameter and the Young's modulus of the material. However on the micro- and nano-scale, the contact area is substantially effected by the surface energy of nanoparticle. Proposed causes of the degradation are moisture absorption and the formation of chemical bonds between adjacent nanoparticles [9]. These factors in turn effect the thermal conduction through the nano-constriction by increasing a, the radius of the contact patch.

For study in this work, two particular high performance nanoparticle mixes were chosen from literature [8], as well a simpler composite blend with only two types of nanoparticle. The two established compositions were three-part nanoparticle blends consisting of varying weights of silica ($30\,nm$), alumina ($< 50\,nm$) and carbon black ($30\ nm$) nanoparticles. The highest performing nanoparticle blends from literature consisted of 1/1/4, and 1/2/3 weight ratios of $SiO_2/Al_2O_3/C$ nano-powders, respectively. These blends had thermal conductivities between

0.005 and 0.010 $W/m-K$, as measured in literature using laser flash calorimetry. There was significant variation in these measurements however, depending on the measurement technique used, and also the size of the samples [8]. When a $100\,mm \times 100\,mm$ tile of the material was measured using a guarded heat calorimeter, its thermal conductivity was approximately 0.08 $W/m-K$ almost ten times that of the laser flash calorimeter measurement.

Due to this, the specific goals of this chapter were to replicate the high performance nanoparticle materials from literature, and add to the pool of results by measuring the samples with the guarded hot plate method, and the 3ω method. This is the first such study of packed nanoparticle beds using the 3ω method. This involved the development of custom patterning and supporting apparatus for the delicate, and soluble samples. In addition to the existing nanoparticle blends, another simpler composition 1/0/1, $SiO_2/Al_2O_3/C$ nano-powders was fabricated and tested as a point of comparison.

4.2 Methods

4.2.1 Nanoparticle blend preparation

In order for the packed nanoparticle bed to be measured by the guarded hotplate method, the nanoparticles were formed into large $\sim 68\,mm$ diameter pucks. A circular form tool was machined from 6061-T6 aluminium (see Figure 4.2 (a)) using the Minitech micro-mill described in Chapter 3. This was used to shape and press the dried nanoparticles into a consistent puck dimensions for measurement.

To prepare the nanoparticles for puck formation, the silica (Sigma Aldrich), alumina (PlasmaChem), and carbon nanoparticles (PlasmaChem) were homogenised using a manual mortar and pestle. CrystalBond 509 (10% (w/w) relative to nanoparticle materials) was dissolved in acetone, and the homogenised nano-powder blend was stirred into the solution. The mixture was heated to $45°C$ on a hotplate, and left for 12 hours for the acetone to evaporate. This left a dried nanoparticle-CrystalBond composite material in the base of the beaker. To break up any agglomeration of alike nanoparticles which may have occurred during the

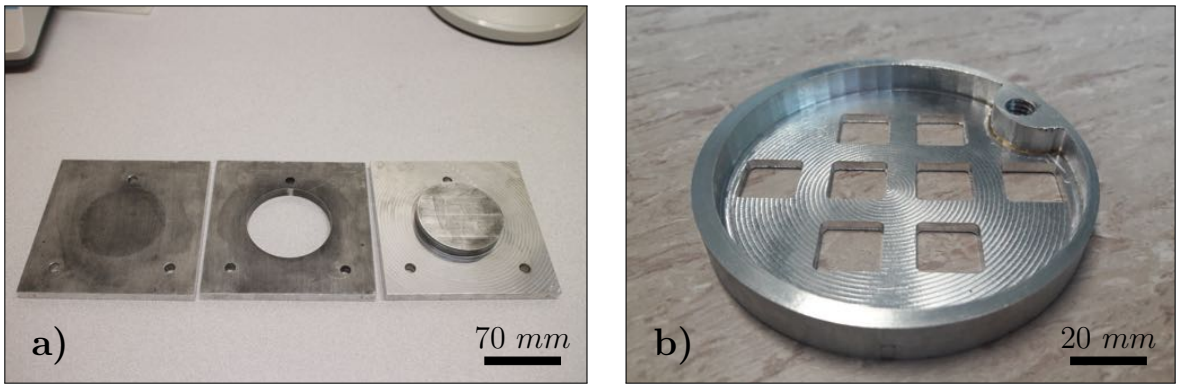

Figure 4.2: *Photographs of the CNC machined experimental apparatus used to fabricate and characterise the nanoparticle puck material.* **a)** *The nanoparticle puck forming press.* **b)** *The evaporation basket used to support the delicate nanoparticle materials while the insulation layer and RT material were evaporated onto the surface. The RT was patterned using a shadow mask, as the other available patterning methods would have destroyed the sample.*

evaporation process, the dried material was then re-powdered and re-homogenised using a manual mortar and pestle.

This blend was then loaded into the form tool, and a 12,000 kg hydraulic press was used to compact the nanoparticles into the puck form. In order to de-mould the puck, the back plate of the form tool was first removed. This allowed the plunger of the tool to be pressed completely through and de-mould the puck.

4.2.2 Calorimeter thermal measurement

The thermal conductivity of the pressed nanoparticle materials was measured with two techniques in this work. The first method used was a standard guarded hot plate calorimeter [137]. The measurement concept is demonstrated in Figure 4.3. An electrical heater is used to apply heat input, and establish a temperature gradient across the material under test. Two thermocouples either side of the sample measure the temperature drop across it. To prevent lateral heat leakage and keep the heat conduction across the sample pseudo one-dimensional, a heated annual "guard ring" laterally surrounds the hot plate.

Once a stable temperature gradient is established, the electrical power required to maintain the temperature gradient across the material can be used to calculate the heat flux through

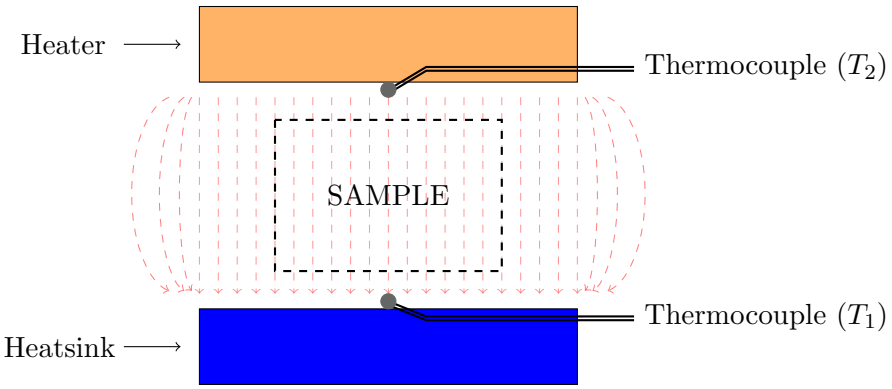

Figure 4.3: *A conceptual diagram of the guarded hot plate calorimeter. An electrical heater applies a DC thermal flux to the sample, whilst two thermocouples measure the static temperature gradient across the sample. Once thermal equilibrium is reached, the electrical power required to maintain the temperature gradient is recorded. Using these measured parameters, the sample thickness, and the hot plate area, the thermal conductivity of the sample can be calculated.*

the sample. The thermal conductivity of the sample can then be calculated from the measured temperature gradient across the material, the power supplied to the heater, and the known thickness of the sample under test. Formally, the thermal conductivity of the sample, k_{sample}, is

$$k_{sample} = \frac{d \cdot P_{electrical}}{A \cdot (T_2 - T_1)} \tag{4.1}$$

where d is the thickness of the material under test, P the power applied to the hot plate to maintain a set temperature, A the area of the hot plate, T_1 the cold plate temperature and T_2 the hot plate temperature. The hot plate calorimeter apparatus used for this work is owned and operated by Callaghan Innovation, Auckland. Nanoparticle pucks were couriered to Auckland from Christchurch, New Zealand for measurement. While, the guarded hot plate method is a reliable and simple measurement technique, its application is limited to macro-size samples. As such, it is not capable of measuring micro- or nano-scale materials like thin films. Once the guarded hot-plate measurements had been completed, the samples were returned to the University of Canterbury for re-measurement with the 3ω method, which was established as a part of this thesis.

4.2.3 3ω method preparation and RT patterning

The large puck structure was initially fabricated to facilitate measurement with the guarded hot plate method. After the calorimeter measurements were complete, the sample needed to be diced into smaller pieces, and a 3ω RT micro-fabricated on the surface. The nanoparticle puck was diced into approximately $15mm \times 15mm$ squares using a scalpel. Following this, an electrical insulation layer was evaporated onto the surface to insulate the RT from the sample. This was required as carbon nanoparticles are electrically conductive. The ideal electrical insulation layer has a large thermal conductivity to minimise its impact on the thermal resistance of the sample, i.e. to minimise any additional thermal resistance measured by the RT. Popular choices in literature include SiO_x [96], Si_3N_4 [138], and Al_2O_3 [139]. For this work, Al_2O_3 was used.

For deposition of the insulation and RT material, the Edwards Auto 500 electron-beam evaporation system was utilised (see Chapter 3). This process required the inverted mounting of the sample above the evaporation plume. To facilitate this with the delicate nanoparticle material, an evaporation basket was machined in 6061-T6 aluminium. This is shown in Figure 4.2 (b), alongside the other custom machined apparatus. The insulation material was evaporated first onto the surface of the puck. Following this, a RT shadow mask was mounted between the evaporation basket aperture and the nanoparticle material itself. The titanium gold RT could then be fabricated on the surface of the puck using the standard shadow mask patterning procedure, described in Chapter 3.

For measurement, the nanoparticle puck samples were mounted in the Cascade Microtech probe-station, described in Chapter 3. The probe station has a temperature controlled chuck, and an external gas line. This allows the chamber temperature to be controlled between $-60°C$ and $180°C$. 3ω measurements were recorded for the nanoparticle materials over a temperature range of -25$°C$ to 120$°C$ in a dry nitrogen environment. These results could then be compared to literature measurements of comparable nanoparticle systems.

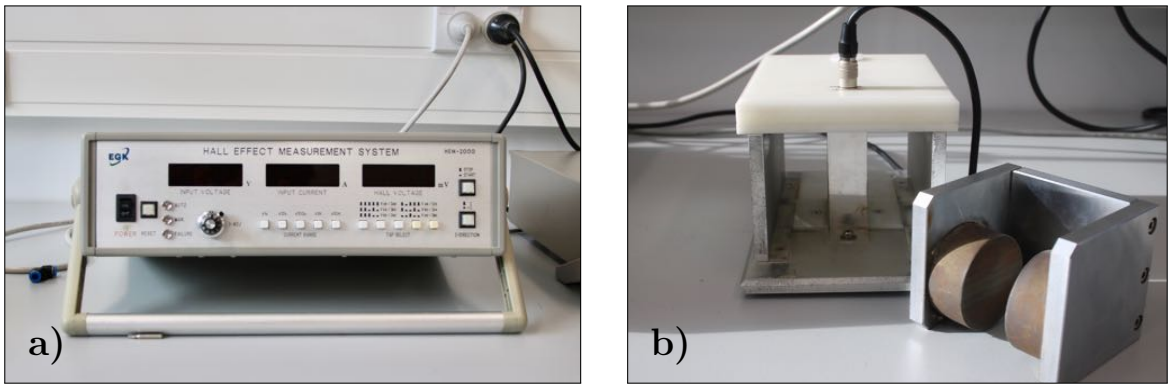

Figure 4.4: *Photographs of the EGK HEM-2000 Hall effect measurement system.* **a)** *The hall effect measurement head unit. b) The 0.5 T magnet used for the development of the Hall voltage, and therefore measurement of carrier concentration.*

4.2.4 Hall effect measurement

In order to characterise the electrical properties of the nanoparticle pucks, a Hall-effect measurement system was used. Generally, the Hall effect refers to the development of a voltage potential perpendicularly across an electrical conductor, due to the deflection of electrical charge carriers under the influence of an applied magnetic field [140]. In physics and materials engineering this effect is used to study the conductivity, charge carrier mobility, and charge carrier concentration in semiconducting materials [141]. The system available in the University of Canterbury micro-fabrication laboratory is the HEM-2000, Hall effect measurement system (EGK Industries). A photograph of this system is shown in Figure 4.4. The system applies a DC current through a sample and uses the developed voltage to calculate the resistivity of the material. A magnetic field of $0.5\,T$ is then applied to the material, perpendicular to the current flow. This causes the charge carriers to deflect creating a voltage across the conductor width. This is termed the Hall voltage and can be used to measure the carrier mobility and concentration. For this work, only the resistivity was of interest.

Literature suggests that the electrically conducting nanoparticles are isolated from each other in such a way that the electrical contribution to thermal conduction is negligible [8]. The resistivity, or conductivity, of blended nanoparticle pucks has not yet been experimentally measured however. In order for the 3ω method to be used on this material, the material

needs to either be an electrical insulator itself, or include an insulation layer between the RT and sample. A Hall measurement on the puck material will establish if an insulation layer is necessary for the 3ω RT. This measurement can also be used to determine the electronic contribution to thermal conduction via the Wiedemann–Franz law [142], described in Chapter 2. This empirical law relates the electrical and thermal conductivity through a proportionality constant called the Lorentz number. The Wiedemann–Franz law is based on a free electrons gas model in metals, and as such may not closely hold for a nanoparticle morphology. However, the Wiedemann–Franz law has been used before on aerogel-based materials, suggesting that it may also be acceptable for this material [143].

4.3 Results and discussion

An example of a circular puck of 1/2/3 $SiO_2/Al_2O_3/C$ blend produced by the form tool is shown in Figure 4.5. The surface finish of the puck was matte and similar to that of the form tool. The latter was observed as artefacts of the CNC milling process on the from tool had been left imprinted on the surface of the puck. While this is not an issue for the guarded hot plate method, the 3ω method requires that the surface finish be adequate to support an electrically continuous and uniform geometry RT. The RT was patterned using shadow masking, which was ideal, as the samples were mechanically delicate and could not sustain any other form of patterning process. This material has not been investigated with the 3ω method before, and in general has not been patterned in any way. Despite concerns about the matte surface finish, the shadow mask patterning technique resulted in an electrically-continuous and regular geometry thermometer, which was sufficient for measurement with the 3ω method. The chosen RT geometry was $50\,\mu m$ wide, and $1\,mm$ long. This satisfies the classical 3ω method condition that $2b \leq d/5$ [6, 102, 103], where b is the RT half-width, and d is the film thickness. In this case the pucks were $\geq 2\,mm$ thick, therefore the thermometer width requirement was well satisfied.

The packed nanoparticle beds were hard, and extremely brittle. Large puck sizes were not possible to form without including the CrystalBond adhesive as a binding agent. However,

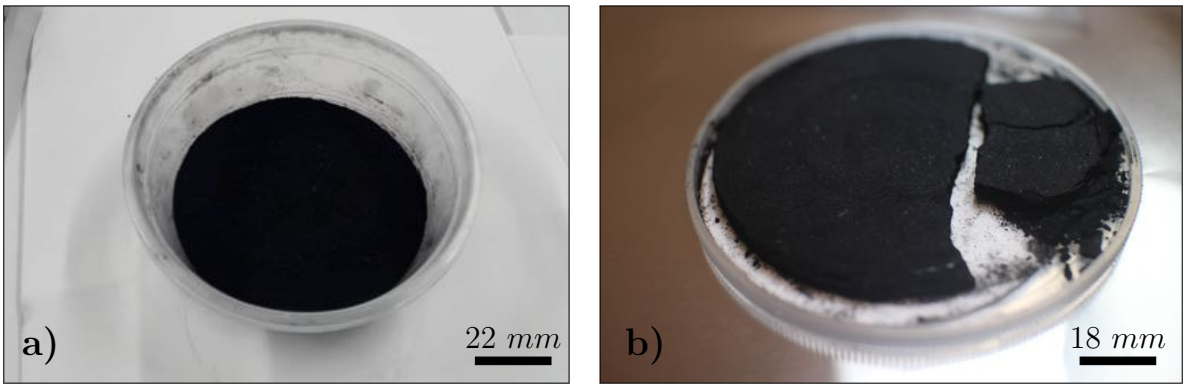

Figure 4.5: *Photographs of the pressed nanoparticle material. The composition of these example is 1/2/3 ($SiO_2/Al_2O_3/C$ weight ratio)* **a)** *The nanoparticle puck immediately after being demoulded from the form tool, and* **b)** *After measurement with the guarded heat calorimeter. The pucks were diced into smaller pieces so that they could be measured with the 3ω method.*

the brittle nature was advantageous in some respects, as it allowed for them to be easily diced into smaller pieces with a scalpel, due to the pucks snapping into pieces without deformation. The dicing was controlled over short distances, but became irregular when propagating over the entire width of the puck. Photographs of the diced nanoparticle puck in the evaporation basket and the diced material with 3ω RT formed on the surface are displayed in Figure 4.6.

4.3.1 Electrical Properties

Initially, the conductivity of the pucks were tested with a simple multimeter continuity test. This confirmed that the materials were nominally conductive and would require an insulation layer. For a more precise test, the resistivity of the nanoparticle materials were measured using the Hall effect measurement system introduced previously. These resistivity values could be then be used to determine the approximate bulk electrical contribution to thermal conductivity using the Wiedemann-Franz law. The resistivity results for the three tested materials, and the electrical contribution to thermal conductivity are shown in Figure 4.7 a) and b), respectively.

The resistivity of the tested nanoparticle compositions were in the range of 12 to 190 $\Omega \cdot cm$.

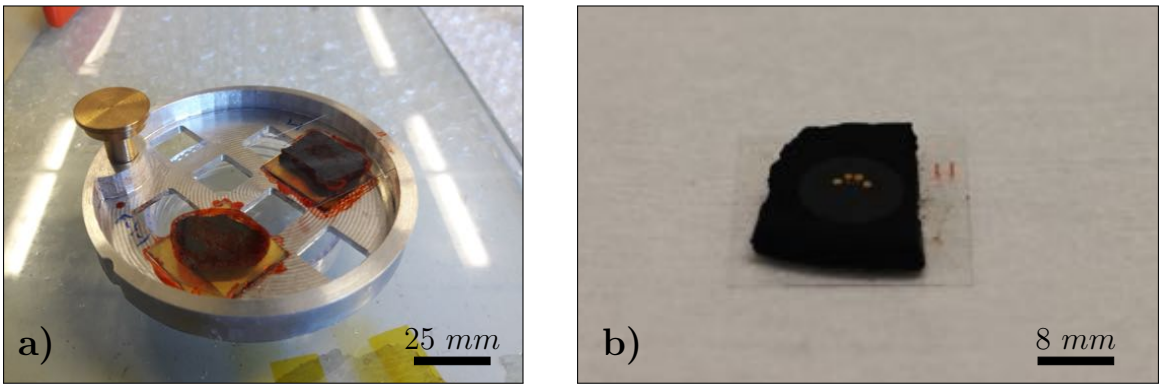

Figure 4.6: *Photographs showing the nanoparticle puck preparation process for 3ω measurement.* **a)** *The diced nanoparticle pucks were mounted onto soda lime cover-slips using AZ1518 photoresist [113] for ease of handling. The samples are then inverted into the evaporation basket, with the shadow mask beneath them. An Al_2O_3 insulation layer is thermally evaporated onto the surface, followed by the titanium–gold resistance thermometer.* **b)** *The completed 3ω RT on the surface of a 1/2/3 nanoparticle puck. The surface finish of the sample was matte, however the resulting RT was electrically continuous and uniform.*

a)

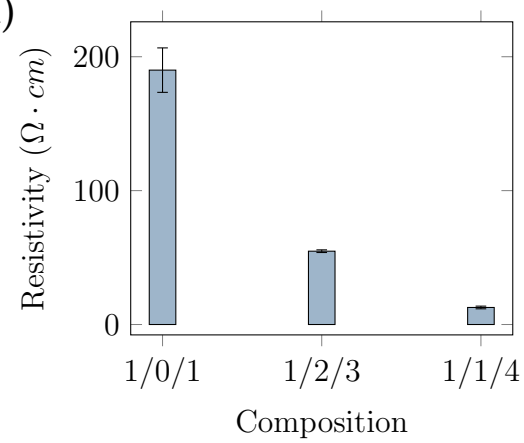

b)

Composition ($SiO_2/Al_2O_3/C$)	$k_{electrical}$ ($W/m-K$)
1/0/1	3.852×10^{-6}
1/2/3	133.65×10^{-6}
1/1/4	0.575×10^{-3}

Figure 4.7: *The electrical properties of the nanoparticle blends. The carbon nanoparticles are electrically conducting, and create varying electrical properties when mixed in a composite.* **a)** *The resistivity of the three nanoparticle materials, as measured by the Hall effect measurement system.* **b)** *The electrical contribution to thermal conductivity, as calculated via the Wiedemann-Franz law.*

The electrical contribution to thermal conduction based on these measured resistivity values, and a Lorentz number of $2.44 \times 10^{-8}\, W\Omega/K^{-2}$, is on the order of $10^{-6}\, W/m - K$. This represents a contribution to thermal conduction between 0.05% and 5% of the total thermal conductivity, when compared to literature values [8].

The electrical insulation layer chosen was $\sim 50\, nm$ of thermally evaporated Al_2O_3. As well as being electrically insulating, Al_2O_3 has a high thermal conductivity of $\sim 25\, W/m - K$ in its bulk crystalline form [61]. The insulation layer was kept as thin as possible in order to minimise its impact on the thermal resistance measured by the RT. This was important for the measurement, as the classical 3ω method is not capable of separating the contribution of an insulation layer from that of the sample [102].

4.3.2 Thermal conductivity measurement

The room temperature (T=23°C) thermal conductivities of the nanoparticle puck materials are shown in Table 4.3 for both the guarded hot plate, and 3ω measurement methods. In addition to numerical table, a comparison graph showing the results from this thesis, and literature is shown in Figure 4.8.

The thermal conductivities of the composites were between four and ten times larger than the lowest values reported in literature, however they did align much better to the values reported by guarded heat calorimetry [8]. The 1/1/4 and 1/2/3 $SiO_2Al_2O_3/C$ weight blends had been reported to have thermal conductivities of approximately $0.007\, W/m - K$ when measured using laser flash calorimetry, and 0.08 W/m-K when a larger tile was measured with guarded heat calorimetry [8]. The value reported by Voges et al. for large tiles, aligns much closer than the values measured by both techniques used in this work.

Interestingly, there is also a large difference between the 3ω measurements and this works' guarded hot plate results. Voges et al. [8] proposed that any difference between the measurement techniques was due to the moisture uptake into the material over the approximately one month of time between fabrication and testing. This is a comparable time frame to the delay between the calorimeter and 3ω method measurements taken in this work. A further

Composition ($SiO_2/Al_2O_3/C$)	**k (Calorimeter)** *(W/m-K)*	**k (3ω method)** *(W/m-K)*
1/1/4	0.079 ± 0.01	0.124 ± 0.01
1/2/3	0.047 ± 0.01	0.109 ± 0.01
1/0/1	0.044 ± 0.01	0.078 ± 0.005

Table 4.3: *The thermal conductivity of the pressed nanoparticle materials as measured by both the hot plate calorimeter and classical 3ω method.*

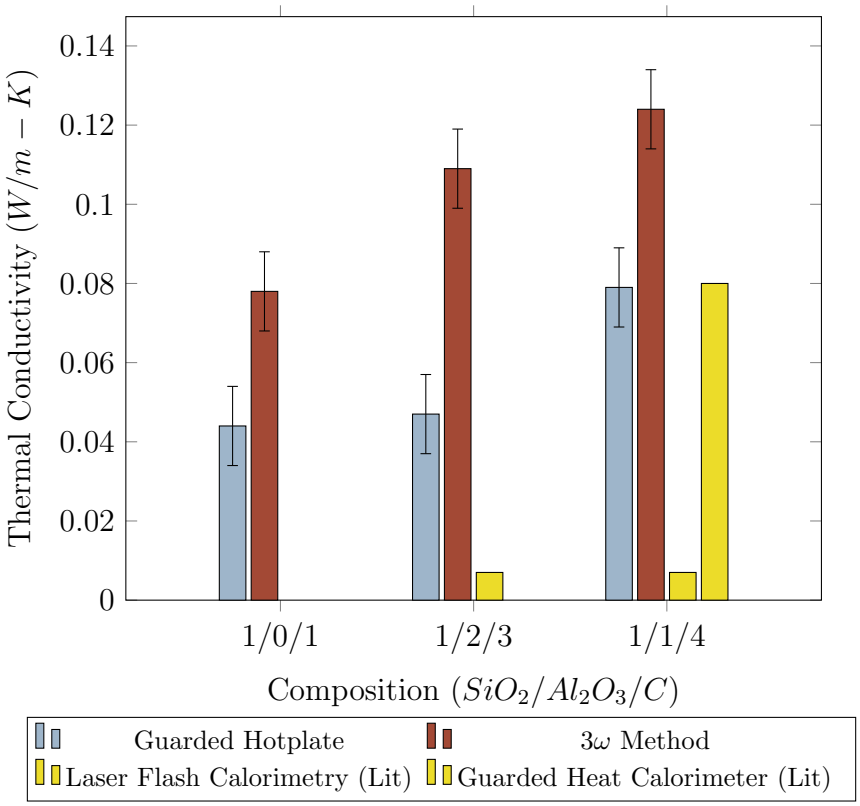

Figure 4.8: *A summary chart of all thermal conductivity results reported in this work and in literature. The results are also separated by measurement technique. From these results it can be seen that the laser flash calorimeter results from literature report the lowest value, while the 3ω reported the highest value. These measurements were not controlled for material age, which may be one reason for the discrepancy between techniques.*

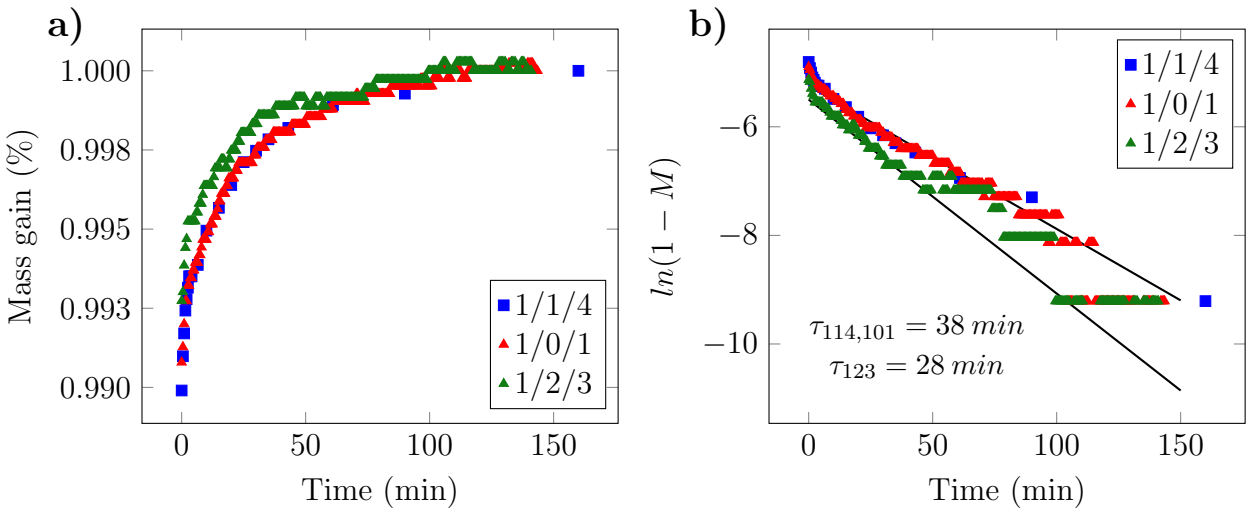

Figure 4.9: *Thermogravimetric analysis of the pressed nanoparticle materials.* **a)** *The normalised mass gain of nanoparticle materials over time. Over 2.5 hours, the materials gained approximately 1% of their mass.* **b)** *An exponential function ($Mass = 1 - e^{-t/\tau}$ where t is time, and τ is the time constant) is fitted to the normalised mass absorption data.*

possibility is that the alumina insulation layer is increasing the thermal resistance measured by the RT. To test this hypothesis more thoroughly, the moisture absorption properties, and any link to the thermal insulation performance, were studied using the 3ω method and thermogravimetric analysis.

Newly pressed nanoparticle blends were placed in a 95 $^{\circ}C$ wafer dehydrating oven for $\sim$ 24 hours to dry. The materials were then weighed on an enclosed digital scale (Metler Toledo, d=0.001 g) at 24% room humidity. The scale was configured to send mass values over serial communication to a PC every 30 seconds. The normalised nanoparticle puck moisture uptake over time, and an exponential fitting to the data is shown in Figure 4.9 (a) and (b) respectively. From a presumed "dry" state, the nanoparticle materials gained mass over the course of 1 to 2 hours, before plateauing at a stable mass. An exponential function fit to the data with a regression coefficient of 0.94. The time constant of mass gain for the 1/2/3 material was 28 minutes, while the 1/1/4 and 1/0/1 had a time constant of 38 minutes. Further thermogravimetric analysis suggested that the moisture absorption was almost entirely related to the carbon black nanoparticles.

Based on these results, two mechanism for moisture incorporation are hypothesized. Firstly,

water may be physically absorbed into the carbon nanoparticles in much the same way it is in activated carbon materials [144,145]. In activated carbon, water is adsorbed onto the surface, and into micropores between the basal planes of the graphitic carbon. Carbon black materials meanwhile can be synthesized as porous or non-porous. Regardless of internal structure however, nanoparticles have a high surface to area ratio which allows water to chemisorb onto the surface [145]. The second mechanism hypothesized is through the condensation larger water droplets onto the surface of the nanoparticle and in the nanoconstriction. The latter mechanism in particular would drastically effect the thermal insulation performance, as it could increase the effective "neck" size of the nanoconstriction (a), introduced in Figure 4.1, via a liquid bridge between the nanoparticles [9,104]. Moisture on the surface would have the largest effect on the thermal conductivity. This is because, under Prashers' model of packed nanoparticle beds, the thermal resistance of the nanoparticle bulk is negligible compared to that of the interface [39].

Figure 4.9 shows that the puck materials take only 2 hours to reached equilibrium. This time frame is much shorter than the hypothesized degradation time frame of weeks to months [8]. As such, these results suggest that the presence of moisture alone is not the primary cause of reduced thermal insulation performance. It is still possible that the presence of moisture is causing internal oxidation, or the formation of chemical bonds between nanoparticles. Chemical bonding between nanoparticles has been shown to reduce the interface thermal resistance between nanoparticles substantially [42].

To further test the latter hypothesis, the nanoparticle materials were measured at elevated temperatures and in low humidity environments. To achieve this, the samples were heated to $100°C$, and the testing chamber purged with N_2 gas (analytical grade). A temperature–humidity sensor (174H, Testo) was used to monitor the chamber humidity during the measurements. The chamber was reduced to a humidity of less than 5% for all measurements, and the thermal conductivities of the samples were measured over the temperature range -$30°C$ to $120°C$. Over the $100°C$ range of measurement, the samples varied from 0.1 $W/m-K$ to 0.12 $W/m-K$. The thermal conductivities of these samples are shown in Figure 4.10. From these results, it can be seen that there has not been a significant change in thermal conduc-

tivities of the nanoparticle materials in the 5% r.h "dry" environment when compared to the previous room temperature, room humidity, measurements (shown in Table 4.3). Furthermore, when the 1/1/4 and 1/2/3 nanoparticle blends were heated above $100°C$, to eliminate any liquid water from the system, the thermal conductivities did not decrease. This supports the hypothesis that the presence of water alone is not the sole reason for the decreased performance. Instead, it may be that the presence of water is allowing a non-reversible degradation mechanism to occur, such as the formation of chemical bonds in the nano-constriction.

One shortcoming of this experiment was that the humidity was not entirely eliminated from the chamber. The lowest humidity in the measurement chamber was only ∼4-5%. To ensure no water was still in the materials, the sample would have to be placed in vacuum. The sample could then be measured while in vacuum, or backfilled with 0% r.h. dry air for atmospheric pressure measurements.

Recent work on this subject investigated the impact of moisture in packed silica nanoparticle beds. Meng et al. used non-equilibrium molecular dynamics to study how the thermal resistance between adjacent nanoparticles changes with humidity [9]. Through simulation, they found that the most substantial reduction in thermal resistance occurred beneath 1% r.h. This was linked to silanol groups forming on the surface of the nanoparticles, which then increased the nano-constriction radius. This is illuminating with respect to the work performed as a part of this thesis. Any change in thermal conductivity from reduced humidity is likely to occur only beneath 1% r.h., which was outside the range tested by in this work. The probe station in which the 3ω measurements were performed was at 4 to 5% r.h. and was not capable of values beneath this due to the weakly sealed nature of the sample chamber.

The highest performing nanoparticle puck found in this work was the 1/2/3, and 1/0/1 weight ratios of $SiO_2/Al_2O_3/C$ nanoparticles. Up to this point in this research, the samples were first transferred to another facility for measurement by the guarded hot plate method, before being returned for measurement with the 3ω method. Due to this time delay, the 3ω measurement had been measuring artificially aged samples. To elucidate this influence, a new 1/0/1 composition puck was prepared using the same methods as previously. The 1/0/1 material was chosen because it was the highest performing sample from previous results. A set

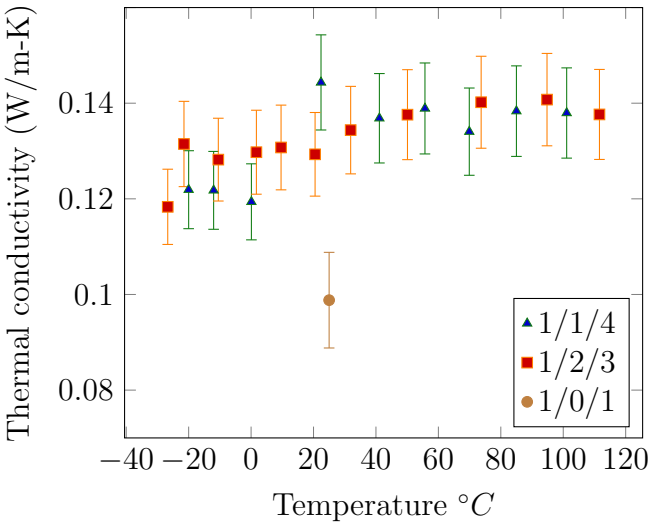

Figure 4.10: *The 3ω thermal conductivity measurements over the temperature range $-25°C$ to $120°C$. The thermal insulation performance was not changed when measured in a dry environment, or even at a temperature above the boiling point of water.*

of 3ω RTs were then fabricated on the surface of the puck, and the thermal measurement performed as soon as possible. The sample was then remeasured multiple times over the course of approximately one month. Results of this experiment are shown in Figure 4.11.

The first measurement after solvent evaporation, and subsequent pressing was taken at three days post-formation. This delay was due to the time taken to fabricate the RT array on the surface of the puck. This first measurement of the nanoparticle puck yielded a thermal conductivity of $0.048\,W/m-K$. This value is in agreement with the guarded hotplate measurement taken previously for this specific nanoparticle blend. Over the course of one month exposed to room humidity ($\sim 25\%$), the sample continued to degrade up to $0.065\ W/m-K$. This final value is much closer to the value measured by the previous 3ω measurements for the 1/0/1, 1/2/3, and 1/1/4 nanoparticle weight blends. An exponential function of the form $k = 1-e^{-t/\tau}$, where k is the thermal conductivity of the packed nanoparticle material, t is the number of days since the puck was formed, and τ is the time constant of degradation. From this crude model, the time constant of degradation was found to be 6.2 days. Extrapolating this model to the "0 day" thermal conductivity gives a value of $0.034\ W/m-K$.

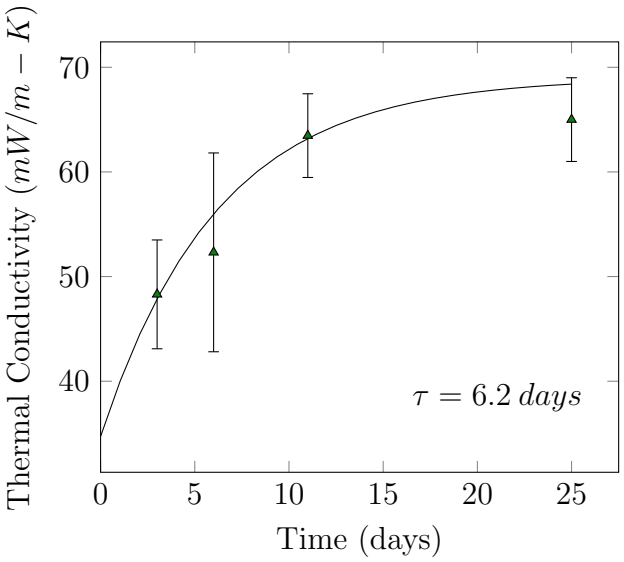

Figure 4.11: *The thermal conductivity degradation of the 1/0/1 nanoparticle material degrading over the course of approximately one month. An exponential function fitted to this data shows a degradation time constant of 6.2 days, and a intercept of* $0.0327\,W/m-K$.

4.4 Conclusion

In this chapter the thermal insulation performance of composite pressed nanoparticle materials were investigated using both the 3ω method, and guarded hotplate method. Three nanoparticle compositions were investigated using these techniques. The highest performing of these were composed of 1/2/3 and 1/0/1 blends of $SiO_2/Al_2O_3/C$. These compositions had thermal conductivities of 0.047 and 0.044 $W/m-K$, respectively. Previous reports of similar nanoparticle blends have varied between 0.007 and 0.08 $W/m-K$ [8]. Further time-based thermal conductivity measurements in this work found that the 1/0/1 weight ratio material degraded substantially over the course of approximately one month. Furthermore the thermal conductivity could not be restored via heating of the samples, and measurement in a "dry" $< 5\%$ r.h. environment. This led to the hypothesis that the presence of moisture may be causing chemical bonds to form in the inter-nanoparticle interfaces. This hypothesis aligns with previous work on similar materials by Voges et al. [8], and simulations performed by Meng et al. [42].

Packed nanoparticle beds, like the ones investigated in this work, provide competitive and

interesting thermal properties. However, there is still work needed for them to be a practical insulation materials. The specific issue which must be addressed is that of nano-constriction degradation. Once this mechanism is understood in depth, then steps can be taken to prevent it occurring. Some experimental techniques which may be of use are, spectral environmental ellipsometry, and environmental SEM. Spectral environmental ellipsometry is used in photonic crystal experiments to measure the porosity of inverse opal [146]. This could be used to measure the porosity of a packed nanoparticle bed, or possibly even the change in porosity with degradation. Environmental SEM is an atmospheric scanning electron microscopy technique which allows for the imaging of liquids on nanomaterials or other "wet" samples which cannot be measure in vacuum [147]. This technique could image moisture wicking around the nano-constriction, and experimentally verify the hypothesised contact radius enlargement [9]. This technique could also be used to measure the contact angle of water and other liquids on the nanoparticles, and as such calculate the nanoparticle surface energy [148]. Once these properties are better understood, more can be done to feasibly prevent them occurring.

In the next chapter another nanoparticle composite, termed a Hybrid Bragg stack [18], is measured using the differential 3ω method. The results of this are then discussed with respect to the constituent materials, and in comparisons to the packed nanoparticle bed results described in this chapter.

Chapter 5

Hybrid Bragg stacks

5.1 Introduction

In this chapter, the thermal conductivity of a structured nanoparticle phononic crystals is measured using the differential 3ω method. It is proposed, based on the work of Schneider et al. [10, 18], that Silicate-PMMA multilayer structures will produce low thermal conductivities. Parts of this chapter were published as "Thermal conductivity of PMMA-SiO_2 phononic crystals measured by AC resistance thermometry" in the proceedings of IEEE Sensors 2017.

As micro-electronics and nanotechnology fabrication methods have advanced, new opportunities have emerged to study thermal energy carriers in contexts never seen before. One such example is the study of thermal phonons as a wave phenomena [76]. This effect has been widely studied in materials which produce phononic bandgaps [1, 16]. A material with a phononic bandgap has a range of phonon energies which cannot propagate inside the material [76]. If the phononic bandgap energy coincides with phonon energies which are significant thermal energy carriers, then thermal conductivity of the material will be reduced relative to its raw material components [12].

One of the most common strategies used to generate phononic bandgaps in thermal metamaterials is by using multi-layered structures, also called superlattices [18, 49, 58]. A basic schematic of a superlattice, or multilayer, is shown in Figure 5.1. This family of structures has been shown to produce ultra-low thermal conductivities in a large variety of different materials [21, 149]. Ultra-low in this context is defined as a thermal conductivity beneath the amorphous limit of the raw material [63].

A wealth of examples exist in literature, which could broadly be grouped as multilayers, superlattices, or phononic crystals [11, 18, 49, 58, 59, 70]. The highest performing "fully-dense" material in literature is tungsten diselenide, a Van der Waals type material, which exhibits extremely low thermal conduction perpendicular to its layering [59]. This material was synthesized through a method called "modulated elemental reactants" [59, 65]. Other researchers have managed to observe wave-like behaviour and phononic bandgaps in layered materials with periods in the nanometer scale, allowing for the reflection and refraction phonons off

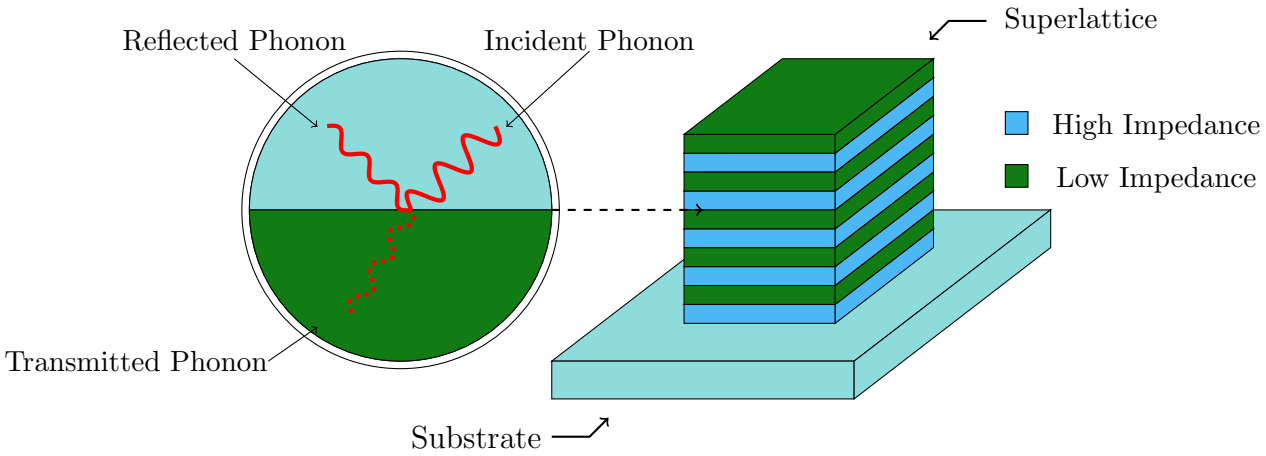

Figure 5.1: *An illustration of a multilayer, or superlattice structure. Substantial variation in the mechanical and acoustic properties of the layers of the superlattice can create forbidden phonon energies in the structure. This in turn can create a large reduction in thermal conductivity of the overall material. (Inset) Phonons traversing the interface will be reflected and transmitted proportional to the acoustic properties either side of the interface.*

the layer interfaces [16, 76].

However, many of the superlattices which are cited by literature as structures with a phononic bandgap use advanced deposition techniques such as atomic/molecular layer deposition (ALD/MLD) [23], molecular beam epitaxy (MBE) [16], or pulse laser deposition (PLD) [62, 64]. In contrast to this, a much simpler approach was taken by Schneider et al. in creating a multilayered polymer-nanoparticle superlattice [10, 11, 18]. This deposited alternating layers of polymer and nanoparticle materials using a relatively simple spin-coating methodology, and has been shown to produce both a phononic and photonic bandgap. High-speed spin-coating is a low cost technique suitable for large scale coating applications. In literature, the phonon dispersion relation of these structures was studied using Brillouin Spectroscopy, and it was found that a tunable phononic, and photonic band-gap was created by the layering [10]. This dual phononic-photonic bandgap is the origin of the term Hybrid Bragg stack. A Bragg stack is a structure which produces a photonic bandgap [150], and with the addition of a phononic bandgap, it has been coined a Hybrid Bragg stack [10].

The thermal conductivity of these Hybrid Bragg Stack has not yet been measured. For this work, a PMMA - SiO_2 nanoparticle Hybrid Bragg stack superlattice was studied using the differential 3ω method. As mentioned above, these structures are of interest as they have

a simple fabrication methodology and produced reliable phononic band-gaps [10]. In the following, a nanoparticle-based superlattice structure is fabricated and characterised, and compared to the thin-film properties of the constituent materials alone.

5.2 Methods

5.2.1 Layer deposition by spin-coating

Micro- and nano- multilayered structures are a relativity common morphology in literature [10,17,18,49,52]. They can be used to engineer a wide variety of properties or purposes, including quantum wells [52], photonic bandgaps [17], thermal conductivity tuning [21,65,149] and phononic bandgaps [11,18,49]. There is an equally diverse range of approaches available to fabricate these kinds of structures. These range from a relatively standard physical vapour deposition (PVD) techniques [21], through to more advanced deposition methodologies like atomic/molecular layer deposition [23].

One very simple, and versatile method of fabricating superlattice structures is high-speed spin-coater deposition [10, 11, 18, 49]. This method uses a standard spin-coater, common to semiconductor manufacturing [106], to sequentially deposit layers onto a substrate. The technique is capable of creating well-defined layers, down to $10nm$ thin [151]. In this method, a liquid solution is deposited onto a substrate, and then accelerated to a desired rotational speed. Any excess material flows off the edge of the substrate through centrifugal force, until an equilibrium thickness is reached. The equilibrium thickness is a complicated function which depends on a range of properties, including the solvent evaporation rate, deposition time, solution viscosity, and spin speed. However, the most common models for layer thickness largely use solution viscosity and spin speed [151]. As such, when fabricating superlattices via this method, the layer thickness is controlled by adjusting the spin-coater speed, and the solutions viscosity (via concentration). After each layer is deposited, the sample was baked on a hotplate to evaporate the solvents and create a solid layer. This process is repeated with alternating materials until the desired thickness or number of superlattice

Figure 5.2: *The Headway Research Inc. PWM32 spin-coater deposition system.* **a)** *The vacuum chuck of the spin-coater. This holds the sample in place while rotating at speeds up to 10,000 rpm.* **b)** *The control unit of the spin-coater deposition system. Users can program a sequence of spin steps, which can vary in spin speed, acceleration, and duration.*

layers is reached.

The spin-coater utilised in this work was a Headway PWM32 spin-coating system, shown in Figure 5.2. The samples are held in place by a vacuum chuck, shown in Figure 5.2 (a). A series of processing steps with different rotational speeds and duration can be programmed using the control unit. This programmable sequencing allows for fine control over the desired layer thickness, and provides the flexibility needed to adjust the motion to suit the solution. After a spin was completed, the sample was released from the vacuum chuck and baked on a hotplate at $100°C$ for 15 min to evaporate the solvents and solidify the layer.

As discussed previously, the desired multilayer structure consisted of alternate layers of SiO_2 nanoparticles and PMMA. The stock solutions for spin-coating deposition of these materials consisted of diluted Ludox AS-30 Colloidal Silica (30 g/L, Sigma Aldrich), and PMMA (35 kDa, Sigma Aldrich). A range of Ludox spinning solutions were prepared by dilution of the stock 30 wt% Ludox with 14% ammonia (analytical reagent grade, Thermofisher). A 10% (w/v) Sodium Dodecyl Sulfate (SDS, Sigma Aldrich) surfactant solution was then prepared with de-ionsised water. This was added in a 1% (v/v) ratio to the dilute Ludox spinning solution. The surfactant was necessary to prevent particle agglomeration in both solution, and in the deposited layer [10]. The PMMA spinning solution consisted of 2.2% (w/v) solid

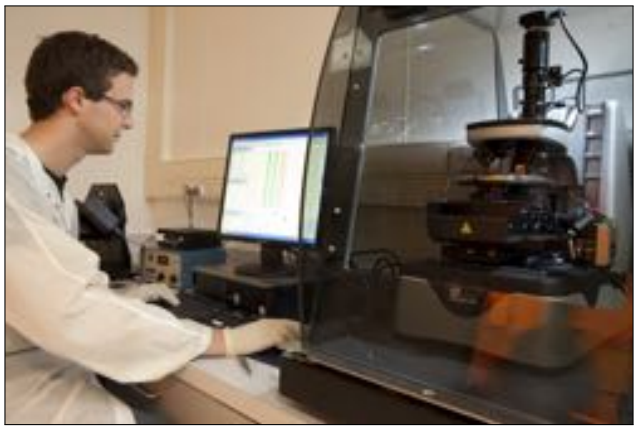

Figure 5.3: *The Vecco Dektak 150 surface profilometer. The system is an accepted standard methodology for measuring the surface topology, roughness and step sizes of materials. In this work, the system was used to measure the thickness of thin films resulting from metallisation or spin-coating processes.*

PMMA dissolved in toluene (analytical reagent grade, Thermo Fisher). For the targeting of 50 nm layers, the samples were spun at 5,000 rpm, for 45 s.

5.2.2 Surface profilometry

The Vecco Dektak 150 surface profilometer, shown in Figure 5.3, is a contact method of measuring the surface contours of a sample. This methodology is particularly useful for measuring step sizes, such as those resulting from thin film deposition processes like thermal evaporation or spin-coater deposition. First, a sample to be measured is placed on the motorized stage of the profilometer. The stage moves so that the 10 μm stylus is dragged, with set force, across the surface of the sample and the desired feature. As the stylus deflects off of features, its displacement is measured, and plotted against the movement of the stage to create a two dimensional profile of the surface. This method is capable of measuring the size of micro- and even nano-scale features [152]. The motorised stage can be configured to take a single line-sweep, or to take an automated series of line-sweeps to generate a three-dimensional surface by interpolation between line-profiles. The force the stylus exerts on the sample can be adjusted between 1 $milli - g$ and 15 $milli - g$, making it suitable to measure even very soft or deformable materials.

Surface profilometry is an accepted standard technique to measure surface roughness, and step size [153]. In this work, the Dektak 150 was used to characterise the formation of individual thin films deposited by high speed spin-coating. In order to form a step in an otherwise continuous spin-coated layer, a pair of tweezers was used make a substrate-deep scratch in the film. A series of line scans were then taken over the scratch and the average step size calculated from this.

5.2.3 Contact angle goniometry

A parameter of interest in packed nanoparticle materials is surface energy. One way to infer information about this parameter is through the contact angle of a liquid droplet on the surface of a material. To measure this, a contact angle goniometer (KSV Instruments Ltd.) is used. Shown in Figure 5.4, this instrument aliquots a precise volume of liquid onto the surface of the sample. It then uses a camera mounted parallel with the surface of the material to record an image of the liquid drop. This image is then used to measure the angle that the edge of the liquid droplet makes with the surface of the material.

In order to measure the absolute surface energy of a material, the contact angle of several different liquids is required. The change in contact angle can then be used to calculate the surface energy of the material of interest [148]. It can also be used to characterise if a material is hydrophobic or hydrophilic [152]. In this work, only the water contact angle is recorded.

5.2.4 Laser ellipsometry

Ellipsometry generally refers to a method of monitoring the optical reflectance properties of a material, using elliptically polarised light [154]. Once measured, the optical reflectance can be related to a large variety of phenomena including, for example, film thickness [155], glass transition and thermal expansion [156], mechanical properties, and porosity [146]. The system used in this work was a Rudolph Instruments single wavelength manual ellipsometer. A photograph of this system is shown in Figure 5.5. This is a form of Polariser-Compensator-

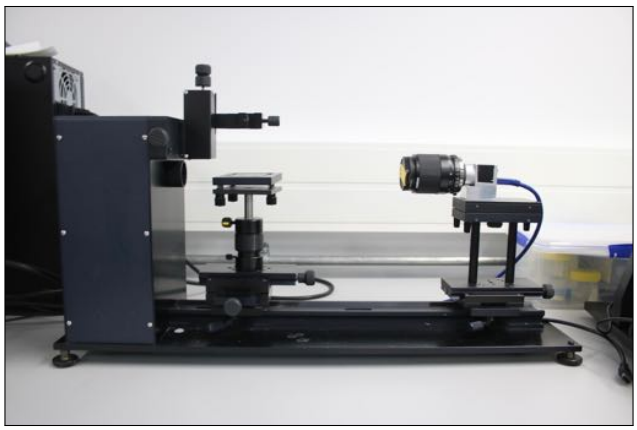

Figure 5.4: *The contact angle goniometer (KSV Instruments Ltd) used in this work. This instrument is used to measure the contact angle between some liquid (often water) and the surface of a material. This angle can be used to infer information about the surface energy of a material [148].*

Sample-Analyser (PCSA) ellipsometer [154] apparatus suited for measuring the thickness of thin-films on substrates. A measurement is conducted by aligning the polariser, compensator and analyser filters in such a way that the light reflected off the sample is completely extinguished by the analyser polarising filter. As the polarisation of the input and output light is known, the Jones optical transformation matrix for the sample can be calculated [154]. This in turn can be used to determine the refractive index and thickness of a film on substrate system through a model of the substrate–thin film and thin film–ambient interfaces [154]. The Rudolph instruments manual ellipsometer has a $HeNe$ ($\lambda = 632.8\,nm$) laser, a quarter-wave compensator, and a digital light meter at the source. The source and detector arms of the ellipsometer are mounted on a goniometer so that the angle of incidence can be adjusted to suit the samples index of refraction, and avoid total internal reflection where it may be an issue. For this work, null-point laser ellipsometry was used to calibrate the layer thicknesses of spin-coated nanoparticle materials in the Hybrid Bragg stack [18]. Although this measurement has been used in the past on nanoparticle thin films [157] it is questionably suitable in its current form. This is because the light will likely traverse multiple interfaces between the individual nanoparticles, rather than the expected two-interface system used in the thickness model. To increase measurement confidence, measurements were taken at two ellipsometer arm angles and in multiple places on the sample.

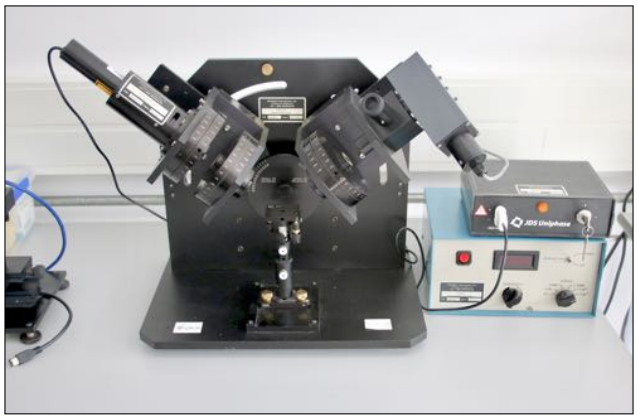

Figure 5.5: *The Rudolph instruments manual ellipsometer used for thin film measurements in this work. A HeNe monochromatic laser shines elliptically-polarised light onto the surface in an orientation that leads to linearly polarised light being reflected from the surface. This allows the Jones matrix to be calculated for the sample, which can then be transformed into film thickness.*

5.2.5 Atomic force microscopy

In packed nanoparticle beds, some of the most critical parameters for the thermal performance are the nanoparticle radius and surface energy [39]. In addition, from the perspective of a multilayer structure, the surface roughness of interfaces is critical to phonon transport [12, 76] as the interface roughness relative to the phonon wavelength defines which phonon transmission model is applicable [12]. In order to characterise these properties for the nanoparticle materials, the SiO_2 nanoparticle layers were measured using Atomic Force Microscopy (AFM) [158].

AFM functions in a similar way to stylus surface profilometry, however with a more refined apparatus. In AFM, an etched silicon tip on a cantilever is moved across the surface of a sample using piezoelectric actuators. As the cantilever is moved across the surface, it deflects off of surface features on the sample. A laser, reflected off the back of the cantilever, then deflects proportionally with its movement. The signal produced by the laser spot deflection is used in a closed-loop control system with a piezoelectric tube actuator to keep the cantilever tip equidistant from the sample surface [158]. A series of line sweeps across the surface of a sample creates a three-dimensional contour of the surface. This is referred to as contact

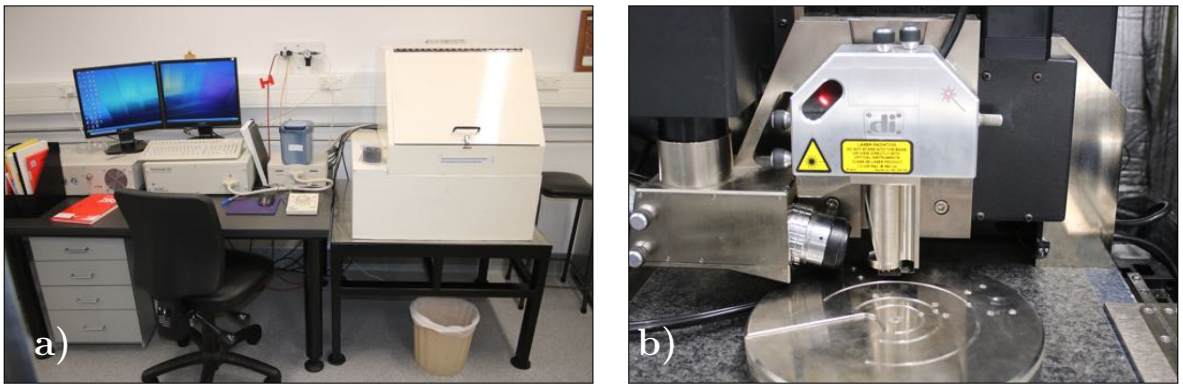

Figure 5.6: *The Nanoscope 3000 contact atomic force microscope.* **a)** *The full atomic force microscopy system. The head of the AFM sits on a vibration-isolation table and is sealed inside a sound isolation enclosure. Measurements are conducted at atmospheric pressure.* **b)** *The AFM head inside the sound isolation enclosure. The laser alignment guide can be seen at the top left of the head.*

AFM [158]. The specific system available in the University of Canterbury Micro- and Nanofabrication laboratory is a Nanoscope 3000, as shown in Figure 5.6.

For this work, AFM was used to measure the surface properties of a range of SiO_2 nanoparticle layers. The resulting data was then processed using Gwyddion AFM processing software (version 2.53) [159]. A series of circles were fitted to nanoparticles exposed on the surface of the sample. Fifty measured nanoparticles were used to determine the average nanoparticle radius and the standard deviation. This result could be used in conjunction with Prashers' model of packed nanoparticle beds to estimate the thermal properties of the layers [39].

5.2.6 Sample cross-sectioning

In order to confirm the correct formation of the superlattice structure, the samples were cross-sectioned and investigated under a scanning electron microscopy (SEM). The thin-film Hybrid Bragg stack was formed on approximately $15\,mm \times 15\,mm$ square sections of silicon wafer (<100>, p-type, University Wafer), and also on soda-lime glass cover-slips (Thermo fisher). To cleanly cross-section the sample, the underside of the substrate was scored with a diamond scribe, and snapped on a brass anvil. This method ensured that the thin film was under extensive force when the substrate snapped, and meant that the layer structure at the

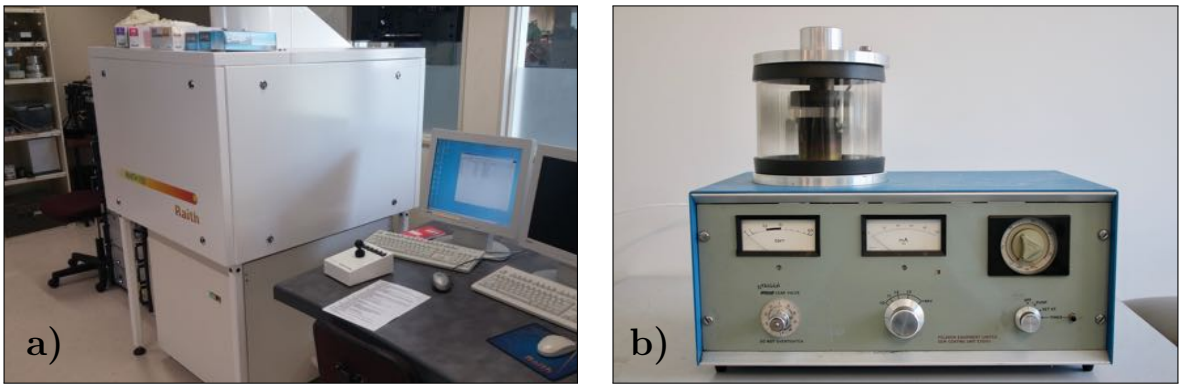

Figure 5.7: *Photographs of the the Raith 150 combination scanning electron microscope and Polaron SEM sputter coater.* **a)** *The Raith 150 scanning electron microscope and electron beam lithography system. This system was used to inspect the morphology of the Hybrid Bragg Stack after cross-sectioning.* **b)** *The Polaron gold-palladium SEM sputter coater. Electrically non-conductive samples require a thin conductive layer, which prevents excessive charge accumulation, to be imaged with SEM.*

edge of the cross-section was typically preserved for imaging.

In order for a non-conductive sample, as is the case with the Hybrid Bragg stack, to be imaged with SEM, a conductive coating had to be applied. For this purpose, a miniature DC sputter-coater was used (Polaron SEM- E5000). Approximately $10\,nm$ of Au-Pd was applied to the edge of the cross-section. The scanning electron microscope used in this work was LEO FEG-SEM & Raith 150 Electron Beam Lithography System. This is a combination electron beam lithography and scanning electron microscope system [160]. The Raith 150 has a fixed mounting stage with 90°, 45°, and 0° mounting positions. The cross-sections were mounted at 90° such that the edge of the cross-section was clearly visible, and the layer formation could be inspected. Photographs of the Raith SEM system and the Polaron SEM Sputter coater are shown in Figure 5.7 (a) and (b), respectively.

5.2.7 Differential 3ω method

The superlattice thin film samples studied in this work were approximately $1\,\mu m$ thick. This thickness is practically out of reach for the classical 3ω method [6]. In order for the classical 3ω methods' RT requirements to be met, the thermometer would need to be $\leq 200nm$ wide [102].

As such, the samples were instead measured using the differential 3ω method, discussed in Chapter 3. The differential 3ω method requires a control sample without the sample thin film. It is desirable that the substrate is as thermally conductive as possible so that the majority of the temperature gradient is across the thin-film under investigation [102]. However, as already mentioned, highly thermally conductive materials are often electrically conductive and require an electrical insulation layer for the 3ω method to be used. The hybrid Bragg stack samples were fabricated on both soda-lime cover-slips (Thermo Fisher) and diced silicon wafers (<100>, p-type, University Wafer). The RT geometry chosen for this experiment had a width of 50 μm and was 1 mm long. RT patterning was achieved with either shadow mask patterning, or an etching-based photolithography procedure, both of these methods were discussed in Chapter 3. The thickness of the Hybrid Bragg stack was measured using SEM cross-sections, and the RT width was measured using stylus surface profilometry. More information about the differential 3ω method can be found in Chapter 3.

5.3 Results and discussion

The spin-coated Hybrid Bragg stacks adhered well to the substrates. 10 bilayers were deposited onto the substrate, making 20 total layers. The resulting films were iridescent due to the mismatch of refractive indexes between the layers [150]. Interestingly, the same morphology is used in literature as *photonic* crystals, in addition to use as phononic crystals [10,11,18]. Photographs of the structures on a silicon and soda lime substrate are shown in Figure 5.8 (a) and (b), respectively. Point defects and comet streaking could be observed on the surface of the structures. This was most likely caused by dust particle impurities landing on the sample during the multiple spin-coater depositions. This could be improved upon by using a higher grade clean room than the UC facility for fabrication, or alternatively fabricating in a clean glove-box.

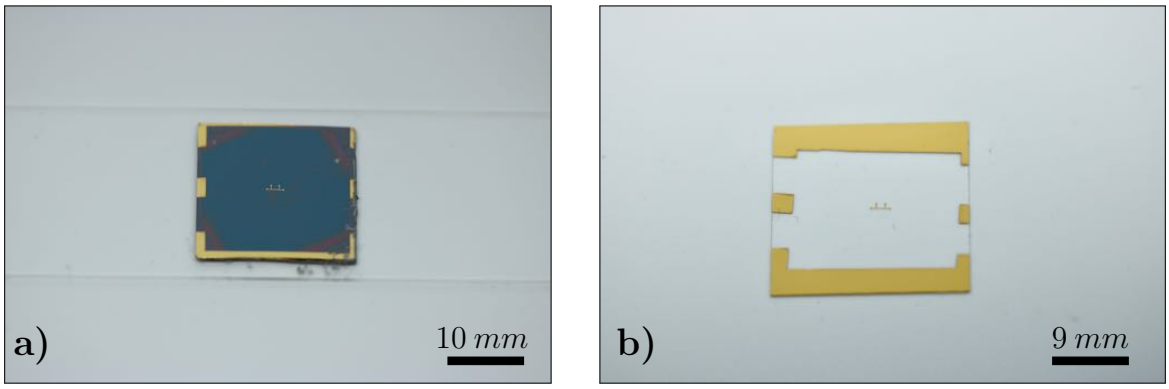

Figure 5.8: *Photographs showing the Hybrid Bragg stack on silicon and soda-lime substrates.* **a)** *The Hybrid Bragg stack on top of silicon shows the iridescent quality of the films. While difficult to observe from a single photograph, layer irregularities near the edges create a noticeable colour shift.* **b)** *The Hybrid Bragg stack on soda-lime glass is completely transparent to the eye. The gold* 3ω *RT can also be seen.*

5.3.1 Layer thickness calibration

In order to lower the thermal conductivity of the samples, it is desirable to increase the interface density as much as possible by targeting the thinnest attainable layers of the constituent materials. It has also been suggested that, in this type of superlattice, changing the superlattice period can be used to tune the centre frequency of the phononic bandgap [10, 18]. As such, individual spin-coated layers were calibrated to find the obtainable layer thicknesses. The layers were measured through surface profilometry, and laser ellipsometry as described previously.

The thickness of the PMMA layers was varied by changing the spin-speed of the spincoater between 500 and 9000 *rpm*, at the same time, the duration and acceleration were held constant at 30 seconds and 5040 rpm/s. The results of this layer optimisation process are shown in Figure 5.9 a). Initially, the Ludox layers were measured with surface profilometry, however the nature of the nano-particle material on the substrates was such that reliable steps in the material could not be easily created. Instead, as also done by Schneider et al. [10], the nano-particle layer thickness was measured with ellipsometry. This method was used to develop a relationship between the layer thickness and the nanoparticle concentration in the spin-coating solution. The ellipsometry process was carried out twice on each sample

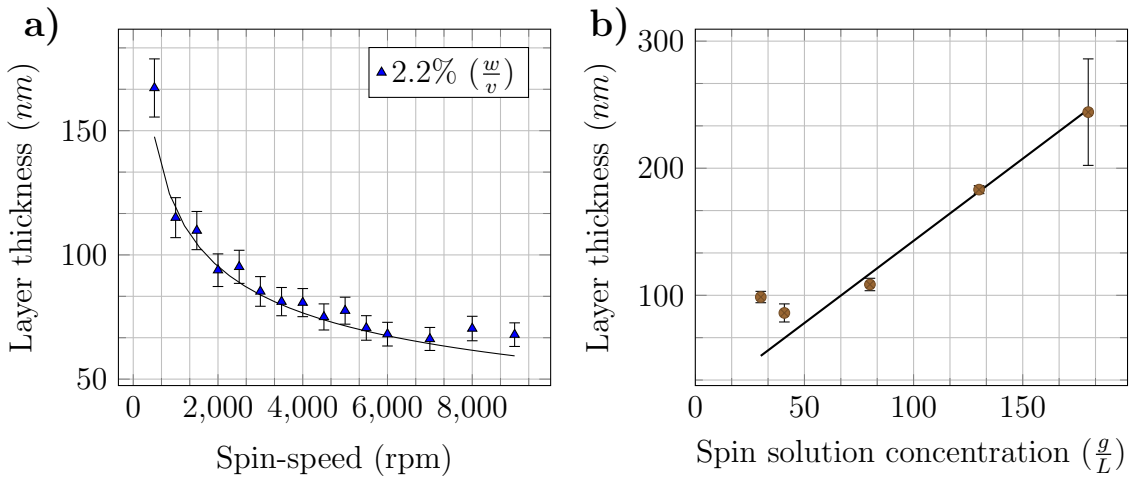

Figure 5.9: *Plots showing the layer thickness calibration of both the PMMA and Ludox (SiO_2 nanoparticle) layers. The PMMA layer thickness was predominantly controlled by setting the spincoater speed. In contrast, the nanoparticle layers were adjusted by controlling the spin-coater solution.* **a)** *The PMMA spin-profile was calibrated over the range 500-9,000 rpm. This resulted in layers varying from 175 nm down to 65 nm.* **b)** *The ellipsometry results for the Ludox nanoparticle material. This result demonstrates that the nanoparticle materials could be controlled with solution concentrations down to approximately 80 nm thickness.*

at 50° and 70° angles of incidence. The Ludox layer thickness was adjusted by varying the solution concentration, while the spin speed was held constant at 5000 rpm. The Ludox concentrations tested were 30, 40, 80, 130, 180 g/L. The samples were baked at 100°C for 15 minutes on a hotplate to evaporate the solvents. The results of the Ludox ellipsometry thickness measurements are shown in Figure 5.9 b).

The thinnest PMMA layer attainable was 65 nm (6000 rpm, 30s) as an individual layer. This thickness may vary when coated in the superlattice morphology. This is due to the surface roughness and porosity of the Ludox layers in which the PMMA will be deposited on top of. These parameters may alter the disjoining pressure and evaporation rate of deposited medium [161], and create a different equilibrium thickness spin-speed relation [151]. The thickness of the Ludox layers could be controlled down to 80 nm using spin-solution concentration (nanoparticle concentration of 30 g/L). However, there was substantial variation in the thickness measured depending on the sample area tested. It was found that at high spin-speeds, comet streaking in the films was significant, and the resulting superlattice were poor overall quality. The cometing effects were much less severe under 6000 rpm however.

As already eluded to, the applicability of using ellipsometry as a thickness measurement technique for nanoparticle materials is uncertain. Null-point laser ellipsometry only models two interfaces (ambient–film, film–substrate [154]), whereas a nanoparticle film will actually be composed of multiple other interfaces between adjacent nanoparticles and also between nanoparticles and the air. There are alternative methods which are able to measure such a film, and even estimate porosity from the measurements [157], however they were not available for this work.

Due to the variability of the spin coating results, it is noted that the layer thickness of these layer can only be coarsely targeted [10]. The final thicknesses of the superlattices and individual layers is measured *in-situ* by SEM cross-section.

From this work, it was concluded that the optimal recipe for these structures was: PMMA was spun at 5000 rpm for 30s. The layer is then baked at $100°C$ on a hotplate for 15 minutes. The Ludox spin solution was diluted to a nanoparticle concentration of 30 g/L and spun at 5000 rpm for 30 s. This layer is then also baked at $100°C$ on a hotplate for 15 minutes. This process is repeated until 10 total bilayers have been deposited.

Post measurement, several SEM images were taken of the PMMA-SiO_2 superlattices in cross-section. These can be seen in Figure 5.10, where the dark layers indicate the PMMA, and the lighter layers show the silicate nanoparticles. In general, SEM micrographs allowed for more precise measurement of the superlattice thicknesses. To obtain the average superlattice period of these samples, three separate superlattices samples were analysed. The thickness of every layer was measured and averaged. The average SiO_2 nanoparticle layer thickness from these samples was 65 nm with $\sigma = 7.68\,nm$ (n=30), while the average PMMA layer thickness was 18.5 nm with $\sigma = 4.7\,nm$ (n=30). Interestingly, the PMMA layers in multilayer were much thinner than those measured as individual thin films previously.

5.3.2 Surface properties

In order to measure the surface properties of the nanoparticle layers, the standard spin-coating recipe was applied to soda-lime glass substrates. Tapping mode atomic force mi-

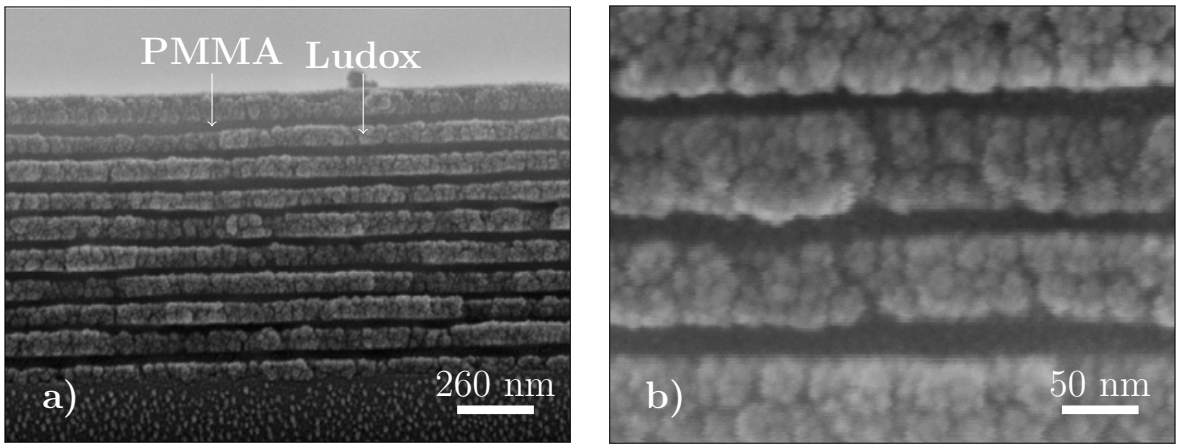

Figure 5.10: *Example SEM micrographs showing a cross-section of a superlattice structure. The dark black layers represent the PMMA, while the lighter layers show the Ludox nanoparticles.* **a)** *A 45k× magnification of the complete superlattice structure.* **b)** *A 250k× magnification micrograph of the superlattice interface, showing the interfaces between the PMMA and SiO_2. The nanoparticles in the layer are visually identifiable in the layer.*

croscopy was then used to measure the surface features of the nanoparticle layers. These measurements were used to quantify the surface roughness, as well as the nanoparticle diameter. Figure 5.11 (a) shows the surface topology of one such sample, while Figure 5.11 (b) shows the nanoparticle diameter measurements.

The particle size distribution was measured using Gwyddion AFM software [159]. The average nanoparticle diameter was found to be 22.1 nm, with a standard deviation of 3.5 nm (n=50) for this sample. The surface of the layer appears to have good packing, however there are visible particle agglomerations, and voids of two or more nanoparticles. The nanoparticle shape can not be reliably observed from this type of thin film morphology AFM measurements, because the nanoparticles are too closely packed together to observe their silhouette. To more reliably observe the nanoparticle shape, the surface of a thin-film sample was imaged using SEM, a standard method for observing nanoparticle shape [162]. As shown in Figure 5.12, the observable two-dimensional silhouette of the nanoparticles was circular. However, the scanning electron microscope used did not have sufficient vibration isolation to resolve the nanoparticles further. Due to this, objective statements about minor/major particle radii can not be made.

These scans of the surface layer show that there are a significant density of nanoparticle

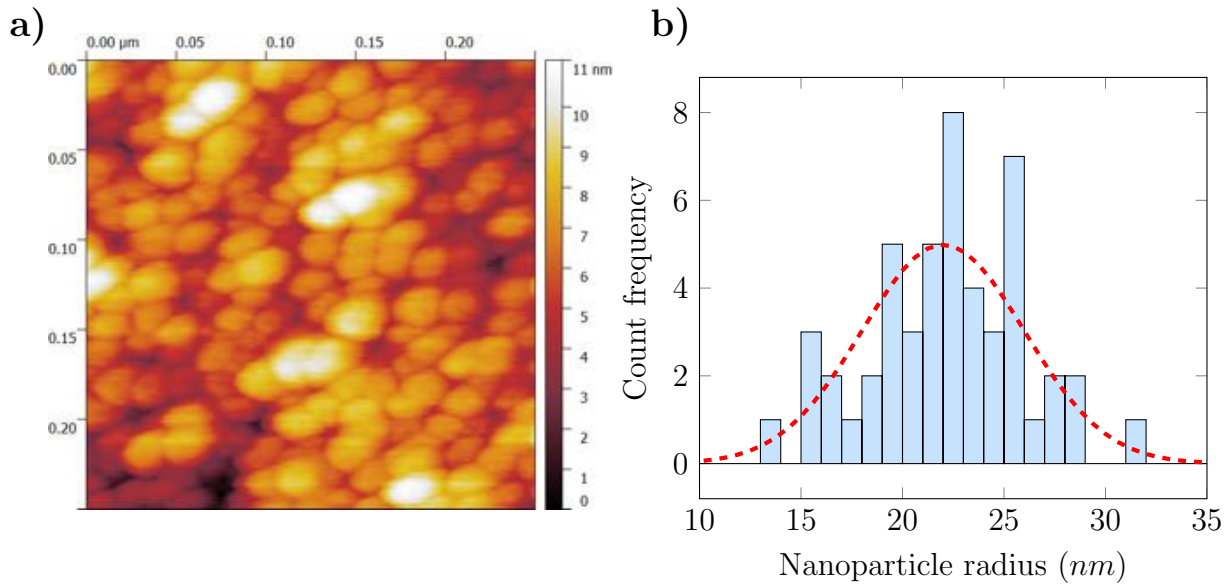

Figure 5.11: *Nanoparticle material characterisation using AFM scanning. A circle was fitted to fifty nanoparticles on the surface of this scan to characterise the average nanoparticle radius and the standard deviation of the radius. This is an important property in the thermal performance of packed nanoparticle beds.* **a)** *An AFM scan of the surface of the nanoparticle material. Gwyddion AFM processing software was used to fit a circle to fifty nanoparticles of this, and another large area scan.* **b)** *Using fifty observations of nanoparticle radii a normal distribution was fitted to the observations. This produced an average nanoparticle radius of approximately* 22 *nm with a standard deviation of* 3.5 *nm.*

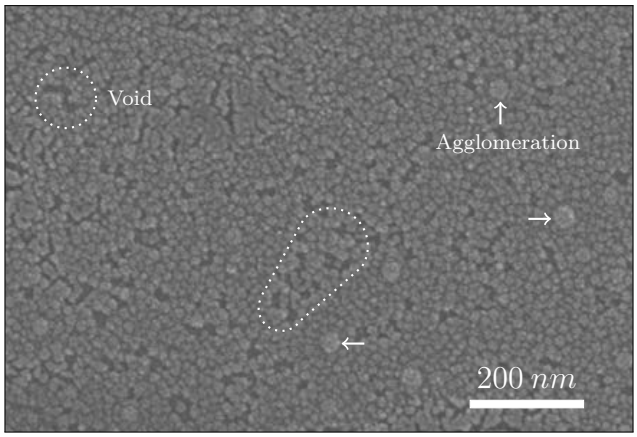

Figure 5.12: *A SEM micrograph of the surface of a nanoparticle thin film. Nanoparticle agglomerations and vacancies are observable in the surface of the film, aligning with the AFM micrograph shown previously. In the image, agglomerations are demonstrated by arrows, while areas with a high density of vacancies are circled. Both of these features will translate into point defects and pinholes in the phononic crystal. This will break the periodicity of superlattice, and effect the centre frequency of the phononic crystal [18]. The effect of this on the macro-thermal properties is still unknown.*

agglomerations and also voids in the layer. In Figure 5.12, the agglomerations are annotated with arrows, while several examples of voids in the nanoparticle packing are circled. Defects like this will break the periodicity of a phononic crystal and effect the phononic bandgap of the material [18]. The effect of these defects on the macro-scale thermal properties of the thin film may be less pronounced, or not measurable however. The overall porosity of the nanoparticle layer, the surface texturing of the nanoparticle thin films, and the significant vacancy defect density is a probable explanation for why the PMMA layers are thinner *in-situ* than when they were individually calibrated. As previously mentioned, the equilibrium thickness of a spin-coated material is a function of solution viscosity, spin speed, solvent evaporation rate, and time. It is generally simplified to viscosity and spin speed alone, however in this ultra-thin layers the other factors may become more relevant [151]. It seems likely from the observations in this thesis, that the spin-speed relationship calibrated does not hold when deposited on top of the nanoparticle thin-films. Furthermore, the surface texture created by the nanoparticles will alter the contact angle of deposited material, and change the evaporation rate (via the surface area [161]).

5.3.3 Individual layer differential 3ω

To establish the effect that the superlattice structure has on the thermal conductivity, first the constituent materials alone were measured using the differential 3ω method. The PMMA used in this work was already tested as a check for the differential 3ω method in Chapter 3. In this section, the PMMA was spin-coated onto both silicon and soda-lime glass substrates to further increase the measurement confidence. The silicon substrates required an electrical insulation layer for the control sample. As PMMA is an electrical insulator however, two samples with PMMA thin films were prepared with 50 nm and 270 nm thicknesses, respectively. This allows the thin film properties to be measured without the additional insulation layer and any error that it may introduce. The thickness of the PMMA layers was measured using surface profilometry, as previously discussed.

The differential 3ω results for PMMA thin films is shown in Figure 5.13. In order to plot the results from both substrates on the same axis, only the change in thermal resistance,

a)

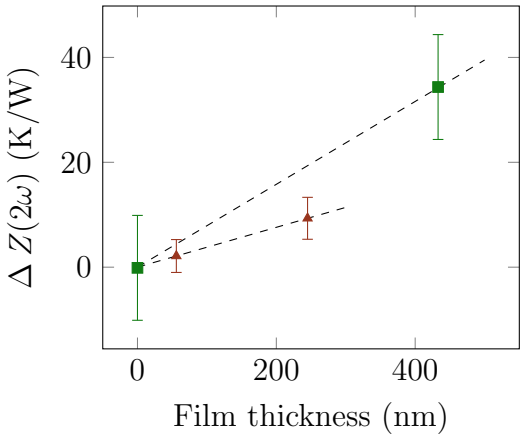

b)

	Soda-lime	Silicon
$R_{e0,sample}$	2.548 Ω	6.854 Ω
$R_{e0,control}$	2.855 Ω	6.818 Ω
b	28.4 μm	28.3 μm
L	1 mm	2 mm
k_{PMMA}	0.24 $\pm$ 0.02	0.23 $\pm$ 0.02 $W/m-K$

Figure 5.13: *A differential* 3ω *measurement on the spin-coated PMMA thin film. The samples were prepared on both soda-lime glass cover-slips, and also on diced silicon wafers. These samples both resulted in thermal conductivities within tolerance of each other.* **a)** *A graph showing the thermal resistance measured by the RT changing with PMMA film thickness. The RT on the silicon substrate sample is twice as long as that on the soda-lime. As a result, the slope of the result is half.* **b)** *A summary of the RT properties for both samples and the results of each measurement. In the table,* $R_{e0,control}$ *is the zero-current resistance of the control RT,* $R_{e0,sample}$ *is the zero current resistance of the RT on thin-film sample, b is the RT half-width, and L its length.*

which represents the contribution of the PMMA thin film, is shown. Despite the thermal conductivities of the substrate materials being two orders of magnitudes apart (approximately $1\ W/m-K$ for soda lime glass [124], and $100\ W/m-K$ for silicon [163]), the results both agreed with each other, and with literature within experimental uncertainty [126]. The thin film measurements on soda-lime and silicon recorded thermal conductivities of $0.24 \pm 0.02\,W/m-K$ and $0.23 \pm 0.02\,W/m-K$, respectively.

The thermal conductivity of the nanoparticle layers were measured next. The substrates for this experiment were diced silicon wafers with 100 nm of thermally grown SiO_2. The silicon substrates were prepared and provided by Dr Amalraj Peter Amalathas. The Ludox colloidal silica was spin-coated onto the substrates in 2, 4 and 8 repetitions of the previously optimised recipe, in order to obtain a well defined range of thicknesses. Similar to the superlattices however, the actual thickness of the layers was measured by SEM cross-section analysis. The range of thicknesses obtained is shown in Figure 5.14 a), b), and c). The morphology of these spin-coated nanoparticle thin films was very similar to that of the packed nanoparticle beds discussed in Chapter 4. As such, the thermal conductivity of this thin film material could be calculated through the application of Prashers' model of single element packed nanoparticle beds [39]. In this model, the degree of phonon filtering is proportional to the contact patch area between two adjacent nanoparticles and the diameter of the nanoparticle [39]. The mean nanoparticle diameter was measured in this work using atomic force microscopy, and was found to be $22.1\ \pm 4.7\,nm$. The contact radius of the nanoparticle meanwhile, can be calculated using Hertzian analysis and Johnson Kendall Roberts (JKR) theory [136].

To calculate the contact area, the surface energy of the nanoparticles is required. This is difficult to measure on nanoparticles, as the "surface" cannot be easily observed. As a substitute for direct measurement on a single nanoparticle, the contact angle of a nanoparticle film is measured, and compared to known values for silica glasses. The water contact angle of three nanoparticle thin film samples were measured using contact angle goniometry. The average water contact angle (WCA) for these samples was $16.54 \pm 4.1°$. This is much less than other nanoparticle WCA measurements, which report near-hydrophobic contact angles of 87° [164]. However literature suggests that any increase in contact angle relative to un-

structured silica glass is predominantly due to surface texturing effects [164]. As such, for this work a range of surface energies above that of clean, bulk, soda-lime glass were used in the Hertzian contact radius analysis. Rhee et al. reported a range of measured surface energies for silicate glasses from 0.084 to 0.254 J/m^2 [148]. These surface energies result in contact radii of 0.17 to 0.57 nm, and thus a nano-constriction with thermal conductivities of 0.05 to 0.5 $W/m-K$. The latter values exclude all gaseous thermal transport [39], and by extension any other effects like moisture condensing in the nanoconstriction is also excluded [104].

The results of the differential 3ω method measurement of SiO_2 nanoparticle thin-films are shown in Figure 5.14, along with a series of SEM micrographs of the packed nanoparticle materials. The micrographs show a good close packing of nanoparticles in the cross-section plane, and consistent layer thickness across the substrate. The thickest layers were approximately 900 nm thick, while the thinnest were 190 nm thick. The packed nanoparticle thin films had a thermal conductivity of $0.179 \pm 0.02\, W/m-K$. This result is inside the 0.05 to 0.5 $W/m-K$ range predicted by Prashers' model, and corresponds with a surface energy of approximately 140 mJ/m^2.

5.3.4 Hybrid-Bragg stack measurement

The thermal resistance versus film thickness for the Hybrid Bragg stacks on soda-lime glass is shown in Figure 5.15. Due to the variability in sample structure, each data series represents an average of repeat measurements on a single sample, rather than the average of multiple samples.

10 total bilayers (20 total layers) were deposited onto the substrates, targeting a 50–50 nm architecture. This would ideally form a film 1 μm thick. The spin-coated stacks exhibited a range of total thicknesses between 848 nm and 992 nm. The superlattice periods also ranged from 85 to 105 nm. This variability is despite identical fabrication procedures for every sample. This highlights the relatively uncontrolled nature of the manual layer-by-layer spin-coating deposition technique. There was a correspondingly large variation in thermal

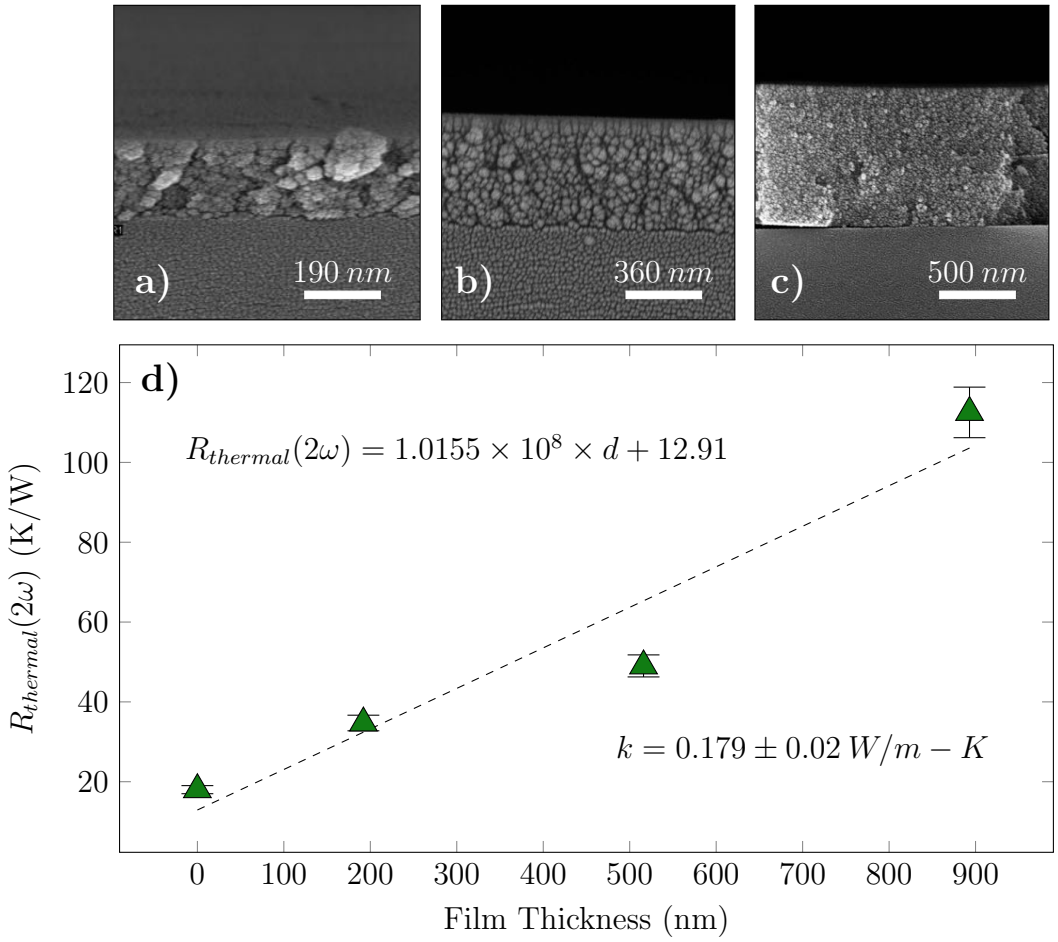

Figure 5.14: *Differential* 3ω *method measurements of the packed* SiO_2 *thin films, and SEM micrographs, which show cross-sections of the measured films.***a)**, **b)**, *and* **c)** *show the increasing thin film thickness from the thinnest (*192 *nm) to the thickest (*890 *nm) film produced. Note that the magnification changes between each of these micrographs.* **d)** *The differential* 3ω *measurement of the* SiO_2 *nanoparticle thin film. The thermal resistances measured were an average value from multiple measurements of a single RT on the thin film. As expected there is a good linear fit between the thermal resistance and film thickness.*

conductivities measured by the differential 3ω method. The Hybrid Bragg stack thermal conductivities ranged between 0.055, and $0.023\,W/m-K$. An average value was $0.043\,\pm\,0.014\,W/m-K$. Despite the high spread of results, the Hybrid Bragg stack morphology did create a reduction in thermal conductivity of 3 to 10 times relative to the constituent materials. The thermal insulation performance of these structures is generally comparable to other packed nanoparticle materials including those investigate in the previous chapter of this thesis [40–43, 104]. However it seems unlikely that the low thermal conductivity is due to the nanoparticle morphology alone. When the Ludox material alone was measured (see Figure 5.14), the thermal conductivity was much larger than the Hybrid Bragg stack structure.

In the previous chapter, it was concluded that moisture/humidity was a potential cause of degradation in the packed nanoparticle materials investigated. A similar mechanisms may also play a role in the thin films investigated here. In that case, the interleaved PMMA may be acting as an encapsulating material surrounding the nanoparticles. This might be allowing them to retain their low thermal conductivity properties even while in room humidity. If this were the case, the measured thermal conductivity of the Hybrid Bragg Stacks would align with the predicted values of Prashers' model [39].

However if this is not the case, another possible source of the thermal conductivity reduction is the acoustic mismatch between the PMMA and SiO_2 materials. In literature, this is proposed to be the source of the phononic bandgaps [18, 49], and it is known to reduce phonon transport perpendicularly across layers in other kinds of materials [16, 23]. Using the tabulated acoustic mismatch model provided by Cheeke et al., the phonon transmission function between PMMA and SiO_2 is between 0.2 and 0.4 depending on which material the phonon originates in [25]. Literature also suggests that there is a relationship between phonon group velocity and film thickness in PMMA [165]. The speed of sound in PMMA thin films was found to triple in 20 nm PMMA films when compared to bulk. These thickness values are comparable to the PMMA layers used in this work. However, using the same directionally averaged transmission function as previously, this would predict an increase this phonon conduction across the SiO_2-PMMA interface to 0.4 to 0.9. In the literature on

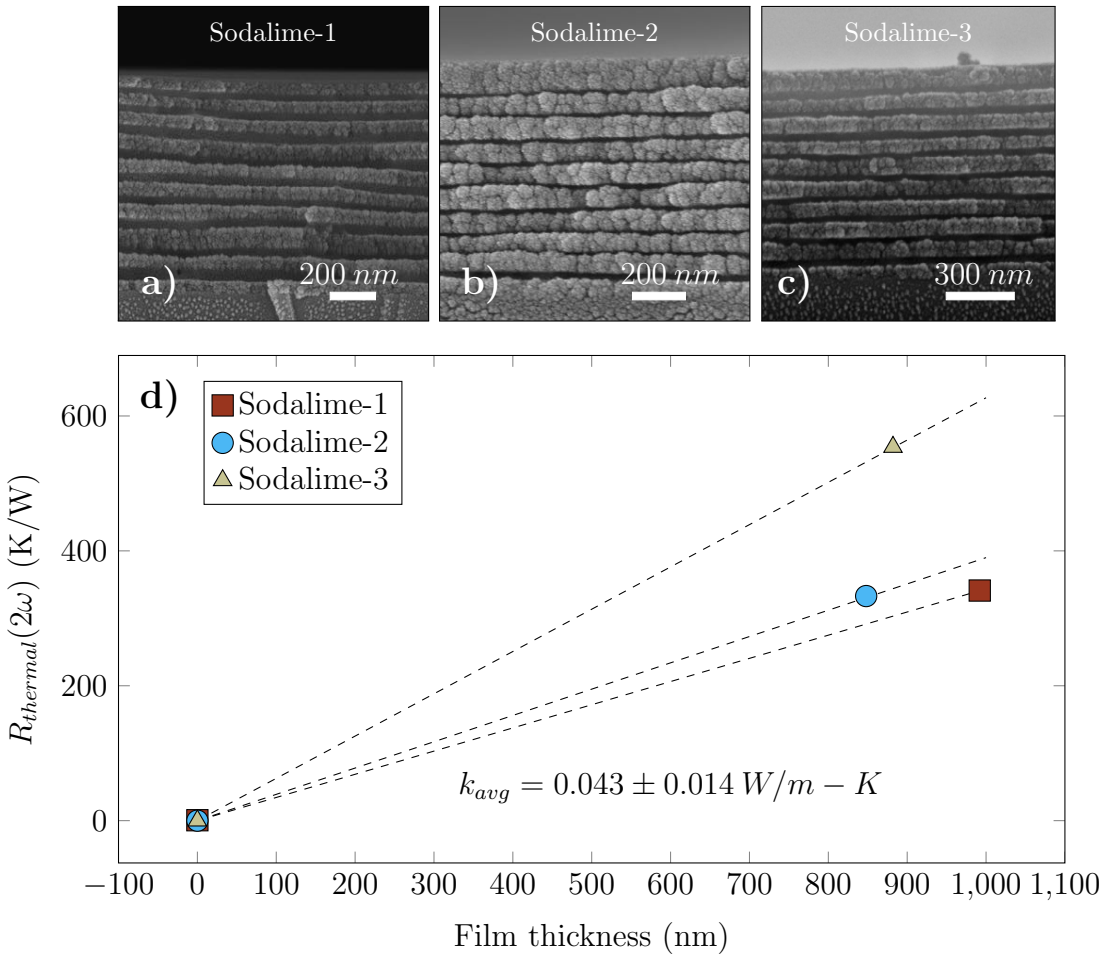

Figure 5.15: *A series of differential* 3ω *measurement on 10 bilayer (20 total layers) PMMA–*SiO_2 *superlattice structures on soda-lime substrates.* **a)**, **b)**, *and* **c)** *show three superlattices on soda lime glass. This showcases the variability in the formed superlattice periods even with identical fabrication procedures.* **d)** *The results of the differential* 3ω *method. Due to the variability, the results are presented as separate differential* 3ω *measurements. This in turn created a large variation in thermal conductivities measured. This is one limitation of the layer-by-layer spin coating procedure used in this work.*

the subject, the increase in speed of sound was measured in the x-y plane of the PMMA film, as opposed to across the thickness of the film. Measurements perpendicular to the thin-film plane would be more applicable to this work, however this measurement has not yet been conducted.

A further interesting property of the Hybrid Bragg Stack, is its utility as a *photonic* crystal. The films were observed to have an iridescent quality, especially noticeable when fabricated on silicon substrates. This quality is thought to be caused by this photonic bandgap. The thermal transport properties could be further manipulated if this photonic bandgap was tuned to wavelengths in the infra-red spectrum, effectively acting as a thermal infrared Bragg Reflector [166]. This would involve increasing the bilayer period to 1.75 to 3μm in order to align with the wavelength of thermal infrared (7-12μm [166]). This may produce some interesting results, but may also negatively effect the thermal conductivity, as the interface density will be greatly reduced. If the photonic bandgap could be shifted out of the visible light spectrum, and into thermal infrared, then the films would be completely transparent and in this case, they could be applied as an additional thermal insulation films on windows, or any application where optical transparency is required. This method of suppressing infrared transport is also worthy of pursuit when compared to the previous chapter. In the previous work, the carbon nanoparticles acted as a radiation suppressing material. However carbon nanoparticles, and carbon nanotubes have been shown to be toxic. This does not place them favourably for residential insulation applications [167, 168]. If infrared thermal transport could be suppressed via refined Bragg structuring, then the performance of these Hybrid Bragg stacks could be even further improved.

In this work, it was not possible to correlate the superlattice period with the thermal conductivity, due to the variation of the structures produced. In the future it would be desirable to carry out this experiment. This would require refinement to the fabrication protocol to eliminate the variance in the deposited layers. One option would be to fabricate the structures in a higher grade clean-room than the one available at the University of Canterbury. Another option would be to automate the spin-coating procedure with an automatic spin-coater. This could precisely control the volume of liquid medium deposited, and the time

between solution dispensing and initiating the spin-coater rotation. These steps would reduce the variance in layer structures, however may still not be a sufficient level of control to correlate thermal conductivity and superlattice period. In this circumstance, an alternative fabrication methodology would need to be sought. Two alternative procedures could be, electrophoretic deposition [169], or block co-polymer nanoparticle self-assembly [170].

5.4 Conclusion

In this chapter, Hybrid Bragg stacks composed of PMMA and SiO_2 nanoparticle layers were fabricated, and the thermal conductivity measured using the differential 3ω method for the first time. The thermal conductivity of the structure was 3 to 10 times lower than the constituent materials. However the dimensions of the interleaved layers varied largely despite identical fabrication procedures. This was attributed to the a lack of control available in the layer-by-layer spin-coating procedure. In turn these structures had a large variance in thermal conductivity. The average thermal conductivity was $0.043 \pm 0.014\, W/m - K$.

This chapter concludes the work on thermal meta-materials in this thesis. In the next chapter, a 3ω resistance thermometer is integrated into a microfluidic channel as a spatially resolved flow sensor. The properties of this system are explored, and new applications suggested for this technology.

Chapter 6

3ω microfluidic flow sensor

6.1 Introduction

This chapter reports on a novel application of the 3ω method to a microfluidic system. In this work, a 3ω resistance thermometer (RT) is used to measure fluid velocity in a microfluidic chip, as well as sense fluid velocity through stationary liquid and behind a membrane. Parts of this chapter were published as "Spatially-resolved 3ω thermal flow sensing for microfluidics and biology" in the proceedings of the 20th conference on Solid-State Sensors, Actuators, and Microsystems.

As covered in Chapters 2 and 3, there are many emerging applications for the 3ω method which reach beyond its use as a thermal conductivity measurement technique. These applications utilise the 3ω method to apply heat stimulus precisely to a system, and interpret the response through some coupling between the thermal domain and the property of interest. Of these, one relatively new application is to use the 3ω RT as a flow sensor. Thermal flow sensors are a well established concept, with the most common design using one heating element and two thermocouples to sense flow magnitude and flow direction [81]. In contrast, a defining property of the 3ω method is that the RT acts as both heating element and thermometer. This characteristic allows the RT to act as a single element flow sensor. This idea was explored by C. Clausen et al. on a millimetre scale RT element to measure bio-film thickness, fluid velocity, and water contact [80]. Other research teams have since used the technique in a biological context to assess cell viability and disease state [89], measure the thermal conductivity of single cells [90], and to detect droplets in microfluidic systems [82]. As demonstrated by these examples, the 3ω method has great future potential in microfluidics. One particularly interesting idea which has not been explored, is to use the finite thermal penetration depth of AC thermal waves to spatially explore fluid flow in microfluidics, and mass transport in growing biological systems.

For microfluidics, the 3ω method could, for example, be used to explore and characterise the laminar flow regime [171]. In laminar flow, there is no mixing between parallel sheets of fluid. This manifests as a parabolic velocity profile in a confined channel. Given this orderly flow profile and the concept of finite thermal penetration depth, it was theorised as a part of this

thesis that a 3ω RT, integrated into the base of a microfluidic channel, would be capable of measuring fluid flow at a distance defined by the thermal wavelength, measuring fluid flow through stationary liquid and solid obstacles, and that the parabolic velocity profile in the channel could be reconstructed through the temperature response.

In a biological context, this ability to spatially sense flow could prove useful as a tool for understanding the growth of filamentous biological species. Some examples of these organisms include, pollen tubes [93], root tips [94], and oomycetes [92, 172, 173]. These species all have internalized fluid flow separated from a typically static environment by a membrane [92, 173]. A well characterised 3ω mass transport sensor could contribute to the understanding of internal mass transport and how this controls the growth of pathogenic or invasive growth.

The following chapter describes the adaption of the 3ω method into a fluid velocimeter and its use to study the temperature response characteristics in laminar flow. The RT was first verified to respond to fluid velocity by integrating a RT into the base of a standard microfluidic channel. A microfluidic chip designed as a scale model of a filamentous biological species, was then fabricated. This chip was used to assess whether the RT could measure the fluid velocity at a distance, and through a solid membrane.

6.2 Methods

In the following sections, the techniques used to fabricate the microfluidic channels and test the 3ω RTs response to fluid flow are described. There are a range of channel designs used in this work, which can be divided into two main channel designs. Each of these used separate mould fabrication procedures. The microfluidic channels themselves were fabricated in polydimethysiloxane (PDMS, Sylgard 184, Dow Corning) using negative replica moulding. The 3ω RT, meanwhile, was fabricated on a microscope slide, and integrated into the bases of the microfluidic channels. This fabrication procedure has been previously described in Chapter 3.

6.2.1 Aluminium mould fabrication

CNC milling is a flexible and versatile method for fabricating microfluidic channel moulds with larger (typically greater than 0.1 mm) features [174]. The range of cutter sizes available (3 mm to 10 μm) in combination with three dimensional machining paths, allows CNC milling to create moulds with large aspect ratios and complicated three-dimensional channel geometries.

For this work, the channel design was modelled in CAD, and g-code generated using computer assisted machining (Autodesk, Fusion 360). As a mould blank, a $12\,mm \times 50\,mm \times 100\,mm$ bar of 6061-T6 aluminium was used. This is a precipitation hardened aluminium alloy with a high level of tempering [175]. Hardened materials help to reduce machining artefacts and improve the quality of the mould. The machining tools used in this work were carbide end-mills (Performance Micro-tool). To attain a high-quality surface finish, a high spindle speed-low chip load machining approach was utilised. The exact spindle speed and feed-rate varied depending on the cutter diameter and tool engagement. More details are provided in Appendix A.

The general approach for machining operations followed the steps of, preparation, roughing, and finishing. To prepare the mould blank for channel formation, the material blank was securely mounted in the vice of the Minitech mini-mill, described in Chapter 3. The surface of the blank was cut flat and parallel with the mill axis using a 26 mm diameter fly-cutting tool (1/4" Shank, Arc Euro Trade). The overall shape of the channel was then formed using roughing operations. For this, a 2 mm flat end-mill (Performance Micro-tool) was used. Finally, a 1 mm flat end-mill (Performance Micro-tool) precisely defined the channel geometry and created a high quality surface finish. In this finishing procedure, low chip-loads and high spindle speeds were used. Photographs of the milling procedure, and finished mould, are shown in Figure 6.1.

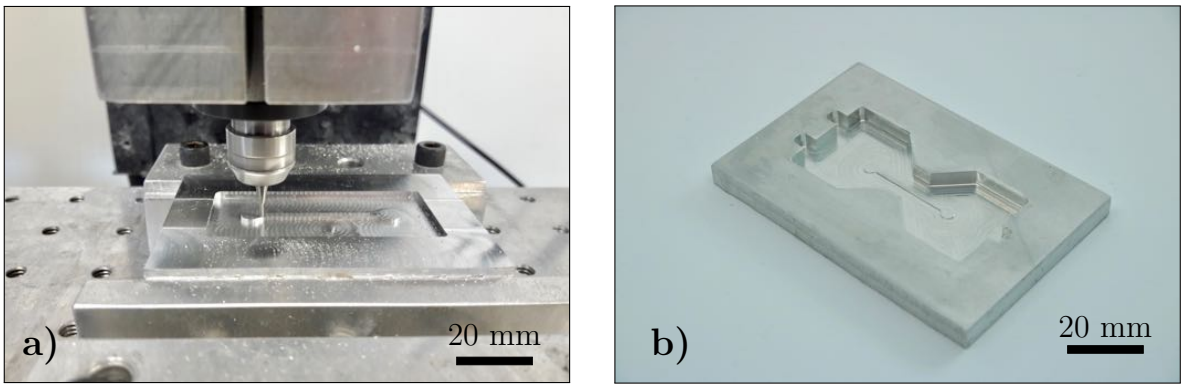

Figure 6.1: *Photographs showing the fabrication of an aluminium microfluidic mould, and the resulting mould.* **a)** *The aluminium negative mould being CNC milled out of 60601-T6 aluminium.* **b)** *A macro photograph of the completed channel mould. The channel design is a basic linear microfluidic device. The overall bow tie shape of the mould allows for easy electrical interfacing. Tabs are added to the end of the mould as a sacrificial de-moulding tab.*

6.2.2 Dry-film mould fabrication

An alternative fabrication method for microfluidic moulds used in this work was dry-resist on silicon. Such moulds are fabricated using UV photolithography, allowing features down to 5 μm to be routinely fabricated. The dry film used in this work was the ADEX series of epoxy photoresists (DJ μ-laminates). These films are pre-formed photoresist laminates on PET carrier sheet. They can be adhered onto silicon using a conventional laminator [172], and then process similarly to other photo-lithography procedures.

A 4" silicon wafer was dehydrated in a 185°C oven for 24 hours. This dehydration step improves the adhesion between the dry-film laminate and wafer. The carrier film was removed from the ADEX dry film, and the resist laminated onto the silicon wafer using the Sky-335R6 laminator (Speed 1, 65°C). The resist was exposed using the Suss MA-6 mask aligner through a UV low-pass filter (PL-360-LP). For a laminate thickness of 50 μm, an exposure energy of 650 mJ/cm^2 was used. This is twice the nominal exposure energy, and was experimentally determined to improve adhesion and exposure clarity [176]. For development, the wafer was inverted on a wire mesh carrier and immersed in cyclohexanone for 10 min. Inverting the wafer assisted with removal of the developed resist, and prevented fine mould features

Figure 6.2: *A complete dry-film-on-silicon microfluidic mould. The channel has a cross-section of* $100\,\mu m \times 100 \mu m$*, and is 35 mm long from inlet to outlet. This design was used for the hypha scale-model microfluidic device, described in Section 6.2.7. A second mould with a mirror image of this design is used to create the top channel of this two-channel device. This in turn is aligned and plasma bonded to the base-channel to form the complete stack. The angled shape of the channel gives the clearance necessary to make four individual fluid connections.*

from becoming clogged. After development was complete, the wafer was removed from the developer bath and rinsed with fresh cyclohexanone. A final wash with acetone, methanol and IPA cleaned any remaining developed resist off of the surface. Prior to use with PDMS, the dry film moulds required treatment with a release agent to assist with future removal of cast channels. For this type of channel, the release agent was silane. This was deposited onto the mould surface by vacuum desiccation with a vial of TOFCS (Trichloro(1H,1H,2H,2H-perfluorooctyl)silane, Sigma Aldrich) [177]. A completed dry-film mould is shown in Figure 6.2.

6.2.3 Single channel negative replica moulding

The microfluidic moulds, described by the previous two sections, were then used to fabricate the microfluidic channels in PDMS using the standard replica moulding procedure [177]. A schematic representation of the negative replica-mould procedure is shown in Figure 6.3. In depth recipes, and alternative procedures, are available elsewhere [178,179]. The recipe used in this work is as follows. Standard PDMS (10:1 w/w, Sylgard 184, Dow Corning) elastomer and curing agent were mixed and then de-gassed in a vacuum desiccator to remove bubbles from the mixture. This was then poured into a negative mould of the desired channel design, the mould being prepared previously using one of the fabrication methodologies described in Section 6.2.2 and Section 6.2.1. The PDMS-filled mould was de-gassed again to remove any air bubbles which may have formed in fine mould features during pouring. The mould was then baked at $80°C$ for two hours on a hot plate to cure the PDMS. Once cured, the solid microfluidic channel was removed from the mould. In order to make external fluid connections to the channel, a $1\,mm$ diameter biopsy punch was used to core inlet and outlet holes to the entrance and exit of the channel. The base of the channel was formed by a standard soda-lime microscope slide (Thermo Fisher). On this slide, the flow sensing RT had been pre-formed using the photolithographic lift-off procedure described previously. This flow sensing RT had to be aligned with the channel manually, so that it was directly exposed to fluid flow.

The PDMS channel and RT patterned microscope slide were manually aligned and bonded with oxygen plasma (100 W, O_2, Tergeo, PIE Scientific). To strengthen the plasma bond, a brass weight was placed on top of the chip and the stack was baked at $80°C$ for a further 2 hours on a hotplate.

6.2.4 Dual channel exclusion moulding

Exclusion moulding is a variant of negative replica moulding (described above), which is used to precisely define the "over-pour", or roof of a device, by expelling excess PDMS from the mould during the pouring process [178]. It is particularly useful for forming thin film PDMS

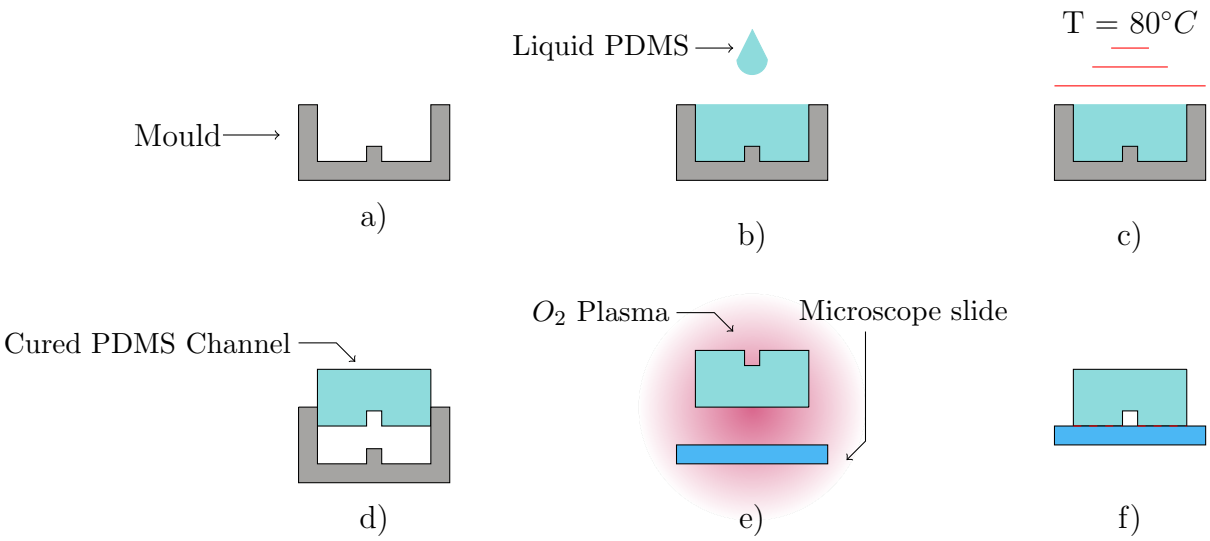

Figure 6.3: *A schematic representation of the negative mould replication process, used for fabricating PDMS microfluidic chips in this work.* **a)** *Mould fabrication. A negative mould of the channel design is fabricated. Several fabrication methods are available for this step depending on exact requirements of the experiment.* **b)** *PDMS casting. PDMS elastomer and curing agent are prepared and cast into the mould. The PDMS and mould are de-gassed in a vacuum desiccator to remove any air bubbles trapped in fine mould features.* **c)** *PDMS Curing. The PDMS-filled mould is baked at 80°C on a hot plate for 2 hours to cure the liquid PDMS.* **d)** *Channel de-moulding. The cured channel is removed from the mould. The mould design is left imprinted in the base of the cured PDMS.* **e)** *Plasma bonding. The PDMS channel and a microscope slide are exposed to oxygen plasma.* **f)** *Bonding. The channel and the microscope slide are manually aligned and pressed together, this permanently bonds the microscope slide base and the PDMS channel into one sealed device.*

devices with precise geometry. This procedure facilitates the formation of three-dimensional microfluidics chips. In this work, exclusion moulding is used to form the triple layer model hypha chip. This design is intended to test the 3ω RTs ability to measure fluid flow through dividing membranes. A schematic diagram of the exclusion moulding procedure is displayed in Figure 6.4.

In the exclusion moulding process, PDMS is prepared in the same way as previously (10:1 base to curing agent, vacuum de-gassed). A small amount of PDMS is then poured onto a relatively shallow mould which contains the negative imprint of the desired channel. After pouring, a borosilicate glass wafer (University Wafer) is pressed onto the top of the mould, separated from the liquid PDMS by a polyethylene sheet. The wafer provides a rigid structure to evenly apply pressure downwards onto the PDMS, expelling any excess out of the mould. This creates a well defined roof, or membrane, to the device. The pressure in this case is exerted by a brass weight placed on top of the wafer. The brass weight and mould stack were then cured on a hotplate, as in the standard PDMS process. These thin film devices can then be bonded (O_2 plasma, 100 W, Tergeo, PIE Scientific) onto soda-lime glass substrates, or on top of other PDMS channels to form three dimensional channel stacks.

6.2.5 Electrical and fluid interfacing

As previously described, the flow sensing RT was fabricated on a soda-lime microscope slide using the standard lift-off pattern procedure, prior to being sealed in the base of the microfluidic channel. In order to electrically connect the RT elements to the 3ω instrumentation, a spring-loaded pogo-pin interfacing board was built. This could be pressed onto the microfluidic chip to quickly and repeatably connect to the RT. To facilitate fluid connections, a $1\,mm$ biopsy punch was used to core holes to the entrance and exit of the microfluidic channel. Following this, 1 mm polytetrafluoroethylene (IDEX Health and Science) tubing was press fit into the cored holes created by the biopsy punch. A slight interference fit between the interfacing tubing and PDMS device assisted in creating a water tight seal. The fluid sealing could then be verified by infusing the chip with food-dye coloured water.

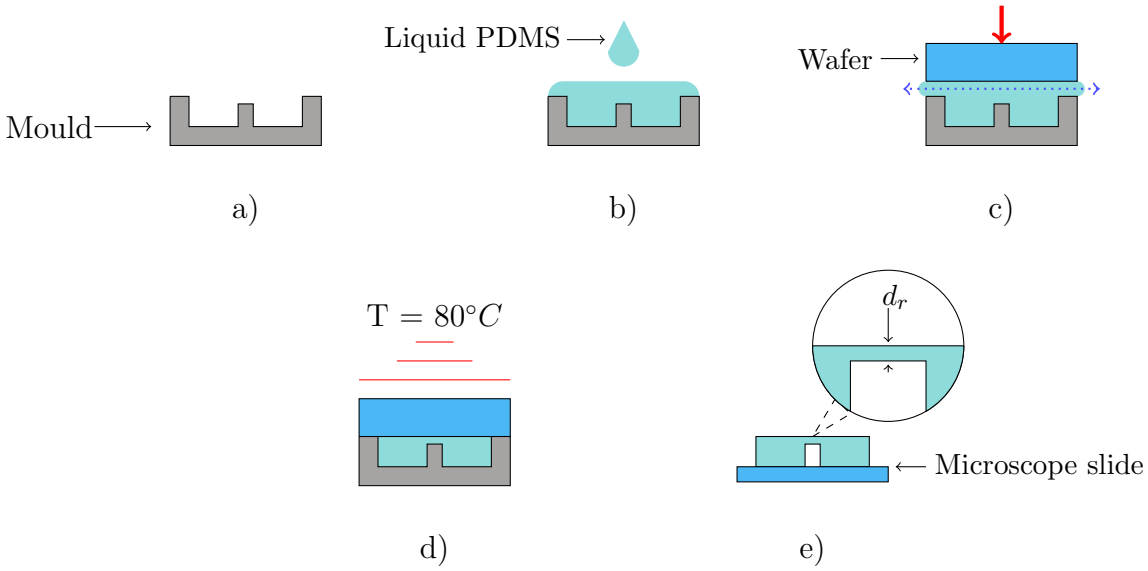

Figure 6.4: *The exclusion-negative replica moulding process.* **a)** *A mould is fabricated.* **b)** *Liquid PDMS is cast into the mould. Care must be taken not to trap bubbles in fine mould features.* **c)** *A borosilicate glass wafer is used to evenly apply pressure onto the mould, expelling any excess PDMS.* **d)** *The mould is baked at 80°C for two hours to cure the PDMS.* **e)** *The PDMS channel is demoulded, and bonded to a microscope slide using oxygen plasma. The thickness of the roof (annotated as d_r) is now precisely defined by the dimensions of the mould as the borosilicate wafer has expelled any excess PDMS material.*

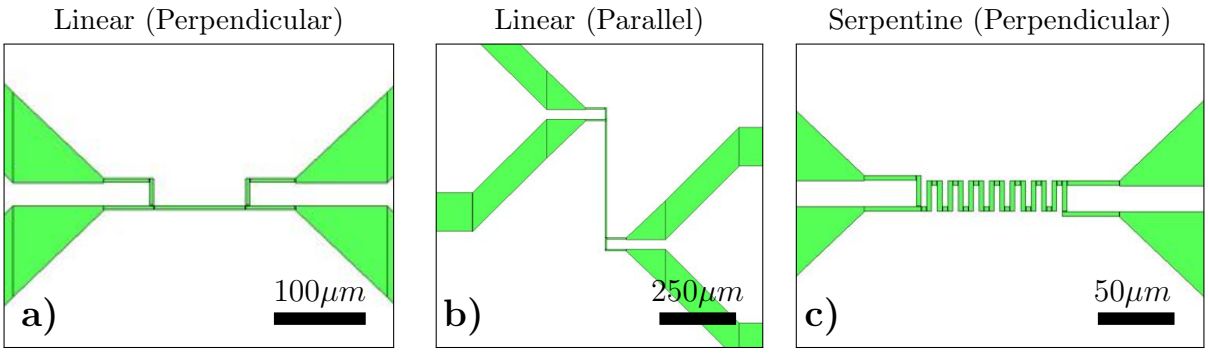

Figure 6.5: *The RT designs used to establish the effect of RT geometry on 3ω temperature response. Fluid velocity is from top to bottom.* **a)** *The simplest possible design. A straight RT with a width of 5 μm maximises the SNR for the available channel width.* **b)** *The standard RT design orientated down the length of the channel.* **c)** *The serpentine RT design, designed to maximise the thermometer length inside of the 125 μm channel footprint.*

This concludes the procedures used to fabricate the physical microfluidic chip, and interface it the required instruments. The next sections describe the procedures used to test the hypothesis' of this chapter, namely that the integrated 3ω RT will be capable of sensing fluid flow, and resolving spatial changes in fluid velocity.

6.2.6 Single channel fluid velocity measurement

In order to characterise the 3ω RT response to fluid flow, a simple single channel microfluidic device was designed. The channel was 20 mm long and had a $125\,\mu m \times 125\,\mu m$ square cross-section. A 3ω RT was integrated into the base of the channel, such that it was directly exposed to fluid in the channel. To fabricate the device, a channel mould was machined using the CNC milling process described previously in Section 6.2.1. Negative replica moulding was used to produce the channel in PDMS. The RT was pre-fabricated on the microscope slide using lift-off patterning, as described in Chapter 3. The microscope slide, RT, and microfluidic channel were then manually aligned and permanently bonded with oxygen plasma. Three RT designs were tested, linear (perpendicular to flow), linear (parallel to flow), and serpentine (perpendicular to flow). These different designs were tested to establish the effect of the RT geometry on the 3ω response to fluid flow. These three designs are shown in Figure 6.5. The linear RT designs are identical to a standard 3ω method RT.

Calibrated fluid flow between 0 and 400 $\mu l/min$ was generated in the channel via a syringe pump (Harvard Apparatus, PHD 2000) and external flow sensor (Elveflow). The process for acquiring the 3ω frequency response followed the same procedure as the "classical" 3ω method measurements. As such, the recorded 3ω voltage can be directly transformed into a temperature [6] via,

$$T(2\omega) = \frac{-2X_{3\omega}}{I_\omega R_{e0}\alpha} \tag{6.1}$$

where $T(2\omega)$ is the temperature response at 2ω, $X_{3\omega}$ the in-phase third harmonic voltage, I_ω the fundamental heating current, R_{e0} the zero current resistance of the RT element, and α the temperature coefficient of resistance. In order to relate the temperature response of the RT to the fluid velocity, a control measurement with the fluid stationary was recorded. This was intended to capture all thermal transport mechanisms not related to fluid motion. A measurement with the fluid in motion would then produce a signal change from the control that is a function of fluid velocity, and thermal wavelength via the thermal frequency. For the purposes of this work, it is proposed that the temperature response due to the fluid motion (convection) can be found by,

$$T_{flow}(\lambda) = T_{fluid-motion}(\lambda) - T_{fluid-stationary}(\lambda) \tag{6.2}$$

where λ is the thermal wavelength of an AC thermal wave, $T_{flow}(\lambda)$ the temperature response due to fluid motion as a function of thermal wavelength, $T_{fluid-motion}(\lambda)$ the temperature response of the substrate and moving fluid, and $T_{fluid-stationary}(\lambda)$ is the temperature response due to the substrate and stationary fluid. This linear subtraction of control and sample response is similar to that of the differential 3ω method, and forms a starting hypothesis for the purposes of this work. It assumes that phonon conduction in the fluid is independent of fluid motion, and that the convection and conduction response are linearly separable. This assumption is supported through literature in the form of the Nusselt number, a dimensionless number expressing the ratio of convective and conductive thermal transport in a fluid. In the calculation of the Nusselt number, the conductive coefficient is a constant property of the material [179]. This supports the assumption that the stationary fluid measurement will sufficiently control for the conductive transport in the system.

In the "classical" 3ω method, the slope of the in-phase response with $ln(2\omega)$, or the magnitude of the out-of-phase response, are both proportional to the thermal conductivity of the material surrounding the RT [6]. In a quasi-static fluid velocity field then, the 3ω temperature response should be related to the fluid velocity at a distance from the RT related to the thermal wavelength (λ). The exact solution to this problem is complicated, and is outside the scope of this thesis. As such, an interim model is proposed purely for this work. This model essentially proposes that, based on the "classical" 3ω method, that the velocity at some distance from the RT will be related to the second derivative of the in-phase response, or the first derivative of the out-of-phase response with respect to thermal wavelength. Formally,

$$c \propto \frac{\delta^2 X_{T2\omega}}{\delta\lambda^2} \qquad and \qquad c \propto \frac{\delta Y_{T2\omega}}{\delta\lambda} \tag{6.3}$$

where c is fluid velocity, $X_{T2\omega}$ is the in-phase temperature response, and $Y_{T2\omega}$ is the out-of-phase temperature response. The fluid velocity inside a microfluidic channel is generally considered to be parabolic [180]. It is stationary at the walls and is at its maximum in the centre of the channel. This can be represented by a piecewise parabola, shifted by the channel dimensions. This is,

$$\nu(r) = \begin{cases} 0 & x < 0 \\ A \cdot (r - \frac{R}{2})^2 - 2RA & 0 < r < 2R \\ 0 & x > 2R \end{cases} \tag{6.4}$$

Where $\nu(r)$ is the velocity as a function of distance r, R the half-width of the channel, and A the peak velocity in the channel. Following Equation 6.3 and 6.2, the expected response will have the a polynomial form of the order x^4 and x^3 for the in-phase and out-of-phase temperature response, respectively.

6.2.7 Membrane separated flow

The next hypothesis of this chapter is that the flow sensing 3ω RT will be capable of measuring fluid flow through membranes and solid dividers. In this case the solid divider symbolizes,

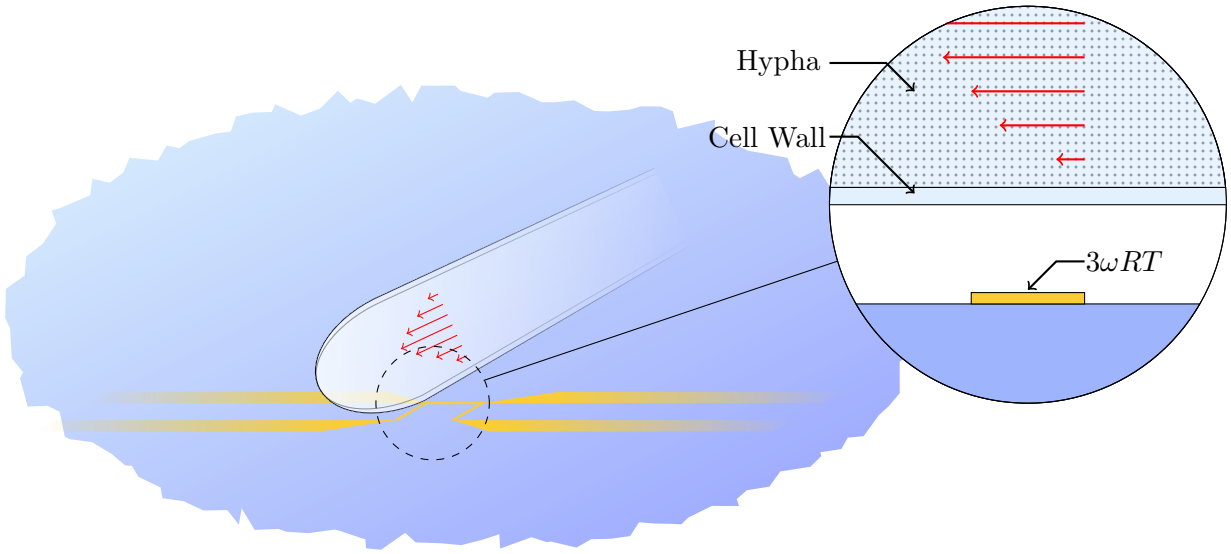

Figure 6.6: *An isometric illustration of a hypha growing across a 3ω RT. Mass transport inside of hypha is thought to be laminar [173]. This is represented by the red arrow annotations inside the hypha. (Inset) A simplified two-dimensional representation, of the hypha-RT system. A similar scale model of this can be fabricated in PDMS. Providing a controlled testing methodology.*

for example, the cell wall of a microorganism. This is desired as it will allow the system to be used as a mass flow sensor for filamentous biological systems such as hyphae. The extension (growth) of hyphae is driven by pressure inside the cell wall (turgor pressure) [92,173]. This internal pressure creates fluid transport inside the hypha [92,172,173,177]. Figure 6.6 shows an illustration of a filamentous species, in this case a fungal hypha, growing across a 3ω RT. Internal fluid velocity is indicated by the red arrow annotations. Inset in this illustration is a simplified two-dimensional representation of the same idea; a 3ω RT on the base of the device while a hypha grows above it. In each case, there is fluid flow separated from the RT by a solid membrane.

To test the 3ω methods ability to function as a mass transport sensor for hypha, a microfluidic chip, which mimics the simplified two-dimensional representation shown in Figure 6.6 Inset), was designed and fabricated. A schematic diagram of this chip is shown in Figure 6.7. This chip allowed the RT response to beyond membrane fluid flow to be characterised in isolation from other factors. While this was the specific goal of the experiment, other interesting aspects which could be tested include, the accuracy of using the thermal wavelength for

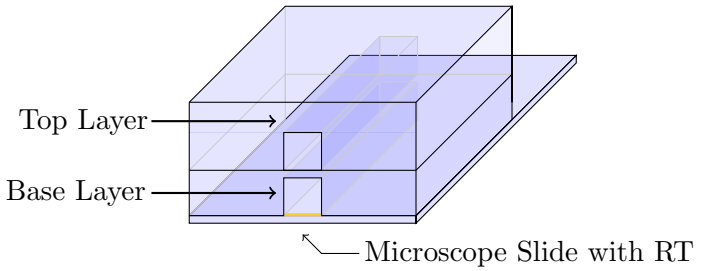

Figure 6.7: *A schematic cross-section diagram of the designed PDMS microfluidic chip. Two PDMS layers are stacked vertically to form two microfluidic channels, separated by a thin PDMS membrane. The base of the channel will be formed by a microscope slide.*

measurement, the systems response to bi-directional fluid flow, AC waves in varying media, and how the RT responds to different fluids.

The chip design consisted of two 100 μm $\times$ 100 μm channels, stacked vertically with a 20 μm PDMS membrane isolating the two channels. The base of the channel was formed by a microscope slide with an integrated 3ω RT. To fabricate this design, a combination of dry-film lithography, negative replica moulding, exclusion moulding, and plasma bonding was used, as described in the previous sections. In brief, the two microfluidic channels were formed by two different PDMS castings. The bottom layer consisted of a $100\mu m \times 100\mu m$ base channel, and a $20\mu m$ membrane. This structure was formed using the exclusion moulding process. The top channel consisted of the second $100\,\mu m \times 100\,\mu m$ microfluidic channel, and a thick PDMS roof greater than 1 mm thick in order to support external fluid connections. The top and bottom channels were manually aligned with each other and the RT, and bonded together with oxygen plasma (Tergeo, PIE Scientific). The sealing of the plasma bonds, tubing interfaces, and membrane were confirmed by infusing two colours of food dye into each of the channels, and visually confirming that no mixing or leaks occurred.

After the correct formation of the chip had been confirmed, the coloured food dye was exchanged for de-ionised (DI) water. In the same manner as Section 6.2.6, a control measurement was recorded with the channels full of stationary fluid. The measurement frequency range was calculated assuming homogenous media above the RT, i.e. a constant thermal

diffusivity. This is a simplification which warrants further discussion; thermal waves in this system will diffuse different lengths through the varying media i.e. thermal waves will travel through water–PDMS–water–PDMS rather than one medium alone. As such, the thermal wavelengths displayed will not accurately represent PDMS features.

A dual syringe pump (Harvard Apparatus, PHD 2000) was used to actuate fluid flow in the channels. The exit of the channel was connected through an external flow sensor (Elveflow, 1.5 - 80 $\mu l/min$) to calibrate the fluid flow rate. A range of flow rates were induced in the microfluidic channels in both simultaneous and exclusive combinations. The 3ω response was then recorded for each of these configurations. Specifically, for each volumetric flow rate a 3ω response was recorded for, both channels no-flow (the control), top channel flow only, bottom channel flow only, and both channels simultaneously.

6.3 Results and Discussion

The results to this experiment are divided into two sections: the single channel fluid velocity response, and the dual channel (through membrane). In the single channel velocity response a 3ω RT is integrated into a microfluidic channel, and its response to fluid velocity is examined. In the dual channel results, a 3ω RT is integrated into a vertically stacked microfluidic device, and the through membrane fluid velocity characteristics are assessed.

6.3.1 Single channel fluid velocity response

The fabricated microfluidic chip for single channel fluid velocity measurements can be seen in Figure 6.8. The channel was found to have sealed well and the RT was well placed in the centre of the channel, despite the manual alignment procedure. The magnitude of the 3ω response is proportional to the resistance (and indirectly length) of the RT. The lengths of the RT were designed such that the linear (parallel to flow), and serpentine RT should have had similar resistance values. However, due to orientation of the RT relative to flow, the convection response from the serpentine RT was much more sensitive to convection/fluid

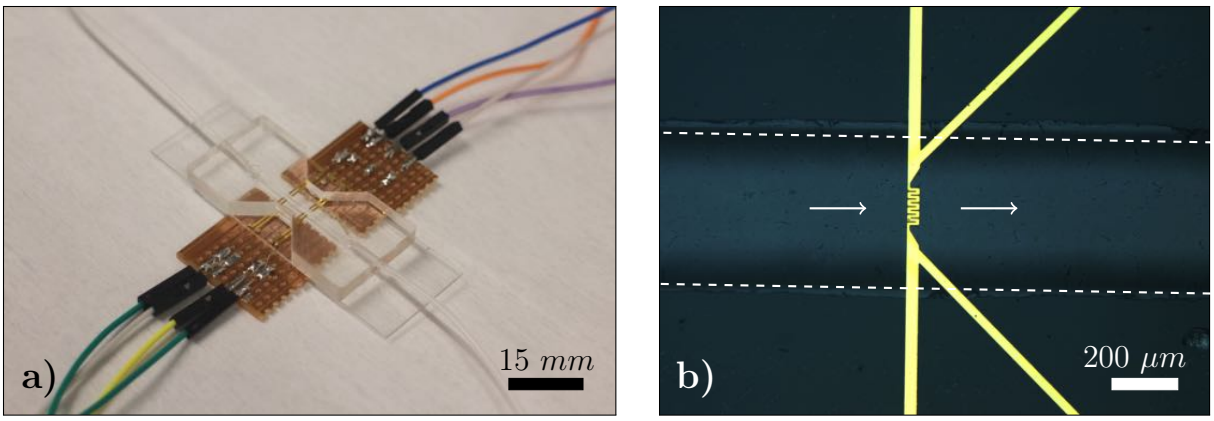

Figure 6.8: *The fabricated microfluidic chip for the pressure driven flow experiment.* **a)** *A photograph of the fabricated microfluidic chip. The electrical interfacing can also be seen, with two RT devices integrated in this particular chip. In this prototype device, the electrical connections were made with conductive epoxy, rather than the pogo-board.* **b)** *An optical micrograph of the gold RT sealed in a* $750\,\mu m \times 750\,\mu m$ *channel. The channel walls are shown with a dotted line annotation. The fluid flow direction is shown with the arrow annotations. A larger channel was initially used to simplify manual alignment. The RT was well centred in the middle of the channel.*

motion. As such, a serpentine RT design was initially used for the characterisation of the 3ω response.

With the serpentine RT connected, the stationary fluid control measurement was recorded, as well as the response for nine flow rates between $25\mu L/min$ and $400\mu L/min$. The unprocessed third harmonic response data is shown in Figure 6.9. The 3rd harmonic frequency responses are presented as complex magnitudes, X and Y[1] to stay consistent with lock-in amplifier and 3ω convention. The electrical frequency was converted to thermal wavelength using Equation 3.1 with an assumed constant thermal diffusivity. As demonstrated by Figure 6.9, the form of the response, notably the control, took the same form as classical 3ω measurements. Aligning with hypothesis, both the in and out-of-phase third harmonic response responded strongly to flow at large thermal wavelengths, and then converged on the control response as the thermal wavelength approached zero.

Figure 6.9 clearly demonstrates that the complex 3ω signals do deviate from the control as a function of the thermal wavelength. When the thermal wavelength was the same as or larger than the channel width, the entire laminar velocity profile was probed. This resulted in a

[1] $R \times sin(\omega t + \phi) = X \times cos(\phi) + iY sin(\phi)$

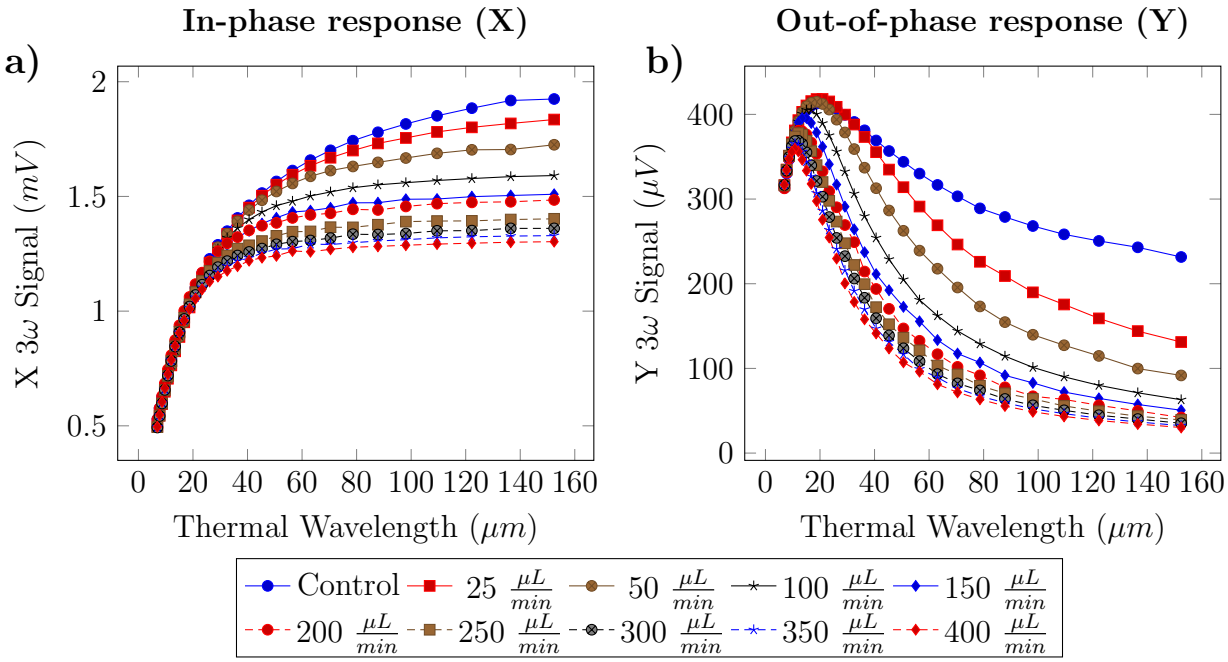

Figure 6.9: *A 3ω RT response inside a microfluidic channel.* **a)** *The in-phase results for 10 fluid velocities between 0 and 400 μL/min ,* **b)** *The out-of-phase results for 10 fluid velocities between 0 and 400 μL/min*

large convection signal change. As the thermal wavelength was decreased, the convection signal decreased in turn until it converged with the control response. This aligns with the hypothesis. By applying Equation 6.2, the control response is subtracted from the flow response, and variation of the X and Y signals can be seen more clearly. This result is shown in Figure 6.10.

The numerical gradient of this result was then taken with respect to thermal wavelength, following the axiom suggested by Equation 6.3. Figure 6.11 shows the calculated gradients, which if the hypothesis is correct, should be proportional to fluid velocity. While the supposed velocity curves shown do vaguely resemble the known parabolic shape of fluid in confined laminar flow, there is significant distortion in the result. It was hypothesized that the X and Y 3ω signal would respond proportionally to fluid flow in the channel. As such, the fluid velocity should be at its maximum value in the centre of the channel ($\lambda = 60\,\mu m$) irrespective of the volumetric flow rate. However, the gradient results appear to suggest that the maximum velocity point (the turning point) moves to lower thermal wavelengths as the volumetric flow rate increases. Observation of Figure 6.10 suggests that there is an underlying trend which

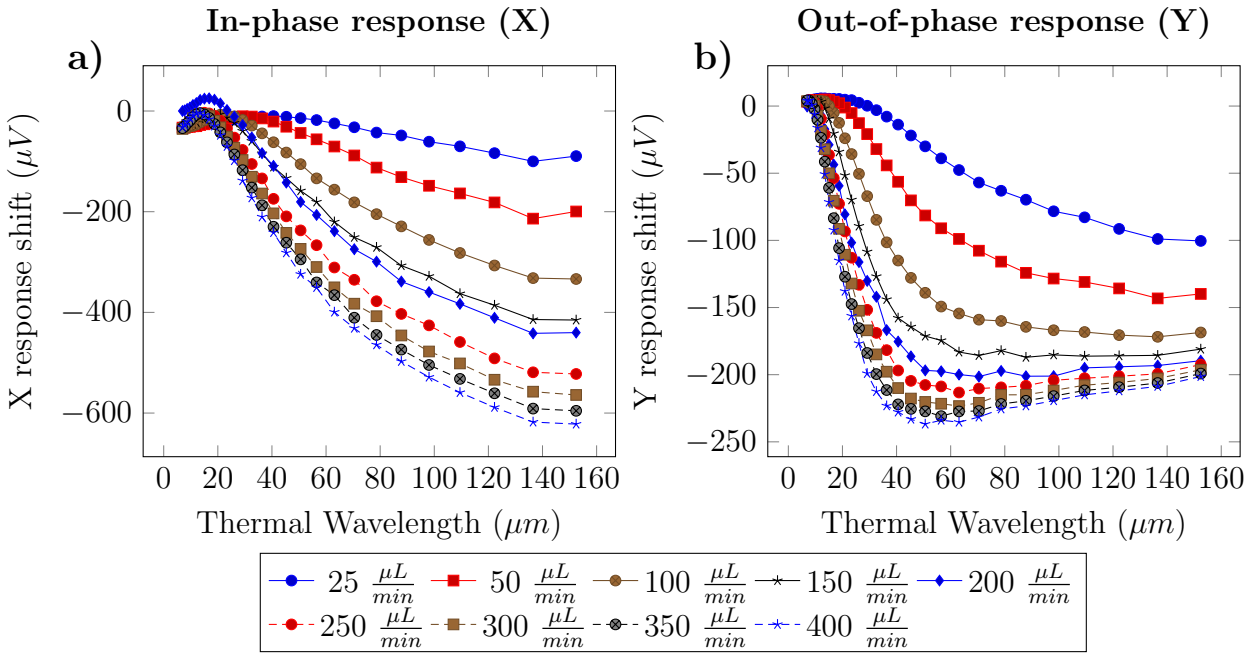

Figure 6.10: *The variation of the 3ω signal from the stationary fluid control* **a)** *The in-phase signal variation as a function of thermal wavelength.* **b)** *The out-of-phase signal variation as a function of thermal wavelength.*

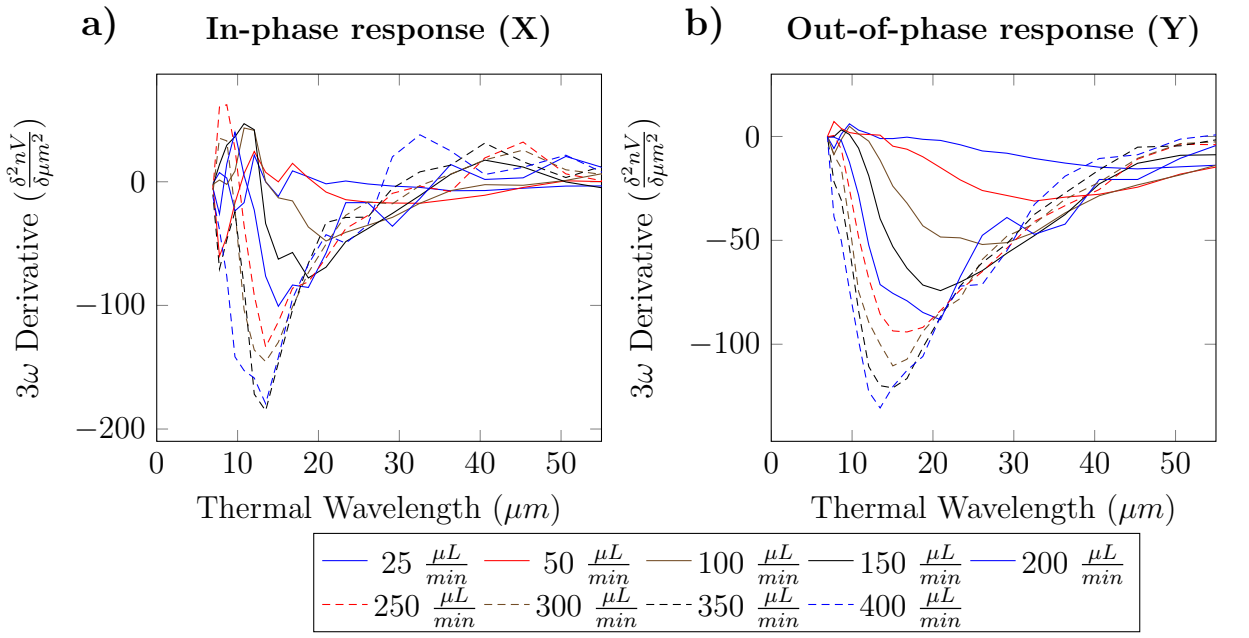

Figure 6.11: *Graphs showing the numerical gradients of the 3ω responses against thermal wavelength. These plots were generated using the approach suggested in Equation 6.3.* **a)** *Velocity profile extracted from the in-phase response. The result has similarities to the parabolic response theorised, however there is significant distortion.* **b)** *The fluid velocity extracted from the out-of-phase signal.*

describes the movement of this turning point or peak. More precisely, the response seems to saturate hyperbolically. The RT convection response to volumetric fluid flow seems to start as linear, but quickly approaches a limit to which the sensor is able to respond. Recent work by Wang et al. may be relevant to this [181]. In their work, the authors adapted the two-dimensional convection equation for use with AC thermal fields in laminar flow, and performed a scaling analysis. The major result from this work was that the temperature response scales with the ratio of the velocity gradient to thermal frequency ($\frac{c}{\omega}$, where c is the fluid velocity gradient, and ω is the thermal frequency). This result is instructive of the behaviour in the system described by this thesis. It states that the velocity gradient and thermal frequency must be comparable in size otherwise the temperature response will not be strongly linked to the rate of convection in the system.

One further source of distortion may arise from numerically deriving discretised signals [182]. When taking a numerical gradient, minuscule amounts of noise are amplified significantly in the calculated gradient. This is especially noticeable in the in-phase calculation, where the numerical gradient has been applied twice. The noise present in the frequency response appears to be inversely proportional to frequency i.e. there is a lower SNR at low measurement frequencies. This is also referred to as pink noise [183, 184]. This is probably due to the long time constants required for low frequency lock-in amplifier operation [185]. However it may also be inherent noise in this liquid system, for example low frequency flow variation from the stepper motor driven syringe pump. The optimal solution to this problem would be to increase the time constant of the lock-in amplifier, or average many frequency sweeps. These solutions are both relatively impractical, as they drastically increase the measurement time. Instead, a smoothing and fitting approach was used as a practical compromise. Due to the frequency dependence of the noise, many filtering approaches fail to adequately smooth the 3ω signal. The most effective filter found was the Savitzky-Golay filter, a digital filter representation of a piecewise polynomial fitting [186].

6.3.2 Linear resistance thermometer

In the previous section, a serpentine RT design was found to result in the largest 3ω signal, and have the strongest convection response. This serpentine shape is not ideal however, as its complicated shape could complicate interpretation of the results. As such, the extracted fluid velocity profile did not match the parabolic response as closely as initially hypothesised. This raised the issue that the serpentine RT shape may be effecting the response. To explore this idea further, two linear RTs were tested at comparable volumetric flow rates to the previous experiment. The two thermometers used were straight 3ω thin film RTs, orientated in the channel such that their length ran either parallel or perpendicular to fluid motion. These designs are shown in Figure 6.5.

The latter in particular is a more direct analogy to the serpentine shape used previously. The linear (parallel to flow) was tested first. Figure 6.12 shows the convection response curves for the linear (parallel to flow) RT at flow rates of 10, 20, 50, and 75 $\mu l/min$.

The convection response curves for the linear RTs have comparable shapes and corner frequencies to the serpentine RT (for reference, the serpentine RT results are shown in Figure 6.10). Relative to the stationary fluid control, the in-phase 3ω signal has an initial positive swing, before steadily decreasing. The out-of-phase response on the other hand exhibits a frequency dependent negative shift. Despite these similarities to the serpentine case however, there is a change in the exact shape of the response. Following Equation 6.3, the numerical gradient of the X and Y 3ω signal was computed, smoothed with a Savitzky-Golay filter, and is shown in Figure 6.13. As can be observed from this graph, the linear RT exhibited the same saturation and peak shifting issues as the serpentine thermometer. However, it is interesting to note that the peak shifting is now toward longer thermal wavelengths, which is the opposite trend to the one observed with the serpentine RT. Although these irregularities do seem to be linked to RT geometry, it would appear that simple geometry adjustments do not inherently solve the problem. As such, further work beyond experimental trial and error is necessary on this.

The linear (perpendicular to flow) RT design was also tested. The short length compared to

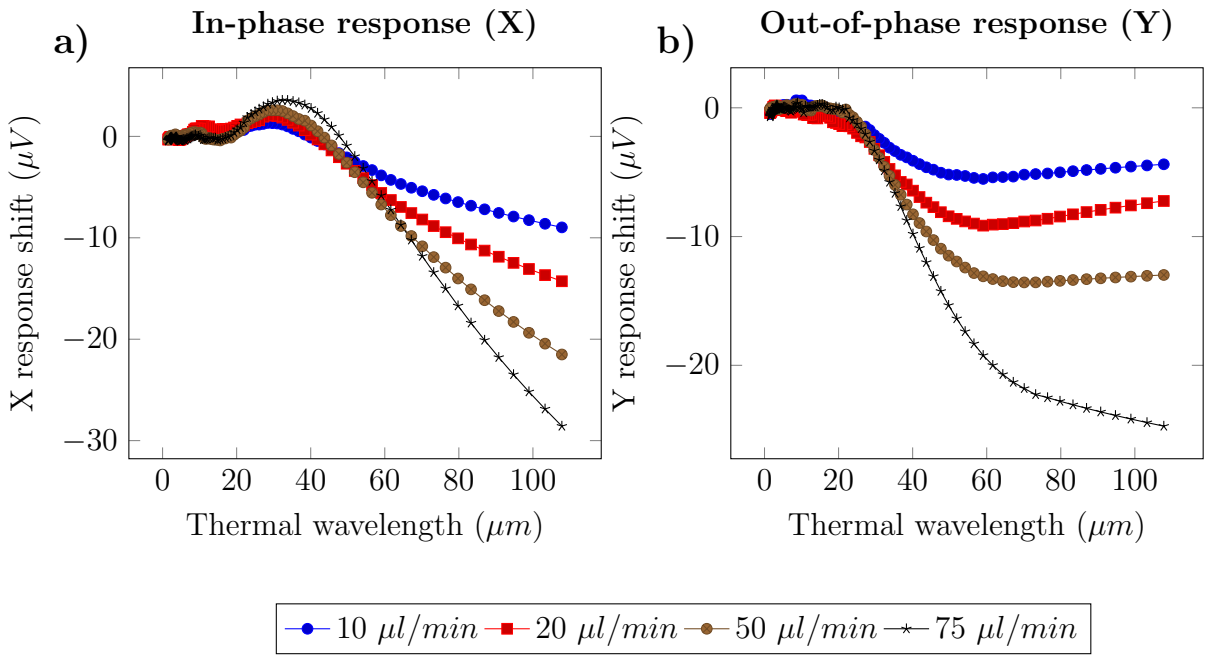

Figure 6.12: *Graphs showing the convection response for a linear (parallel to flow) RT.* **a)** *The in-phase response from the linear RT exposed to fluid motion. The result has a similar form to the serpentine RT.* **b)** *The complex out-of-phase response of a linear resistance thermometer exposed to fluid flow. There is a negative phase shift relative to the stationary fluid control proportional to the fluid velocity.*

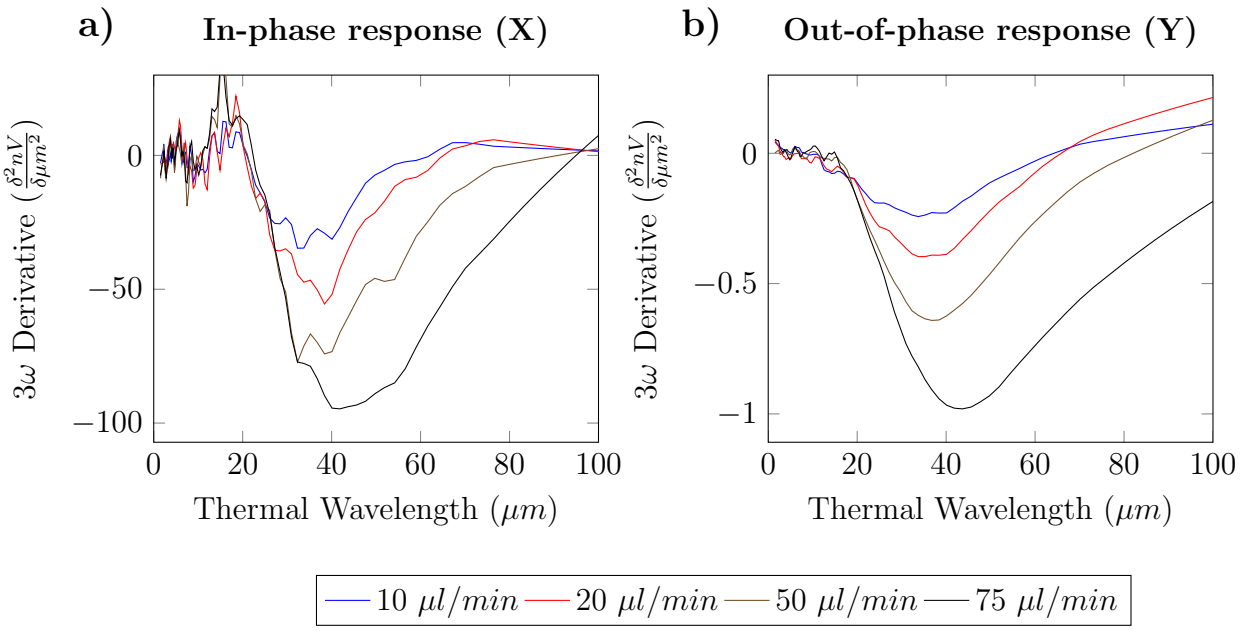

Figure 6.13: *Graphs showing the numerical gradient of the* 3ω *linear (parallel to flow) RT response to fluid flow. a) The second derivative of complex in-phase temperature response (X). b) The first derivative of the complex out-of-phase temperature response (Y).*

the other designs resulted in a smaller 3ω response, as previously discussed. The form of the flow response was directly comparable to that of the linear (parallel to flow) thermometer. For brevity, these results have been moved to Appendix C. After examining the effect of RT arrangement, the next issue was that of RT saturation and sensitivity. The work of Wang et al. showed that the temperature response becomes decoupled from convection if the probing thermal frequency and velocity gradient are substantially mismatched [181]. This creates a sensitivity ceiling, which relates to the channel dimensions via the thermal wavelength and maximum fluid velocity. This effect is most clearly demonstrated in Figure 6.9, where the curves cluster together as the flow rate increases. Using the serpentine RT, the lower limit of flow sensitivity was explored using a single $100\,\mu m \times 100\,\mu m$ microfluidic channel. The flow rate was lowered until the convection response was no longer distinguishable from the system noise. Following this, a range of flow rates above this value were tested. This approach should circumvent the issues regarding a sensitivity ceiling at higher flow rates. Further to this, a least-squares fitting approach was used to fit a polynomial function to the smoothed data. A fourth order polynomial function was fit to the data, and a regression coefficient greater than 0.99 was achieved for all flow rates. Following this, the analytical derivative

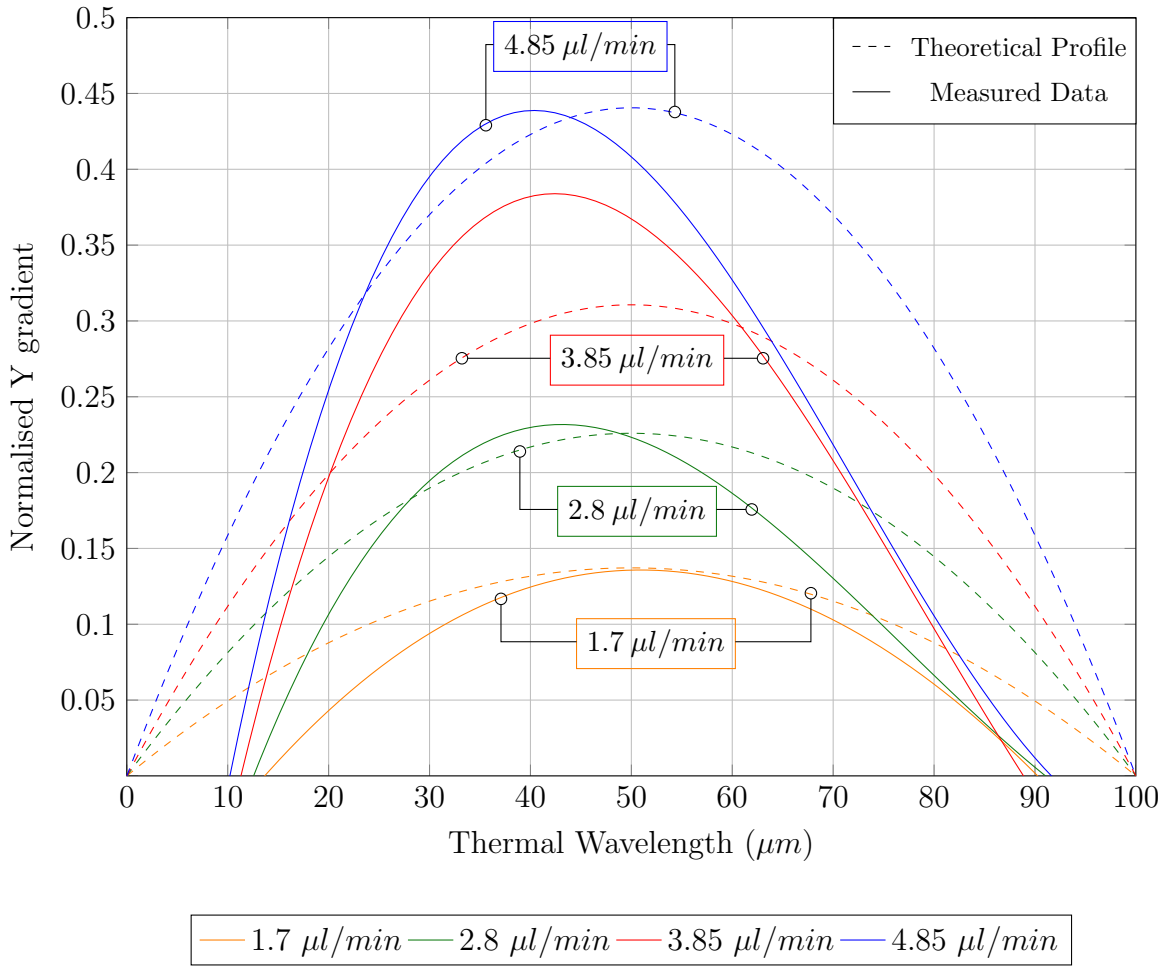

Figure 6.14: *A graph showing the analytical gradient of the 4th order polynomial fitted to the 3ω Y convection response. The theoretical Hagen-Poiseuille flow profile for the nominal channel dimensions are shown as dashed lines for comparison. The form of the response is much closer to the predicted parabola, however the measured parabolas are offset from the channel walls by* $\approx 10\,\mu m$.

of the fitted function could be taken. This circumvented the numerical gradient issue. The out-of-phase Y results of this procedure are shown in Figure 6.14. The theoretical velocity profile of fluid flow in a $100\,\mu m$ channel was calculated using the Hagen-Poiseuille solution to the Navier stokes equation, and is plotted alongside the measured results [187].

The minimum measurable volumetric flow rate found for the $100 \times 100\,\mu m$ channel was 1 $\mu l/min$, an average channel velocity of 1.6 mm/s. The calculated velocity response is a substantial improvement over the previous results. The Y convection response did not saturate, and the resulting velocity profile aligns more closely to the nominal microfluidic channel di-

mensions as a result. The measured response is offset from the walls by approximately 10 μm however. One explanation for this, is the height of the channel may actually be different than designed, due to deformation of shrinking of the PDMS cast, which could have occurred during the curing and bonding process. To verify this theory, an *in situ* measurement of channel height would be required.

6.3.3 Membrane separated flow

As has been demonstrated in the previous sections, a 3ω RT integrated into a microfluidic channel is capable of measuring fluid velocity, and probing flow profiles. For the purposes of biological applications in particular, it is desirable to further adapt the method into a mass transport measurement technique. This could be used, for example, for measuring internal fluid transport in filamentous micro-organisms. For this purpose, the RT needs to be able to measure fluid motion from behind a solid barrier or membrane, analogous in this case to a cell wall. To test this principle, a unique three layer PDMS chip was designed and fabricated. An illustration of how this chip is analogous to a filamentous micro-organism was previously presented in Figure 6.6. The fabricated device consisted of two vertically stacked $100\,\mu m \times 100\,\mu m$ microfluidic channels. The channels are isolated from each other by a thin 20 μm PDMS membrane. The completed device is shown in Figure 6.15 a). To confirm that the membrane remained intact after bonding, the channels were filled with two different colours of food dye. If the membrane was confirmed to be intact, the dye was then exchanged for DI water for flow measurements. Once experimentation was completed, the channel and membrane dimensions were inspected by cross-sectioning the chip with a scalpel and diamond scribe. An optical micrograph of this is shown in Figure 6.15 b).

Initially, it was not known if, and to what extent, a membrane would reduce the RTs response to fluid flow in the top. Due to this, a large initial flow rate of 0.1 ml/min in combination with the serpentine RT, was tested to maximise the response. In a $100\,\mu m \times 100\,\mu m$ channel 0.1 ml/min is equivalent to an average velocity of 16 cm/s, it is acknowledged that this flow would almost certainly saturate the RT convection response. Figure 6.16 shows the RT response for this high flow rate as the complex in-phase and out-of-phase responses (X

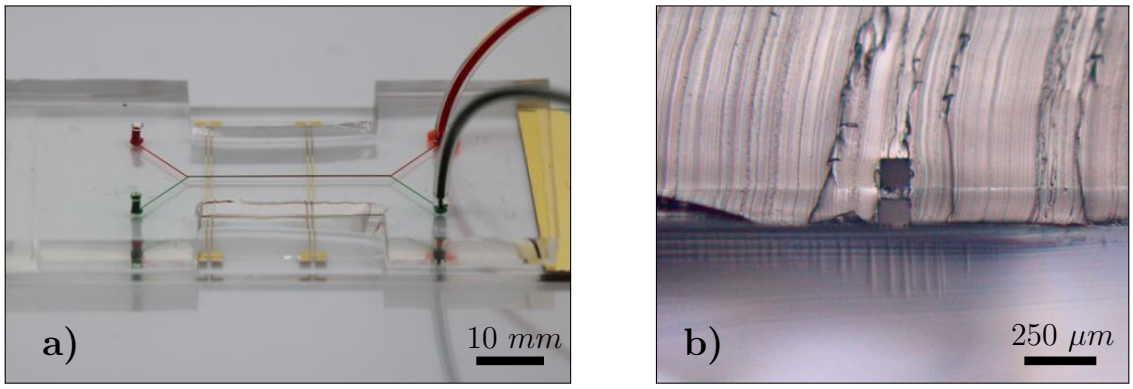

Figure 6.15: *The two-channel membrane chip designed as an analogy to a filamentous organisms in extension.* **a)** *The fabricated PDMS chip with external tubing attached to the inlets of the chip. Coloured food dye was infused into the separate channels to confirm that the isolation membrane was intact.* **b)** *Post measurement, the channel was cross-sectioned to inspect the channel and membrane dimensions, as well as the horizontal alignment of top and bottom channels.*

and Y). Due to the relatively complex nature of the channel, the results have been overlaid with a lengthwise schematic of the system. The pale blue sections represent areas inside the microfluidic channels, while the grey cross-hatching represents the PDMS membrane. The thermal wavelength is shown on the y axis, and the convection response is shown on the x axis such that it aligns with the direction of fluid motion (from left to right). For simplicity, the thermal wavelength was calculated assuming homogeneous material above the RT. This is an approximation and it should be noted that thermal waves will travel further in PDMS than in water [126].

The both in phase and out-of-phase temperature responded to fluid flow behind the membrane. In both cases the reaction to fluid velocity was between 3 and 5 times smaller in the top channel, than in the base channel. This was not entirely unanticipated, as the thermal diffusivity of PDMS is ≈ 750 times larger than water [126]. As a result, the thermal wavelength of a temperature wave in PDMS is 30 times longer than the same temperature wave in water (using Equation 3.1). As a result, thermal waves in the PDMS will travel comparatively longer distances, and as such reduce the heat flux density intersecting with the top channel. In addition, Figure 6.16 only represents the 3ω response in a two dimensional cross-section of the channel. In the real three-dimensional device, heat flux will travel in many directions

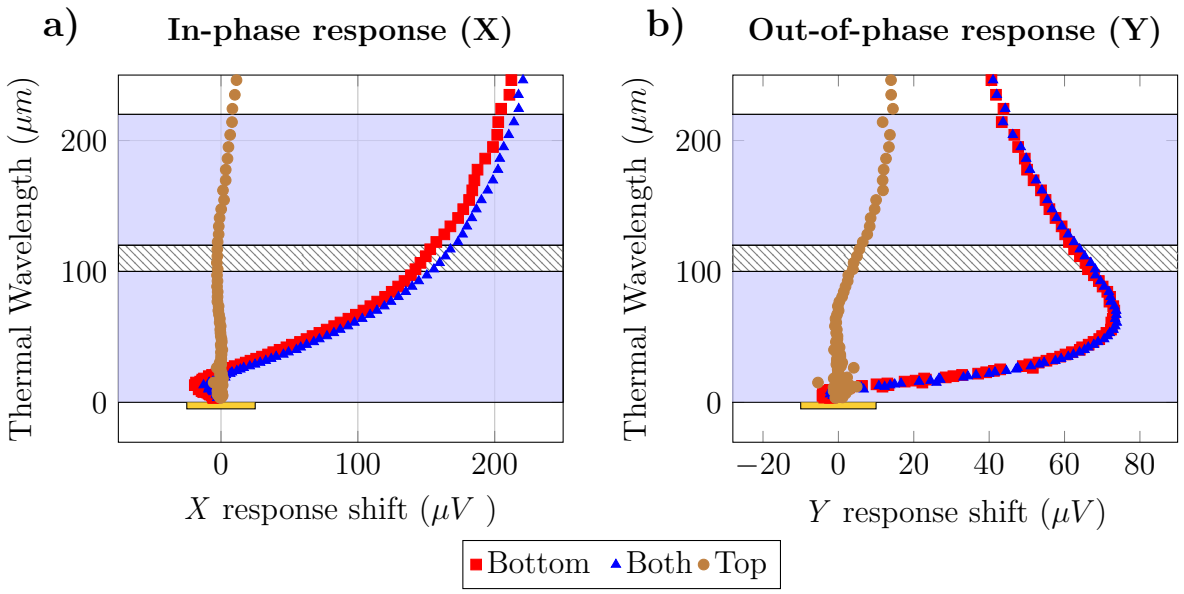

Figure 6.16: *The complex temperature response of the 3ω RT to a large flow rate in exclusive and simultaneous combinations of the flow in the two channels.* **a)** *The complex magnitude response to fluid flow both above and below the membrane.* **b)** *The complex phase response to fluid flow on both sides of the membrane. Note that the shape of the response does not perfectly align with the nominal physical dimensions of the channel.*

through the PDMS membrane. It is suspected that this will result in a smaller heat flux intersecting with the fluid flow in the top channel, and thus reduce the overall temperature response as a result. While this represents a limitation in the context of this chip, the cell wall of biological organisms will be much thinner, and differ in composition to PDMS.

What can also be observed from Figure 6.16 is that the signal shape did not align well with the nominal height of the channel ($100\,\mu m$) and membrane thickness ($20\,\mu m$). In both positions the signal shift occurred at a smaller thermal wavelength than expected. This indicates that more work on this is necessary to fully characterise this aspect of the system. The purpose of this experiment was to verify that a flow sensing 3ω RT could distinguish fluid motion from behind a membrane. This specifically has been confirmed by this initial experiment. In addition to confirming the suitability of the method, the experiment also identified that the out-of-phase 3ω voltage gives a more intuitive way to interpret result. As a consequence, in the following sections the out-of-phase results only are presented, while the in-phase results are included in Appendix B for comparison.

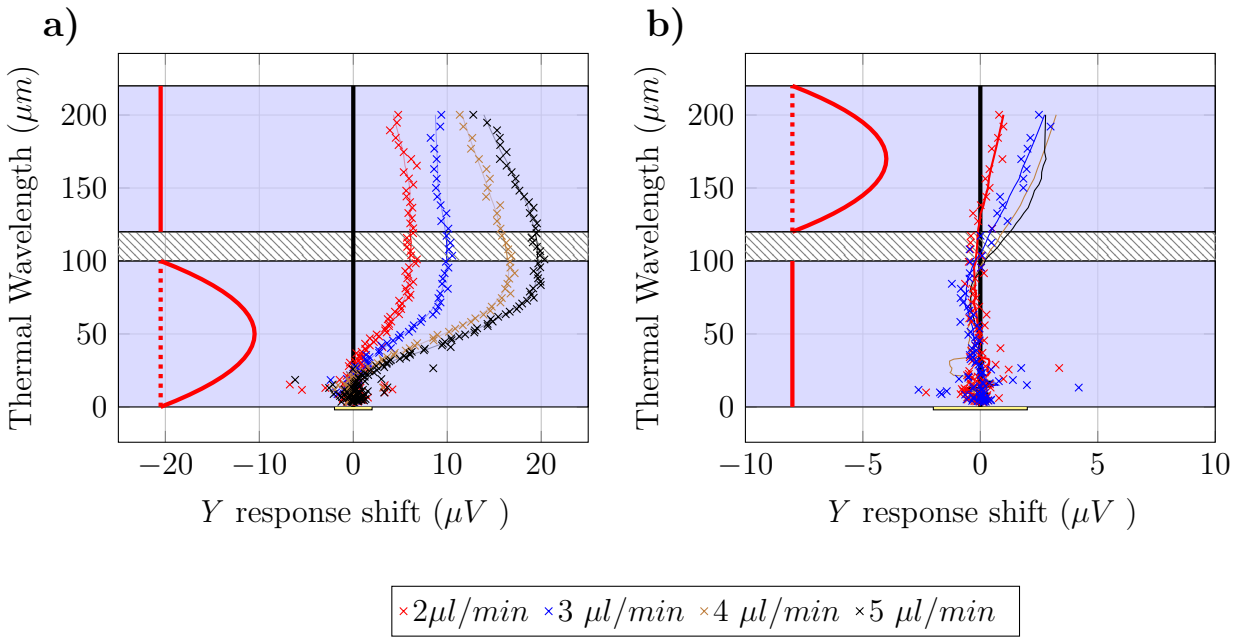

Figure 6.17: *Graphs showing the complex out-of-phase (Y) response to fluid flow in exclusive combinations of the channels.* **a)** *The complex out-of-phase response to 2, 3, 4 and 5 $\mu l/min$ fluid flow in the base channel only* **b)** *The complex out-of-phase response to 2,3,4 and 5 $\mu l/min$ fluid flow in the top channel only.*

Following this initial experiment, the flow rate was reduced until the minimum measurable value was found ($1\,\mu l/min$), and a range of flow rates increasing from this value were tested. In the last section it was noted that large flow rates shifted and distorted the measured peak velocity profile. It was proposed that this may be due to the response of the RT saturating. To observe if this was the case, multiple measurements well beneath the observed saturation ceiling were made, to test how they aligned with the physical dimensions of the channel. This approach was taken again in this chip to determine the spatial resolving capability with respect to the membrane, and top microfluidic channel. The flow results are presented overlaid with a schematic interpretation of the channel to assist the reader. In addition, a red parabola has been added to indicate the stabilised flow profile in the channel as a result of pressure driven flow, as well as indicating which channel is being actuated. Figure 6.17 shows this for four different volumetric flow rates which were applied in the indicated channel configurations.

As mentioned above, the minimum measurable flow rate for the current device was $1\,\mu l/min$, which corresponds to an average fluid velocity of $1.6\,mm/s$. In comparison, the fluid flow

inside of a hypha in extension can range from 1.8 $\mu m/s$ [92, 173, 188] to 70 $\mu m/s$ [189]. As such, the average velocity inside a hypha is currently between 20 and 300 times smaller than the minimum measurable flow on this chip. Even so, there are a range of changes which could be made to improve the RT sensitivity to this level. For example, the RT material in the current microfluidic chip is titanium-gold, which was found in Section 3.2.4.3 to have a greatly reduced temperature coefficient of resistivity in thin-film form. Gold was chosen as an RT material due to its wide use in literature and compatibility with microfabrication procedures [96–98]. Choosing another material with a higher resistivity and temperature coefficient of resistivity would substantially improve the sensitivity to flow. Platinum is one such material, which would be highly recommended for this purpose [190]. Platinum is a standard high performance (DC) resistance thermometer in industry. Further advances could be made through instrumentation adjustments, like increasing the gain of the differential amplifiers. The addition of an instrumentation amplifier that has a larger gain could potentially improve this and further lower the limit of detection.

Referring again to Figure 6.17, the corner frequencies of the low flow responses aligned closely with the physical channel dimensions. This was true, with the exception of the top channel flow response, which began at a thermal wavelength on the lower side of the membrane. This was most likely because the thermal wavelength was calculated based on the thermal diffusivity of water. Such an approach will compress PDMS features by 30 times in the two-dimensional representation shown. The RT Y response was 3-5 times smaller beyond the membrane than in the base channel, similar as to what was observed in the high flow rate experiment.

Also of interest is the response to simultaneous flow in the base and the top channel. In the example of a filamentous microorganism, this would correspond to an extension in external flow, either in or against the direction of growth. Figure 6.18 shows the RT response to fluid flow with both channels being actuated simultaneously at a flow rate of 3.5 $\mu l/min$. The simultaneous flow result is represented in red, and the equivalent exclusive responses are overlaid for comparison. This shows for one volumetric flow rate that the responses are approximately linearly separable i.e. that the simultaneous response can be obtained from

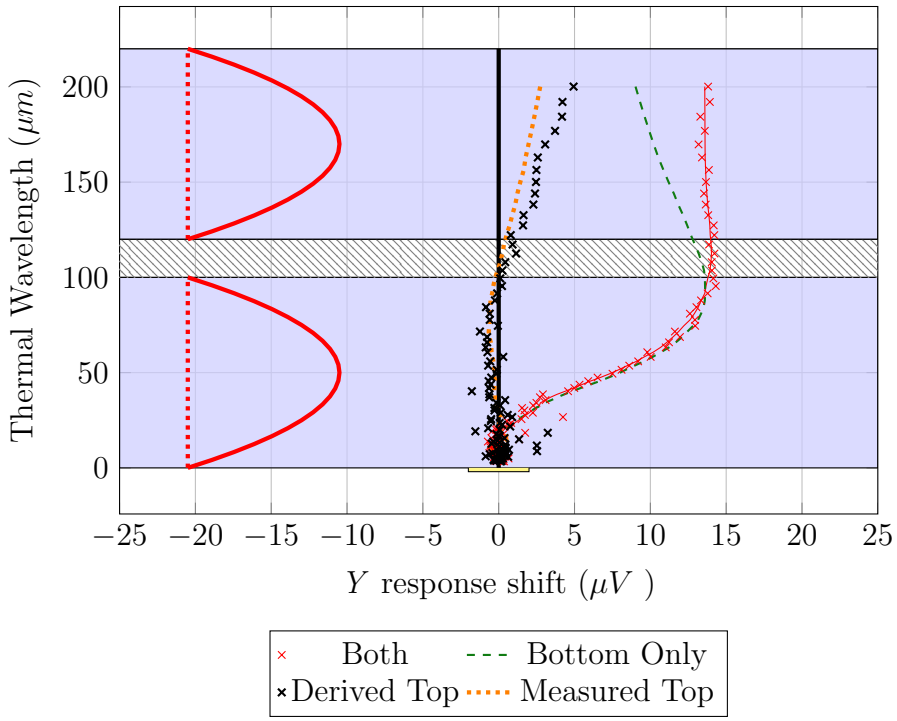

Figure 6.18: *A graph showing the RT out-of-phase response to fluid flow of* $3.5\mu l/min$ *in both channels simultaneously. The measured result is shown in red, while the equivalent exclusive responses are overlaid for comparison. Also shown is a "derived response" for the top channel, where the bottom channel result is subtracted from the simultaneous response. This demonstrates that the responses are approximately linearly separable.*

the summation of the exclusive flow measurements. There is a noticeable difference between the measured and derived response to fluid flow in the top channel. A possible explanation for this is that fluid flow in the base channel will further reduce the heat flux intersecting with the top channel, creating a reduced response.

One advantage of a 3ω based flow sensor over the established form of DC thermal flow sensors, is that only one element is required for operation. Conventional thermal flow sensors use two thermometers either side of a central heating element to measure fluid flow in both directions [81, 191]. The 3ω flow sensor in this work however is a single element device, which essentially measures the magnitude of convection away from the RT. Due to this, it should respond symmetrically to fluid motion irrespective of direction. With this in mind, the structure of this dual channel device allows an interesting special case to be studied: fluid motion in opposing directions. For this experiment equal flow rates were actuated through the top and bottom channel in opposing directions simultaneously and directly compared

to that of the unidirectional simultaneous response already studied. Although this seems like a niche case, this may also be relevant for biological organisms. In initial hypha-on-a-chip experiments [172, 177, 192, 193] the channel would typically be filled with static fluid which the hypha will extend through. For more realistic experiments in this area, external channel flow will be required to simulate more complex micro-environments. For example, to study the extension of hypha in a hypoxic environment, an external channel flow will be necessary to establish an oxygen gradient [194,195]. Given these potential uses, bi-directional flow response was measured at 4 $\mu l/min$ and results are shown in Figure 6.19. The data is presented in the same manner as in Figure 6.18. The red trace represents the flow response to bi-directional flow, while the other traces are overlaid for comparison. As can be observed, the sensor did respond to flow above the membrane, however the total out-of-phase signal shift was greatly diminished in this more complex case. While this is an interesting and exciting first result, this work currently lacks a sufficient theoretical framework to confidently interpret the response curve.

So far in this chapter, all flow experiments have been conducted with DI water as a fluid. However for fungal hypha, the liquid media will need to be Peptone Yeast Glucose broth (PYG broth) [196]. PYG is a liquid media which acts as a food source for the hypha [197]. While its mineral composition is precisely defined, the base solvent is mineral water. In general the dissolved minerals should not change the thermal properties significantly, and this was confirmed by repeating flow experiments with the PYG broth as the fluid media. Response curves for this experiment are included in Appendix E.

6.3.4 Interim model examination

In the discussion leading to Equation 6.3, it was noted that this approach was only an interim model to facilitate the exploration of this sensing concept. In this section, further analysis is provided and displayed as a un-solved problem which is requires a solution for the useful integration of the 3ω method as a spatially resolved microfluidic flow sensor. Simply, there is not currently a rigorously defined relation between the sensor response, thermal wavelength (equivalently thermal frequency), and fluid velocity.

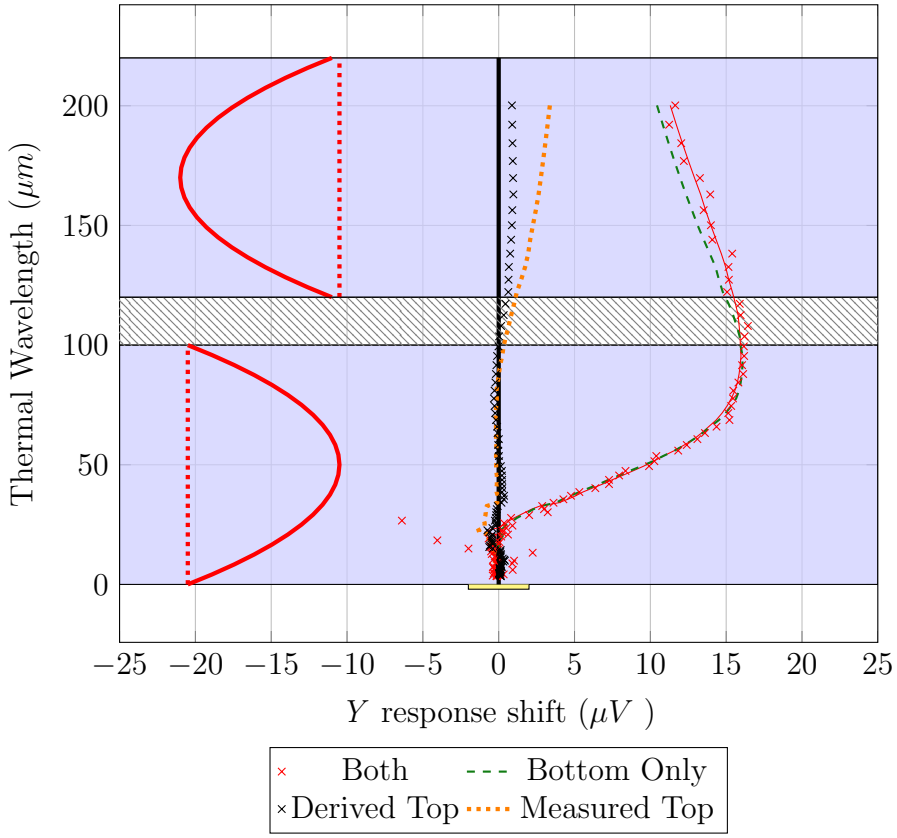

Figure 6.19: *Graph showing the 3ω out-of-phase response shift for dual fluid flow in opposing directions. While a distinguishable response can be observed, the magnitude is diminished compared to the uni-directional measurement shown in Figure 6.18.*

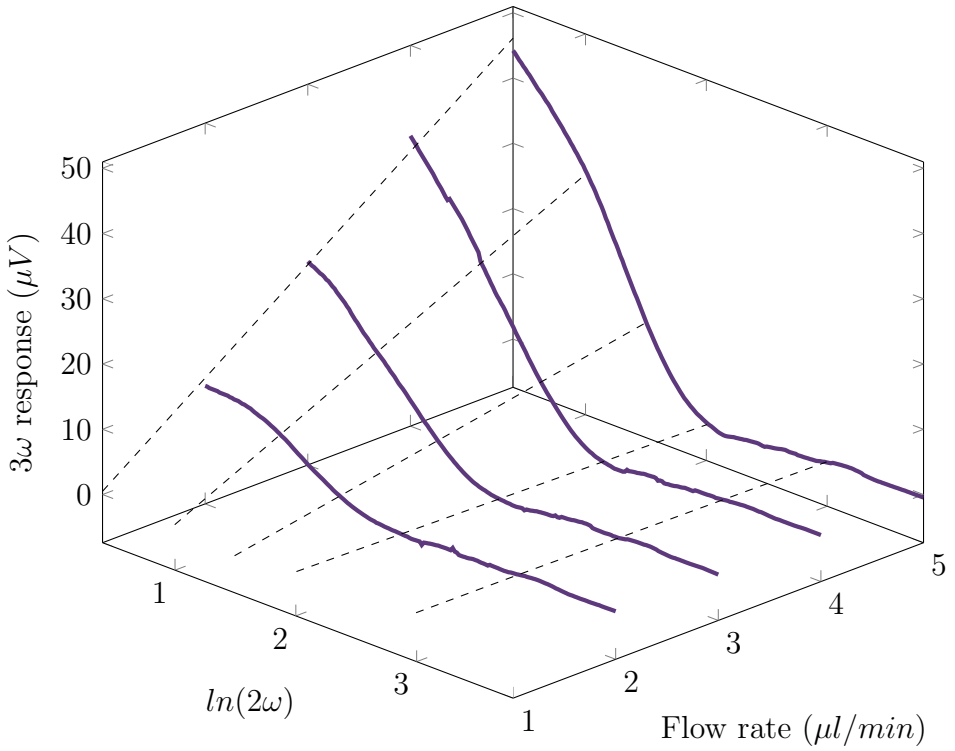

Figure 6.20: *The in-phase 3ω responses to volumetric flow in the 100 μm × 100 μm microfluidic channel (shown in blue) with linear regressions showing how the response varies with flow speed (shown as dashed lines).*

Figure 6.20 shows the in-phase 3ω response to four different fluid flow rates over a range of thermal frequencies.

The linear regressions, shown as dashed black lines in Figure 6.20, demonstrate that there is a linear relationship between fluid velocity and sensor response at any single constant thermal wavelength. This is exactly what would be expected for a parabolic velocity field. Given this, the unsolved problem in this work is a rigorous exploration of how the thermal frequency/thermal wavelength can be related to a specific height in the microfluidic channel. This may eventually result in a set of constraints or design requirements (such as fluid velocity range, RT geometry, and operating frequency) for a flow sensing 3ω RT.

Two approaches which could resolve this problem are finite element modelling, and analysis of the two-dimensional convection equation [181].

6.4 Conclusion

The primary goal of the work presented into this chapter was to investigate the use of a 3ω RT as a flow sensor with spatial resolving capabilities. In the process, the RTs ability to measure fluid flow from behind an internal membrane was also characterised for the first time.

The flow response of a serpentine and a linear 3ω RT were both investigated. Both were found to respond to fluid flow as a function of volumetric flow rate, and thermal wavelength. In particular the serpentine RT was found to respond to fluid flow behind a solid membrane. The lower detection limit with the current RT configuration was found to be 1 $\mu l/min$, corresponding to a average fluid velocity of 1.6 mm/s. This is currently not sensitive enough to measure the fluid transport inside a fungi or oomycete, and improvements to this system have been proposed. Future work in this area could include optimising the RT geometry for convection response, choosing a more sensitive RT material to maximise the temperature coefficient of resistivity, changing the base material to silicon to increase the 3ω voltage size, and using an instrumentation amplifier with gain > 1 to amplify the temperature signal.

This work may have applications as a method of assessing the internal mass transport in filamentous biological species. Especially interesting for this work are oomycetes and fungi, which can act as a plant pathogens. As such, the next and final chapter discusses the initial advances towards the culture and 3ω measurement of the oomycete *Achlya bisexualis* in a microfluidic channel, using the developed sensor.

Chapter 7

3ω measurements on filamentous microorganisms (*Achlya bisexualis*)

7.1 Introduction

In the previous chapter, the 3ω method was adapted into a novel integrated flow sensor for microfluidic systems. A scale model of a hyphal system was tested to establish the response to fluid flow beyond a solid membranes. In this chapter, this concept is extended by culturing the oomycete *Achlya bisexualis* in the microfluidic device, and recording the 3ω response while its hypha grew across the RT. The thermal response in the presence of *A. bisexualis* hyphae was measured using the 3ω method, constituting the first measurement of its kind on hyphae, live or otherwise. While only a proof-of-concept experiment, the work reported in this chapter demonstrates the potential of the 3ω method for use with filamentous biological microorganisms.

Oomycetes are plant pathogens, which have a filamentous structure similar to fungi. The study of oomycetes and fungi is of special interest in New Zealand, as the oomycete *Phytophthora agathidicida* is the cause for Kauri Dieback, a fatal disease for New Zealand Kauri (*Agathis australis*) trees [198]. Kauri trees are of national significance to New Zealand, with mature trees living to over 1000 years old and growing to over 50 metres tall [199–201]. One

particular example is the Kauri tree Tāne Mahuta, named after the Māori god of the forest and of birds. Tāne Mahuta is estimated to be more than 1250 years old. The tree itself is clear of Dieback, however nearby trees have contracted the disease [202]. Similar to Kauri Dieback, the fungal disease Myrtle Rust was also detected in May 2017, and since then 936 sites around NZ have reported the infection [203]. Caused by the fungus *Austropuccinia psidii*, this disease attacked plants in the myrtle family, which includes iconic New Zealand trees such as the Pōhutukawa, mānuka, and rātā [204].

The hyphal tip growth of fungi and oomycetes is a crucial part of their pathogenicity and is thought to be caused by a combination of turgor pressure (pressure internal to the cell membrane) [92] and mass flow within the hypha [173]. Current methods of measuring mass-flow in the hypha of oomycetes and fungi are contact methods, which involved injection of silicone oil or radioactive tracers [92,173]. These methods are both relatively invasive [92,173]. The establishment of a non-contact method of measuring mass-flow behind a membrane could provide novel insight into the flow mechanisms in filamentous biological species, and could help to develop new treatment strategies for major diseases like Kauri Dieback.

As a part of this thesis, it was theorised that the 3ω method could be configured as a non-contact tool for assessing the mass flow inside of hyphae, and to monitor the growth of oomycetes in hypha-on-a-chip systems. The latter, for example, is of interest in order to automate platforms of multiplexed protrusive force arrays [205]. These systems would greatly benefit from detection of an approaching hypha to the force measuring array, as it would reduce the time the hyphae would need to be exposed to microscopy illumination [172]. As such, the specific goals of this chapter were to determine whether the oomycete *A. bisexualis* would generate a 3ω response relative to a stationary fluid control, and to verify if the flow resolution was sufficient to investigate distinguish any fluid movement within the hypha.

7.2 Methods

7.2.1 Chip Modifications

To measure the 3ω response of a hypha, a single channel variant of the microfluidic chip used in Section 6.3.3 was fabricated. This chip consisted of the top layer (Refer to Figure 6.7) of the dual channel chip, manually aligned and bonded to a patterned microscope slide. This created a single $100\,\mu m \times 100\ \mu m$ microfluidic channel with an integrated 3ω RT at the base. To allow hypha to grow into the chip, the channel entrance was cored using a 4 mm biopsy punch to accommodate an agar plug which contained an oomycete culture. The PDMS channel was fabricated using negative replica moulding and bonded using oxygen plasma as described previously. Electrical connections to the chip were made using the spring loaded prototyping board introduced in Section 6.3.3.

7.2.2 Oomycete culturing

The biological work necessary to culture the oomycete and inoculate the modified microfluidic chip was assisted by Dr Ayelen Tayagui, a postdoctoral fellow with the Biomolecular Interaction Centre at the University of Canterbury. A full description of the process of culturing the oomycete can be found in literature [172], however a brief overview of the culture and inoculation process is provided here.

A. bisexualis was initially cultured on agar plates. Once the culture was well established, a sterilized $4\,mm$ biopsy punch was used to cut a plug of agar (with hypha) from the culture. The mycelial plug was taken from the outer edge of the organism, as the hyphae at the edge were in extension (actively growing outwards). Meanwhile, the microfluidic channel was back-filled with PYG broth, so that the mycelial plug could be inserted into the 4 mm inlet to the chip. An inverted bright field microscope (T5-100, Nikon) was used to align the hyphae in the same direction and focal plane as the channel entrance. Hyphae took an average of 30 minutes to resume growing after being cut from the culture, which was comparable to

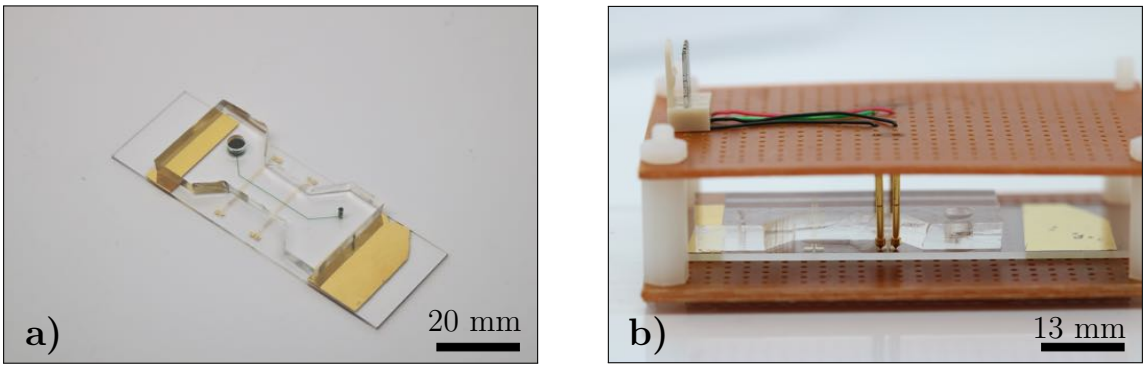

Figure 7.1: *Photographs of the modified microfluidic chip for use with the oomycete.* **a)** *The modified chip used to characterise the* 3ω *response of* A. bisexualis *hyphae. The channel entrance was cored to 4 mm so that a mycelial plug could be inserted.* **b)** *The modified chip mounted in the electrical interfacing cradle.*

previous work [172].

In this experiment, two 3ω measurements were taken. The first was a control measurement taken with the channel full of PYG broth. The second measurement was taken with the hypha on top of the RT. After the measurement was complete, the hypha was confirmed to be alive, and still in extension, using the inverted microscope.

7.3 Results and discussion

A photograph of the modified chip and electrical connection mechanism is shown in Figure 7.1. Fabrication methods developed and described in Chapter 6 were easily adapted to enable oomycete maintenance on chip. Coring of the existing inlets was sufficient to facilitate reliable and sterile manual loading of mycelial plugs. Growth media could be added using standard pipettes.

The culturing and growth process of a bundle of hyphae on the device is shown in Figure 7.2 as a series of optical micrographs. In this example, the hyphae took approximately 48 hours to reach the RT from the inlet. This corresponded to an average growth rate of $3.83\,\mu m/min$. Published results for the growth rate of *A. bisexualis* in hypha-on-a-chip devices report a growth rate of $6 \pm 1.6\,\mu m/min$ [172]. The growth rate of the hyphae on this chip was

1.4 standard deviations away from this reported value. The slower growth rate may have been due increased exposure to light, due to the currently unrefined electrical connection mechanism. The culturing time was comparatively long because the device had been modified from the previous flow based microfluidic chip. Ideally the devices total length would be closer to 0.5 mm, locating the RT much closer to the inlet and resulting in a culturing time of 35 min.

Initially, it was not known if the hypha would survive the probing heat flux from the RT [206]. Due to this, three increasing measurements at 9, 14, and 17 mA heating current were taken to progressively measure the thermal response. In the first experiments, a bundle of hyphae were grown though the channel at once to measure the accumulated effect of the oomycete biomass. Figure 7.3 shows both the in-phase and out-of-phase 3ω voltage of the hyphae compared to the control at 17 mA heating current. The heating currents did not visibly effect hypha growth, and so the largest signal measured is presented here for clarity. A semi-log X-axis was used in this case, to more clearly display differences between the control and response in the presence of hyphae.

After the measurement, the hyphae were confirmed to still be alive and growing by inspection under a microscope. If hypha continued to grow at a growth rate comparable to that prior to the 3ω measurement it was determined that the hyphae were unaffected by the exposure to heat. Figure 7.3 shows that both the X and Y response changed while the hyphae grew across the RT. The in-phase response experienced a slope change and the out-of-phase response showed an overall change in magnitude. This means that the thermal *conduction* in the system had changed with the hyphae on top of the RT. This suggests that the static PYG Broth measurement was not an adequate control. The cell wall of the hyphae represents an uncontrolled for thermal conduction mechanism in the channel. This, coupled with the fact that the hyphae are completely filling the channel and are in intimate thermal contact with the RT, creates a situation where the empty channel control is no longer relevant.

This conclusion suggests that Equation 6.2 cannot be applied to extract the convection response from the hyphae bundle. However, the thermal conductivity of live hypha can still be extracted, and this alone is an interesting property, and could warrant future research. Other

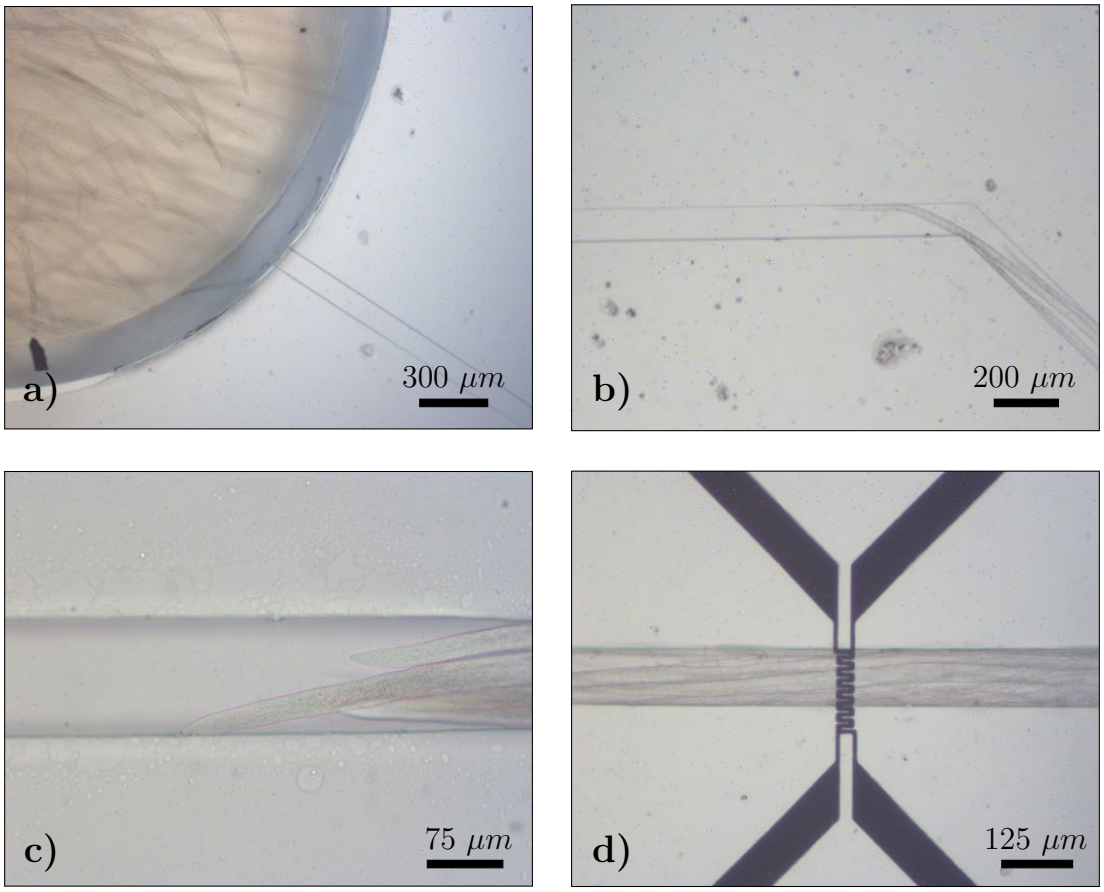

Figure 7.2: *A series of optical micrographs showing the growth of the oomycete* A. bisexualis *through the modified microfluidic device.* **a)** *The hyphal plug inserted into the chip and aligned with the channel entrance. Hyphae took an average of 30 minutes to recover from being cut from the agar culture before resuming extension.* **b)** *Channel bed at 23 hours post-innoculation. The visible hyphae had extended approximately* 5*mm at this point.* **c)** *The main channel straight 48 hours post-translational Multiple hyphae grew through the channel stacked horizontally and vertically as a "plug".* **d)** *48 hours post-innoculation. The hyphal plug can be seen covering the RT integrated into the base of the channel.*

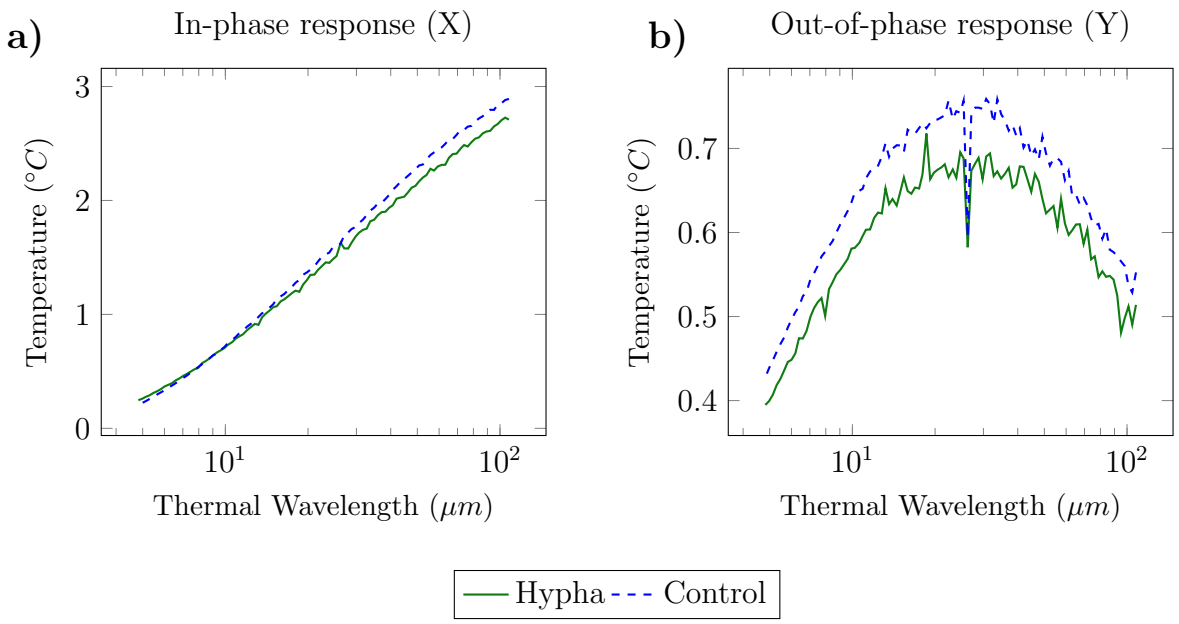

Figure 7.3: *The 3ω magnitude and phase response to hypha growing in the channel compared to the media filled control. A semi-log x-axis is used to show the difference between the measurement and control.* **a)** *The 3ω magnitude response shows an overall change in slope, and therefore conduction properties in the system.* **b)** *The phase response of the hypha compared to the static media control. The phase experiences a constant offset from the control measurement.*

researchers have correlated the thermal conductivity of single cells and cell sheets with cell viability and disease state [89, 90], and similar ideas can be applied to filamentous biological microorganisms, which may hold a link to their pathogenicity. The cell wall of oomycetes is generally composed of cellulose, and varying $\beta - Glucans$ polymers [207]. While the thermal properties of cellulose are well understood, the cellulose/$\beta - Glucans$ composites which make up the cell wall are less so. Using the classical slope 3ω method, discussed in Chapter 3, the thermal conductivity of the control and the hyphae measurement can be calculated. The thermal conductivity measured by the empty channel control was $0.7156\, W/m - K$. After the hyphae grew on top of the RT, a reduction of $0.223\, W/m - K$ occurred, a 30% shift from the control. Park et al observed an approximately 10% shift in their work on single biological cells. While these numbers are interesting, the serpentine RT geometry invalidates the result, because the classical 3ω method is based on a line source and cylindrical heat flow model [6, 95]. Repetition with a standard linear RT is needed. This may yield more reliable, and relevant, results.

Now returning to the convection response. In order to measure internal hyphal mass transport, a control which better captures the conduction response is required. An ideal control would involve the hypha being stationary on top of the RT. One way to achieve this is would be to chemically fix the hypha once it had grown over the RT. There are fixative solutions available which can achieve this. For *A. bisexualis*, the known fixative solution is Formaldehyde based [208]. This fixative functions by cross-linking the hypha cytoskeleton and thus stopping its growth [208]. This may not be an ideal control either however, because the thermal conductivity of polymers changes with cross-linking [209], and if this is the case for *A. bisexualis* hypha, a cross-linked cytoskeleton may also be an inadequate control. To overcome this, a potential alternative fixative solution, such as sodium cyanide, could be used [173]. Cyanide based fixative solutions are thought to stop internal mass transport via respiratory inhibition [173, 210]. For example, Lew et al. used cyanide fixative to successfully fix the hyphae of the fungus *Neurospora crassa* [173]. Although this fixative may not be suitable for *A. bisexualis*, respiratory inhibition may still provide an alternative control approach for future experiments with other filamentous microorganisms.

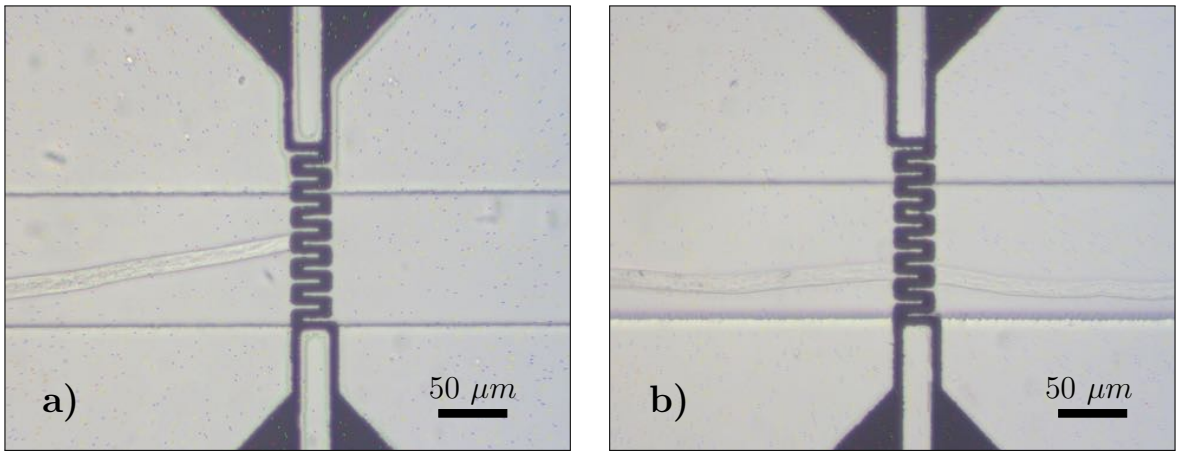

Figure 7.4: *Composite (focus stacked) optical micrographs showing a single hypha growing across the RT.* **a)** *The tip of the hypha just crossing the RT.* **b)** *Several minutes later, the hypha has completely grown across the RT.*

After recording the 3ω response of hyphae bundles, the experiment was adjusted with the goal of measuring a single hypha in extension. Figure 7.4 shows two focus composite images of an individual hypha growing across a RT. Focus composites were generated by taking multiple images at different focal lengths, these could be combined into a single image using software (Zerene Stacker).

The 3ω response of the single hypha and the empty channel control are shown in Figure 7.5. As illustrated by Figure 7.5, the single hypha result was very close to the control. No definitive conclusions could be drawn from this result. There was however a slight observable shift in out-of-phase voltage, which occurred over approximately the known width of the hypha. While the magnitude of the shift was close to the noise floor of the measurement, it does warrant future work in this area. To further support this observation, a detailed view of observed shift is displayed in the inset of Figure 7.5 b). This experiment was then repeated three times, however these results showed similar or even less distinct results. In general, the hyphal convection response was not anticipated to be large, given the results shown in the previous chapter. Literature values for internal hypha fluid velocities are on the order of $\sim 5\,\mu m/s$ [173]. This value is currently well out of range of the 3ω flow sensor. Furthermore, in this proof of concept experiment, only a small fraction of the RT width was covered by the individual hypha. This fact will have also limited the size of the response. It should be noted

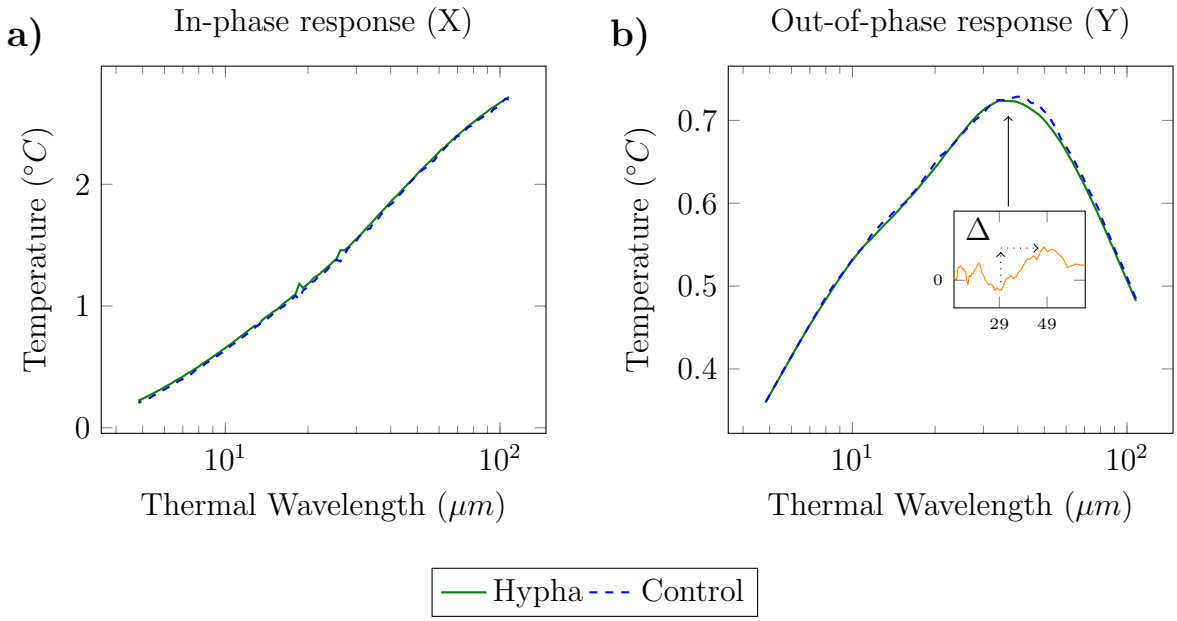

Figure 7.5: *The 3ω response to a single hypha on top of a serpentine RT.* **a)** *The in-phase temperature response (X) for a single hypha, and the empty channel control. There is no discernible difference between the control and the single hypha response.* **b)** *The out-of-phase temperature response to a single hypha growing across the RT. While it mostly appears that there is no response, a small variation can be observed which approximately matches the width of the hypha. Inset) The phase shift from the hypha measurement. The response is* $\sim 12\,m°C$ *tall and varies over* $\sim 20\,\mu m$*; approximately the width of the recorded hypha.*

at this point that *A. bisexualis* hyphae with widths greater than $50\,\mu m$ have been regularly observed in related work [172]. As such, more work with an RT of increased sensitivity and optimised microfluidic setup could yet provide clearer results, and be able to conclusively judge the suitability of this technique for the proposed application.

In the previous chapter, additional improvements to the RT and measurement methodology were discussed which are expected to improve the sensitivity of fluid flow based experiments. These same ideas would also be beneficial for the mass flow measurement introduced in this chapter. As mentioned, changing the RT material to platinum will improve the overall sensitivity of the RT to temperature. Platinum is one of the best performing resistance thermometers in industry, albeit at a prohibitive cost. Nickel-chromium is another material with a high resistivity, and high temperature coefficient of resistivity. This was tested as an alternative RT material, however it performed poorly in thin film form. This is briefly shown in Appendix F. The serpentine RT design could also be improved using an alternative, higher

resolution, patterning procedure, such as Electron Beam Lithography (EBL) [160]. This technique could be used to make smaller serpentine RTs to artificially increase the length of the RT, relative to the microfluidic channel width. The microfluidic chip in this experiment could also be improved. A constricting microfluidic channel, already used in literature [172, 192], could guide hypha such that they repeatably cover the active RT surface.

One of the main benefits of a 3ω-based technique for these filamentous microorganisms, is that it is a non-contact technique. At present however, the hyphae are in direct contact with the surface of the RT. In future, the addition of an electrical insulation layer will be necessary. If PDMS microfluidics are to be used, the material used for the insulation layer needs to be compatible with plasma bonding. Interestingly, this additional layer could actually improve sensitivity to fluid flow as it will lower the thermal frequencies needed to probe the channel, thus allowing fluid flow near the wall to be probed [181].

7.4 Conclusion

In this chapter, the oomycete *A. bisexualis* was cultured and grown through a modified microfluidic channel as a proof of concept experiment for use of the 3ω method with filamentous microorganisms. A 3ω flow sensing RT was used to measure the thermal response of both bundles of multiple hyphae, and an individual hypha. As the first measurement of oomycetes, alive or otherwise by the 3ω method, the results presented in this chapter support the usefulness of the method for use with filamentous biological species. While only oomycetes were tested, the measurement of mass transfer is also topical for other biological systems such as pollen tubes [93], root tips, and hairs [94]. It was found that clusters of live hyphae were clearly identifiable from an empty channel control, however no mass transport parameters were able to be identified. Given the current setup, the response of a single hypha response was indistinguishable from the control measurement. Small variations in the Y response could be observed, however they were too close to the noise floor of the measurement to be reliable. For future work, the sensitivity of the RT needs to be increased to improve measurement confidence.

In the next chapter, the conclusions and contributions of this thesis are discussed, and potential future work based on this is suggested.

Chapter 8

Conclusions and Future work

8.1 Conclusions

In this thesis, the 3ω method was used for a variety of purposes. From its most popular use as a pure thermal conductivity measurement technique, through its adjustment to measure thin films, and finally to a new application in the field of microfluidics. The simplicity, accessibility, and flexibility of the general 3ω method makes it an extremely adaptable technique across many fields.

In Chapters 2, the relevant literature to the fields of thermal meta-materials and microfluidics were summarised. In Chapter 3, the steps needed to establish and calibrate the 3ω method at the University of Canterbury, New Zealand, were described.

In Chapter 4, the thermal conductivity of several packed nanoparticle materials was investigated. The thermal conductivity of a 1/2/3 blend of SiO_2/Al_2O_3/Carbon nanoparticles was found to be $0.039\,W/m-K$. This measurement was substantially higher than those reported in literature. It was found that the material increased in thermal conductivity by 60-70% over the course of approximately one month exposed to room humidity. In Chapter 5, a $1\,\mu m$ thick Hybrid Bragg stack, composed of $22\,nm$ diameter SiO_2 nanoparticles and PMMA was measured with the differential 3ω method. The thermal conductivity of this structure varied between 0.023 and $0.055\,W/m-K$ due to the variability in the fabrication procedure. The average value was $0.043 \pm 0.014 \;\; W/m-K$. The composition of the Hybrid Bragg stack structures varied substantially due to the relatively uncontrolled nature of layer-by-layer spin coating deposition technique. These results show that nanoparticle based thermal insulation materials can produce large thermal conductivity reductions compared to the bulk constituent materials. However there are outstanding durability issues with this class of materials which are not fully understood. More experimental work is needed in this area to fully understand, and counteract, these factors.

Chapter 6 explored a modified flow sensing 3ω RT. The RT was integrated into a novel microfluidic device, and used to demonstrate the sensing of fluid velocities as low as $1.6\,mm/s$, measure fluid flow with spacial resolution, and sense fluid flow through membranes and other solid dividers. This system has a wide range of applicability from pure flow sensing

applications, to the assay of micro-organisms. Of particular interest is the assay of filamentous microorganisms. This was further discussed in Chapter 7, where the growth and thermal properties of the oomycete *Achlya bisexualis* was measured in a microfluidic/3ω system. The thermal response of the hypha was found to be distinct from a static fluid control, however more repetition is necessary for further conclusions to be drawn.

8.2 Future work

The packed nanoparticle materials did produce very low thermal conductivities for solid state materials, however they did degrade substantially over time. Future work in this area could endeavour to isolate and counter act this degradation through the following methods.

- In-vacuum measurement of pressed nanoparticle materials.
- Humidity chamber measurements of pressed nanoparticle materials.
- Encapsulation methods to preserve high thermal performance.
- Nanoparticle surface modification.

The Hybrid Bragg Stack created a thermal conductivity reduction of between 3 and 10 times when compared to the constituent materials. While this is promising, the deposition method was too uncontrolled to reliably correlate the superlattice periodicity and thermal insulation performance. In the future, if the reliability of the fabrication could be improved upon, then a more in depth study into the structure could be undertaken. Some ways to achieve this control are listed below.

- Investigate alternative deposition techniques such as electrophoretic deposition [169], or self-assembly [170]. Alternatively the existing technique could be refined through automation.
- Investigate potential correlation between superlattice periodicity, nanoparticle diameter and thermal conductivity.

- Investigate infrared optical bandgap properties, and if this could also be utilised to reduce thermal conductivity.

In Chapter 6, a 3ω resistance thermometer was modified into a flow sensing element with some spacial resolving capabilities. The performance can be better characterised, and also improved on through the following.

- Investigate the 3ω convection response in electro-osmotic flow, and compare to finite element modelling
- Improve minimum measurable velocity via resistance thermometer adjustments, signal amplification, and changing support material to silicon.
- Add electrical insulation layer to resistance thermometer.

Finally, Chapter 7 used the 3ω method to measure the thermal response of live *A. bisexualis* hyphae. This provided promising first results, but more repetition is needed for conclusions to be drawn. Future work on this system will cover the following.

- Adjust the microfluidic channel geometry and resistance thermometer orientation to allow for the repeatable measurement of a single hypha.
- Repeat thermal conductivity measurements of *A. bisexualis* and test correlation with environmental conditions, and hypha growth.

Chapter 9

Bibliography

[1] M. N. Luckyanova, J. Garg, K. Esfarjani, A. Jandl, M. T. Bulsara, A. J. Schmidt, A. J. Minnich, S. Chen, M. S. Dresselhaus, Z. Ren, E. A. Fitzgerald, and G. Chen, "Coherent phonon heat conduction in superlattices," *Science*, vol. 338, no. 6109, pp. 936–939, 2012.

[2] A. Balandin and K. L. Wang, "Significant decrease of the lattice thermal conductivity due to phonon confinement in a free-standing semiconductor quantum well," *Physical Review B*, vol. 58, no. 3, p. 1544, 1998.

[3] B. Li, H. Wang, Y. Kawakita, Q. Zhang, M. Feygenson, H. Yu, D. Wu, K. Ohara, T. Kikuchi, K. Shibata *et al.*, "Liquid-like thermal conduction in intercalated layered crystalline solids," *Nature Materials*, vol. 17, no. 3, p. 226, 2018.

[4] H. Zhu, J. Yi, M.-Y. Li, J. Xiao, L. Zhang, C.-W. Yang, R. A. Kaindl, L.-J. Li, Y. Wang, and X. Zhang, "Observation of chiral phonons," *Science*, vol. 359, no. 6375, pp. 579–582, 2018.

[5] P. Ben-Abdallah and S.-A. Biehs, "Near-field thermal transistor," *Physical Review Letters*, vol. 112, no. 4, p. 044301, 2014.

[6] D. G. Cahill, "Thermal conductivity measurement from 30 to 750K: the 3ω method," *Review of Scientific Instruments*, vol. 61, no. 2, pp. 802–808, 1990.

[7] D. G. Cahill, K. Goodson, and A. Majumdar, "Thermometry and thermal transport in micro/nanoscale solid-state devices and structures," *Journal of Heat Transfer*, vol. 124, no. 2, pp. 223–241, 2002.

[8] K. Voges, M. Vadala, and D. C. Lupascu, "Dense nanopowder composites for thermal insulation," *Physica Status Solidi (a)*, vol. 212, no. 2, pp. 439–442, 2015.

[9] F. Meng, J. Liu, and R. F. Richards, "Effect of water vapor on the thermal resistance between amorphous silica nanoparticles," *Journal of Applied Physics*, vol. 124, no. 5, p. 054303, 2018.

[10] D. Schneider, F. Liaqat, E. H. El Boudouti, Y. El Hassouani, B. Djafari-Rouhani, W. Tremel, H.-J. Butt, and G. Fytas, "Engineering the hypersonic phononic band gap of hybrid bragg stacks," *Nano Letters*, vol. 12, no. 6, pp. 3101–3108, 2012.

[11] N. Gomopoulos, D. Maschke, C. Y. Koh, E. L. Thomas, W. Tremel, H. J. Butt, and G. Fytas, "One-dimensional hypersonic phononic crystals," *Nano Letters*, vol. 10, no. 3, pp. 980–984, 2010.

[12] T. Fisher, *Thermal Energy at the Nanoscale*. World Scientific, 2013.

[13] A. F. Mills, *Heat Transfer*. Irwin, 1992.

[14] A. Waygood, *An introduction to electrical science*. Routledge, 2018.

[15] R. Soto, *Kinetic theory and transport phenomena*. Oxford University Press, 2016, vol. 25.

[16] J. Ravichandran, A. K. Yadav, R. Cheaito, P. B. Rossen, A. Soukiassian, S. J. Suresha, J. C. Duda, B. M. Foley, C.-H. Lee, Y. Zhu, A. W. Lichtenberger, J. E. Moore, D. A. Muller, D. G. Schlom, P. E. Hopkins, A. Majumdar, R. Ramesh, and M. A. Zurbuchen, "Crossover from incoherent to coherent phonon scattering in epitaxial oxide superlattices," *Nature Materials*, vol. 13, no. 2, pp. 168–172, 2014.

[17] K. Kuriki, O. Shapira, S. D. Hart, G. Benoit, Y. Kuriki, J. F. Viens, M. Bayindir, J. D. Joannopoulos, and Y. Fink, "Hollow multilayer photonic bandgap fibers for NIR applications," *Optics Express*, vol. 12, no. 8, pp. 1510–1517, 2004.

[18] D. Schneider, F. Liaqat, E. H. El Boudouti, O. El Abouti, W. Tremel, H.-J. Butt, B. Djafari-Rouhani, and G. Fytas, "Defect-controlled hypersound propagation in hybrid superlattices," *Physical Review Letters*, vol. 111, no. 16, p. 164301, 2013.

[19] W. Bies, R. Radtke, and H. Ehrenreich, "Phonon dispersion effects and the thermal conductivity reduction in GaAs/AlAs superlattices," *Journal of applied physics*, vol. 88, no. 3, pp. 1498–1503, 2000.

[20] N. Zen, T. A. Puurtinen, T. J. Isotalo, S. Chaudhuri, and I. J. Maasilta, "Engineering thermal conductance using a two-dimensional phononic crystal," *Nature Communications*, vol. 5, p. 3435, 2014.

[21] E. Dechaumphai, D. Lu, J. J. Kan, J. Moon, E. E. Fullerton, Z. Liu, and R. Chen, "Ultralow thermal conductivity of multilayers with highly dissimilar debye temperatures," *Nano Letters*, vol. 14, no. 5, pp. 2448–2455, 2014.

[22] E. Pokatilov, D. Nika, and A. Balandin, "Acoustic-phonon propagation in rectangular semiconductor nanowires with elastically dissimilar barriers," *Physical Review B*, vol. 72, no. 11, p. 113311, 2005.

[23] J.-P. Niemela, A. Giri, P. E. Hopkins, and M. Karppinen, "Ultra-low thermal conductivity in $TiO_2 : C$ superlattices," *Journal of Materials Chemistry A*, vol. 3, pp. 11 527–11 532, 2015.

[24] K. Termentzidis, *Nanostructured Semiconductors: Amorphization and Thermal Properties*. CRC Press, 2017.

[25] J. Cheeke, H. Ettinger, and B. Hebral, "Analysis of heat transfer between solids at low temperatures," *Canadian Journal of Physics*, vol. 54, no. 17, pp. 1749–1771, 1976.

[26] B. P. Jelle, "Traditional, state-of-the-art and future thermal building insulation materials and solutions properties, requirements and possibilities," *Energy and Buildings*, vol. 43, no. 10, pp. 2549–2563, 2011.

[27] Arena, L.B. and Building America (Program : U.S.), *Construction Guidelines for High R-value Walls Without Exterior Rigid Insulation*, ser. NREL/SR. National Renewable Energy Laboratory, 2016.

[28] P. Tsilingiris, "Thermophysical and transport properties of humid air at temperature range between 0 and 100°C," *Energy Conversion and Management*, vol. 49, pp. 1098–1110, 2008.

[29] F. C. Winkelmann, "Modeling windows in energyplus," in *Proceedings of IBPSA Building Simulation*, 2001.

[30] Y. Fang, T. J. Hyde, and N. Hewitt, "Predicted thermal performance of triple vacuum glazing," *Solar Energy*, vol. 84, no. 12, pp. 2132–2139, 2010.

[31] R. Baetens, B. P. Jelle, A. Gustavsen, and S. Grynning, "Gas-filled panels for building applications: A state-of-the-art review," *Energy and Buildings*, vol. 42, no. 11, pp. 1969–1975, 2010.

[32] A. Pye, "A review of asbestos substitute materials in industrial applications," *Journal of Hazardous Materials*, vol. 3, no. 2, pp. 125–147, 1979.

[33] I. J. Selikoff, E. C. Hammond, and J. Churg, "Asbestos exposure, smoking, and neoplasia," *Journal of Occupational and Environmental Medicine*, vol. 204, no. 2, pp. 106–112, 1968.

[34] 'United States Geological Survey', "Images of fibrous and asbestiform minerals," Online, 2015, http://usgsprobe.cr.usgs.gov/picts2.html.

[35] NASA. "Ideas that Gel". [Online]. Available: https://www.nasa.gov/vision/earth/technologies/aerogel.html

[36] A. S. Dorcheh and M. Abbasi, "Silica aerogel; synthesis, properties and characterization," *Journal of Materials Processing Technology*, vol. 199, no. 1-3, pp. 10–26, 2008.

[37] C. J. Brinker and G. W. Scherer, *Sol-gel science: the physics and chemistry of sol-gel processing*. Academic press, 2013.

[38] M. Schmidt and F. Schwertfeger, "Applications for silica aerogel products," *Journal of Non-Crystalline Solids*, vol. 225, pp. 364–368, 1998.

[39] R. Prasher, "Ultralow thermal conductivity of a packed bed of crystalline nanoparticles: A theoretical study," *Physical Review B*, vol. 74, no. 16, p. 165413, 2006.

[40] M. Elsahati, K. Clarke, and R. Richards, "Thermal conductivity of copper and silica nanoparticle packed beds," *International Communications in Heat and Mass Transfer*, vol. 71, pp. 96–100, 2016.

[41] L. Bippus, M. Jaber, B. Lebeau, D. Schleich, and Y. Scudeller, "Thermal conductivity of heat treated mesoporous silica particles," *Microporous and Mesoporous Materials*, vol. 190, pp. 109–116, 2014.

[42] F. Meng, M. Elsahati, J. Liu, and R. F. Richards, "Thermal resistance between amorphous silica nanoparticles," *Journal of Applied Physics*, vol. 121, no. 19, p. 194302, 2017.

[43] X. J. Hu, R. Prasher, and K. Lofgreen, "Ultralow thermal conductivity of nanoparticle packed bed," *Applied Physics Letters*, vol. 91, no. 20, p. 203113, 2007.

[44] E. Tervo, O. Adewuyi, J. Hammonds, and B. Cola, "High thermal conductivity in polaritonic SiO_2 nanoparticle beds," *Materials Horizons*, vol. 3, no. 5, pp. 434–441, 2016.

[45] P. Wan, L. Gao, and J. Wang, "Approaching ultra-low thermal conductivity in β-SiC nanoparticle packed beds through multiple heat blocking mechanisms," *Scripta Materialia*, vol. 128, pp. 1–5, 2017.

[46] K.-C. Fang, C.-I. Weng, and S.-P. Ju, "An investigation into the structural features and thermal conductivity of silicon nanoparticles using molecular dynamics simulations," *Nanotechnology*, vol. 17, no. 15, p. 3909, 2006.

[47] G. S. Rohrer, *Structure and bonding in crystalline materials*. Cambridge University Press, 2001.

[48] R. C. Schroden, M. Al-Daous, C. F. Blanford, and A. Stein, "Optical properties of inverse opal photonic crystals," *Chemistry of Materials*, vol. 14, no. 8, pp. 3305–3315, 2002.

[49] E. Alonso-Redondo, H. Huesmann, E.-H. El Boudouti, W. Tremel, B. Djafari-Rouhani, H.-J. Butt, and G. Fytas, "Phoxonic hybrid superlattice," *American Chemical Society Applied Materials & Interfaces*, vol. 7, no. 23, pp. 12 488–12 495, 2015.

[50] G. Pernot, M. Stoffel, I. Savic, F. Pezzoli, P. Chen, G. Savelli, A. Jacquot, J. Schumann, U. Denker, I. Mönch *et al.*, "Precise control of thermal conductivity at the nanoscale through individual phonon-scattering barriers," *Nature Materials*, vol. 9, no. 6, p. 491, 2010.

[51] P. Hyldgaard and G. Mahan, "Phonon superlattice transport," *Physical Review B*, vol. 56, no. 17, p. 10754, 1997.

[52] H. Cong, F. Yang, C. Xue, K. Yu, L. Zhou, N. Wang, B. Cheng, and Q. Wang, "Multilayer graphene–GeSn quantum well heterostructure SWIR light source," *Small*, vol. 14, no. 17, p. 1704414, 2018.

[53] F.-L. Arthur, M. Samy, A. Tristan, L. David, and T. Konstantinos, "Thermal properties of amorphous/crystalline silicon superlattices," *Journal of Physics: Condensed Matter*, vol. 26, no. 35, p. 355801, 2014.

[54] M. H. Check, D. S. Dudis, J. B. Ferguson, J. J. Gengler, H. A. Seibel, B. C. Elliott, Z. S. Votaw, and A. A. Voevodin, "Synthesis of zinc fulleride (Zn_xC60) thin films with ultra-low thermal conductivity," *Journal of Applied Physics*, vol. 110, no. 12, p. 124320, 2011.

[55] G. Chen, "Size and interface effects on thermal conductivity of superlattices and periodic thin-film structures," *Journal of Heat Transfer*, vol. 119, no. 2, pp. 220–229, 1997.

[56] F. J. Ye, Z. G. Zeng, C. Lin, and Z. Y. Hu, "The investigation of electronphonon coupling on thermal transport across metalsemiconductor periodic multilayer films," *Journal of Materials Science*, vol. 50, no. 2, pp. 833–839, 2015.

[57] I. Savi, D. Donadio, F. Gygi, and G. Galli, "Dimensionality and heat transport in Si-Ge superlattices," *Applied Physics Letters*, vol. 102, no. 7, p. 073113, 2013.

[58] A. Giri, J.-P. Niemelä, C. J. Szwejkowski, M. Karppinen, and P. E. Hopkins, "Reduction in thermal conductivity and tunable heat capacity of inorganic/organic hybrid superlattices," *Physical Review B*, vol. 93, no. 2, p. 024201, 2016.

[59] C. Chiritescu, D. G. Cahill, C. Heideman, Q. Lin, C. Mortensen, N. T. Nguyen, D. Johnson, R. Rostek, and H. Bttner, "Low thermal conductivity in nanoscale layered materials synthesized by the method of modulated elemental reactants," *Journal of Applied Physics*, vol. 104, no. 3, p. 033533, 2008.

[60] D. Zhiwei, J. Jin-Wu, P. Qing-Xiang, and Z. Yong-Wei, "In-plane and cross-plane thermal conductivities of molybdenum disulfide," *Nanotechnology*, vol. 26, no. 6, p. 065703, 2015.

[61] K. An, K. S. Ravichandran, R. E. Dutton, and S. Semiatin, "Microstructure, texture, and thermal conductivity of single-layer and multilayer thermal barrier coatings of Y_2O_3-stabilized ZrO_2 and Al_2O_3 made by physical vapor deposition," *Journal of the American Ceramic Society*, vol. 82, no. 2, pp. 399–406, 1999.

[62] F. Döring, H. Ulrichs, S. Pagel, M. Müller, M. Mansurova, M. Müller, C. Eberl, T. Erichsen, D. Huebner, P. Vana *et al.*, "Confinement of phonon propagation in laser deposited tungsten/polycarbonate multilayers," *New Journal of Physics*, vol. 18, no. 9, p. 092002, 2016.

[63] H. Mizuno, S. Mossa, and J.-L. Barrat, "Beating the amorphous limit in thermal conductivity by superlattices design," *Scientific Reports*, vol. 5, p. 14116, 2015.

[64] R. R. Das, Y. I. Yuzyuk, P. Bhattacharya, V. Gupta, and R. Katiyar, "Folded acoustic phonons and soft mode dynamics in $BaTiO_3/SrTiO_3$ superlattices," *Physical Review B*, vol. 69, no. 13, p. 132302, 2004.

[65] C. Chiritescu, D. G. Cahill, N. Nguyen, D. Johnson, A. Bodapati, P. Keblinski, and P. Zschack, "Ultralow thermal conductivity in disordered, layered WSe_2 crystals," *Science*, vol. 315, no. 5810, pp. 351–353, 2007.

[66] M. Noh, C. D. Johnson, M. D. Hornbostel, J. Thiel, and D. C. Johnson, "Control of reaction pathway and the nanostructure of final products through the design of modulated elemental reactants," *Chemistry of Materials*, vol. 8, no. 8, pp. 1625–1635, 1996.

[67] P. Erhart, P. Hyldgaard, and D. O. Lindroth, "Microscopic origin of thermal conductivity reduction in disordered Van der Waals solids," *Chemistry of Materials*, vol. 27, no. 16, pp. 5511–5518, 2015.

[68] J.-K. Yu, S. Mitrovic, D. Tham, J. Varghese, and J. R. Heath, "Reduction of thermal conductivity in phononic nanomesh structures," *Nature Nanotechnology*, vol. 5, no. 10, pp. 718–721, 2010.

[69] J. Tang, H.-T. Wang, D. H. Lee, M. Fardy, Z. Huo, T. P. Russell, and P. Yang, "Holey silicon as an efficient thermoelectric material," *Nano Letters*, vol. 10, no. 10, pp. 4279–4283, 2010.

[70] T. Gorishnyy, C. K. Ullal, M. Maldovan, G. Fytas, and E. L. Thomas, "Hypersonic phononic crystals," *Physical Review Letters*, vol. 94, no. 11, p. 115501, 2005, pRL.

[71] N. K. Ravichandran and A. J. Minnich, "Coherent and incoherent thermal transport in nanomeshes," *Physical Review B*, vol. 89, p. 205432, 2014.

[72] L. Cui, S. Shi, Z. Li, G. Wei, and X. Du, "Reduction of thermal conductivity in silicene nanomesh: insights from coherent and incoherent phonon transport," *Physical Chemistry Chemical Physics*, vol. 20, no. 42, pp. 27 169–27 175, 2018.

[73] S. Neogi, J. S. Reparaz, L. F. C. Pereira, B. Graczykowski, M. R. Wagner, M. Sledzinska, A. Shchepetov, M. Prunnila, J. Ahopelto, C. M. Sotomayor-Torres, and D. Donadio, "Tuning thermal transport in ultrathin silicon membranes by surface nanoscale engineering," *American Chemical Society Nano*, vol. 9, no. 4, pp. 3820–3828, 2015.

[74] B. L. Davis and M. I. Hussein, "Nano metamaterial: Thermal conductivity reduction by local resonance," *Physical Review Letters*, vol. 112, no. 5, p. 055505, 2014.

[75] L. Yang, N. Yang, and B. Li, "Extreme low thermal conductivity in nanoscale 3d Si phononic crystal with spherical pores," *Nano Letters*, vol. 14, no. 4, pp. 1734–1738, 2014.

[76] M. Maldovan, "Phonon wave interference and thermal bandgap materials," *Nature Materials*, vol. 14, no. 7, p. 667674, 2015.

[77] ——, "Narrow low-frequency spectrum and heat management by thermocrystals," *Physical Review Letters*, vol. 110, no. 2, p. 025902, 2013.

[78] N. O. Birge and S. R. Nagel, "Wide-frequency specific heat spectrometer," *Review of Scientific Instruments*, vol. 58, no. 8, pp. 1464–1470, 1987.

[79] O. Kwon, J. S. Lee, Y. K. Choi, S. Park, and W. S. Chung, "AC type flowmeter and method of mapping flow rate data for the same," 2006, uS Patent 7,007,549.

[80] C. Clausen, T. Pedersen, and A. Bentien, "The 3-omega method for the measurement of fouling thickness, the liquid flow rate, and surface contact," *Sensors*, vol. 17, no. 3, p. 552, 2017.

[81] M. Ashauer, H. Glosch, F. Hedrich, N. Hey, H. Sandmaier, and W. Lang, "Thermal flow sensor for liquids and gases based on combinations of two principles," *Sensors and Actuators A: Physical*, vol. 73, no. 1-2, pp. 7–13, 1999.

[82] N. Yi, B. K. Park, D. Kim, and J. Park, "Micro-droplet detection and characterization using thermal responses," *Lab on a Chip*, vol. 11, no. 14, pp. 2378–2384, 2011.

[83] S. R. Choi, J. Hong, and D. Kim, "A micromachined AC thermal sensor for monitoring the liquid–gas interface in a microchannel," *Sensors and Actuators A: Physical*, vol. 150, no. 1, pp. 40–45, 2009.

[84] A. S. Cubukcu, D. F. R. Romero, and G. A. Urban, "A dynamic thermal flow sensor for simultaneous measurement of thermal conductivity and flow velocity of gases," *Sensors and Actuators A: Physical*, vol. 208, pp. 73–87, 2014.

[85] S. R. Choi and D. Kim, "Real-time thermal characterization of 12 nl fluid samples in a microchannel," *Review of Scientific Instruments*, vol. 79, no. 6, p. 064901, 2008.

[86] F. Chen, J. Shulman, Y. Xue, C. Chu, and G. S. Nolas, "Thermal conductivity measurement under hydrostatic pressure using the 3ω method," *Review of Scientific Instruments*, vol. 75, no. 11, pp. 4578–4584, 2004.

[87] S. Doganay, A. Turgut, and L. Cetin, "Magnetic field dependent thermal conductivity measurements of magnetic nanofluids by 3ω method," *Journal of Magnetism and Magnetic Materials*, vol. 474, pp. 199–206, 2019.

[88] F. Cao, Y. Liu, J. Xu, Y. He, B. Hammouda, R. Qiao, and B. Yang, "Probing nanoscale thermal transport in surfactant solutions," *Scientific Reports*, vol. 5, p. 16040, 2015.

[89] B. K. Park, N. Yi, J. Park, Y. Kim, and D. Kim, "Development of a thermal sensor to probe cell viability and concentration in cell suspensions," *American Institute of Physics Advances*, vol. 4, no. 4, p. 047120, 2014.

[90] B. Kyoo Park, N. Yi, J. Park, and D. Kim, "Thermal conductivity of single biological cells and relation with cell viability," *Applied Physics Letters*, vol. 102, no. 20, p. 203702, 2013.

[91] B. K. Park, Y. Woo, D. Jeong, J. Park, T.-Y. Choi, D. P. Simmons, J. Ha, and D. Kim, "Thermal conductivity of biological cells at cellular level and correlation with disease state," *Journal of Applied Physics*, vol. 119, no. 22, p. 224701, 2016.

[92] A. Muralidhar, E. Swadel, M. Spiekerman, S. Suei, M. Fraser, M. Ingerfeld, A. B. Tayagui, and A. Garrill, "A pressure gradient facilitates mass flow in the oomycete *Achlya bisexualis*," *Microbiology*, vol. 162, no. 2, pp. 206–213, 2016.

[93] J. Bove, B. Vaillancourt, J. Kroeger, P. K. Hepler, P. W. Wiseman, and A. Geitmann, "Magnitude and direction of vesicle dynamics in growing pollen tubes using spatiotemporal image correlation spectroscopy and fluorescence recovery after photobleaching," *Plant Physiology*, vol. 147, no. 4, pp. 1646–1658, 2008.

[94] V. Couvreur, M. Faget, G. Lobet, M. Javaux, F. Chaumont, and X. Draye, "Going with the flow: multiscale insights into the composite nature of water transport in roots," *Plant Physiology*, vol. 178, no. 4, pp. 1689–1703, 2018.

[95] D. d. Koninck, "Thermal conductivity measurements using the 3-omega technique: Application to power harvesting microsystems," Masters Thesis, McGill Univeristy, 2008.

[96] P. B. Kaul, K. A. Day, and A. R. Abramson, "Application of the three omega method for the thermal conductivity measurement of polyaniline," *Journal of Applied Physics*, vol. 101, no. 8, p. 083507, 2007.

[97] M. Bogner, G. Benstetter, and Y. Q. Fu, "Cross-and in-plane thermal conductivity of aln thin films measured using differential 3-omega method," *Surface and Coatings Technology*, vol. 320, pp. 91–96, 2017.

[98] V. Mishra, C. L. Hardin, J. E. Garay, and C. Dames, "A 3 omega method to measure an arbitrary anisotropic thermal conductivity tensor," *Review of Scientific Instruments*, vol. 86, no. 5, p. 054902, 2015.

[99] Y. Xu, S. Petit-Watelot, V. Polewczyk, G. Parent, F. Montaigne, J.-E. Wegrowe, S. Mangin, D. Lacroix, M. Hehn, and D. Lacour, "Towards thermal reading of magnetic states in hall crosses," *Physical Review Applied*, vol. 9, no. 3, p. 034028, 2018.

[100] G. Pennelli, E. Dimaggio, and M. Macucci, "Note: Improvement of the 3 ω thermal conductivity measurement technique for its application at the nanoscale," *Review of Scientific Instruments*, vol. 89, no. 1, p. 016104, 2018.

[101] J. Jin, M. P. Manoharan, Q. Wang, and M. Haque, "In-plane thermal conductivity of nanoscale polyaniline thin films," *Applied Physics Letters*, vol. 95, no. 3, p. 033113, 2009.

[102] C. Dames, "Measuring the thermal conductivity of thin films: 3 omega and related electrothermal methods," *Annual Review of Heat Transfer*, vol. 16, no. 16, pp. 7–49, 2013.

[103] C. Dames and G. Chen, "1ω, 2ω, and 3ω methods for measurements of thermal properties," *Review of Scientific Instruments*, vol. 76, no. 12, p. 124902, 2005.

[104] M. O. Elsahati and R. Richards, "Effect of moisture on nanoparticle packed beds," *International Journal of Heat and Mass Transfer*, vol. 112, pp. 171–184, 2017.

[105] R. Serway and J. Jewett, *Physics for scientists and engineers with modern physics*. Nelson Education, 2013.

[106] G. S. May, S. M. Sze *et al.*, *Fundamentals of semiconductor fabrication*. Wiley New York, 2004.

[107] P. Demester, L. Buydens, I. Moerman, D. Lootens, and P. Van Daele, "Non-planar MOVPE growth using a novel shadow-masking technique," *Journal of Crystal Growth*, vol. 107, no. 1-4, pp. 161–165, 1991.

[108] W. Tsang and M. Ilegems, "The preparation of GaAs thin-film optical components by molecular beam epitaxy using Si shadow masking technique," *Applied Physics Letters*, vol. 35, no. 10, pp. 792–795, 1979.

[109] Y. Zhou, J. Hone, A. T. Johnson, W. F. Smith, and N. Pinto, "Shadow mask evaporation and its application in nano-electronics," in *APS Meeting Abstracts*, 2002.

[110] D. P. Adams, M. J. Vasile, G. Benavides, and A. N. Campbell, "Micromilling of metal alloys with focused ion beamfabricated tools," *Precision Engineering*, vol. 25, no. 2, pp. 107–113, 2001.

[111] K. Kolari, "Deep plasma etching of glass with a silicon shadow mask," *Sensors and Actuators A: Physical*, vol. 141, no. 2, pp. 677–684, 2008.

[112] C.-H. Lu and K. Wang, "Filling through-silicon vias with conductive ferromagnetic silver-iron composite," in *The 9th IEEE International Conference on Nano/Micro Engineered and Molecular Systems (NEMS)*. IEEE, 2014, pp. 366–369.

[113] Microchemicals, *AZ 1500 Series Datasheet*, available online.

[114] Gammacril. Chemical resistance of p.m.m.a. [Online]. Available: www-eng.lbl.gov/~shuman/XENON/MATERIALS&COMPONENTS/TMA_PMMA/Acrylic-Rod-and-Tube_chemical-resistance.pdf

[115] Microchemicals, *AZ15nXT (450 CPS) Datasheet*, available online.

[116] J. Steele and T. Green, "Tame those versatile current source circuits," *Electronic Design*, vol. 61, pp. 1–7, 1992.

[117] Texas Instruments, *AN-1515 A Comprehensive Study of the Howland Current Pump.*

[118] K. Rao and G. U. Kulkarni, "A highly crystalline single au wire network as a high temperature transparent heater," *Nanoscale*, vol. 6, no. 11, pp. 5645–5651, 2014.

[119] T. Gilani and D. Rabchuk, "Electrical resistivity of gold thin film as a function of film thickness," *Canadian Journal of Physics*, vol. 96, no. 3, pp. 272–274, 2017.

[120] W. F. Leonard and R. Ramey, "Temperature coefficient of resistance in thin metal films," *Journal of Applied Physics*, vol. 37, no. 9, pp. 3634–3635, 1966.

[121] A. Oliva, J. Lugo, R. Gurubel-Gonzalez, R. Centeno, J. Corona, and F. Avilés, "Temperature coefficient of resistance and thermal expansion coefficient of 10-nm thick gold films," *Thin Solid Films*, vol. 623, pp. 84–89, 2017.

[122] G. Tang, Y. Zhao, G. Zhai, and C. Bi, "Phonon boundary scattering effect on thermal conductivity of thin films," *Journal of Applied Physics*, p. 046102, 2011.

[123] W. Martienssen and H. Warlimont, *Springer handbook of condensed matter and materials data*. Springer Science & Business Media, 2006.

[124] N. P. Bansal and R. H. Doremus, *Handbook of glass properties*. Elsevier, 2013.

[125] J. Zarzycki, *Glasses and the vitreous state*, 9th ed. Cambridge University Press, 1991.

[126] J. E. Mark *et al.*, *Physical properties of polymers handbook*. Springer, 2007, vol. 1076.

[127] P. Hofman, *Solid State Physics : An Introduction*, 2nd ed. John Wiley and Sons, Incorporated, 2015.

[128] S. Hostler, A. Abramson, M. Gawryla, S. Bandi, and D. Schiraldi, "Thermal conductivity of a clay-based aerogel," *International Journal of Heat and Mass Transfer*, vol. 52, no. 3-4, pp. 665–669, 2009.

[129] L. N. Acquaroli, P. Newby, C. Santato, and Y.-A. Peter, "Thermal properties of methyltrimethoxysilane aerogel thin films," *American Institute of Physics Advances*, vol. 6, no. 10, p. 105007, 2016.

[130] A. Polian, D. Vo-Thanh, and P. Richet, "Elastic properties of a-SiO_2 up to 2300 k from brillouin scattering measurements," *Europhysics Letters*, vol. 57, no. 3, p. 375, 2002.

[131] J. F. Shackelford, Y.-H. Han, S. Kim, and S.-H. Kwon, *CRC materials science and engineering handbook*. CRC press, 2016.

[132] E. J. P. Miranda Jr and J. Dos Santos, "Phononic band gaps in Al_2O_3/epoxy composite," in *Materials Science Forum*, vol. 912, 2018, pp. 112–117.

[133] L. Zhang and A. Chopelas, "Sound velocity of Al_2O_3 to 616 kbar," *Physics of the Earth and Planetary Interiors*, vol. 87, no. 1-2, pp. 77–83, 1994.

[134] R. O. Pohl, X. Liu, and E. Thompson, "Low-temperature thermal conductivity and acoustic attenuation in amorphous solids," *Reviews of Modern Physics*, vol. 74, no. 4, p. 991, 2002.

[135] A. J. Bullen, K. E. OHara, D. G. Cahill, O. Monteiro, and A. von Keudell, "Thermal conductivity of amorphous carbon thin films," *Journal of Applied Physics*, vol. 88, no. 11, pp. 6317–6320, 2000.

[136] K. L. Johnson, K. Kendall, and A. Roberts, "Surface energy and the contact of elastic solids," *Proceedings of the Royal Society of London.*, vol. 324, no. 1558, pp. 301–313, 1971.

[137] D. Salmon, "Thermal conductivity of insulations using guarded hot plates, including recent developments and sources of reference materials," *Measurement Science and Technology*, vol. 12, no. 12, p. R89, 2001.

[138] J. Alvarez-Quintana and J. Rodriguez-Viejo, "Extension of the 3ω method to measure the thermal conductivity of thin films without a reference sample," *Sensors and Actuators A: Physical*, vol. 142, no. 1, pp. 232–236, 2008.

[139] X. Li, W. Park, Y. P. Chen, and X. Ruan, "Absence of coupled thermal interfaces in Al_2O_3/Ni/Al_2O_3 sandwich structure," *Applied Physics Letters*, vol. 111, no. 14, p. 143102, 2017.

[140] E. Hall, "On a new action of the magnet on electric currents," *American Journal of Science*, no. 111, pp. 200–205, 1880.

[141] T. S. Moss, W. Paul, and S. P. Keller, *Handbook on semiconductors*. North-Holland Amsterdam, 1980.

[142] W. Jones and N. H. March, *Theoretical Solid State Physics: Perfect Lattices in Equilibrium*. Courier Corporation, 1985, vol. 1.

[143] X. Lu, O. Nilsson, J. Fricke, and R. W. Pekala, "Thermal and electrical conductivity of monolithic carbon aerogels," *Journal of Applied Physics*, vol. 73, no. 2, pp. 581–584, 1993.

[144] D. Do and H. Do, "A model for water adsorption in activated carbon," *Carbon*, vol. 38, no. 5, pp. 767–773, 2000.

[145] M. Dubinin, "Fundamentals of the theory of adsorption in micropores of carbon adsorbents: characteristics of their adsorption properties and microporous structures," *Carbon*, vol. 27, no. 3, pp. 457–467, 1989.

[146] M. Baklanov, K. Mogilnikov, V. Polovinkin, and F. Dultsev, "Determination of pore size distribution in thin films by ellipsometric porosimetry," *Journal of Vacuum Science & Technology B: Microelectronics and Nanometer Structures Processing, Measurement, and Phenomena*, vol. 18, no. 3, pp. 1385–1391, 2000.

[147] A. Bogner, G. Thollet, D. Basset, P.-H. Jouneau, and C. Gauthier, "Wet STEM: A new development in environmental SEM for imaging nano-objects included in a liquid phase," *Ultramicroscopy*, vol. 104, no. 3-4, pp. 290–301, 2005.

[148] S. K. Rhee, "Surface energies of silicate glasses calculated from their wettability data," *Journal of Materials Science*, vol. 12, no. 4, pp. 823–824, 1977.

[149] M. D. Losego, I. P. Blitz, R. A. Vaia, D. G. Cahill, and P. V. Braun, "Ultralow thermal conductivity in organoclay nanolaminates synthesized via simple self-assembly," *Nano Letters*, vol. 13, no. 5, pp. 2215–2219, 2013.

[150] S. Y. Choi, M. Mamak, G. Von Freymann, N. Chopra, and G. A. Ozin, "Mesoporous bragg stack color tunable sensors," *Nano Letters*, vol. 6, no. 11, pp. 2456–2461, 2006.

[151] D. B. Hall, P. Underhill, and J. M. Torkelson, "Spin coating of thin and ultrathin polymer films," *Polymer Engineering & Science*, vol. 38, no. 12, pp. 2039–2045, 1998.

[152] S. Beckford and M. Zou, "Micro/nano engineering on stainless steel substrates to produce superhydrophobic surfaces," *Thin Solid Films*, vol. 520, no. 5, pp. 1520–1524, 2011.

[153] D.-S. Lim, J. Ahn, H. Park, and J. Shin, "The effect of CeO_2 abrasive size on dishing and step height reduction of silicon oxide film in STI–CMP," *Surface and Coatings Technology*, vol. 200, no. 5-6, pp. 1751–1754, 2005.

[154] H. Tompkins and E. A. Irene, *Handbook of Ellipsometry*. William Andrew, 2005.

[155] A. Rothen, "The ellipsometer, an apparatus to measure thicknesses of thin surface films," *Review of Scientific Instruments*, vol. 16, no. 2, pp. 26–30, 1945.

[156] G. Beaucage, R. Composto, and R. Stein, "Ellipsometric study of the glass transition and thermal expansion coefficients of thin polymer films," *Journal of Polymer Science Part B: Polymer Physics*, vol. 31, no. 3, pp. 319–326, 1993.

[157] D. Lee, M. F. Rubner, and R. E. Cohen, "All-nanoparticle thin-film coatings," *Nano Letters*, vol. 6, no. 10, pp. 2305–2312, 2006.

[158] N. Yao and Z. L. Wang, *Handbook of Microscopy for Nanotechnology*. Springer, 2005.

[159] D. Neas and P. Klapetek, "Gwyddion: an open-source software for SPM data analysis," *Central European Journal of Physics*, vol. 10, pp. 181–188, 2012.

[160] V. Nock, L. M. Murray, M. M. Alkaisi, and R. J. Blaikie, "Patterning of polymer-encapsulated optical oxygen sensors by electron beam lithography," in *Proceedings of 2010 International Conference on Nanoscience and Nanotechnology*. IEEE, 2010, pp. 237–240.

[161] D. Brutin, *Droplet wetting and evaporation: from pure to complex fluids*. Academic Press, 2015.

[162] M. Hosokawa, K. Nogi, M. Naito, and T. Yokoyama, *Nanoparticle Technology Handbook*. Elsevier, 2012.

[163] C. J. Glassbrenner and G. A. Slack, "Thermal conductivity of silicon and germanium from 3k to the melting point," *Physics Review*, vol. 134, pp. A1058–A1069, 1964.

[164] T. J. Athauda, D. S. Decker, and R. R. Ozer, "Effect of surface metrology on the wettability of SiO_2 nanoparticle coating," *Materials Letters*, vol. 67, no. 1, pp. 338–341, 2012.

[165] Y.-C. Lee, K. C. Bretz, F. W. Wise, and W. Sachse, "Picosecond acoustic measurements of longitudinal wave velocity of submicron polymer films," *Applied Physics Letters*, vol. 69, no. 12, pp. 1692–1694, 1996.

[166] M. Tuohiniemi and M. Blomberg, "Surface-micromachined silicon air-gap bragg reflector for thermal infrared," *Journal of Micromechanics and Microengineering*, vol. 21, no. 7, p. 075014, 2011.

[167] A. Magrez, S. Kasas, V. Salicio, N. Pasquier, J. W. Seo, M. Celio, S. Catsicas, B. Schwaller, and L. Forró, "Cellular toxicity of carbon-based nanomaterials," *Nano Letters*, vol. 6, no. 6, pp. 1121–1125, 2006.

[168] J. Muller, F. Huaux, N. Moreau, P. Misson, J.-F. Heilier, M. Delos, M. Arras, A. Fonseca, J. B. Nagy, and D. Lison, "Respiratory toxicity of multi-wall carbon nanotubes," *Toxicology and Applied Pharmacology*, vol. 207, no. 3, pp. 221–231, 2005.

[169] T. Teranishi, M. Hosoe, T. Tanaka, and M. Miyake, "Size control of monodispersed Pt nanoparticles and their 2D organization by electrophoretic deposition," *The Journal of Physical Chemistry B*, vol. 103, no. 19, pp. 3818–3827, 1999.

[170] H. Kang, F. A. Detcheverry, A. N. Mangham, M. P. Stoykovich, K. C. Daoulas, R. J. Hamers, M. Müller, J. J. de Pablo, and P. F. Nealey, "Hierarchical assembly of nanoparticle superstructures from block copolymer-nanoparticle composites," *Physical review letters*, vol. 100, no. 14, p. 148303, 2008.

[171] S. Colin, *Microfluidics*. John Wiley & Sons, 2013.

[172] A. Tayagui, Y. Sun, D. A. Collings, A. Garrill, and V. Nock, "An elastomeric micropillar platform for the study of protrusive forces in hyphal invasion," *Lab on a Chip*, vol. 17, no. 21, pp. 3643–3653, 2017.

[173] R. R. Lew, "Mass flow and pressure-driven hyphal extension in *Neurospora crassa*," *Microbiology*, vol. 151, no. 8, pp. 2685–2692, 2005.

[174] D. J. Beebe, G. A. Mensing, and G. M. Walker, "Physics and applications of microfluidics in biology," *Annual Review of Biomedical Engineering*, vol. 4, no. 1, pp. 261–286, 2002.

[175] J. R. Davis *et al.*, *ASM specialty handbook*. ASM International Materials Park, OH, 1993.

[176] D. microlaminates, *ADEX Epoxy Thin Film Rolls/Sheets Datasheet*, 2019.

[177] Y. Sun, A. Tayagui, H. Shearer, A. Garrill, and V. Nock, "A microfluidic platform with integrated sensing pillars for protrusive force measurements on neurospora crassa," in *Proceedings of 2018 IEEE Micro Electro Mechanical Systems (MEMS)*. IEEE, 2018, pp. 1116–1119.

[178] B.-H. Jo, L. M. Van Lerberghe, K. M. Motsegood, and D. J. Beebe, "Three-dimensional micro-channel fabrication in polydimethylsiloxane (PDMS) elastomer," *Journal of Microelectromechanical Systems*, vol. 9, no. 1, pp. 76–81, 2000.

[179] P. Tabeling, *Introduction to Microfluidics*. Wiley Online Library, 2006, vol. 45.

[180] B. J. Kirby, *Micro-and nanoscale fluid mechanics: transport in microfluidic devices*. Cambridge university press, 2010.

[181] Z. Wang and R. B. Peterson, "Thermal wave applications in flow fields with steady velocity profile," *Journal of Heat Transfer*, vol. 132, no. 5, p. 054501, 2010.

[182] I. Knowles and R. J. Renka, "Methods for numerical differentiation of noisy data," *Electronic Journal of Differential Equations*, vol. 21, no. 2012, pp. 235–246, 2014.

[183] P. Szendro, G. Vincze, and A. Szasz, "Pink-noise behaviour of biosystems," *European Biophysics Journal*, vol. 30, no. 3, pp. 227–231, 2001.

[184] F. Hooge, "1/f noise sources," *IEEE Transactions on Electron Devices*, vol. 41, no. 11, pp. 1926–1935, 1994.

[185] Stanford Research Systems, *"About Lock-In Amplifiers - Application Note 3"*, 1999, available online, Accessed on: 9/05/2019.

[186] R. W. Schafer *et al.*, "What is a savitzky-golay filter," *IEEE Signal Processing Magazine*, vol. 28, no. 4, pp. 111–117, 2011.

[187] F. M. White, *Fluid Mechanics.*, 7th ed. McGraw Hill, 2011.

[188] A. Abadeh and R. R. Lew, "Mass flow and velocity profiles in neurospora hyphae: partial plug flow dominates intra-hyphal transport," *Microbiology*, vol. 159, no. 11, pp. 2386–2394, 2013.

[189] D. Jennings, "Translocation of solutes in fungi," *Biological Reviews*, vol. 62, no. 3, pp. 215–243, 1987.

[190] C. Barber, "Platinum resistance thermometers of small dimensions," *Journal of Scientific Instruments*, vol. 27, no. 2, p. 47, 1950.

[191] T. H. Kim and S. J. Kim, "Development of a micro-thermal flow sensor with thin-film thermocouples," *Journal of Micromechanics and Microengineering*, vol. 16, no. 11, p. 2502, 2006.

[192] V. Nock, A. Tayagui, and A. Garrill, "Elastomeric micropillar arrays for the study of protrusive forces in hyphal invasion," in *In MicroTAS 2015 - 19th International Conference on Miniaturized Systems for Chemistry and Life Sciences*, 2015.

[193] K. K. Lee, C. H. Ahn, and C. I. Hong, "Circadian rhythms in neurospora crassa on a polydimethylsiloxane microfluidic device for real-time gas perturbations," *Biomicrofluidics*, vol. 7, no. 4, p. 044129, 2013.

[194] L. Orcheston-Findlay, A. Hashemi, A. Garrill, and V. Nock, "A microfluidic gradient generator to simulate the oxygen microenvironment in cancer cell culture," *Microelectronic Engineering*, vol. 195, pp. 107–113, 2018.

[195] V. Nock and R. J. Blaikie, "Spatially resolved measurement of dissolved oxygen in multistream microfluidic devices," *IEEE Sensors Journal*, vol. 10, no. 12, pp. 1813–1819, 2010.

[196] Dalynn Biologicals, *Peptone Yeast Glucose Broths Datasheet*, available online, Accessed 2018.

[197] Y. Takeuchi, J. Schmid, J. H. Caldwell, and F. M. Harold, "Transcellular ion currents and extension of *Neurospora crassa* hyphae," *The Journal of Membrane Biology*, vol. 101, no. 1, pp. 33–41, 1988.

[198] N. Waipara, S. Hill, L. Hill, E. Hough, I. Horner *et al.*, "Surveillance methods to determine tree health, distribution of kauri dieback disease and associated pathogens," *New Zealand Plant Protection*, vol. 66, pp. 235–241, 2013.

[199] G. Boswijk, A. Fowler, A. Lorrey, J. Palmer, and J. Ogden, "Extension of the New Zealand kauri (agathis australis) chronology to 1724 bc," *The Holocene*, vol. 16, no. 2, pp. 188–199, 2006.

[200] C. Ecroyd, "Biological flora of New Zealand 8. *Agathis australis* (d. don) lindl.(araucariaceae) kauri," *New Zealand Journal of Botany*, vol. 20, no. 1, pp. 17–36, 1982.

[201] W. Silvester and T. Orchard, "The biology of kauri (agathis australis) in New Zealand. production, biomass, carbon storage, and litter fall in four forest remnants," *New Zealand Journal of Botany*, vol. 37, no. 3, pp. 553–571, 1999.

[202] Kauri dieback. [Online]. Available: www.kauridieback.co.nz

[203] New Zealand Plant Producers Incorporated. Myrtle rust stakeholders update - february 2019. Accessed, March 2019. [Online]. Available: www.nzppi.co.nz/documents/pests/Myrtle\%20Rust\%20Stakeholder\%20Update.pdf

[204] Ministry for Primary Industries. Myrtle rust. Accessed, March 2019. [Online]. Available: www.mpi.govt.nz/protection-and-response/responding/alerts/myrtle-rust/

[205] Y. Sun and V. Nock, "A monolithic polydimethylsiloxane platform for zoospore capture, germination and single hypha force sensing." in *Digest Technical Papers Transducers Conference*, 2019.

[206] I. Mori and Y. Ohshima, "Neural regulation of thermotaxis in *Caenorhabditis elegans*," *Nature*, vol. 376, p. 344, 1995.

[207] H. Mélida, J. V. Sandoval-Sierra, J. Diéguez-Uribeondo, and V. Bulone, "Analyses of extracellular carbohydrates in oomycetes unveil the existence of three different cell wall types," *Eukaryotic Cell*, vol. 12, no. 2, pp. 194–203, 2013.

[208] Y. P. Yu, S. L. Jackson, and A. Garrill, "Two distinct distributions of f-actin are present in the hyphal apex of the oomycete *Achlya bisexualis*," *Plant and Cell Physiology*, vol. 45, no. 3, pp. 275–280, 2004.

[209] O. Yamamoto and H. Kambe, "Thermal conductivity of cross-linked polymers. a comparison between measured and calculated thermal conductivities," *Polymer Journal*, vol. 2, no. 5, p. 623, 1971.

[210] C. Slayman and D. Gradmann, "Electrogenic proton transport in the plasma membrane of neurospora," *Biophysical Journal*, vol. 15, no. 9, pp. 968–971, 1975.

A CNC Micro-milling

A note for "easy" replication here. While the milling parameters are important, the sample mounting and cooling will have a equally large effect on initial success. Tool breakages are very common and can become expensive if care is not taken. Always use some form of coolant when using an end-mill smaller than 0.2 mm. Ensure that the shadow mask blank has a solid and uniform coat of adhesive binding it to the wood. If the blank is not firmly attached, the material will vibrate and break the bit. The depth of cut per pass should be kept reasonably light; 25% of the tool diameter, compared to 50% that is common in macro-scale machining. The full flute depth available in Performance microtool cutters is generally 3 times the diameter of the tool. When undertaking a slotting operation however, the feed-rate must be substantially smaller, or the overall depth of cut must be reduced (1/1 aspect ratio).

B Membrane Separated Flow - Magnitude response

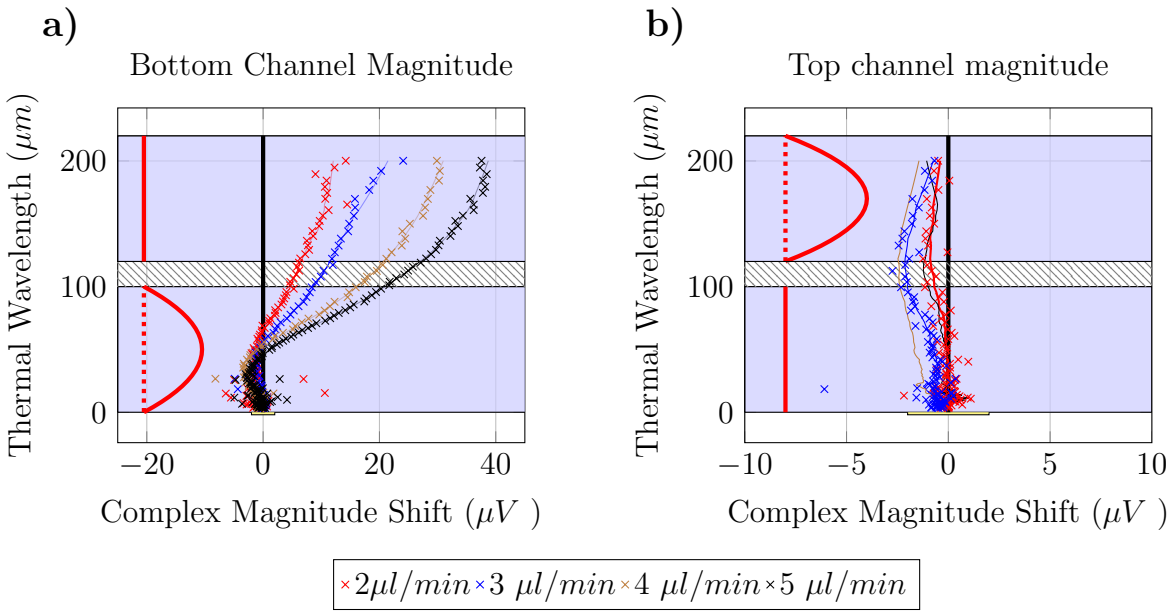

Figure B.1: *The 3ω magnitude responses to fluid flow in behind membrane fluid flow microfluidic chip.*

C Linear RT Perpendicular to fluid flow

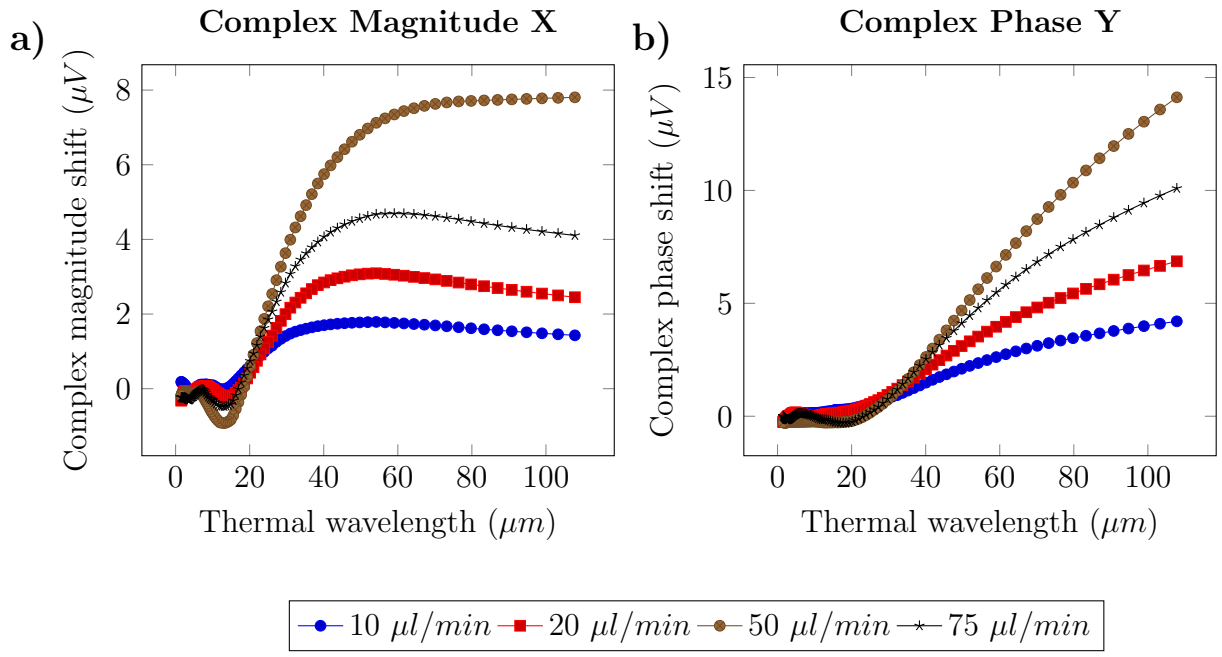

Figure C.1: *The convection response to a linear (perpendicular to flow) RT in a 100 μm channel.* **a)** *The complex magnitude response to fluid flows ranging between 10 and 75 μl/min, and* **b)** *the complex phase response for the same.*

D Membrane Separated Flow - Numerical Gradient

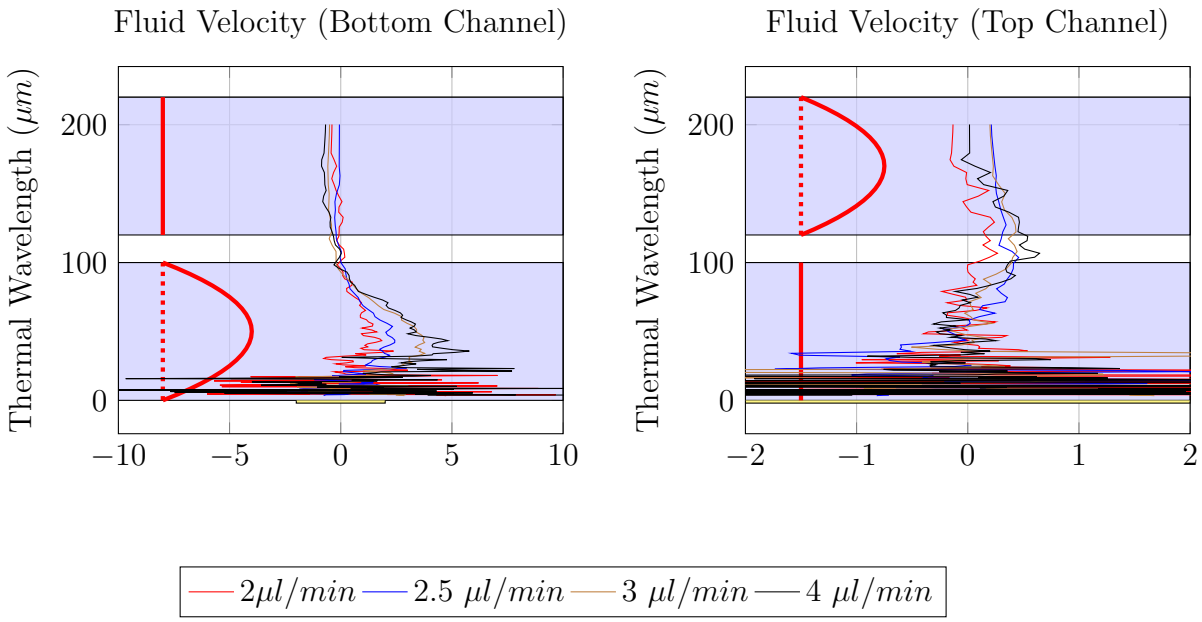

Figure D.1: *The numerical gradient of the conduction phase results in an extremely noisy signal. This is not easy to remedy, even with extremely strict filtering. Due to this a fitting procedure is used, so an analytical gradient can be used.*

E PYG Broth Response

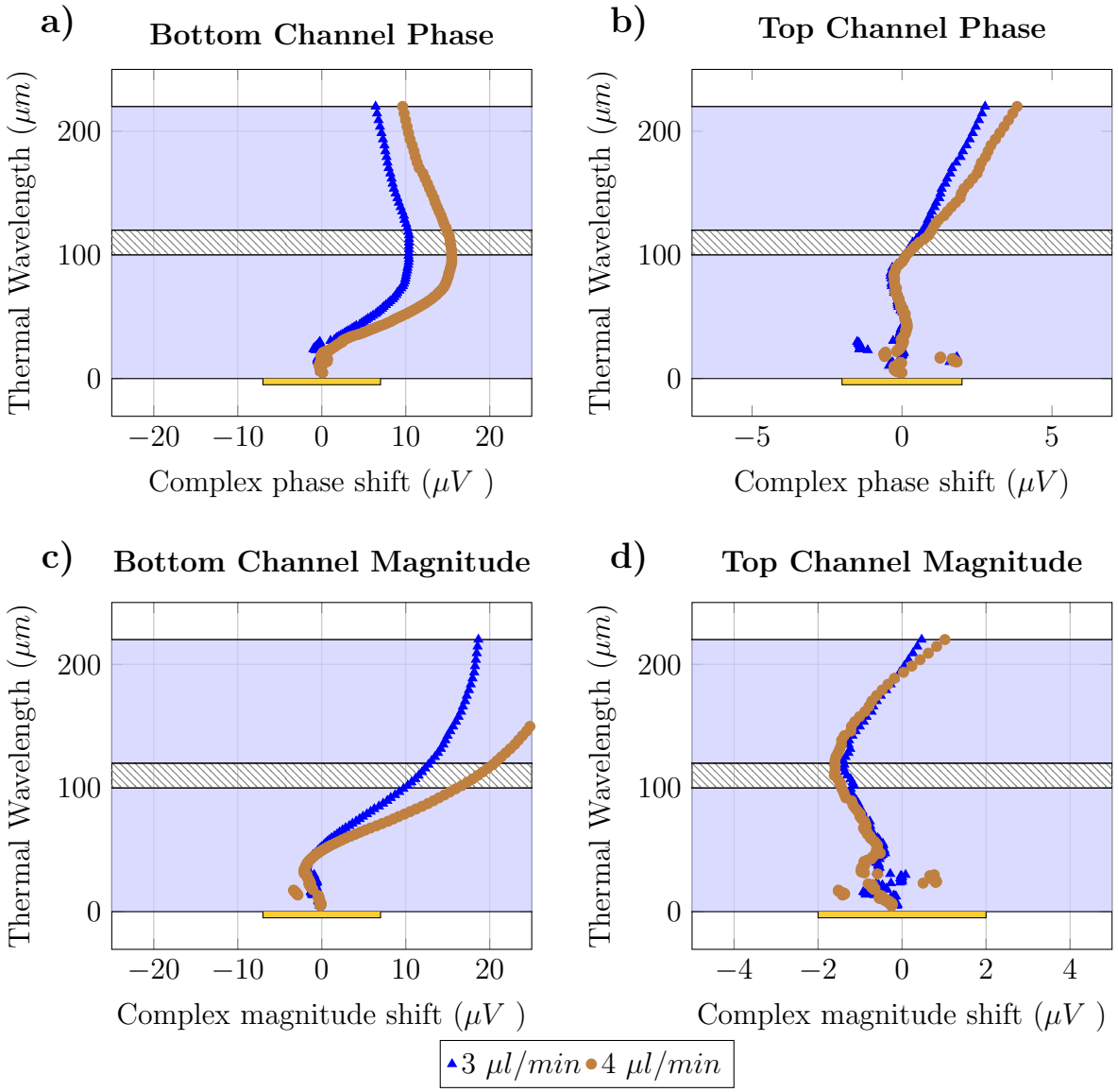

Figure E.1: *The magnitude and phase responses for PYG Broth in the triple layer "behind membrane" microfluidic chip.*

F Self annealing of Nichrome RT

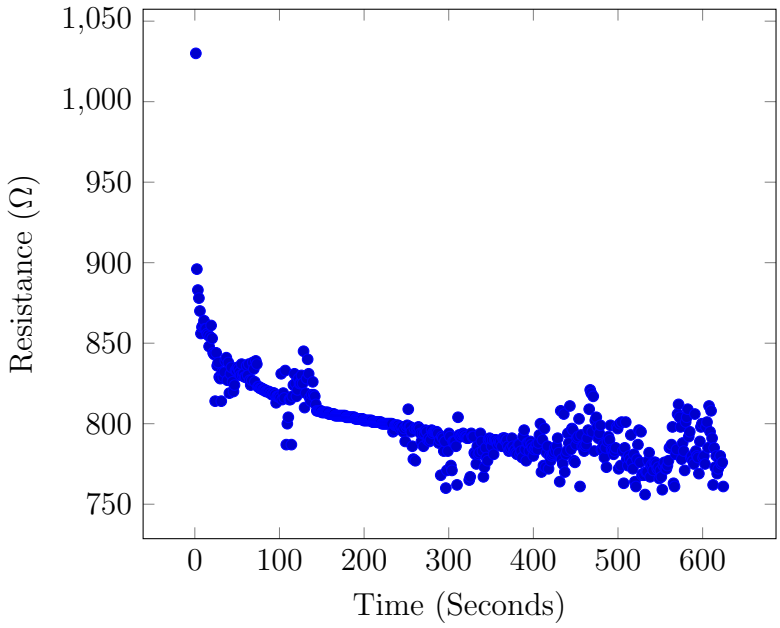

Figure F.1: *The self-annealing of the nichrome thermometer with time, with an annealing current of 5 mA. The resistance thermometer had a temperature coefficient of resistance of* $1.7 \times 10^{-4}/°C$. *Although more resistive, the TCR was extremely low, making it unsuitable for use as a* 3ω *thermometer.*